Novel Analysis Techniques and High-Speed Readout to Search for New Physics

Inauguraldissertation

der Philosophisch-naturwissenschaftlichen Fakultät
der Universität Bern

vorgelegt von

Armin Ilg

von Niederweningen ZH

Leiter der Arbeit:

Prof. Dr. Michele Weber

Albert Einstein Center for Fundamental Physics
Laboratorium für Hochenergiephysik
Physikalisches Institut

This work is licensed under the
Creative Commons Attribution-NonCommercial-ShareAlike 4.0
International License.

Novel Analysis Techniques and High-Speed Readout to Search for New Physics

Inauguraldissertation

der Philosophisch-naturwissenschaftlichen Fakultät
der Universität Bern

vorgelegt von

Armin Ilg

von Niederweningen ZH

Leiter der Arbeit:

Prof. Dr. Michele Weber

Albert Einstein Center for Fundamental Physics
Laboratorium für Hochenergiephysik
Physikalisches Institut

Von der philosophisch-naturwissenschaftlichen Fakultät angenommen.

Bern, 26. August 2021

Der Dekan
Prof. Dr. Zoltán Balogh

Abstract

The ATLAS experiment at the Large Hadron Collider is one of the most powerful tools for the measurement of the Standard Model properties and the search for new physics beyond it. This thesis describes a search for such a Beyond the Standard Model theory and also the development of the readout system of the future ATLAS Inner Tracker Pixel detector. Supersymmetric expansions of the Standard Model can solve some of the fundamental problems of it, but no sign of Supersymmetry has been found so far. This work presents the search for a Supersymmetry model that does not adhere to the Minimal Flavour Violation paradigm that is usually followed by simplified Supersymmetry searches. This opens the door to a possible mixing between the second and third generation supersymmetric partners of the quarks, the top-squark ($\tilde{t}$) and the charm-squark ($\tilde{c}$). In this Supersymmetry realisation, the decay of pair-produced $\tilde{t}_1$ can lead to final states with a b-jet, a c-jet and missing transverse momentum coming from the pair of neutralinos ($\tilde{\chi}_1^0$), which are the lightest supersymmetric particles in this model. I performed a search for this $tc + E_{\mathrm{T}}^{\mathrm{miss}}$ final state using simultaneous b- and c-tagging and also top-tagging techniques. In this context, I developed a Neural Network classifier to target compressed signal scenarios, where the jets have low transverse momenta. Limits on the cross section of generic new physics models and of the $tc + E_{\mathrm{T}}^{\mathrm{miss}}$ simplified model will be derived at the 95% confidence level, if no significant deviation from the Standard Model will be found once unblinded. Models featuring light neutralinos of $m(\tilde{\chi}_1^0) = 1\,\mathrm{GeV}$ are expected to be excluded up to $m(\tilde{t}_1) \sim 1050\,\mathrm{GeV}$, while signal scenarios with $\Delta m(\tilde{t}_1, \tilde{\chi}_1^0) \sim m_t$ are excluded up to neutralino masses of 425 GeV. To enable more precise tests of the Standard Model and to expand the discovery reach for new physics, the Large Hadron Collider will be upgraded to drastically increase the collision rate in the context of the High Luminosity Large Hadron Collider project. The innermost part of the ATLAS detector will be replaced with the new Inner Tracker to cope with the higher requirements on radiation tolerance and the larger pile-up. The increased trigger rate and larger occupancy and number of readout channels call for a new readout system. This thesis describes the development and tests of the Optosystem, which is responsible for the recovery, aggregation and electrical-optical conversion of all Inner Tracker Pixel data links. The Optosystem successfully passed a preliminary design review and is scheduled to be installed in ATLAS in the next long shutdown during 2026.

Acknowledgements

I first want to thank Antonio and Michele who gave me the chance to dive deep into the world of particle physics during lectures and with their support for me to participate in particle physics schools. Thank you for giving me the opportunity to write my Master and PhD theses in Bern.

During my time in the Bern ATLAS group, I had the great luck of working together with very knowledgeable and supportive postdocs, who also became good friends. Thank you Antonello, John, Laura and Niklaus. Thanks is also due to my PhD student colleagues, with whom I shared a lot of time and endless discussions about life and death. Thank you Claudia, Tom, Yves, Megh, Lea, Roman and Meinrad.

My work would not have been possible without the electronics and mechanics workshop as well as the LHEP scientific computing team. Special thanks goes to Roger and Camilla, who spent countless hours designing the Optosystem with me, teaching me a lot. Thanks goes also to all the other great people that I was able to work with in Bern, at CERN and via video.

During my time in Bern, I got to know many amazing people in ExWi, without whom my studies and life would not have been the same. I am also grateful for the continuous support, uplifting words and counsel of my family: thank you Albert, Marianne, Rahel and Roland.

Finally, I want to thank my wife Susanne who always believed in me and supported me. Without you, I would not be the person I am today.

Contents

Introduction

Humankind has always strived to understand the working principles of nature. One of the most fundamental questions that can be asked is: *what is the world around us made of?* The periodic table, developed one and a half centuries ago, identifies elements as the fundamental building blocks of the universe. Later, smaller and smaller constituents of matter were found with the advent of particle physics: the elementary particles. Today, the Standard Model (SM) of particle physics [1–4] describes all known elementary particles and all their interactions except for gravity.

The SM has withstood many precision tests and was completed by the discovery of the Higgs boson at the Large Hadron Collider (LHC, [5]) by the ATLAS and CMS collaborations in 2012 [6, 7]. Although extremely successful at characterising particle interactions over wide ranges of energy, the SM still leaves us with many open questions. The SM, for example, does not explain the observed phenomena of dark matter and dark energy and also only describes three out of the four fundamental forces. Even more fundamentally, the SM cannot explain why our universe is predominantly made of matter and not anti-matter. Lastly, assuming the SM to be correct up to the Planck scale, the Hierarchy Problem [8, 9] emerges: a large amount of fine-tuning is needed to keep the Higgs mass down at the observed mass of 125.1 GeV [10], which goes against the principle of naturalness [11–13].

Since the inception of the SM, many expansions of the it were proposed to solve some of these issues. One of the most promising candidates is Supersymmetry (SUSY, [14–20]), which introduces a symmetry between fermions and bosons. It can for example solve the Hierarchy Problem and introduces particles that can explain the dark matter abundance. Although well motivated, no proofs of this Beyond the SM (BSM) theory have been found so far. Searches at the LHC were able to exclude many SUSY models to masses of ~ 1 TeV or more [21,22]. The ATLAS experiment [23] searches for a wide range of SUSY states, such as the supersymmetric partners of the top and charm quarks (*squarks*). In final states containing two top and missing transverse momentum ($tt + E_{\mathrm{T}}^{\mathrm{miss}}$, [24]) or two charm quarks with missing transverse momentum ($cc + E_{\mathrm{T}}^{\mathrm{miss}}$, [25]), ATLAS derived exclusion limits to squark masses of up to 1.25 and 0.85 TeV correspondingly. SUSY is however far from excluded because merely very simple realisations of it have been considered so far.

In my thesis work, I wanted to search for a SUSY model that does not abide by the Minimal Flavour Violation paradigm [26] usually followed. This is motivated by Reference [27] which showed that models featuring substantial mixing between the second and third generation squarks are not yet excluded. Searches for third generation squarks therefore may not be able to detect mixed-flavour SUSY [28,29]. References [30] and [31]

therefore proposed searching for mixed final states containing both a top and a charm quark with missing transverse momentum ($tc+E_{\mathrm{T}}^{\mathrm{miss}}$), in contrast to the above mentioned $tt + E_{\mathrm{T}}^{\mathrm{miss}}$ and $cc + E_{\mathrm{T}}^{\mathrm{miss}}$ searches.

The targeted SUSY model predicts both a jet from a bottom and from a charm quark and requires a fully-hadronic decay of the bottom quark. To discriminate the SUSY signal from the SM background, both bottom and charm flavour tagging techniques are employed simultaneously. Signal topologies with boosted jets are tackled by also using large-radius tagging of the top quark (top-tagging). Contrary to this, compressed signal scenarios feature mostly jets with low transverse momentum, making discrimination to the SM backgrounds difficult and negating the usage of top-tagging. I therefore planned to develop and train a Neural Network using low-level event information as input to discriminate between SM and SUSY events in this region of phase space. The ATLAS Run 2 dataset, consisting of 139 fb^{-1} of proton-proton collisions recorded at the LHC at a centre-of-mass energy of 13 TeV, is used to look for this unique mixed-flavour SUSY signature for the first time.

The Run 3 of the LHC will produce another $\sim 300\,\mathrm{fb}^{-1}$ of proton-proton collisions at 13–14 TeV until 2024. Much more integrated luminosity is needed however for higher precision tests of the SM such as measurements of the Higgs self-coupling and to look for heavier and more elusive BSM signatures. The LHC will be upgraded between 2025 and 2027 in the context of the High-Luminosity LHC (HL-LHC, [32]) project. With an integrated luminosity of up to $4000\,\mathrm{fb}^{-1}$, the HL-LHC for example enables the discovery (exclusion) of top squarks with masses of up to 1.25 (1.7) TeV and the determination of the Higgs boson couplings at the percent level [33]. The high luminosity is achieved through a threefold increase of the number of simultaneous collisions and leads to a more hostile radiation environment around the interaction points. To deal with the busier collision signatures and larger radiation damage, also the LHC experiments needs to be improved.

The largest upgrade of ATLAS experiment for the HL-LHC is the Inner Tracker (ITk, [34, 35]) that is replacing the currently used Inner Detector. The ITk is an all-silicon tracker consisting of an inner Pixel and an outer Strip detector. Not only the sensing elements of the ITk are new, but also the readout system is completely replaced to deal with the increased amount of radiation and also the faster and more numerous data links needed to read out the detector. This thesis describes the ITk Pixel data transmission system concept, which foresees to transmit the data electrically inside of the ITk, followed by the optical transmission at speeds of 10.24 Gb/s through fibres out of the ATLAS detector to the counting room. The centrepiece of the Pixel data transmission system is the *Optosystem*. It is responsible for the aggregation and electrical-optical conversion (and vice versa) of all 26'000 Pixel links. In my thesis work I planned to develop the Optosystem conceptual design and the technical implementation of it, addressing aspects such as grounding and shielding, configuration and control, powering, and many more. I also planned to verify the Optosystem design in terms of high-speed data transmission performance, by the means of eye diagrams and bit error rate measurements. To do so, I envisaged to develop test setups using Field-programmable Gate Arrays (FPGAs) to both characterise individual Optosystem components and first Optosystem prototypes.

Chapter 1 first describes the SM and introduces SUSY. Then the LHC and the ATLAS experiment are detailed in Chapter 2. This is followed by a description of the particle

reconstruction and identification in Chapter 3. Next, Chapter 4 describes the analysis searching for mixed-flavour SUSY using the ATLAS dataset recorded between 2015 and 2018. Finally, Chapter 5 presents the High-Luminosity program of the LHC and the associated upgrade of the ATLAS detector, and focuses on the development and testing of the Optosystem for the ITk Pixel detector.

Chapter 1

The Standard Model and Supersymmetry

Since the advent of Quantum Mechanics, with Planck's hypothesis in 1900 stating that energy is quantised [36, 37], our understanding of the physical laws governing nature has increased tremendously. It was found that matter is made of *atoms*, themselves consisting of positively charged *nuclei* and negatively charged *electrons*. The electrons were later found to be lying on discrete energy levels as predicted by Quantum Mechanics, and a first theory of Quantum Electrodynamics (QED) was developed by Dirac [38] to describe the electromagnetic interaction between these charged particles and the particle of light, the *photon*. QED is the first of many Quantum Field Theories (QFTs), which combine field theory, quantum mechanics and special relativity to describe particles and their interactions by means of *Lagrangians*.

After the discoveries of the *proton* by Rutherford [39] and of the *neutron* by Chadwick [40,41], also the constituents of the nuclei and with that all building blocks of the periodic table and its isotopes were discovered. This however was not the end of the search for the constituents of matter, but merely the start.

By observing naturally occurring cosmic rays and accelerating charged particles to higher energies in the laboratory, more and more particles were found until in 1964 Gell-Mann [42] and Zweig [43] introduced the concept of *quarks* with charges of $-\frac{1}{3}e$ and $+\frac{2}{3}e$, where e is the elementary charge. Two such quarks would bind together to form *mesons* such as the pions, while three would constitute *baryons*. Both the mesons and the baryons are part of a group of particles called *hadrons*. Electron-scattering experiments conducted at the Stanford Linear Accelerator Center at the end of the 1960's then proved that this picture was indeed true [44] and the proton and neutron are not elementary, but composite particles. They are built of *up* (u) and *down*-type (d) quarks (proton: uud, neutron: udd), which are held together by the strong interaction with *gluons* as the mediator particle. Quantum Chromodynamics (QCD) is the theory that describes this interaction.

The next fundamental force in particle physics is the weak interaction. It is for example responsible for the nuclear fusion taking place in stars as well as β-decays, involving also the only weakly interacting *neutrinos*. The W and Z bosons, which are the mediators of the weak force, were discovered by the UA1 and UA2 experiments at the CERN Super

Proton Synchrotron in 1983 [45]. Already in the 1960's, Glashow, Weinberg and Salam [1–3] developed the Electro-weak (EW) theory that explains both the electromagnetic and weak interactions in an unified way. To give mass to the W and Z bosons, but not to the photon, the EW theory includes a neutral massive scalar field, the *Higgs field* [46–49]. This field also provides mass to the quarks and the charged *leptons*, which are the electron and its heavier siblings, the *muon* and the *tau*. The excitation of this field is the *Higgs boson*. This particle was discovered by the ATLAS and CMS collaborations in 2012 [6, 7], completing the Standard Model of particle physics.

1.1 The Standard Model of Particle Physics

The Standard Model (SM) of particle physics [1–4] is the union of QCD and the EW theory. As illustrated by Figure 1.1, the SM is precisely describing all known elementary particles and the strong, electromagnetic and weak interactions between them. The SM is a QFT that is invariant under local transformations (local *gauge* invariance). It has an underlying $\mathrm{SU(3)_C \times SU(2)_L \times U(1)_Y}$ symmetry. The most general Lagrangian invariant under this symmetry then defines the dynamics of the SM [50]. This section discusses the structure and working principles of the SM, where in the following *natural* units are used, setting both the speed of light and the reduced Planck constant to 1 ($c = \hbar = 1$) and using electron-volts ($1\,\mathrm{eV} = 1\,\mathrm{V} \cdot e$).

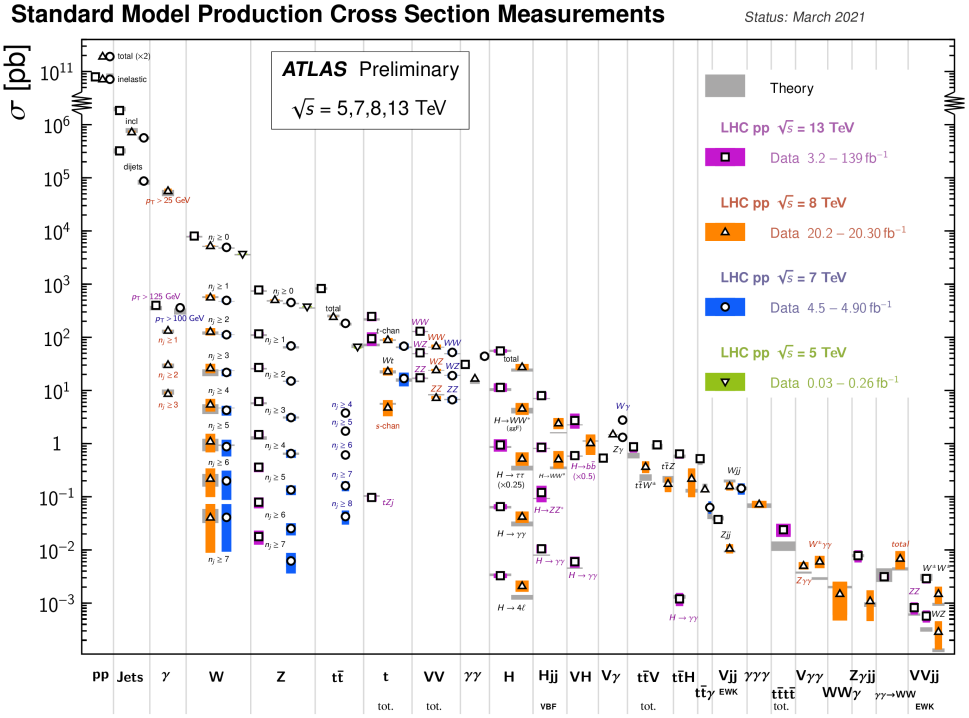

Figure 1.1: Comparison between SM predictions and ATLAS measurements of the total and fiducial production cross sections of various processes at different centre-of-mass energies ($\sqrt{s}$). Taken from Reference [51].

Figure 1.2 shows a diagrammatic representation of the SM particles and interactions.

The matter content of the SM is particles with a spin of 1/2 (*fermions*) that obey Fermi-Dirac statistics [52,53]. Each fermion (f) has an associated anti-fermion ($\bar{f}$) with opposite charges. Particles with a spin of 1 (*bosons*) are force mediators and obey Bose-Einstein statistics [54, 55]. Each fundamental force of the SM has one or more bosons associated to it, which is exchanged between the fermions in an interaction. The matter content can be split into two categories: The quarks interact via the strong force, while the leptons do not.

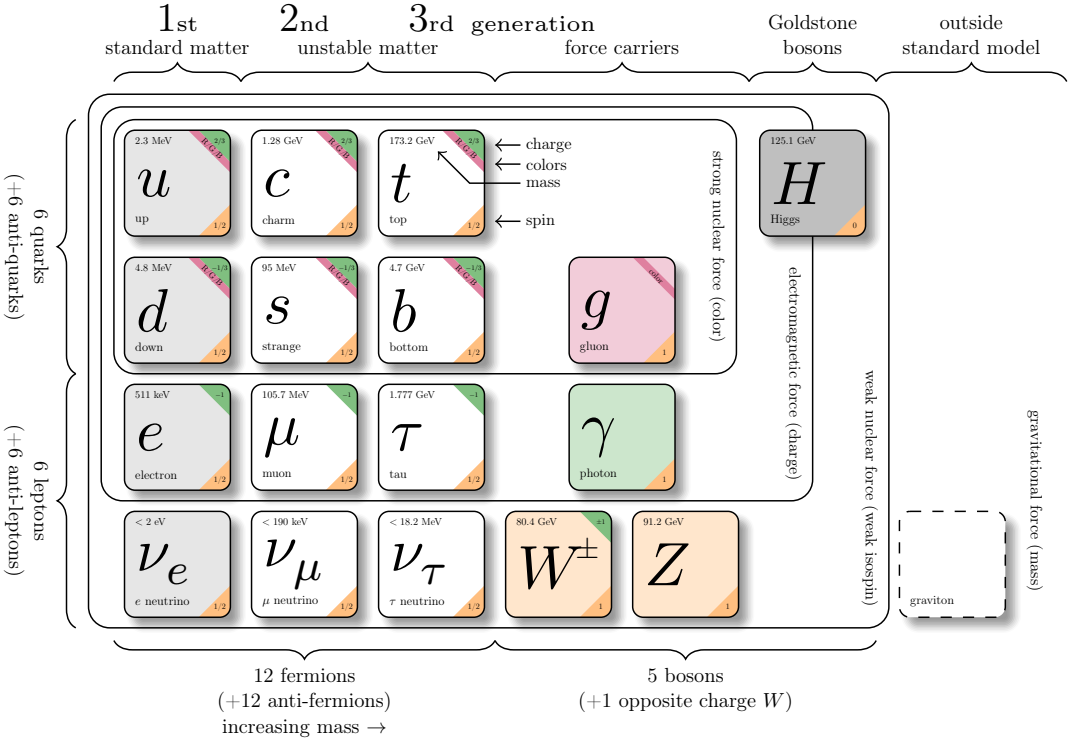

Figure 1.2: Diagrammatic representation of the particles and interactions of the SM of particle physics. Taken from Reference [56].

There are three generations of quarks. Each generation features a doublet of quarks with one component of it having an electric charge of $+\frac{2}{3}e$ (u, c, t) and the other of $-\frac{1}{3}e$ (d, s, b). These six types of quarks are referred to as *flavours*. Due to their electric charge, quarks can interact by the electromagnetic force. The quarks also carry another conserved charge called *colour* [57–59] that is governed by the non-abelian SU(3) gauge group [60]. The colour charge of a quark can either be in a red, green or blue colour state (anti-red, anti-green and anti-blue for anti-particles), while there are eight different active gluons that also carry colour charge. Coloured particles interact via the strong force, with the gluon being the mediator of the force. Quarks and gluons do not exist as free particles by virtue of *colour confinement*. This is due to the dependence of the QCD coupling constant α_s on the momentum transfer of the interaction Q^2 [61,62] that is given by

$$\alpha_s(Q^2) = \frac{g_s(Q^2)}{4\pi} = \frac{1}{\beta_0 \log\left(\frac{Q^2}{\Lambda^2_{\mathrm{QCD}}}\right)} \qquad \left(\text{with } \beta_0 = \frac{11N_c - 2n_f}{12\pi}\right). \tag{1.1}$$

The gauge coupling constant of SU(3) is g_s, one of the free parameters of the SM, Λ_{QCD} is the energy scale where non-perturbative dynamics of QCD dominate [10] and β_0 depends on the number of colours ($n_c = 3$) and the number of active flavours with mass thresholds below Q (n_f). Since β_0 is positive, the coupling constant increases for smaller momentum transfers Q. Therefore the coupling becomes stronger for larger distances, where smaller momentum is transferred. Figure 1.3 shows this predicted behaviour and measured values of α_s on a large range of Q. The more quarks are pulled apart, the stronger the force. The result of this is that quarks (and gluons) can never be isolated as more and more energy is required to pull them apart. A process called *hadronisation* takes place where colour-neutral hadrons are created from the vacuum. In contrast to this, α_s decreases at small distances – the quarks can be treated as *quasi-free*. This is known as *asymptotic freedom* and enables perturbative QCD calculations. As a consequence of the energy dependence of α_s, quarks and gluons cannot be observed directly. They emit additional particles until they reach the hadronisation-scale, where confinement takes place, and hadronise into mesons or baryons. If the energy of the original quark or gluon is high ($\gtrsim 10\,\text{GeV}$), this can be observed by the detection of a stream of collimated hadrons, called a *jet*.

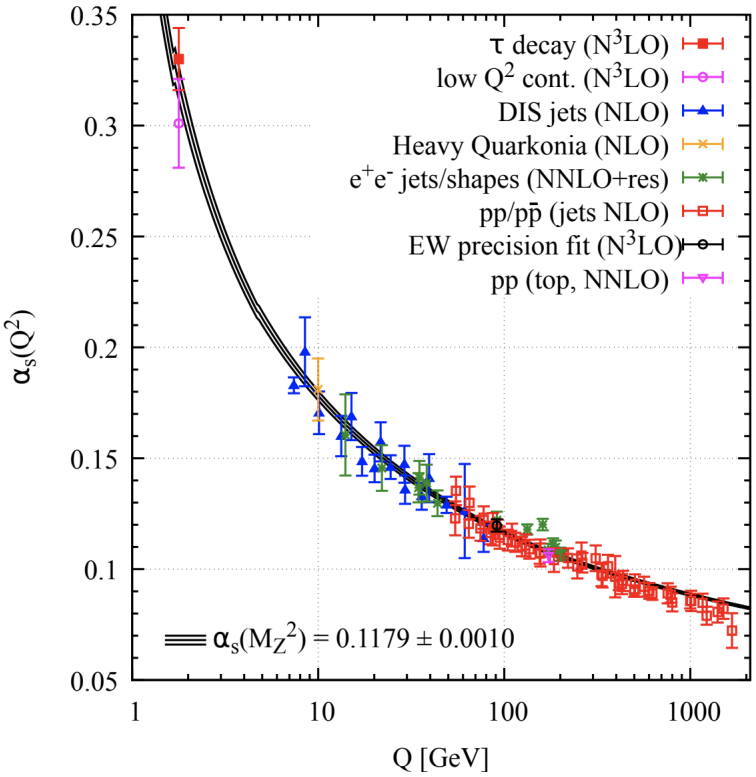

Figure 1.3: Theoretical predictions and measurements of the strong coupling constant α_s for different energy scales Q. The order of QCD perturbation theory used in the various measurements to extract α_s is given in brackets. Taken from Reference [10].

Similarly to the quarks, the leptons are organised in three generations of doublets, each containing a charged lepton (e, μ, τ) and the neutral neutrino (ν_e, ν_μ, ν_τ). The charged leptons have an electric charge of $\pm e$ and therefore can interact by the electromagnetic force. Conversely, the *neutrinos* bear no electric charge and only interact via the weak force.

In the SM the weak and electromagnetic forces are unified into the EW force [1–3]. Firstly discussing the weak interaction part of the EW theory, experiments showed that only particles with a left-handed chirality are subject to charged current interactions, which leads to the introduction of a new quantum number, the *weak-isospin*. The third component of the weak isospin (T_3) then is the charge of this interaction. It is $T_3 = +\frac{1}{2}$ for the upper component of the left-chiral fermion doublets (neutrinos and up-type quarks) and $-\frac{1}{2}$ for the lower components (charged leptons and down-type quarks). The right-handed fermions form singlets and have $T_3 = 0$. As a consequence of this, only left-handed fermions can interact weakly and the corresponding symmetry group is $\mathrm{SU(2)_L}$. The mediators are the W^0, W^1 and W^2 bosons and the coupling strength is g_W. The neutral-current and electromagnetic interacting part of the EW theory is described by the $\mathrm{U(1)_Y}$ symmetry group, which is considered similar to QED, but the force does not act upon the electric charge, but the *hypercharge* (Y). It is defined as $Y = 2(Q - T_3)$ with a coupling strength of g_Y and the mediator is not the photon as in QED but the B boson. At this point the EW bosons are all still massless particles, even though only one is measured as such, which is the photon. The theory is therefore expanded by a mechanism to give mass to the W and Z bosons to match experimental observations.

The Higgs mechanism [46–49] introduces a complex scalar SU(2) doublet, the Higgs field. As shown in Reference [63], the unitary gauge allows to express the Higgs field (Φ) as

$$\Phi = \frac{1}{\sqrt{2}} \begin{pmatrix} 0 \\ v + H(x) \end{pmatrix} , \tag{1.2}$$

where v is a free parameter of the SM, the vacuum expectation value, and $H(x)$ is an excitation of the Higgs field, the spin-0 *Higgs boson*. v can be expressed in terms of a mass term (μ) and a self-interaction term (λ) by

$$v^2 = -\frac{\mu^2}{2\lambda} . \tag{1.3}$$

The *spontaneous symmetry breaking* (SSB) of the EW symmetry then gives rise to three massless Goldstone bosons which can be removed from the Lagrangian [64]. Moving to the unitary gauge, the physical W and Z bosons receive masses, with the B and W^0 related to the photon γ and the Z boson by

$$\begin{pmatrix} \gamma \\ Z \end{pmatrix} = \begin{pmatrix} \cos\theta_\mathrm{W} & \sin\theta_\mathrm{W} \\ -\sin\theta_\mathrm{W} & \cos\theta_\mathrm{W} \end{pmatrix} \begin{pmatrix} B \\ W^0 \end{pmatrix} , \tag{1.4}$$

where $\theta_\mathrm{W} = \tan^{-1}(g_\mathrm{Y}/g_\mathrm{W})$ is the Weinberg angle. The charge-current mediators W^1 and W^2 can be redefined to $W^\pm = \frac{1}{\sqrt{2}}\left(W^1 \mp iW^2\right)$. In this way the $W^\pm$ and Z bosons receive masses depending on v of

$$m_W = \frac{1}{2} g_\mathrm{W} v, \qquad m_\mathrm{Z} = \frac{1}{2} \frac{g_W v}{\cos\theta_\mathrm{W}} \tag{1.5}$$

while the photon stays massless as observed in nature. The newly added Higgs boson also features a mass of

$$m_\mathrm{H}^2 = 2v^2\lambda . \tag{1.6}$$

In contrast to the W and Z bosons, the fermions do not receive their mass through the

SSB but via Yukawa couplings between the fermions and the Higgs field. This adds the Yukawa couplings to the list of free parameters of the SM. Since the weak flavour eigenstates of the quarks are not aligned to the corresponding mass eigenstates, the CKM matrix (V_{CKM}, [65, 66]) is introduced to describe this by

$$\begin{pmatrix} d' \\ s' \\ b' \end{pmatrix} = V_{\mathrm{CKM}} \begin{pmatrix} d \\ s \\ b \end{pmatrix} = \begin{pmatrix} V_{\mathrm{ud}} & V_{\mathrm{us}} & V_{\mathrm{ub}} \\ V_{\mathrm{cd}} & V_{\mathrm{cs}} & V_{\mathrm{cb}} \\ V_{\mathrm{td}} & V_{\mathrm{ts}} & V_{\mathrm{tb}} \end{pmatrix} \begin{pmatrix} d \\ s \\ b \end{pmatrix} \tag{1.7}$$

with (d', s', b') being the flavour and (d, s, b) the mass eigenstates. Since this matrix is unitary, V_{CKM} can be parametrised by three angles (θ_{12}, θ_{13} and θ_{23}) and a complex phase (δ_{CP}). This phase allows for charge-parity (CP) symmetry violating flavour-changing processes in the SM.

The phase and angles in the CKM matrix are free parameters of the SM, which are completed by the QCD vacuum angle (θ_{QCD}) as summarised in Table 1.1. As discussed at the start of this section, the SM successfully describes particle interactions in many different processes through the strong and electroweak forces and the Higgs mechanism. The SM however bears some intrinsic problems and there are physical phenomena the SM can not explain. The next section discusses some of these flaws and limitations of the SM.

Parameters	**Description**
g_{s}, g_{W}, g_{Y}	$\mathrm{SU(3)_c}$, $\mathrm{SU(2)_L}$ and $\mathrm{U(1)_Y}$ gauge couplings
v, λ	Higgs vacuum expectation value and self-coupling
Y_{u}, Y_{d}, Y_{s}, Y_{c}, Y_{b}, Y_{t} Y_{e}, Y_{μ}, Y_{τ}	Fermion Yukawa couplings
θ_{12}, θ_{23}, θ_{13} and δ_{CP}	CKM mixing angles and CP phase
θ_{QCD}	QCD vacuum angle

Table 1.1: Free parameters of the Standard Model.

1.2 Limitations of the Standard Model

The first limitation of the SM is that it does not explain the matter-antimatter asymmetry of the universe. The Sakharov conditions [67] state that CP violation is one of the three requirements to produce matter and antimatter at sufficiently different rates in baryogenesis. Since θ_{QCD} is observed to be very small, the only source of CP violation of the SM is coming from the CKM mixing phase δ_{CP}. This contribution however is not sufficiently large to explain the matter-antimatter asymmetry in the universe [68–70]. Another source of CP violation may come from the mixing of the neutrinos, that has similar characteristics as the weak flavour mixing described by the CKM matrix. This is however not part of the SM which considers neutrinos to be massless – another limitation of the SM.

Next, the SM does not offer a particle that can behave as *dark matter* and explain the

abundance of such dark matter in the universe. Measurements of the rotation speeds of stars in galaxies showed that their velocities do not follow the radial dependency expected from the mass of ordinary matter (stars, gas, etc.) [71]. There is instead another contribution to the mass distribution of the galaxy that is non-luminous, which can also not be accounted for by the SM neutrinos.

Probably the most important shortcoming of the SM is that it does not include the gravitational force. Gravity is negligible at the atomic or nuclear scale, but is the dominant force for the large-scale evolution of the universe. A first step to a theory containing gravity would be a *Grand Unified Theory* (GUT), where the running coupling constants of the strong, electromagnetic and weak interaction converge at energies of $E_{\text{GUT}} \sim 1 \times 10^{16}\,\text{GeV}$ [72], which the SM does not predict.

The last issue of the SM discussed here is the *Hierarchy Problem* [8, 9], which is bound to the discovery of the final jigsaw piece of the SM. The Higgs boson is measured to have a mass of $m_{\text{H}} = 125.1\,\text{GeV}$ [10] which is equal to the sum of the bare mass term $m_{\text{H},0}$ and quantum loop corrections (Δm_{H}) coming from particles interacting with the Higgs field. Δm_{H} is dominated by the contributions from heavy fermions such as the top quark because of its strong Yukawa coupling to the Higgs boson. In order to regulate the loop integral, a cut-off scale (Λ) is introduced that signifies the scale at which the SM breaks down. In this way m_H is at leading order (LO) given by

$$m_{\text{H}}^2 = m_{\text{H},0}^2 + \Delta m_{\text{H, fermions}}^2 + \Delta m_{\text{H, bosons}}^2 \approx m_{\text{H},0}^2 - \sum_{\text{fermions}} \frac{|\lambda_f|^2}{8\pi^2} \left(\Lambda^2 + \dots\right) , \quad (1.8)$$

where λ_f is the Yukawa coupling of a fermion. At $\Lambda \sim m_{\text{H}}$ these corrections are small but assuming the SM to be correct up to the Planck scale ($\Lambda \sim E_{\text{Planck}}$), the corrections will be on the order of the E_{Planck}. This requires the bare mass to be of the same size, fine-tuned in such a way that its difference to the correction term equals $m_H = 125.1\,\text{GeV}$. This fine-tuning goes against the principle of *naturalness* [11–13], which states that the parameters of a theory should all be on the same order of magnitude.

The following section introduces *Supersymmetry* (SUSY) as one of many *beyond the Standard Model* (BSM) theories and explains how it can expand the SM to solve some of these issues.

1.3 Supersymmetry

SUSY [14–20] is an extension of the SM that introduces a symmetry between fermions and bosons. The operator Q transforms fermions to bosons and vice versa:

$$Q\,|\text{Boson}\rangle \propto |\text{Fermion}\rangle\ , \qquad Q\,|\text{Fermion}\rangle \propto |\text{Boson}\rangle\ . \quad (1.9)$$

Supersymmetry is the only possible symmetry that can extend the Poincaré algebra of the SM as it evades the Coleman-Mandula theorem [73] since Q is a fermionic operator [74]. This new symmetry produces a group orthogonal to the SM, which can be expressed as $\text{SU}(3)_{\text{C}} \times \text{SU}(2)_{\text{L}} \times \text{U}(1)_{\text{Y}} \times \text{SUSY}$. Each SM fermionic (bosonic) degree of freedom is accompanied by a bosonic (fermionic) degree of freedom, called a *superpartner*. Since this new set of particles is orthogonal to the SM ones, the quantum numbers of the particles

are unchanged in the transformation except for the spin that changes by 1/2.

These additional particles provide an inherent solution to the Hierarchy Problem. This can be seen by looking at quantum loop corrections to m_{H} that arise from scalars interacting with the Higgs field, as shown in Figure 1.4:

$$\Delta m^2_{\mathrm{H,scalars}} = \sum_{\text{scalars}} \frac{\lambda_S}{16\pi^2} \left(\Lambda^2 + \dots \right) , \tag{1.10}$$

with λ_S being the Yukawa couplings of these scalar particles. Comparing to the correction coming from the fermions in Equation (1.8), we can see a very similar result, but with a different sign. The quadratic terms in Λ of the two correction terms exactly cancel if

$$\sum_{\text{fermions}} \frac{\left|\lambda_f\right|^2}{8\pi^2} = \sum_{\text{scalars}} \frac{\lambda_S}{16\pi^2} , \tag{1.11}$$

which is the case when $\lambda_S = \left|\lambda_f\right|^2$ for all for every fermion-scalar pair and there are twice as many additional scalar particles than SM fermions. This is the case in SUSY since a bosonic superpartner is added for each SM fermion degree of freedom, of which the fermions have two ($s = \pm 1/2$).

Since the loop corrections are largest for particles with high mass (large Yukawa couplings), the SM corrections are dominated by the contribution from the top quark. This means the superpartner of the top plays a crucial role in the solution of the Hierarchy Problem in SUSY. Such a symmetry between fermions and bosons however must be broken as otherwise the supersymmetric particles would have masses identical to the SM ones, which is discussed in Section 1.6.

Figure 1.4: LO quantum corrections to the Higgs propagator due to fermions and scalars. Taken from Reference [20].

Each SM particle and its superpartner can be put either into a chiral or gauge *supermultiplet*.

1.4 Particle Content of Supersymmetry

Table 1.2 lists the chiral supermultiplets, which are formed by the SM fermions and their spin-0 superpartners. Since there are three generations of SM fermions, there are as well three generations of chiral supermultiplets. Because the SM fermions are chiral spinors, they have two degrees of freedom that must be accounted for in the bosonic sector. Therefore each fermion has two scalar superpartners – one partner of the left-handed fermion ($\tilde{f}_{\mathrm{L}}$) and another for the right-handed fermion ($\tilde{f}_{\mathrm{R}}$.) Since they have the same gauge charges, the superpartners are exposed to the same gauge interactions as their

SM counterparts. The supersymmetric partners of the fermions receive a prefix 's-' to indicate their scalar nature, so the SUSY partner of the top is the *stop* ($\tilde{t}$) and the one of the charm is the *scharm* ($\tilde{c}$).

Name	**Symbol**	**Supermultiplet** spin 0	spin 1/2	$\mathbf{SU(3)_C, SU(2)_L, U(1)_Y}$
squarks and quarks One per generation	Q	$(\tilde{u}_\mathrm{L}\ \tilde{d}_\mathrm{L})$	$(u_\mathrm{L}\ d_\mathrm{L})$	$(3, 2, \frac{1}{6})$
	$\bar{u}$	$\tilde{u}^*_\mathrm{R}$	$u^\dagger_\mathrm{R}$	$(\bar{3}, 1, -\frac{2}{3})$
	$\bar{d}$	$\tilde{d}^*_\mathrm{R}$	$d^\dagger_\mathrm{R}$	$(\bar{3}, 1, \frac{1}{3})$
sleptons and leptons One per generation	L	$(\tilde{\nu}\ \tilde{e}_\mathrm{L})$	$(\nu\ e_\mathrm{L})$	$(1, 2, -\frac{1}{2})$
	$\bar{e}$	$\tilde{e}^*_\mathrm{R}$	$e^\dagger_\mathrm{R}$	$(1, 1, 1)$
Higgs and higgsinos	H_u	$(H^+_\mathrm{u}\ H^0_\mathrm{u})$	$(\tilde{H}^+_\mathrm{u}\ \tilde{H}^0_\mathrm{u})$	$(1, 2, +\frac{1}{2})$
	H_d	$(H^0_\mathrm{d}\ H^-_\mathrm{d})$	$(\tilde{H}^0_\mathrm{d}\ \tilde{H}^-_\mathrm{d})$	$(1, 2, -\frac{1}{2})$

Table 1.2: Chiral supermultiplets of SUSY. The mass eigenstates are mixtures of the gauge eigenstates and are discussed in Section 1.5. Table adapted from Reference [20].

The SM Higgs boson and its superpartners also form chiral supermultiplets as shown in Table 1.2. Before being able to assign superpartners to the Higgs doublet, we must extend the SM Higgs sector with an additional Higgs doublet. This is necessary since in the SM the Higgs field (Φ) couples to the up-type quarks and its charge conjugate (Φ^*) to the down-type quarks. Introducing the superpotential, this is no longer possible due to charge conservation prerequisites. One Higgs field now generates masses for the up-type quarks, while the added Higgs field provides masses to the down-type quarks and charged leptons. The four gauge eigenstates introduced then are H^0_u, H^+_u, H^0_d, H^-_d, which mix into the mass eigenstates h^0, H^0, A^0 and $H^\pm$ with h^0 being the SM Higgs boson. The superpartners of this extended SM Higgs sector then are the *higgsinos* $\tilde{H}^0_\mathrm{u}$, $\tilde{H}^+_\mathrm{u}$, $\tilde{H}^0_\mathrm{d}$, $\tilde{H}^-_\mathrm{d}$.

Name	**Supermultiplet** spin 1/2	spin 1	$\mathbf{SU(3)_C, SU(2)_L, U(1)_Y}$
gluinos and gluons	$\tilde{g}$	g	$(8, 1, 0)$
winos and W bosons	$\tilde{W}^\pm\ \tilde{W}^0$	$W^\pm\ W^0$	$(1, 3, 0)$
bino and B boson	$\tilde{B}^0$	B^0	$(1, 1, 0)$

Table 1.3: Gauge supermultiplets of SUSY. The mass eigenstates are mixtures of gauge eigenstates and are discussed in Section 1.5. Table adapted from Reference [20].

Finally, the gauge supermultiplets are displayed in Table 1.3. They consist of the SM gauge bosons of the EW symmetry (W^0, W^1, W^2 and B) and their superpartners, the *gauginos*. The latter are the *winos* ($\tilde{W}^0$, $\tilde{W}^1$, $\tilde{W}^2$) and the *bino* ($\tilde{B}$).

1.5 Supersymmetric Mass Eigenstates

In the same way as in the mixing of the EW gauge bosons and the mixing of the quark flavours, also the supersymmetric particles introduced in Section 1.3 are mixed as shown in Table 1.4.

Name	Spin	R	Gauge Eigenstates	Mass eigenstates
Higgs bosons	0	+1	$H_{\mathrm{u}}^0\ H_{\mathrm{d}}^0\ H_{\mathrm{u}}^+\ H_{\mathrm{d}}^-$	$h^0\ H^0\ A^0\ H^\pm$
squarks	0	−1	$\tilde{u}_{\mathrm{L}}\ \tilde{u}_{\mathrm{R}}\ \tilde{d}_{\mathrm{L}}\ \tilde{d}_{\mathrm{R}}$	(same)
			$\tilde{s}_{\mathrm{L}}\ \tilde{s}_{\mathrm{R}}\ \tilde{c}_{\mathrm{L}}\ \tilde{c}_{\mathrm{R}}$	(same)
			$\tilde{t}_{\mathrm{L}}\ \tilde{t}_{\mathrm{R}}\ \tilde{b}_{\mathrm{L}}\ \tilde{b}_{\mathrm{R}}$	$\tilde{t}_1\ \tilde{t}_2\ \tilde{b}_1\ \tilde{b}_2$
sleptons	0	−1	$\tilde{e}_{\mathrm{L}}\ \tilde{e}_{\mathrm{R}}\ \tilde{\nu}_{\mathrm{e}}$	(same)
			$\tilde{\mu}_{\mathrm{L}}\ \tilde{\mu}_{\mathrm{R}}\ \tilde{\nu}_{\nu}$	(same)
			$\tilde{\tau}_{\mathrm{L}}\ \tilde{\tau}_{\mathrm{R}}\ \tilde{\nu}_{\tau}$	$\tilde{\tau}_1\ \tilde{\tau}_2\ \tilde{\nu}_{\tau}$
neutralinos	1/2	−1	$\tilde{B}^0\ \tilde{W}^0\ \tilde{H}_{\mathrm{u}}^0\ \tilde{H}_{\mathrm{d}}^0$	$\tilde{\chi}_1^0\ \tilde{\chi}_2^0\ \tilde{\chi}_3^0\ \tilde{\chi}_4^0$
charginos	1/2	−1	$\tilde{W}^\pm\ \tilde{H}_{\mathrm{u}}^+\ \tilde{H}_{\mathrm{d}}^-$	$\tilde{\chi}_1^\pm\ \tilde{\chi}_2^\pm$
gluino	0	−1	$\tilde{g}$	(same)

Table 1.4: Relationship between gauge and mass eigenstates of the extended SM Higgs sector and the supersymmetric particles. The gravitino is not included and the first two generations of squarks and sleptons are assumed to be decoupled. Adapted from Reference [20].

The bino, the neutral wino and higgsinos mix and form the neutral particles $\tilde{\chi}_{1\text{-}4}^0$, referred to as *neutralinos*. The charged winos and higgsinos also mix in a similar way into mass eigenstates called *charginos*, the $\tilde{\chi}_1^\pm$ and $\tilde{\chi}_2^\pm$. In the squark and slepton sector, it is customary to assume mixing only to be present inside the third generation. In this way, the top and bottom squark gauge eigenstates, which are the superpartners of the left- and right-handed top and bottom, mix into $\tilde{t}_1$, $\tilde{t}_2$, $\tilde{b}_1$, $\tilde{b}_2$, where the eigenstates with an index of '1' are defined to be lighter.

1.6 The Minimal Supersymmetric Standard Model and Supersymmetry Breaking

The Minimal Supersymmetric Standard Model (MSSM, [75, 76]) describes the simplest supersymmetric extension of the SM that is needed to form a consistent and viable theory. Even this minimal realisation of SUSY leads to the unification of the EW and strong forces through additional contributions to the renormalisation of the couplings [77–81] as seen in Figure 1.5.

If SUSY, as described until here, was to be the theory describing nature, one would however expect to already have detected supersymmetric particles as they would have the same masses as their SM partners. SUSY therefore needs to be a broken symmetry at the EW scale. Such a breaking mechanism should be realised without losing the

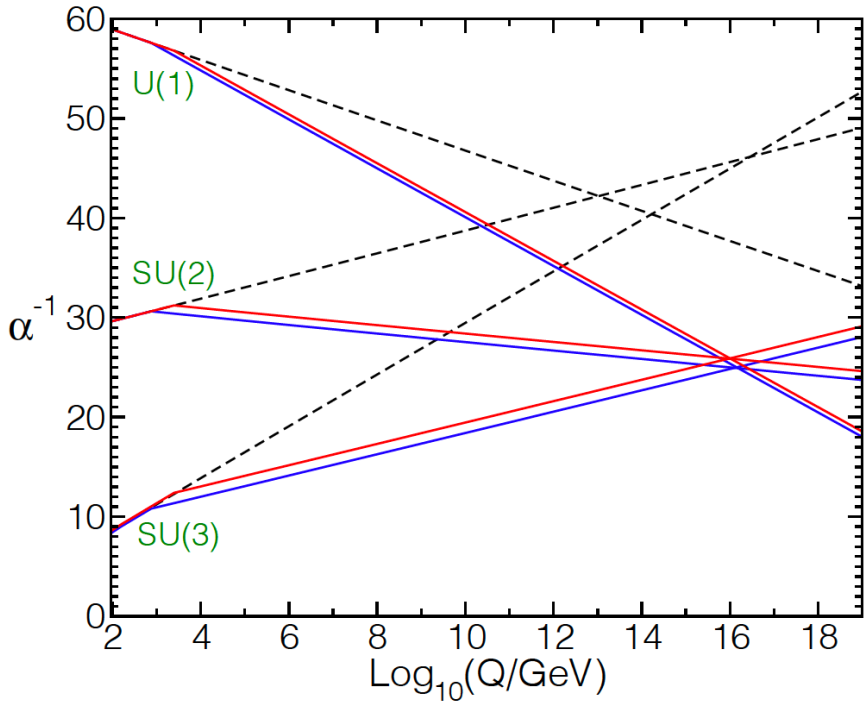

Figure 1.5: Evolution of the inverse gauge couplings in the SM (dashed lines) and for MSSM models featuring SUSY particles with lower (blue solid) or higher(red solid) masses. Taken from Reference [20].

LO cancellation of the Higgs mass corrections, the SUSY breaking should be *soft*. The consequence of such a breaking mechanism is that the lightest supersymmetric particles are likely to have masses not much larger than the TeV scale [20]. The result of this soft SUSY breaking is that the MSSM introduces 105 free parameters additional to the 19 of the SM [82]. This is why the *phenomenological MSSM* (pMSSM, [83, 84]) is introduced by constraining the MSSM with experimental and theoretical constraints. The pMSSM reduces the set of 105 additional free parameters to only 19 [83] that are listed in Table 1.5. The reduced complexity of the pMSSM allows for a phenomenological tests at scales relevant for experiments.

Parameters	**Description**
M_1, M_2, M_3	Bino, wino and gluino mass parameters
$\tan\beta$	Ratio of the vacuum expectation values of the two Higgs doublets
M_A	Mass of the pseudoscalar Higgs boson
μ	Higgs-higgsino mass parameter
$m_{\tilde{q}}$, $m_{\tilde{u}_R}$, $m_{\tilde{d}_R}$, $m_{\tilde{l}}$, $m_{\tilde{e}_R}$	First/second generation sfermion masses
$m_{\tilde{Q}}$, $m_{\tilde{t}_R}$, $m_{\tilde{b}_R}$, $m_{\tilde{L}}$, $m_{\tilde{\tau}_R}$	Third generation sfermion masses
A_t, A_b, A_τ	Third generation trilinear couplings

Table 1.5: Free parameters of the pMSSM. Taken from Reference [83].

The introduction of new couplings by SUSY would lead to the disintegration of the proton within fractions of a second [20], while observations of the proton lifetime show limits on the order of $\sim 10^{33}$ yrs [85–87]. In order to prevent this, a new symmetry, referred to as R-parity, is introduced that is assumed to be conserved in all interactions:

$$R = (-1)^{3(B-L)+2S} \,. \tag{1.12}$$

B is the baryon number, L the lepton number and S the spin. While R-parity conservation is important to forbid proton decay, it has crucial phenomenological consequences. Since R-parity is $R = +1$ for SM particles and $R = -1$ for supersymmetric particles, the latter can only be produced in even numbers at a vertex to conserve the symmetry. They then decay into lighter SUSY particles until the lightest supersymmetric particle (LSP) is reached. The LSP is stable since no decay is possible while conserving R-parity. This property makes the LSP a viable dark matter candidate – addressing another limitation of the SM. The SUSY scenario described in Section 1.7 contains such a LSP, that behaves as a weakly interacting massive particle (WIMP).

As discussed in Section 1.5, the first and second generation squarks are assumed not to take part in the mixing of the gauge eigenstates, which is called the *Minimal Flavour Violation* (MFV) paradigm [26]. MFV only allows for flavour mixing through the Yukawa couplings, which means that small masses lead to small mixings. This is a useful assumption for mixings involving the first generation quarks, where Kaon decay data constrain such mixings to small values [88]. Models featuring substantial mixing between the second and third generation squarks are however still possible [27]. Consequentially, searches for third generation squarks may not be able to detect mixed-flavour SUSY [28, 29]. The analysis contained within this thesis investigates mixed-flavour SUSY that could have evaded detection due to the MFV paradigm normally followed in MSSM scenarios.

1.7 Searching for Flavour-violating Supersymmetry

A search for final states containing a top and a charm quark with missing transverse momentum was already proposed in 2011 by Reference [30]. Reference [31] then reinterpreted the ATLAS 36.1 fb^{-1} searches for top pair production with one lepton, jets and missing transverse momentum ($E_{\mathrm{T}}^{\mathrm{miss}}$) [89] and another search for charm pair production with missing transverse momentum [25]. They considered a simplified model with two active flavours of squarks: The superpartner of the right-handed top quark ($\tilde{t}_{\mathrm{R}}$) and of the right-handed charm quark ($\tilde{c}_{\mathrm{R}}$) that mix into the two physical eigenstates $\tilde{t}_1$ and $\tilde{t}_2$ by

$$\begin{pmatrix} \tilde{t}_1 \\ \tilde{t}_2 \end{pmatrix} = \begin{pmatrix} \cos\theta_{\mathrm{tc}} & \sin\theta_{\mathrm{tc}} \\ -\sin\theta_{\mathrm{tc}} & \cos\theta_{\mathrm{tc}} \end{pmatrix} \begin{pmatrix} \tilde{c}_{\mathrm{R}} \\ \tilde{t}_{\mathrm{R}} \end{pmatrix} \tag{1.13}$$

where $\tilde{t}_1$ is defined to be lighter than $\tilde{t}_2$ and θ_{tc} is the newly introduced mixing angle. Pair-produced $\tilde{t}_1$'s then can either decay to $t/\bar{t} + \tilde{\chi}_1^0$ or to $c/\bar{c} + \tilde{\chi}_1^0$, where $\tilde{\chi}_1^0$ is a bino-like neutralino, the LSP and therefore a possible dark matter candidate. The resulting exclusion limits are shown in Figure 1.6. It can be seen that for large mixings of $\theta_{\mathrm{tc}} \sim \frac{\pi}{4}$ the exclusion limit is reduced to less than 600 GeV. Reference [31] as well investigated a dedicated search for the $t\bar{c}/\bar{t}c + E_{\mathrm{T}}^{\mathrm{miss}}$ final state (referred to as $tc + E_{\mathrm{T}}^{\mathrm{miss}}$) and showed that such a final state would be ideal to target this phase space.

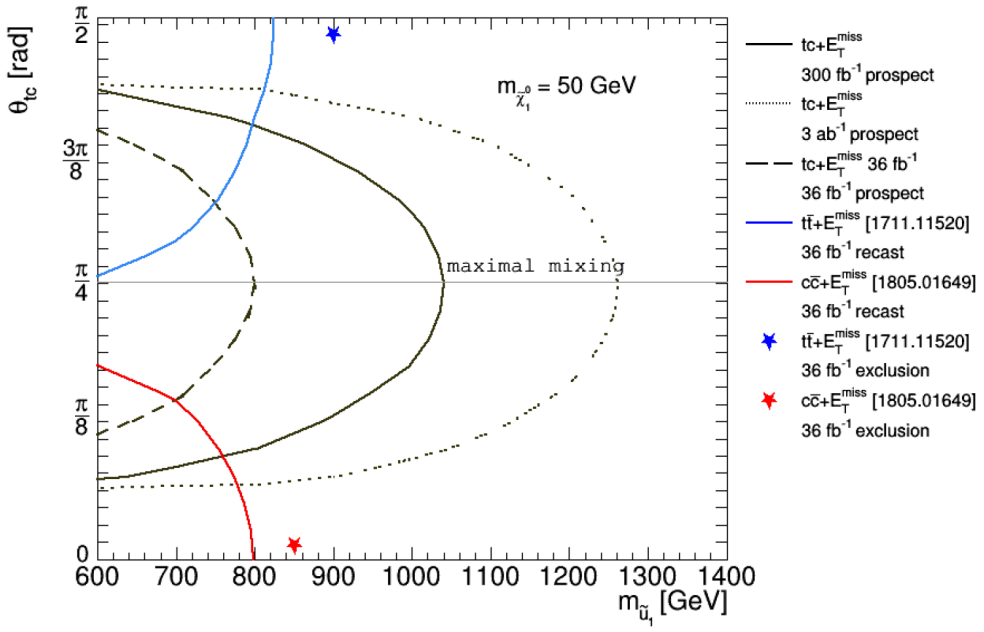

Figure 1.6: Exclusion limits for simplified $tc + E_{\mathrm{T}}^{\mathrm{miss}}$ SUSY scenario by reinterpreting the ATLAS 36.1 fb^{-1} $tt + E_{\mathrm{T}}^{\mathrm{miss}}$ (blue limit curve) and $cc + E_{\mathrm{T}}^{\mathrm{miss}}$ (red limit curve) analyses, as well as the expected exclusion limits for a hypothesised dedicated $tc + E_{\mathrm{T}}^{\mathrm{miss}}$ search (black limit curves). $\tilde{u}_1$ is taken to be the $\tilde{t}_1$. Taken from Reference [31].

The analysis presented in this work follows the approach of Reference [31] and searches for non-MFV SUSY using 139.1 fb^{-1} of ATLAS proton-proton collisions at a centre-of-mass energy of 13 TeV at the Large Hadron Collider (LHC). The targeted final state is $t\bar{c}/\bar{t}c + E_{\mathrm{T}}^{\mathrm{miss}}$, where the mixing angle in Equation (1.13) is set to $\theta_{\mathrm{tc}} = \frac{\pi}{4}$. As shown in Figure 1.7, this leads to branching ratios (BR) of

$$\mathrm{BR}(\tilde{t}_1 \to t\tilde{\chi}_1^0) \approx \mathrm{BR}(\tilde{t}_1 \to c\tilde{\chi}_1^0) \approx 0.5\,. \tag{1.14}$$

Since $\tilde{t}_1$ is produced in pairs in pp collisions, with the corresponding event representations given in Figure 1.8, the probability to have a mixed-flavour final state is

$$\begin{aligned} \mathrm{P}(pp \to tc + E_{\mathrm{T}}^{\mathrm{miss}}) &= \mathrm{P}(pp \to t\bar{c} + E_{\mathrm{T}}^{\mathrm{miss}}) + \mathrm{P}(pp \to \bar{t}c + E_{\mathrm{T}}^{\mathrm{miss}}) \\ &= 2 \cdot \mathrm{P}(\tilde{t}_1 \to t\tilde{\chi}_1^0) \cdot \mathrm{P}(\tilde{t}_1 \to c\tilde{\chi}_1^0) \\ &\approx 0.5\,. \end{aligned} \tag{1.15}$$

The topology of the SUSY signal depends on the mass difference $\Delta(m(\tilde{t}_1), m(\tilde{\chi}_1^0)) = m(\tilde{t}_1) - m(\tilde{\chi}_1^0)$ as shown in Figure 1.9. If the mass difference is larger than the mass of the top quark ($m(t)$), then the top will be produced on-shell and decay to a bottom quark and a W boson – the kinematics are that of a two-body decay. For mass differences of $m(W) < \Delta(m(\tilde{t}_1), m(\tilde{\chi}_1^0)) < m(t)$, the top quark is produced off-shell and the resulting decay is a three-body decay. Finally if $\Delta(m(\tilde{t}_1), m(\tilde{\chi}_1^0))$ is smaller than the mass of the b quark also the W boson is produced off-shell and the kinematics follow a four-body

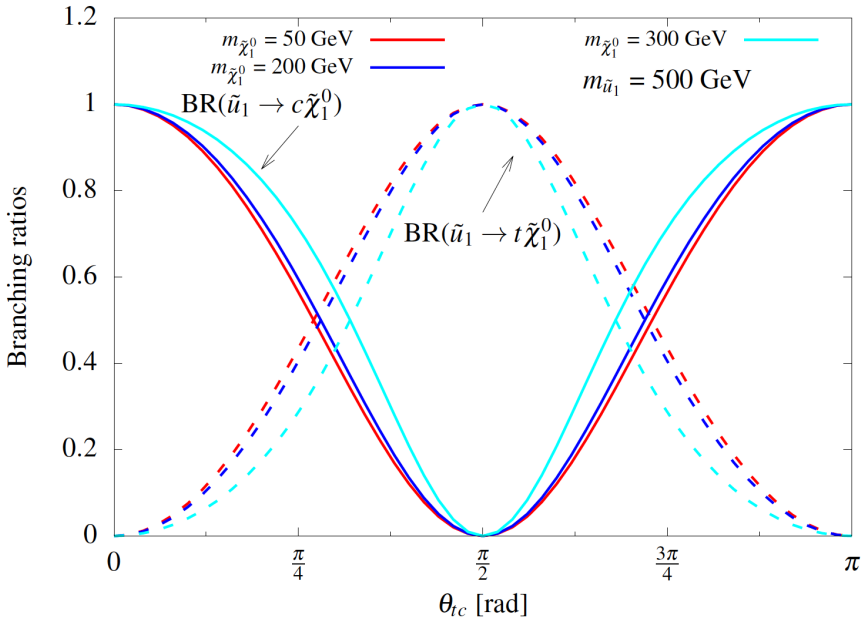

Figure 1.7: Dependence of the branching ratios BR($\tilde{t}_1 \to t\tilde{\chi}_1^0$) (dashed) and BR($\tilde{t}_1 \to c\tilde{\chi}_1^0$) (solid) on the mixing angle θ_{tc} for $m(\tilde{t}_1) = 500\,\mathrm{GeV}$ and various $m(\tilde{\chi}_1^0)$ (red, blue, cyan). $\tilde{u}_1$ is taken to be the $\tilde{t}_1$. Taken from Reference [31].

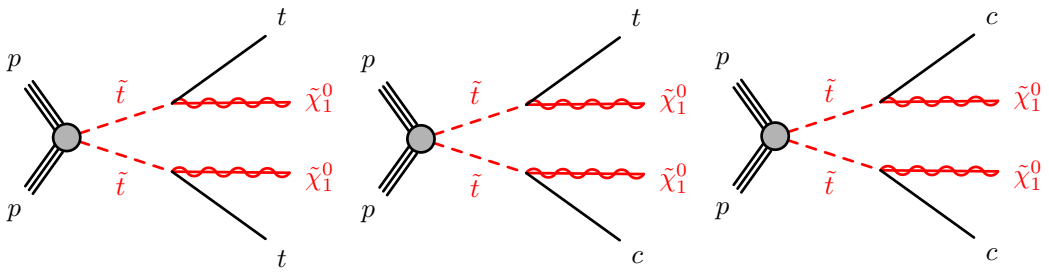

(a) $pp \to t\bar{t} + \tilde{\chi}_1^0 + \tilde{\chi}_1^0$ (b) $pp \to t\bar{c}/\bar{t}c + \tilde{\chi}_1^0 + \tilde{\chi}_1^0$ (c) $pp \to c\bar{c} + \tilde{\chi}_1^0 + \tilde{\chi}_1^0$

Figure 1.8: Diagrammatic representations of the SUSY signals considered in this thesis.

decay scheme. The analysis presented in this thesis assumes $\Delta(m(\tilde{t}_1), m(\tilde{\chi}_1^0)) > m(t)$, leading to the two-body decay scenario.

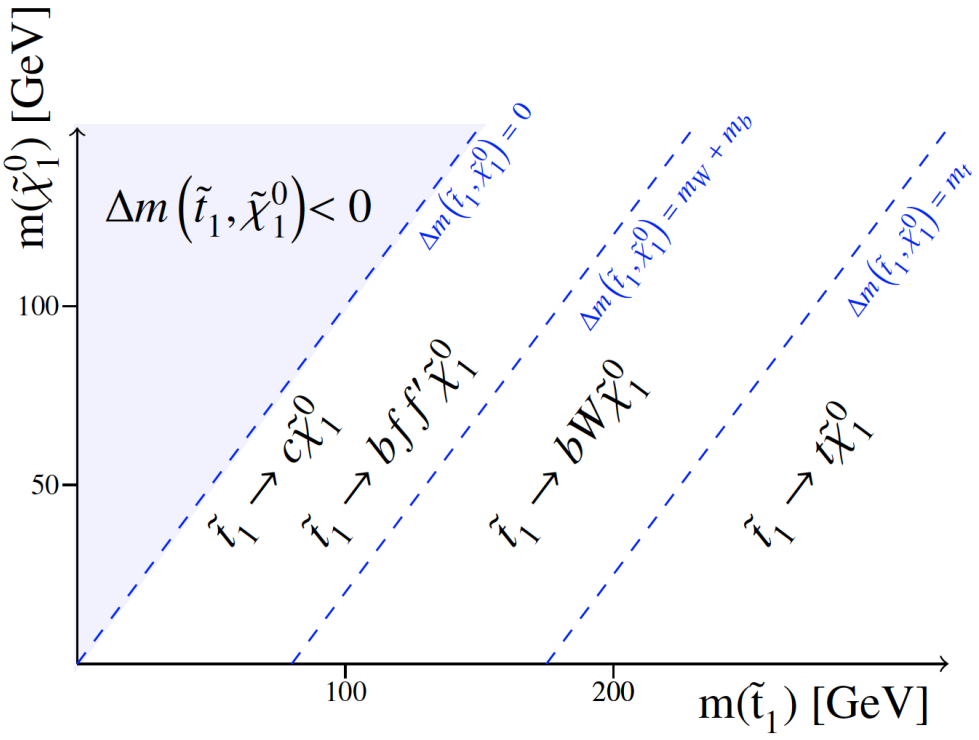

Figure 1.9: Different decay modes of $\tilde{t}_1$ decay depending on $\Delta(m(\tilde{t}_1), m(\tilde{\chi}_1^0))$. Taken from Reference [90].

The following chapter introduces the LHC used to create proton-proton collisions as well as the ATLAS experiment that detects and records these collision that are used for the $tc + E_{\mathrm{T}}^{\mathrm{miss}}$ analysis presented in this thesis.

Chapter 2

The ATLAS Experiment at the Large Hadron Collider

Particle colliders enable us to expand our knowledge of the fundamental working principles of nature beyond what cosmic rays can reveal. This is because both the type of particles and their energies can be controlled in a particle accelerator. This chapter introduces the LHC that collides high-energy protons and also the ATLAS experiment used to record these collisions for the $tc + E_{\mathrm{T}}^{\mathrm{miss}}$ analysis presented in Chapter 4 of this thesis.

2.1 The Large Hadron Collider

The LHC [5] at the European Organization for Nuclear Research (CERN) in Geneva, Switzerland, is the world's largest and most powerful particle accelerator. It is a synchrotron accelerator with a circumference of 26.7 km which accelerates charged hadrons in opposing directions. It features superconducting NbTi dipole magnets with nominal fields of 8.33 T to steer beams of particles along a quasi-circular trajectory. Quadrupole magnets are used to shape and focus these beams. The LHC can either collide protons (pp), protons with heavy nuclei (p+Pb or p+Xe) or heavy nuclei (Pb+Pb or Xe+Xe). Given the circumference and magnetic field strength, the LHC has a design centre-of-mass energy ($\sqrt{s}$) of 14 TeV for pp-collisions. Run 2 of the LHC between 2015 and 2018 produced pp-collisions at $\sqrt{s} = 13$ TeV, which are the particle collisions investigated in this thesis.

Before entering the LHC, the protons go through a chain of pre-accelerators as seen in Figure 2.1. At the start, hydrogen gas is stripped off its electrons and the linear accelerator Linac 2 is accelerating the resulting protons to energies of 50 MeV. The beam of protons then is injected into the Proton Synchrotron Booster (PSB). Both the PSB and the following accelerators are synchrotrons, that guide the hadrons along an almost circular trajectory using magnets. In each revolution, the energy of the beam is increased slightly by radio frequency (RF) cavities until the extraction beam energy is reached, which is when the beam is guided to the next accelerator or experiment. Inside the PSB, the beam is accelerated to an energy of 1.4 GeV. The next synchrotron, the Proton Synchrotron (PS), then accelerates the beam to an energy of 25 GeV and clusters

the protons into *bunches*. The last pre-accelerator, the Super Proton Synchrotron (SPS), accelerates the beam to 450 GeV. The bunches of protons in the SPS are then injected into the two beam pipes of the LHC, in which the bunches travel in opposite directions and are accelerated to their final energy at which they are collided.

The LHC accelerates the beams using RF cavities with frequencies of 400 MHz and an acceleration gradient of 16 MV/m. The RF cavities are also responsible for keeping the hadrons in the beams concentrated in bunches. The LHC can accommodate a maximum number of bunches per beam (n_b) of 2808 that are separated by 25 ns which results in bunch collisions at a rate of up to $f = 40$ MHz. During Run 2, the LHC operated with n_b of up to 2556 populated with a number of protons per bunch (N_b) between 1.1–1.25 $\times 10^{11}$ [91]. When the bunches have been accelerated to the desired energy, the quadrupole settings are adjusted to collide the beams at the interaction points.

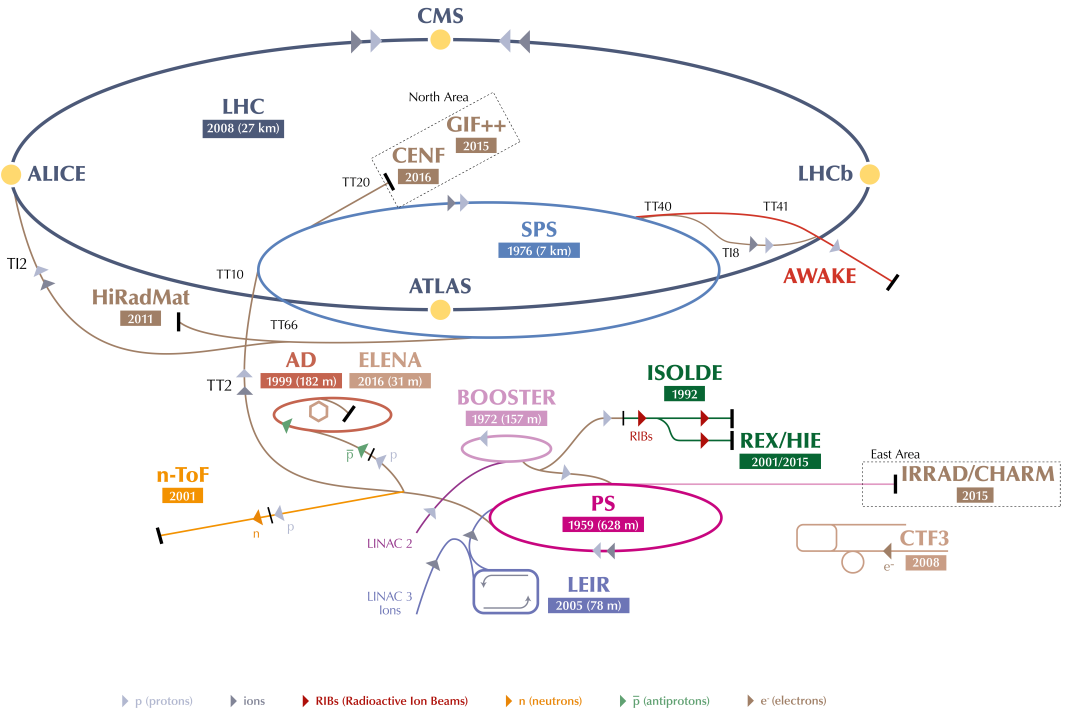

Figure 2.1: The CERN accelerator complex as of 2018. Taken from Reference [92].

The two most important characteristics describing the collision properties of a collider are the centre-of-mass energy ($\sqrt{s}$) and the *instantaneous luminosity* ($\mathcal{L}$), which describes the intensity of the collisions. Given an interaction cross-section (σ) for a certain particle physics process, the collision rate is calculated with

$$\frac{\mathrm{d}N}{\mathrm{d}t} = \sigma \cdot \mathcal{L}\,. \tag{2.1}$$

The unit of the cross-section is the *barn* ($1\,\mathrm{b} = 10^{-28}\,\mathrm{m}^2$) so therefore the unit of the instantaneous luminosity $\mathcal{L}$ is $\mathrm{b}^{-1}/\mathrm{s}$, but can also be expressed in units of $\mathrm{cm}^{-2}s^{-1}$. The *integrated luminosity* (L) then describes how much luminosity has been gathered during a period of time. The number of expected events (N) for a given physics process then

can be calculated using σ and L as

$$N = \sigma \cdot L = \sigma \cdot \int \mathcal{L}\, \mathrm{d}t\,. \tag{2.2}$$

Run 2 of the LHC featured a peak $\mathcal{L} = 2.2 \times 10^{34}\,\mathrm{cm}^{-2}\,\mathrm{s}^{-1}$ in 2017 [93] and yielded a total integrated luminosity of $L = 139\,\mathrm{fb}^{-1}$ recorded by ATLAS. So given for example a top squark pair production with $m(\tilde{t}_1) = 1000\,\mathrm{GeV}$ with a production cross-section of $6.8\,\mathrm{fb}^{-1}$ [94], a total of $N \approx 950$ events would be expected to be produced by the LHC in the whole of Run 2.

The instantaneous luminosity of the LHC [5] depends on various parameters and is calculated as

$$\mathcal{L} = \frac{N_\mathrm{b}^2 n_\mathrm{b} f_\mathrm{rev} \gamma}{4\pi \epsilon_\mathrm{n} \beta^*} F\,, \tag{2.3}$$

where f_rev is the revolution frequency and γ the relativistic Lorentz factor of the protons in the LHC. The normalised transverse emittance (ϵ_n), the beta function at the collision point (β^*) and also the geometric luminosity reduction due to the crossing angle at the interaction point (F) affect the instantaneous luminosity as well. For high $\mathcal{L}$ such as at the LHC, there are multiple inelastic proton-proton interactions happening at the interaction points during each bunch crossing. This is referred to as *pile-up* with $\langle\mu\rangle$ expressing the mean number of simultaneous interactions per bunch crossing. Figure 2.2 shows the peak instantaneous luminosity per fill in 2018 and the resulting pile-up profiles during the complete Run 2 of the LHC as recorded by the ATLAS experiment.

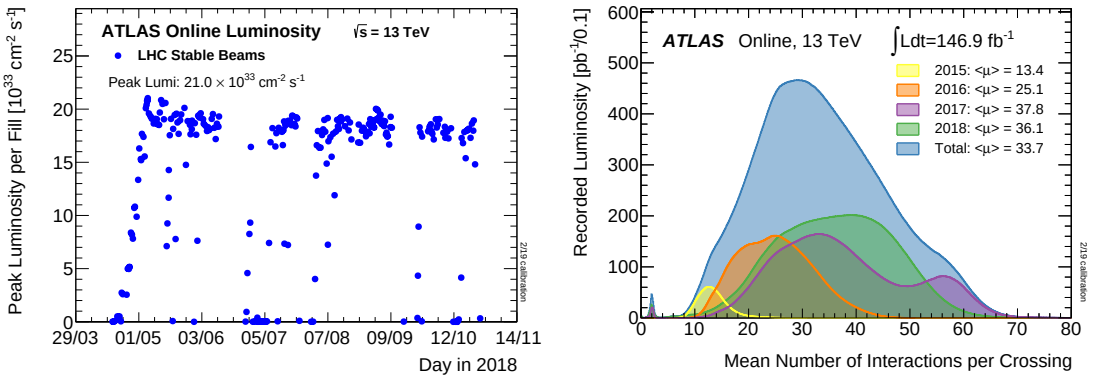

(a) (b)

Figure 2.2: Peak instantaneous luminosity for each fill of the 2018 *pp* data taking (a) and the resulting pile-up profiles for all of Run 2 (b) measured at the ATLAS experiment. Taken from Reference [95].

ATLAS is one of the four large experiments placed around the interaction points of the LHC, with the others being the CMS, LHCb and ALICE experiments. The following sections present the current layout of the ATLAS experiment, its detectors and how they detect the signatures of the particles produced by the LHC.

2.2 The ATLAS Experiment

ATLAS (**A** **T**oroidal **L**HC **A**pparatu**S**, [23]) is a general purpose detector and with dimensions of 44 m × 25 m it is the largest detector at the LHC. The most important subsystems and their arrangement are shown in Figure 2.3. ATLAS covers almost the whole solid angle, with the exception of the area close to the beam pipe. It features a cylindrically symmetric geometry where *barrel* parts are located parallel to the beam axis and *end-caps* are adjacent to the ends of the barrels.

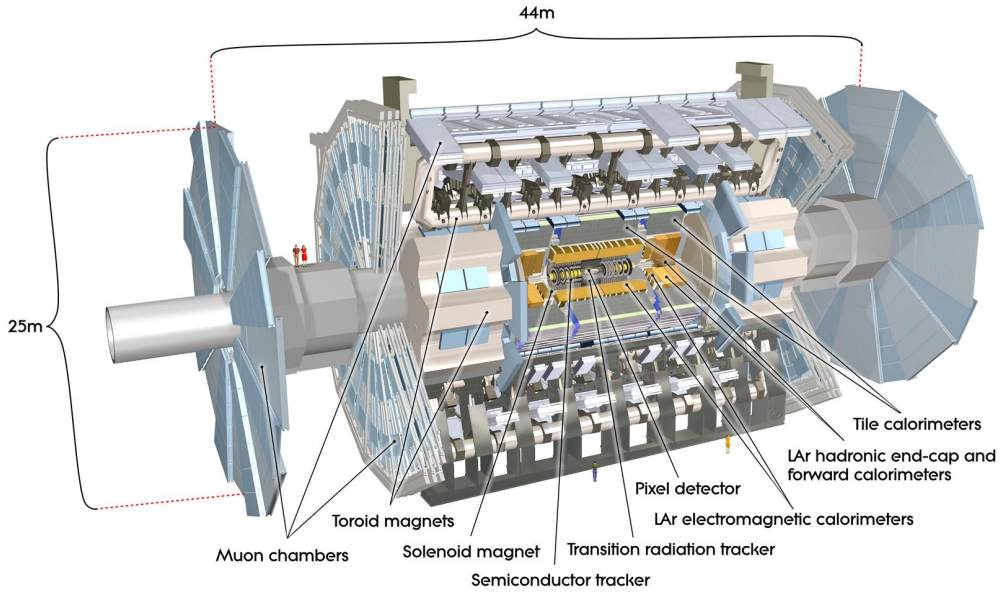

Figure 2.3: Layout of the ATLAS detector showing its various detector components: the Inner Detector with its solenoid magnet, the electromagnetic and hadronic calorimeters and the Muon Spectrometer with the toroidal magnet system. Taken from Reference [96].

The ATLAS detector is described by a right-handed Cartesian coordinate system with its origin at the nominal interaction point. The z-axis is parallel to the beam pipe, while the x-axis points towards the centre of the LHC. The y-axis is therefore pointing upwards. Because ATLAS has a cylindrical shape, polar coordinates are used to describe the detector and collision events. The azimuthal angle ($\phi \in [-\pi, \pi]$) is going around the beam axis z and lies in the x-y plane, that is referred to as the *transverse plane*. Because of momentum conservation, it is useful to consider the momentum of particles in this plane, the transverse momentum ($\vec{p_{\mathrm{T}}}$). The imbalance of all $\vec{p_{\mathrm{T}}}$'s then defines the missing transverse momentum ($\mathbf{E}_{\mathrm{T}}^{\mathrm{miss}}$) by

$$\mathbf{E}_{\mathrm{T}}^{\mathrm{miss}} = -\sum_{i} \vec{p_{\mathrm{T},i}}\,, \tag{2.4}$$

used to infer the existence of feebly interacting particles such as neutrinos and neutralinos. The reconstruction of $\mathbf{E}_{\mathrm{T}}^{\mathrm{miss}}$ is further discussed in Section 3.6. Next, instead of using

the polar angle (θ), the rapidity (y) and pseudorapidity (η) are defined by

$$y = \frac{1}{2} \ln \left(\frac{E + p_z}{E - p_z} \right) \text{ and} \tag{2.5}$$

$$\eta = -\ln \left(\tan \frac{\theta}{2} \right) , \tag{2.6}$$

where p_z is the momentum of a particle in z-direction and E is the energy. y is useful since a similar amount of particles pass through each unit of y and differences of rapidities are invariant under Lorentz boosts along the beam axis. The pseudorapidity does not depend on the energy of a particle an is identical to y for highly relativistic particles. Both η and y take values from 0 in the transverse plane to $|\eta| = |y| = \infty$ parallel to the beam axis. Lastly, η and ϕ can be used to describe the angular distance between two particles by

$$\Delta R_{1,2} = \sqrt{(\eta_1 - \eta_2)^2 + (\phi_1 - \phi_2)^2} . \tag{2.7}$$

ATLAS is designed to be able to look for various kinds of event signatures. It enabled the discovery of the Higgs boson and allows for BSM searches as well as precision measurements of the properties of the SM. To do so, the following requirements are set for the detector performance:

- Maximised geometrical acceptance.
- Precise charged particle momentum measurement and efficient reconstruction of the primary and secondary vertices. This is necessary for correctly identifying the original parton of a jet, a process called *flavour-tagging* that will be discussed in Section 3.3.
- Identification and energy measurement of jets, photons and electrons which is crucial for the search for WIMPs using $E_{\mathrm{T}}^{\mathrm{miss}}$ as discussed in Section 3.6.
- Identify muons and measure their momenta precisely over wide ranges of momentum.
- Readout, selection and recording of as many interesting collision events as possible, based on fast analysis of event properties.

These requirements must be fulfilled in pp-collision events featuring up to $\langle \mu \rangle \approx 60$ at the LHC. The large integrated luminosity also leads to a high-radiation environment especially damaging detector components close to the beam pipe. To efficiently fulfil all the requirements mentioned here, ATLAS consists of numerous different detectors organised in concentric layers, where each detector is responsible for the measurement of some of the various particle signatures.

Directly outside of the beam pipe is the Inner Detector (ID), which is responsible for *tracking*. Charged particles that pass through matter undergo ionisation following the Bethe-Bloch equation [97, 98], which can be measured by appropriate sensors. Since the trajectories of charged particles are bent in a magnetic field, position measurements of multiple layers of sensing elements can be combined to reconstruct the individual ionisation traces called *hits* to a *track*, the bent trajectory that the charged particle went along. The same information can also be used to determine the primary and secondary

vertices of the collision. The ID is the innermost part of ATLAS so that the charged particle tracks are the least affected by multiple-scattering with detector components and to maximise the resolution of the vertex parameters. The magnetic field in the ID is created by a solenoid magnet that surrounds the ID.

The next detector of ATLAS is the calorimeter consisting of the electromagnetic (EM) and hadronic calorimeters (ECAL and HCAL). They are responsible for absorbing and measuring the energy of electromagnetically and strongly interacting particles respectively by measuring the *showers* of particles they generate when interacting with matter. Electromagnetic showers are caused by high-energetic electrons, positrons and photons that interact with matter by the processes of pair-production and bremsstrahlung. The resulting electrons and photons undergo the same processes until other effects become dominant at the critical energy. The radiation length (X_0) is the mean distance over which the initial energy of an electron (E_0) is reduced to E_0/e, with e being Euler's number, and is a useful detector characteristic. Conversely, hadronic showers are induced by high-energy hadrons that ionise in the detector but also interact with nuclei by the strong force and decay spontaneously. The property analogous to X_0 for hadrons is the nuclear interaction length (λ_0). In order to measure the energy of the showering particles correctly, the ECAL and HCAL must completely contain their corresponding showers. Since λ_0 is typically larger than X_0, the EM calorimeter is located closer to the interaction point than the hadronic one. In this way, the EM showers are contained in the ECAL, while the hadrons are able to pass the ECAL and are then fully contained in the HCAL. The only particles of the SM that are not absorbed by the calorimeters are the muons and neutrinos .

Muons interact less with matter than other particles produced in collisions (except for the neutrinos). This is why the Muon Spectrometer (MS) is the outermost detector of ATLAS. The toroidal magnet system, eponymous to the ATLAS experiment, creates a magnetic field that bends the muon trajectories. Muon tracking chambers measure these trajectories, inferring the momenta of the muons in a similar manner as for other charged particles in the ID.

Section 2.3–2.5 discuss the four detector systems of ATLAS in more detail, starting with the ID which is closest to the beam pipe. Section 2.6 then describes the trigger and data acquisition system of ATLAS.

2.3 Inner Detector

The ID [23, 99] is located inside a 2 T axial solenoid magnet, which allows the ID to measure the momenta of charged particles in the transverse plane. It consists of three subdetectors: closest to the beam pipe is the Pixel Detector including the Insertable B-Layer [100] (IBL), then comes the Semi-Conductor Tracker (SCT) in the middle and the outermost subdetector is the Transition Radiation Tracker (TRT). A schematic view of the barrel section of the ID is shown in Figure 2.4. The barrel section of the ID contains four pixel layers (one of which is the IBL), four SCT layers and the TRT barrel. The overall layout of the ID, shown in Figure 2.5, is optimised to minimise the amount of material. A small *material budget* leads to the suppression of multiple scattering inside the ID, which is beneficial for the tracking performance. The three pixel end-cap disks each are located at $|z| > 495\,\text{mm}$, while the 9 SCT end-cap disks and the TRT end-cap

start at $|z| > 848\,\text{mm}$. This design features full coverage in ϕ and up to $|\eta| < 2.5$ in pseudorapidity as shown in Figure 2.5.

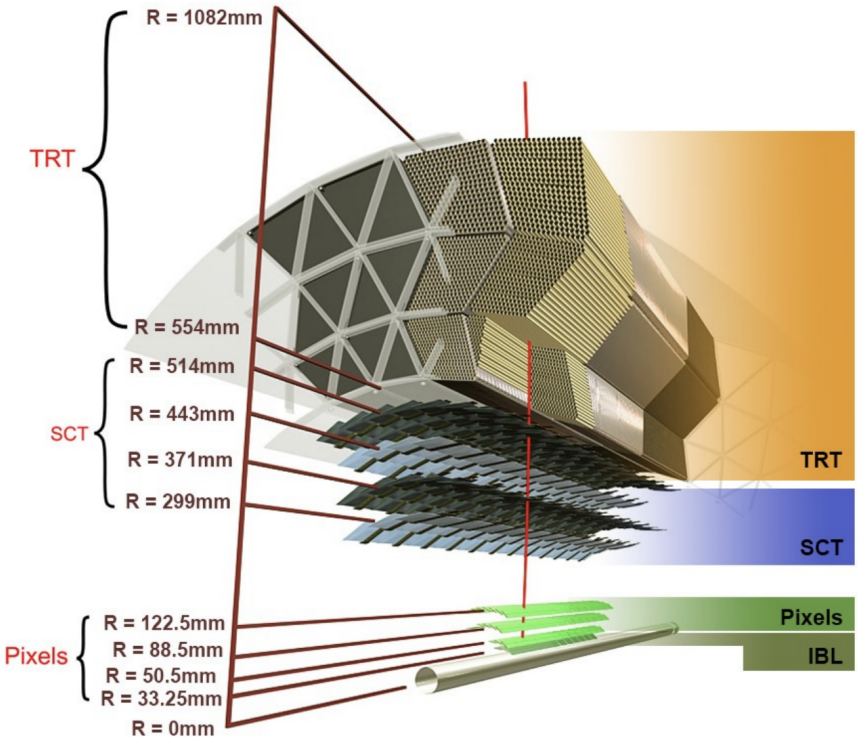

Figure 2.4: Schematic view of the barrel section of the ID and its three subdetectors, as well as the distance of their layers to the centre of ATLAS. Taken from Reference [101].

The closer to the beam pipe a subdetector is, the better its intrinsic resolution must be in order to achieve the same relative track resolution. This is why the innermost IBL and Pixel sensors are designed to have smaller pitches and superior intrinsic resolution (σ) compared to the SCT and the TRT as shown in Table 2.1.

Due to the high amount of channels and the proximity to the collision point, the IBL and the other three Pixel layers have the largest hit rate, which leads to a large amount of data to be read out and a high-radiation environment. Especially the Pixel detector therefore must be designed in a radiation resistant manner, which is why hybrid planar and 3D sensors are utilised. The FE-I3 (Pixel detector) and the FE-I4B (IBL) *front-end* (FE) chips configure the sensor and send its data out at speeds of up to 160 Mb/s. The FE-I4B Application-specific Integrated Circuit (ASIC) is specified for ionising doses of up to 250 Mrad (= 2.5 MGy, Gy = J/kg) [100]. The data from the FEs is transmitted over a distance of 6 m to *Optoboards* located outside of the ID, on the ID end-plate located at $|z| = 3.5\,\text{m}$ (visible in Figure 2.5). The Optoboards convert the electrical data signals from the IBL and Pixel sensors to optical signals that are sent out over optical fibres to the back-end electronics. In the same manner, the Optoboards also convert the optical signals from the back-end, containing the timing, trigger and control (TTC) information for the FEs to electrical signals [100, 103].

The SCT is a silicon strip detector that is adding another four hits in silicon sensors (*silicon hits*) for charged particles with $|\eta| < 2.5$. Since each sensor module is double

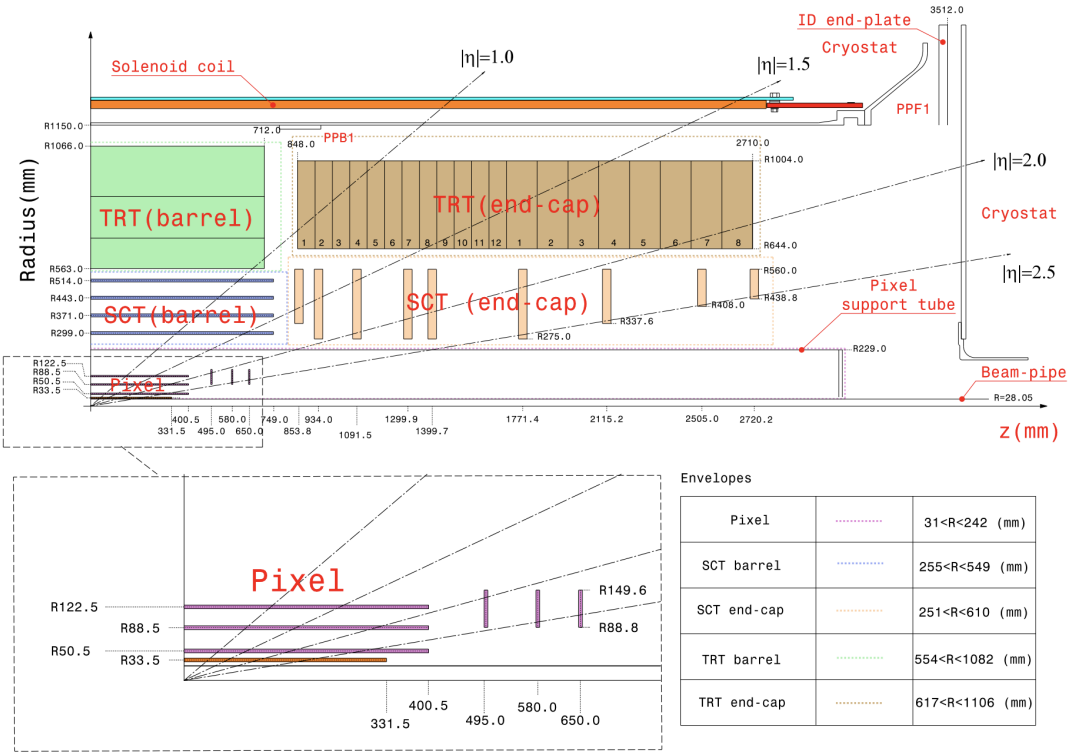

Figure 2.5: r–z cross-section view of the layout of one quadrant of the ATLAS ID during Run 2. The top part shows all subdetectors, while the bottom part is a magnified view of the Pixel region. Taken from Reference [102].

System	Pitch [μm]	σ [μm]	Channels	Si surface area [m^2]
IBL [104]	50×250	8×40	12M	0.15
Pixel [104]	50×400	10×115	80M	1.73
SCT [105]	80	17	6.2M	61
TRT [106]	4000	130	250k	–

Table 2.1: Comparison of the subdetectors of the ID, taking the Insertable B-Layer separately to the Pixel Detector. σ is the intrinsic resolution of the components. Taken and complemented from Reference [107].

sided, the SCT can record a total of 8 hits, resulting in a total of up to 12 hits in the Pixel and SCT (8 silicon hits). Since the SCT is farther away from the interaction region than the Pixel layers, a larger pitch and segmentation only in the r–ϕ plane are sufficient to achieve good tracking performance together with the other subdetectors.

The last part of the ID is the TRT, that uses a different detection method than the previous two subdetectors. As charged particles traverse regions of differing dielectric constants, they emit photons proportional to the Lorentz factor $\gamma = E/m$. The TRT is composed of straw tubes and interleaved fibres or foils. The straws are filled with a gas mixture mainly composed of Xenon and a 30 μm diameter gold-plated tungsten wire in the middle acting as anode. In this way, the strawtubes act as a proportional drift tube [108]. They amplify and collect the charge that was deposited by the transition radiation. The interleaved fibres or foils are needed to create a boundary region with different dielectric constants. As electrons have a much smaller mass than hadrons, such as pions, the radiation measured by the TRT can be used to discriminate between them.

The ID will as well be used for the upcoming Run 3 of the LHC, but will be replaced by the new Inner Tracker in the context of the High-Luminosity LHC (HL-LHC) project, which will be discussed in Chapter 5.

2.4 Calorimeters

The ATLAS calorimeter system [23] is located outside of the solenoid magnet and consists of various subdetectors as shown in Figure 2.6. To fully contain almost all EM and hadronic showers, the ECAL and HCAL feature depths of more than $22X_0$ respectively 11λ (at η=0) and cover pseudorapidities of $|\eta| < 4.9$. Both the ECAL and HCAL are *sampling* calorimeters where the energy of the particles is absorbed in high-density materials, but the measurement takes place in some other active equipment of different composition. These two components are alternated to measure the evolution of the showers. The performance goals of this calorimetry system in terms of energy resolution are presented in Table 2.2.

Detector component	**Required resolution**	**η coverage**	
		Measurement	Trigger
EM calorimetry	$\sigma_E/E = 10\%/\sqrt{E} \bigoplus 0.7\%$	± 3.2	± 2.5
Hadronic calorimetry			
barrel and end-cap	$\sigma_E/E = 50\%/\sqrt{E} \bigoplus 3\%$	± 3.2	± 3.2
forward	$\sigma_E/E = 100\%/\sqrt{E} \bigoplus 10\%$	$3.1 < \|\eta\| < 4.9$	$3.1 < \|\eta\| < 4.9$

Table 2.2: Calorimeter energy resolution goals of ATLAS. Taken from Reference [23].

The ECAL is subdivided into a barrel and two end-caps. The barrel ECAL is in the same cryostat as the solenoid, while the end-caps share a cryostat each with the adjacent HCAL end-caps. All ECAL parts consist of accordion-shaped lead absorbers and liquid argon ionisation chambers as the sensing element. The barrel section consists of three ECAL layers, of which the first layer has a granularity of 0.0031×0.0982 in $\eta \times \phi$ as can be seen in Figure 2.7. This small granularity in η allows to distinguish between photon

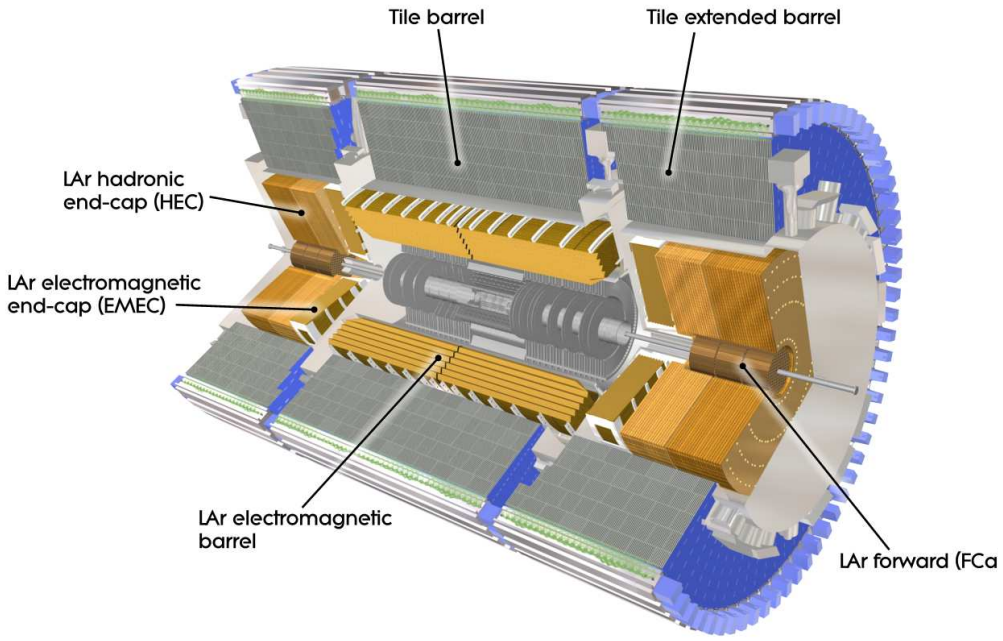

Figure 2.6: The ATLAS calorimeter system and its various subdetectors. Taken from Reference [23].

pairs (from pions) and individual photons. The middle layer absorbs most of the EM showers and features a granularity of 0.025×0.0245, while the last layer is measuring how much EM activity is leaking to the HCAL, having the coarsest granularity of the three layers. The central region of the barrel ($|\eta| < 1.7$) additionally features a presampler that measures how much energy is lost before the ECAL systems. The ECAL end-caps consist of two co-axial wheels and feature three ECAL layers each for $1.5 < |\eta| < 2.5$, where again the first layer is finely segmented in η. In contrast to the barrel, there are only two ECAL layers for $|\eta| < 1.5$ and $2.5 < |\eta| < 3.2$, which feature a coarser granularity. The end-cap presamplers are located at $1.5 < |\eta| < 1.8$.

Finally, the forward calorimeter (FCAL) covers the region of $3.1 < |\eta| < 4.9$, being in the same cryostat as the HCAL and ECAL end-caps. The FCAL as well uses LAr to measure energy depositions, but also measures hadronic showers and therefore is as well part of the HCAL system. The FCAL is important for the calculation of missing transverse momentum and the reconstruction of forward jets.

The HCAL adopts two different technologies to measure the energy deposits from hadronic showers. The end-caps use liquid argon calorimeters as in the ECAL and consist of two wheels per end-cap that cover $1.5 < |\eta| < 3.2$. They use copper instead of lead for absorbing the energy. The barrel part of the HCAL is called the tile-calorimeter and uses steel as the absorber and scintillators as sensing elements. It covers the region of $|\eta| < 1.7$ and consists of a central and two extended barrels that are composed of three layers of tile calorimeters, featuring granularities of 0.1×0.1 in $\eta \times \phi$ in the first two layers [109]. The readout of the scintillating tiles is done by wavelength-shifting fibres measured by photomultiplier tubes.

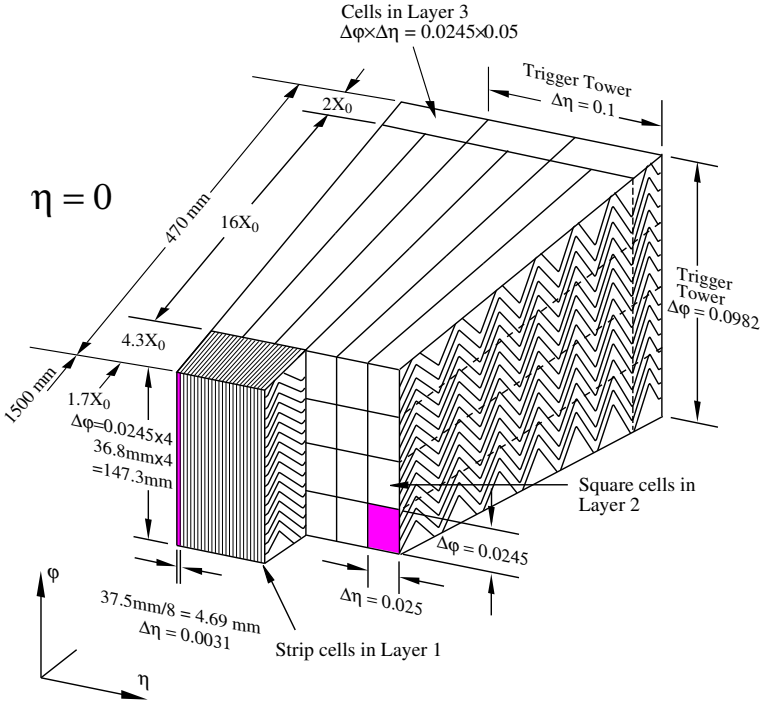

Figure 2.7: Schematic sketch of an ECAL barrel module with its three layers consisting of accordion-shaped electrodes. Taken from Reference [23].

2.5 Muon Spectrometer

The outermost detector system of ATLAS is the MS and its toroidal magnet system shown in Figure 2.8. The MS is responsible for providing high precision tracking of the muons and for providing information to the trigger system, which is achieved by four different subdetectors whose properties are listed in Table 2.3.

Muon track measurements are provided by two different systems. Three layers of Monitored Drift Tube (MDT) chambers cover the barrel region of $|\eta| < 2$ (first MDT layer) and $|\eta| < 2.7$ (second and third layer). Each chamber consists of three to eight layers of drift tubes and achieves a resolution of 35 μm in z [23]. Cathode Strip Chambers (CSC) are utilised for the forward region of $2.0 < |\eta| < 2.7$, where they make up two discs per end-cap.

Type	**Function**	**Chamber resolution (RMS) in**			**Measurements/track**		**Number of**	
		z/r	ϕ	time	barrel	end-cap	chambers	channels
MDT	tracking	35 μm (z)	–	–	20	20	1150	354k
CSC	tracking	40 μm (r)	5 mm	7 ns	–	4	32	30.7k
RPC	trigger	10 mm (z)	10 mm	1.5 ns	6	–	606	373k
TGC	trigger	2-6 mm (r)	3-7 mm	4 ns	–	9	3588	318k

Table 2.3: Parameters of the four subdetectors of the Muon Spectrometer. Taken from Reference [23].

The Resistive-Plate Chambers (RPC) and the Thin-Gap chambers (TGC) are the sub-

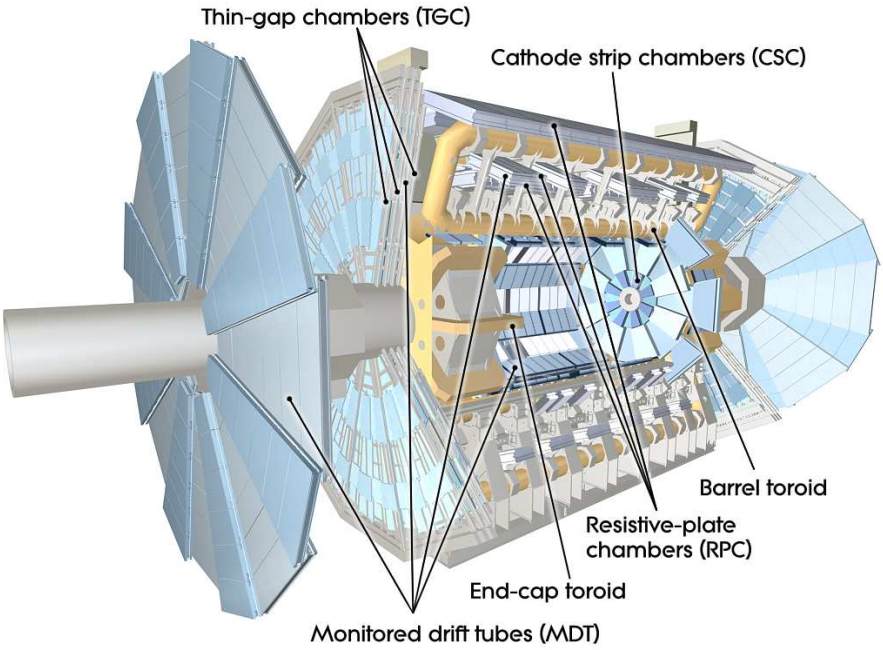

Figure 2.8: The Muon Spectrometer with its subdetectors and the toroidal magnet system. Taken from Reference [23].

detectors used to enable triggering on muons. To do so they feature time resolutions of $O(\text{ns})$, which enables them to correlate muon signatures to a specific bunch crossing. RPCs are covering $|\eta| < 1.05$ while the TGCs are located at $1.05 < |\eta| < 2.4$.

The magnet system of the MS, enabling the muon momentum measurement, consists of three toroids: a barrel toroid with a field strength of $\approx 0.5\,\text{T}$ and two end-cap toroids with $\approx 1\,\text{T}$. They are air-core magnets which reduces the material budget inside the MS, minimising the scattering of muons.

2.6 Trigger and Data Acquisition

At instantaneous luminosities of $2 \times 10^{34}\,\text{cm}^{-2}\text{s}^{-1}$, the LHC produces bunch collisions at a rate of 40 MHz, with $\langle\mu\rangle \approx 50$ pp interactions during each bunch crossing. Not all detector data is read out and analysed for all the events because of two reasons. Firstly, the bandwidth to read out, the computing resources to analyse and the storage capacity to save all 40 million events would be enormous. Especially detector systems subject to large particle multiplicities and featuring a fine granularity, such as the Pixel detector, are heavily constrained by these physical limitations. The second reason is that the benefit of reading out and analysing all pp-collision events would be marginal since the great majority are inelastic proton scattering events that do not contain interesting signatures. ATLAS therefore employs a *trigger* that decides whether to further investigate a collision event based on certain criteria. The ATLAS Trigger and Data Acquisition (TDAQ) system [23, 110] is designed to select events containing interesting physics processes to read out and write to disk storage.

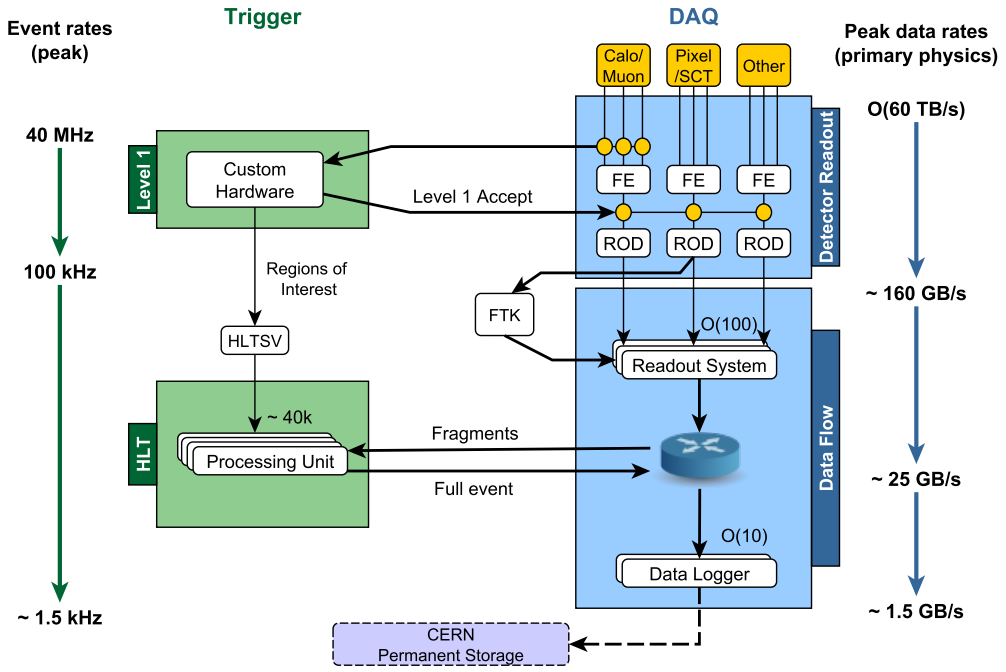

Figure 2.9: Diagrammatic representation of the ATLAS Trigger and Data Acquisition system during Run 2. Taken from Reference [111].

The TDAQ system is diagrammatically depicted in Figure 2.9 and employs a two-stage approach. The Level 1 trigger (L1) reduces the event rate from 40 MHz to 100 kHz, which the High Level Trigger (HLT) then further trims to a rate of $\sim$ 1.5 kHz events that are saved to disk storage.

The L1 is a hardware trigger implemented in custom-made electronics, running with a fixed latency of 2.5 μs. It searches for signatures with electrons and photons, jets, muons and hadronically decaying τ-leptons, as well as $E_{\mathrm{T}}^{\mathrm{miss}}$ and transverse energy. It decides whether to accept an event based on data from Regions of Interest (RoI) in $\eta \times \phi$ provided by the MS (L1Muon), the calorimeter (L1Calo) and the association between L1Muon and L1Calo trigger objects (L1Topo) [23, 112].

Events accepted by the L1 trigger then are further analysed by the HLT. This software-based system receives the complete information about the triggered event from the muon and calorimetry systems, as well as tracking information from the Pixel and SCT systems (FTK). The HLT conducts an offline-like reconstruction allowing it to look for more advanced signatures such as for example jets originating from b-quarks. The HLT typically selects around 1500 events per second to be saved in the offline storage within 300 ms, where precise offline reconstruction of the events is taking place [112].

The following Chapter 3 discusses how the raw detector data stored by the HLT are used to identify and reconstruct the different particle objects later used for the BSM search in Chapter 4.

Chapter 3

Particle Reconstruction and Identification

This chapter introduces how the particles used in the $tc + E_{\mathrm{T}}^{\mathrm{miss}}$ search, discussed in Chapter 4, are identified and reconstructed using the various ATLAS detector systems. Section 3.1 discusses the track and vertex reconstruction that is used in Section 3.2 and Section 3.3 for the reconstruction of jets and the identification of the quark content. Section 3.4 and Section 3.5 concern the reconstruction of electrons and muons respectively. Finally, Section 3.6 describes how this information is used to calculate the missing transverse momentum ($E_{\mathrm{T}}^{\mathrm{miss}}$).

3.1 Tracks and Vertices

The charged particle track reconstruction uses information from the ID [113–115] and is conducted in two complementary approaches. The *inside-out* track reconstruction first assembles clusters from the raw hits in the Pixel and SCT subdetectors. These clusters are then used to create three-dimensional space-points that mark the location where a charged particle traversed the active material of a sensor. In the SCT, clusters from the two sides of the SCT sensors must first be combined to obtain three-dimensional space-points. Sets of three such space-points are then used as seeds for a first track finding algorithm that uses a combinatorial Kalman filter [116]. It adds additional space-points of the remaining Pixel and SCT layers, which are compatible with the trajectory from the seeds, and creates corresponding track candidates. Ambiguities due to incorrectly assigned or overlapping track candidates are resolved by an ambiguity-solving stage. The remaining track candidates then undergo a high-resolution fit and are used to search for a compatible extension of the track outside of the Pixel+SCT region using TRT hits as shown in Figure 3.1.

The second track reconstruction approach is called *outside-in* tracking and builds track segments from TRT data that have not been assigned to tracks yet. Extending these track segments inwards to the SCT and Pixel subdetectors allows for the identification of previously missed short track segments. Such segments can, for example, originate from long-lived particles that decay inside the ID or from converted photons that do not produce a hit in the innermost silicon layers. Figure 3.2 shows that, for example,

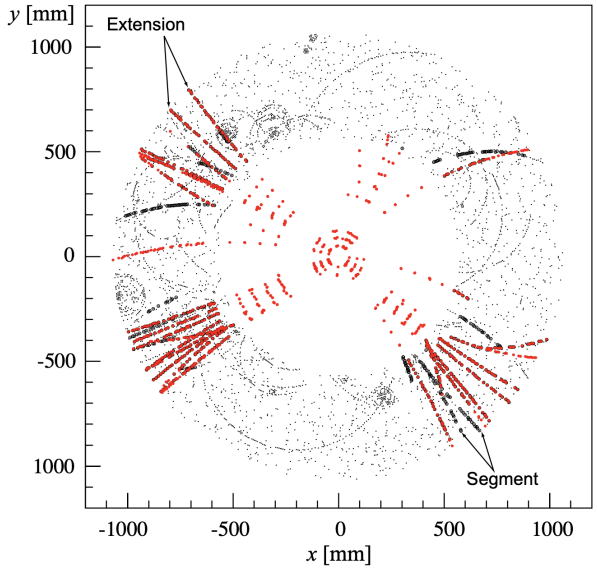

Figure 3.1: Reconstruction in the ID of a Monte Carlo simulated $t\bar{t}$ event. TRT measurements are used both in the inside-out track reconstruction (red circles) to build silicon track extensions an also in outside-in tracking (black circles) to find TRT track segments and possibly corresponding silicon track segments. Taken from Reference [115].

a single-track reconstruction efficiency between 80 and 95% is achieved for B^0-hadron decays.

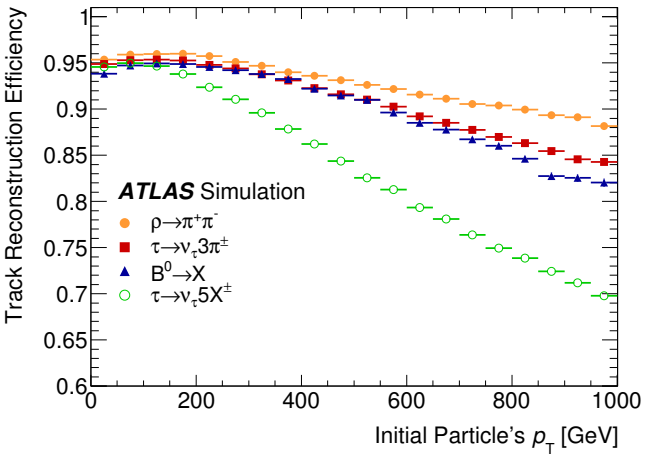

Figure 3.2: Single-track reconstruction efficiency versus the initial particle p_{T} for various decays, where the parent particle is required to decay before the IBL. Taken from Reference [113].

ID tracks that fulfil a set of requirements [117] are then used to reconstruct primary and secondary vertices. The requirements are:

- Track $p_{\mathrm{T}} > 400\,\mathrm{MeV}$ and $|\eta| < 2.5$.
- At least 9 (11) silicon hits (Pixel/SCT) for $|\eta| \leq 1.65$ ($|\eta| > 1.65$) of which there is at least one hit in the first two pixel layers.

- Not more than one pixel hit (two SCT hits) shared by the tracks.
- No Pixel and not more than one SCT *hole*, where a hole is an expected but not observed hit from a reconstructed track in a sensor.

A seed position is selected as a first assumption for a vertex. The reconstructed tracks and this vertex are then used to update the original vertex location. The fit is then repeated in an iterative fashion, down-weighting tracks that feature a smaller compatibility with the vertex. When the vertex location is fixed, tracks incompatible with this vertex are removed and can be used for other vertices instead. This is repeated until all tracks have been associated with vertices or no additional vertex compatible with the remaining tracks can be found. The *primary vertex* is defined as the one with the largest sum of squared p_{T}, while the other vertices are called *secondary vertices* [118]. The location of the primary vertex is described by the distance to the origin of ATLAS in the transverse plane (d_0) and along the z-axis (z_0). The ID achieves a primary vertex resolution of 25–90 μm (σ_{d_0}) and 70–170 μm (σ_{z_0}) [101]. The precise measurement of the primary and secondary vertices is of great importance in the determination of the flavour of jets discussed in Section 3.3.

3.2 Jets

As discussed in Section 1.1, quarks and gluons generated in high-energy collisions hadronise and produce a collimated stream of colour-neutral hadrons. The signatures of these hadrons can be seen by the ID and the calorimeters and are used to construct an object associated to these tracks and energy deposits – a *jet*. By estimating the energy and direction of these jets, information about the initial quark or gluon can be recovered.

The construction of jets starts with the clustering of hadronic energy deposits in the HCAL to so-called *topo-clusters* [119–121]. The topological clustering algorithm groups HCAL cells based on how much the energy deposits are above the total noise level. It starts with seed cells that are significantly above the total noise (signal-to-noise ratio $> 4\sigma$) and groups them together iteratively with neighbouring cells with high energy deposits ($> 2\sigma$). Adjacent cells are then added and a cluster-splitting algorithm is employed to avoid overlaps between topo-clusters. The resulting clusters then are treated as massless objects to construct a four-vector originating from the primary vertex with an energy associated to it equal to the sum of the topo-cluster cells.

The topo-clusters and the ID tracks then are combined by the Particle Flow (PF) algorithm [122] into Particle Flow Objects (PFOs) later used for the construction of jets. PF firstly removes overlaps between the momentum measurements in the ID and the energy measurements in the calorimeters. It then matches individual topo-clusters to well measured tracks, creating a track/topo-cluster system. The track is then used to calculate the average expected energy deposit ($\langle E_{\mathrm{dep}} \rangle$) in the calorimeter, which is compared with the actual energy of the topo-cluster. If necessary, the PF algorithm then adds additional topo-clusters to the track/topo-cluster system. The energy in these topo-clusters is then subtracted cell-by-cell by $\langle E_{\mathrm{dep}} \rangle$, leaving topo-cluster remnants that are removed if their energy is consistent with the energy fluctuations expected in the shower.

The tracks matched to the primary vertex ($|z_0 \sin\theta| < 2\,\mathrm{mm}$) and the energy-subtracted

topo-clusters form PFOs and the topo-clusters are used as inputs to the anti-k_t algorithm clustering algorithm [123]. It is part of the group of sequential recombination algorithms that use the distances between clusters i and j (d_{ij}) and also between a cluster i and the beam (d_{iB}) to sequentially construct jets. These distances are defined as

$$d_{ij} = \min\left(p_{\mathrm{T},i}^{2p}, p_{\mathrm{T},j}^{2p}\right)\frac{\Delta R_{i,j}^2}{R^2} \quad \text{and} \tag{3.1}$$

$$d_{iB} = p_{\mathrm{T},i}^{2p}\,, \tag{3.2}$$

with R being the desired radius of the constructed jets. The algorithm then proceeds as follows:

- Calculate all distances d_{ij} and d_{iB}.
- If a distance d_{iB} is the smallest, then define the corresponding cluster as jet and remove the cluster from subsequent calculations.
- If a d_{ij} is smallest, then replace the corresponding clusters i and j by a new, combined cluster.

This procedure is repeated until all clusters have been combined and/or classified as jets. The anti-k_t algorithm sets $p = -1$ which implies that it starts with the most energetic clusters and combines it with neighbouring low-energetic clusters. The benefit of this approach is that the anti-k_t algorithm is *infra-red* and *collinear* safe, meaning that emission of soft gluons and the collinear splitting of a parton does not significantly change the constructed jet properties [124]. The search presented in this thesis uses both small-R jets with $R = 0.4$, where the topo-clusters associated with PFOs are used as inputs to the anti-k_t algorithm, as well as large-R jets with $R = 1.0$ that instead directly use the topo-clusters for clustering.

Since the topo-clusters originally are calibrated at the EM scale [122], a jet calibration needs to be performed to retrieve the jet energies at the hadronic scale. The Jet Energy Scale calibration [125] corrects the energy scale of the jets using simulated truth jets. This accounts for the change of the jet energy due to a wrong jet origin, pile-up, dependence on the flavour of the original parton and on η [121]. The associated jet energy resolution needs to be calibrated as well.

A further suppression of pile-up induced jets is conducted using the Jet Vertex Tagger (JVT) algorithm [126]. The JVT is a multivariate combination of the Jet Vertex Fraction, that is defined as the fraction of the total momentum of the tracks coming from the primary vertex, and the number of primary vertices in the event. A selection on the JVT improves the rejection of pile-up events and yields a flat efficiency in the number of primary vertices.

Jets can also be constructed from sources other than pp-collisions. The main contributions are beam induced backgrounds (BIB) due to proton losses away from the interaction point, cosmic-ray showers and calorimeter noise. Such jets need to be removed before performing an analysis, which is done by applying quality criteria depending on the signal pulse shape in the LAr calorimeters, track-based and energy ratio based variables [127].

3.3 Charm and Bottom Jets

The construction of the jets discussed in the previous section provides information about the kinematics of the jets. Additional to this, many data analyses also require information about the original parton that created the jet. The flavour-tagging of jets originating from hadrons containing a b-quark (b-tagging) or from hadrons containing a c-quark (c-tagging) are of crucial importance for the physics analysis presented in this thesis as the targeted final state only consists of a top quark, that rapidly decays to a b-quark and a W boson, a c-quark and $E_{\mathrm{T}}^{\mathrm{miss}}$. This requires a high flavour-tagging efficiency and good rejection of incorrectly-tagged jets.

Bottom and charm jets can be distinguished from *light jets* (u-, d-, s- or gluon-initiated jets) due to the presence of hadrons containing a b-quark or a c-quark, referred to as b-hadrons and c-hadrons respectively. These particles have a distinct lifetime of $\approx 1.5\,\mathrm{ps}$ (b-hadrons [128]) and 0.15 to 1 ps (c-hadrons [10]) that enable them to travel significant distances within the detector before decaying, calculated by $d = \gamma\beta c\tau$ with $\gamma\beta$ being the relativistic boost. Assuming a b-hadron with a momentum of 50 GeV, this leads to $d \approx 4.4\,\mathrm{mm}$. Experimentally this can be seen as a secondary vertex displaced from the primary vertex as shown in Figure 3.3. The *impact parameter* then is defined as the displacement of a track from the primary vertex in the longitudinal (z_0) and transverse direction (d_0). Another difference to light-jets is the large mass of the b- and c-hadrons that leads to a larger multiplicity of decay products [129].

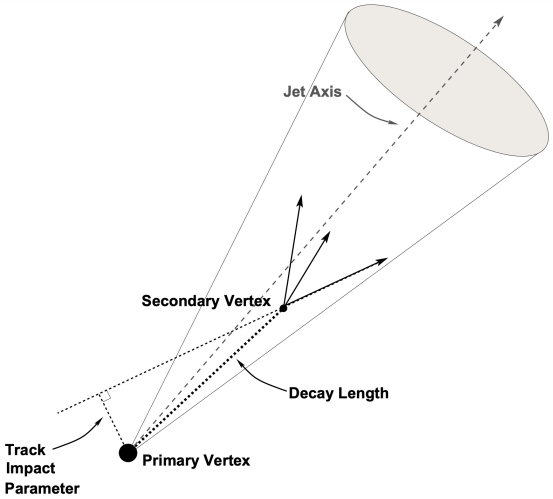

Figure 3.3: Drawing of tracks originating from a secondary vertex and the enclosing constructed jet. The track impact parameter is the displacement of these extended tracks from the primary vertex resulting from a long decay length of a b- or c-hadron. Taken from Reference [130].

ATLAS uses different kinds of algorithms to extract information to enable the tagging of jets [131, 132]. The SV1 and JetFitter algorithms aim at directly reconstructing secondary vertices, while IP3D and RNNIP are using the impact parameters to estimate the probability of a jet to have a certain flavour. The working principles of these algorithms are described in the following:

- The SV1 algorithm [133] uses tracking information to reconstruct a single displaced

secondary vertex. It starts by identifying vertices with two tracks and rejects all tracks in the jet that are compatible with originating from long-lived particles, hadronic interactions with the detector or the conversion of a photon into an electron in an ID layer (photon conversion). It then iteratively runs over every vertex and tries to reconstruct a single secondary vertex with all the other tracks. The track that is least compatible with the fitted vertex is removed and the procedure is repeated until the fit of the vertex and the tracks has a low χ^2 and the vertex has an invariant mass of less than 6 GeV.

- The topological features of the full b-hadron decay chain are analysed by the JetFitter algorithm [134]. The decay topology of $b \to c \to s$ leads to two detached vertices that can both have a high invariant mass and multiple charged tracks associated to them. The algorithm assumes a common line, on which the primary and the two secondary vertices lie, to explicitly reconstruct the displaced vertices, similarly to SV1.
- The IP3D algorithm [135] does not explicitly reconstruct the displaced vertices but rather uses the large impact parameters of the tracks from b- and c-hadrons. Probability density functions (PDFs) of the signed longitudinal and transverse impact parameter significances of b-, c- and light-jets are derived from Monte Carlo simulation. These PDFs then are used to calculate ratios between the three flavour probabilities for each track and corresponding log-likelihood discriminants are defined.
- RNNIP [136] is a Recurrent Neural Network (RNN) based algorithm. In contrast to the other impact-parameter based algorithm IP3D, which assumes all tracks in a jet to be independent, RNNIP can use the spatial and kinematic correlations among the tracks in a jet that are coming from the same b- or c-hadron.

The outputs of IP3D, SV1, JetFitter and RNNIP are combined by the Neural Network based DL1r flavour-tagging algorithm [132,137]. The DL1r network is trained on a hybrid sample consisting of simulated events decaying into hadronic jet pairs [131]. The DL1r algorithm features a multidimensional output consisting of the probabilities for a jet to be a b-jet (p_b), a c-jet (p_c) or a light-jet (p_{light}). Introducing the effective b- and c-tag fractions in the background training sample (f_b and f_c), the DL1r b-tagging and c-tagging discriminants are defined as log likelihood ratios by

$$\text{DL1r}_b = \ln\left(\frac{p_b}{f_c \cdot p_c + (1 - f_c) \cdot p_{\text{light}}}\right) \text{ and} \tag{3.3}$$

$$\text{DL1r}_c = \ln\left(\frac{p_c}{f_b \cdot p_b + (1 - f_b) \cdot p_{\text{light}}}\right) . \tag{3.4}$$

The optimal trade-off between rejecting c- and light-jets (b- and light-jets) for the tagging of b-jets (c-jets) can be received by tuning f_c (f_b). The threshold used for the DL1r_b (DL1r_c) discriminant then defines the desired tagging efficiency ϵ_b (ϵ_c), where a higher efficiency comes with a worse rejection $1/\epsilon$ on differently-flavoured jets. Figure 3.4 shows the b-tagging efficiency of the MV2, DL1 and DL1r taggers for different light-jet and c-jet rejections.

The analysis contained in this thesis uses the 77% b-jet working point (WP) ($\epsilon_b = 0.77$) commonly used in ATLAS analyses. This WP features a c-jet rejection of $\epsilon_c^{-1} = 5$ and a

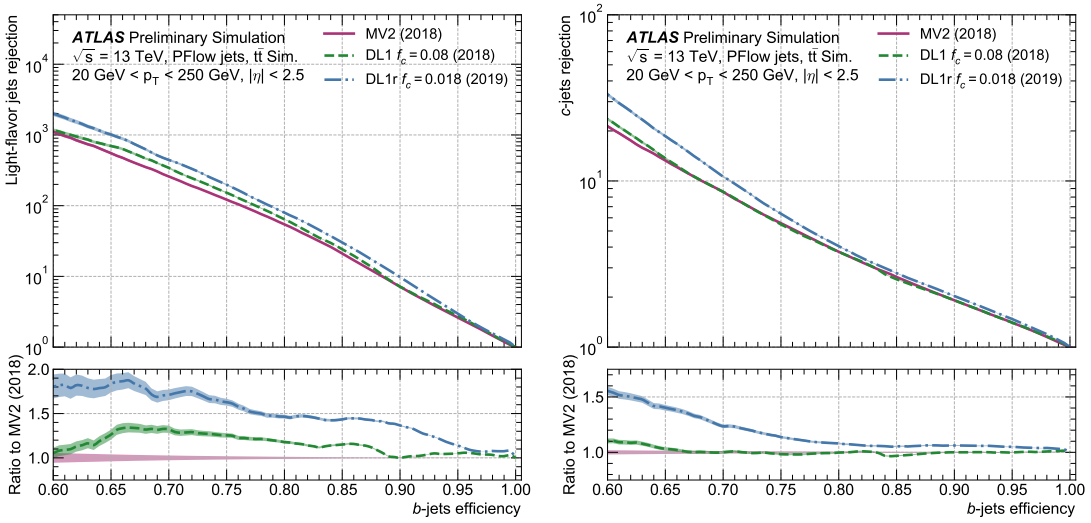

(a) (b)

Figure 3.4: b-tag efficiency versus light-jet (a) and c-jet rejection (b) for the MV2, DL1 [135] and DL1r flavour-tagger. Taken from Reference [138].

light-jet rejection of $\epsilon_{\text{light}}^{-1} = 170$ (see Figure 3.4). Figure 3.5 shows the scaling factors and their uncertainties for multiple bins in p_{T} of this WP. The c-tagging calibration specific to this analysis is discussed in Section 4.4.

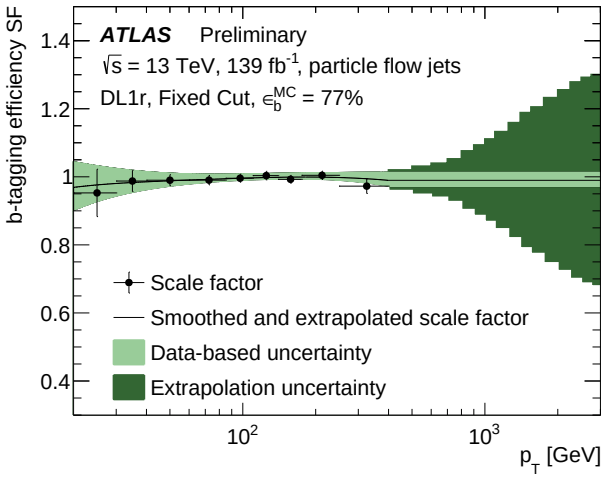

Figure 3.5: Scaling factors and their uncertainties derived for multiple bins in p_{T} for the 77% b-jet WP [139]. The vertical error bars indicate the statistical uncertainty in the data while the coloured show the total uncertainty also taking into account systematic uncertainties.

3.4 Electrons

Electron reconstruction [140] is based on three key principles: electrons leave tracks in the ID, they generate clusters of energy in the EM calorimeter and their tracks can be

matched with the EM activity in $\eta \times \phi$ space. In contrast to this, the photon does not leave a track in the ID, except for conversion photons.

In a first step, the EM activity of a *tower* is calculated, which is the summed energy deposition in all layers of the ECAL in granularities of 0.025×0.0245 in $\eta \times \phi$. These towers are fed into a sliding-window algorithm [119] to search for EM cluster candidates with transverse energies of more than 2.5 GeV. Tracks with at least four silicon hits, that are close in $\eta \times \phi$ to the EM clusters, are then going through a second fitting procedure using a Gaussian-Sum filter (GSF, [141]) that better takes into account the energy loss of the electrons in the detector. These GSF-tracks are then matched to calorimeter seed clusters to form electron candidates.

The electron candidates are further evaluated using a likelihood-based (LH) technique. The matching of the EM clusters and the tracks, the track properties as well as variables describing the shape of the EM showers in the lateral and longitudinal direction are given to the LH. The output of the LH is used to define WPs with different electron reconstruction efficiencies and background rejection factors for the electron. Figure 3.6 shows the comparison of the identification efficiency between data and simulation for the *loose*, *medium* and *tight* WPs.

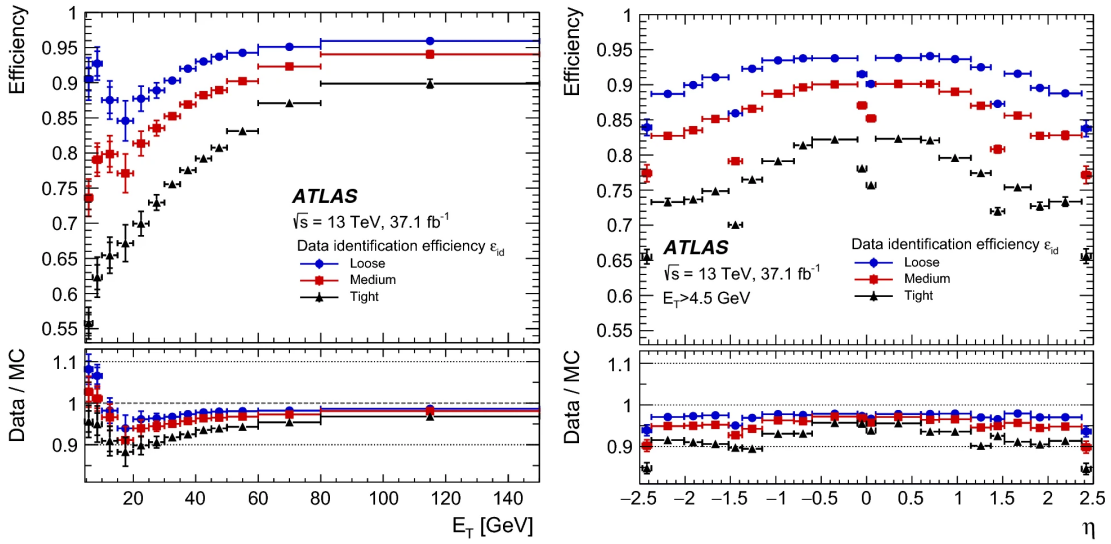

(a) (b)

Figure 3.6: Comparison of the LH electron-identification efficiencies between data and simulation in $Z \to e^+e^-$ in p_{T} (a) and η (b). Taken from Reference [140].

As a last step, calorimeter- and track-based isolation criteria are defined to quantify how much activity is present close to the electron candidate [142]. The identification and reconstruction procedure is similar for photons [143].

3.5 Muons

Muon reconstruction [144] uses tracks in the ID (as discussed in Section 3.1) and in the MS, with the additional usage of calorimeter information in regions where the MS is not fully instrumented.

The reconstruction of muon tracks in the MS starts with the formation of segments inside the individual muon chambers. Segments from different MS layers are used to build muon track candidates, which then can be used together with the information from the ID and calorimeters to define different muon *types*.

Combined muons are reconstructed using both outside-in and inside-out pattern recognition. ID tracks can also be matched to a MDT or CSC track segments only, resulting in a *segment-tagged muon*. Due to ID and calorimeter services at $|\eta| < 0.1$, muons in this region are built by matching ID tracks to energy deposits compatible with a minimum-ionising-particle to build *calorimeter-tagged muons*. The last muon type is *extrapolated muons* that are reconstructed purely by MS tracks, which is important in the region of $2.5 < |\eta| < 2.7$ that is not covered by the ID.

Different WPs are defined for the identification and isolation of the muon, similarly to the jets and electron. Figure 3.7 shows the muon reconstruction efficiency as a function of η for the medium WP used in the data analysis presented in Chapter 4.

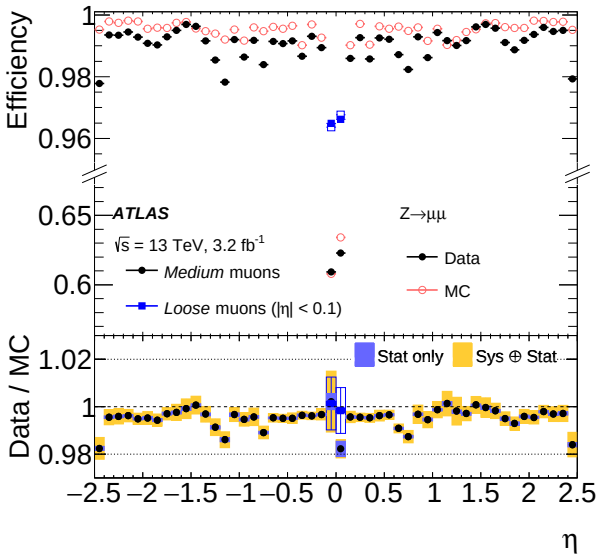

Figure 3.7: Data to simulation comparison of muon reconstruction efficiency as a function of η for the medium WP in $Z \to \mu^+\mu^-$ events for $p_{\mathrm{T}} > 10\,\mathrm{GeV}$. In the region of $|\eta| < 0.1$ the loose WP is shown as well.

After the reconstruction of all relevant particles, an overlap removal (OR) procedure is applied to remove overlapping objects. This is discussed in detail in Section 4.4. The objects passing the OR then are used to reconstruct the $E_{\mathrm{T}}^{\mathrm{miss}}$ as presented in the following section.

3.6 Missing Transverse Momentum

The $E_{\mathrm{T}}^{\mathrm{miss}}$ calculation [145] uses all reconstructed objects discussed in this chapter, the *hard objects*, as well as *soft* contributions. The latter are energy deposits not associated with a hard object. The total missing transverse momentum vector ($\mathbf{E}_{\mathrm{T}}^{\mathrm{miss}}$) can be

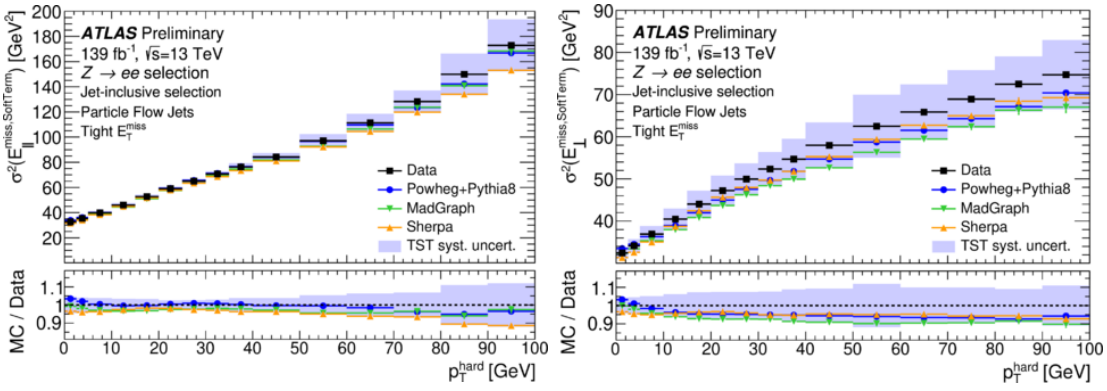

Figure 3.8: Comparison between data and simulation of the squared standard deviation of the TST distributions projected in the direction longitudinal (a) and transverse (b) to the vector sum of the hard objects. $Z \to ee$ and jet-inclusive selections are employed, where the $E_{\mathrm{T}}^{\mathrm{miss}}$ is reconstructed using particle flow jets and the tight $E_{\mathrm{T}}^{\mathrm{miss}}$ WP. The shaded band indicates the TST systematic uncertainty. Taken from Reference [146].

calculated [145] as the sum of these terms as

$$\begin{aligned}\mathbf{E}_{\mathrm{T}}^{\mathrm{miss}} &= \sum_{i\in\{\text{hard objects}\}} \mathbf{E}_{\mathrm{T}}^{\mathrm{miss},i} + \sum_{j\in\{\text{soft contributions}\}} \mathbf{E}_{\mathrm{T}}^{\mathrm{miss},j} \\ &= \sum \mathbf{E}_{\mathrm{T}}^{\mathrm{miss,\ e}} + \sum \mathbf{E}_{\mathrm{T}}^{\mathrm{miss,\ }\mu} + \sum \mathbf{E}_{\mathrm{T}}^{\mathrm{miss,\ jets}} + \sum \mathbf{E}_{\mathrm{T}}^{\mathrm{miss,\ soft}} . \end{aligned} \tag{3.5}$$

The magnitude of $\mathbf{E}_{\mathrm{T}}^{\mathrm{miss}}$ then is the scalar $E_{\mathrm{T}}^{\mathrm{miss}}$, while ϕ_{miss} is the direction of the $E_{\mathrm{T}}^{\mathrm{miss}}$ in the transverse plane.

To calculate the total $E_{\mathrm{T}}^{\mathrm{miss}}$ correctly, the individual contributions are summed in a defined order: first electrons, then muons and lastly jets. Objects are rejected if they have shared energy depositions with previously counted objects. Finally, the soft contribution is added, which is taken to be the *track soft term* (TST). The TST is the $E_{\mathrm{T}}^{\mathrm{miss}}$ resulting from reconstructed tracks originating from the hard-scatter vertex, but not associated with a hard object. Figure 3.8 shows a comparison between the predicted and observed values of the $E_{\mathrm{T}}^{\mathrm{miss}}$ in $Z \to e^+e^-$ events using the *tight* $E_{\mathrm{T}}^{\mathrm{miss}}$ WP [145] also employed in the data analysis of this thesis.

Lastly, it is important to note that fake contributions to the $E_{\mathrm{T}}^{\mathrm{miss}}$ from detector noise and inefficiencies, the finite detector resolution and pile-up are affecting the $E_{\mathrm{T}}^{\mathrm{miss}}$ and must be taken into account.

Chapter 4

Search for Top Squarks in Mixed-Flavour Final State

This chapter presents the ATLAS Run 2 analysis with the $tc + E_{\mathrm{T}}^{\mathrm{miss}}$ final state arising from the process introduced in Section 1.7. Firstly, Section 4.1 describes the strategy of the analysis, followed by a description of the statistical interpretation that will be used. The dataset and Monte Carlo (MC) simulated samples are introduced in Section 4.3, while the subsequent sections discuss object selections and the first set of selections used in this analysis (*preselection*), together with a description of the used variables. Section 4.6 and Section 4.7 then present the development and training of the Neural Network (NN) discriminator used in the analysis. Section 4.8 and Section 4.9 discuss the selections of the signal regions and the estimation of the SM backgrounds. Finally, Section 4.10 and Section 4.11 present the systematic uncertainties and the results.

4.1 Analysis Strategy

The topology of the $tc + E_{\mathrm{T}}^{\mathrm{miss}}$ simplified model introduced in Section 1.7 depends heavily on $\Delta(m(\tilde{t}_1), m(\tilde{\chi}_1^0))$. For mass differences of more than $m(t)$, as considered in this work, the simplified model features only two-body decays. Furthermore requiring the all-hadronic decay of the W, signal events are expected to contain one b-jet, one c-jet, further jets from the W decay, no electrons or muons (from now on referred to as *leptons*) and $E_{\mathrm{T}}^{\mathrm{miss}}$ from the two $\tilde{\chi}_1^0$ as shown in Figure 4.1.

The kinematics of the events depend on $\Delta(m(\tilde{t}_1), m(\tilde{\chi}_1^0))$. To ensure a high signal selection efficiency and good rejection of the SM background, three kinematic regions have been defined that target different $\Delta(m(\tilde{t}_1), m(\tilde{\chi}_1^0))$ as illustrated in Figure 4.2.

Boosted Region A

This region targets models with $\Delta(m(\tilde{t}_1), m(\tilde{\chi}_1^0)) \gg m(t)$, which leads to a highly boosted c-jet and a collimated decay of the top quark. The latter can be reconstructed within a $R = 1.0$ jet. Top-tagging [147] is applied on these large-R jets, where events are required to contain at least one top-tagged large-R jet to suppress background events. The jet

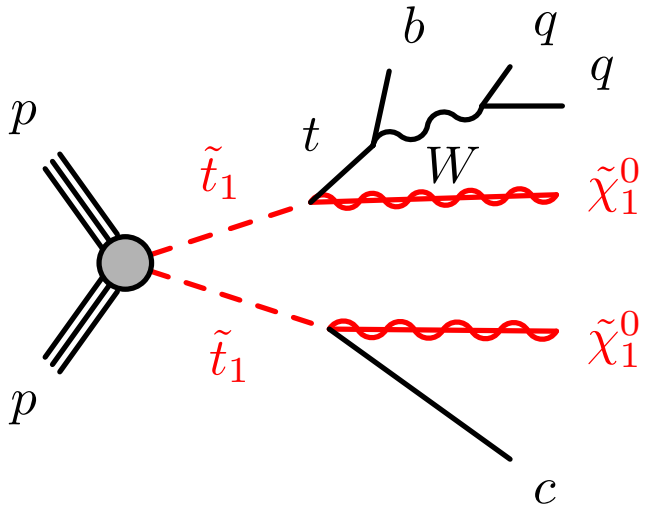

Figure 4.1: Diagrammatic representations of the 2-body decay $tc + E_{\mathrm{T}}^{\mathrm{miss}}$ SUSY signal in the zero leptons (0L) channel.

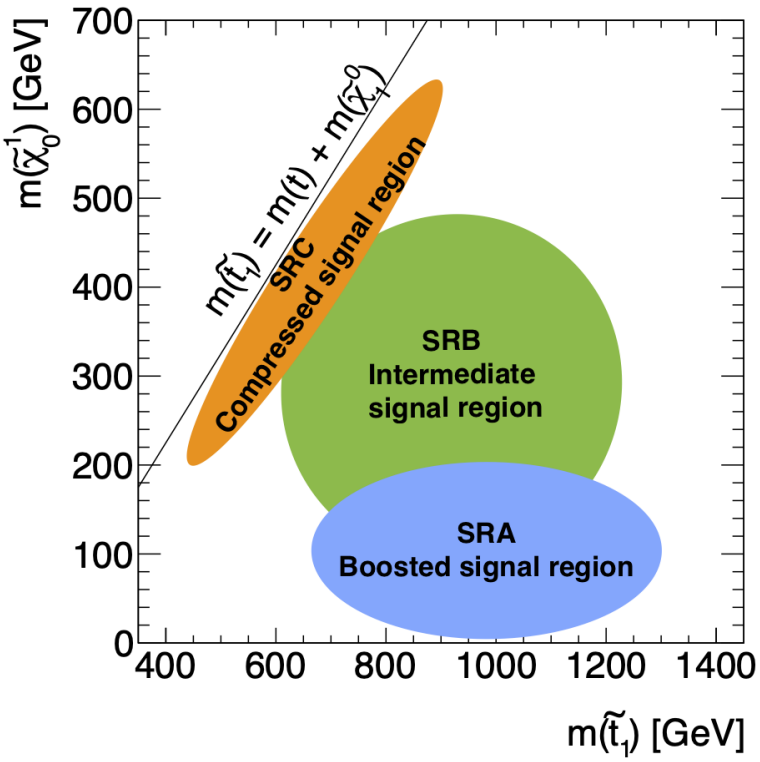

Figure 4.2: Schematic drawing of the different kinematic regions in the $tc + E_{\mathrm{T}}^{\mathrm{miss}}$ analysis.

with the highest p_{T} (*leading* jet) is expected to most often be a b- or c-jet and a large $E_{\mathrm{T}}^{\mathrm{miss}}$ is expected.

Intermediate Region B

Region B targets kinematics where $\Delta(m(\tilde{t}_1), m(\tilde{\chi}_1^0)) > m(t)$ leads to more moderate jet p_{T}'s and lower $E_{\mathrm{T}}^{\mathrm{miss}}$ compared to Region A. The decay topology of the top is on average also less collimated than in Region A. To still benefit from top-tagging, Region B will be split into two parts: one requiring at least one top-tagged large-R jet, while the other part targets less boosted signal events by requiring no top-tagged jets. Both Region A and B require a leading b- or c-jet to ensure orthogonality to the last region.

Compressed Region C

This region is designed to be sensitive to signal models with $\Delta(m(\tilde{t}_1), m(\tilde{\chi}_1^0)) \approx m(t)$, which leads to soft-$p_{\mathrm{T}}$ jets. To still enable a good discrimination from the SM background (especially $t\bar{t}$), an Initial State Radiation (ISR) topology is enforced by requiring a leading light-jet. The ISR jet recoils against the $\tilde{t}_1\tilde{t}_1$-system and leads to higher $E_{\mathrm{T}}^{\mathrm{miss}}$ and jet p_{T}'s. Further distinction between the signal and background is achieved by employing a NN classifier using low-level event information such as the kinematics of the jets.

All regions follow a similar strategy to model the SM backgrounds. Regions enriched with signal events are called *signal regions* (SRs) and use the $E_{\mathrm{T}}^{\mathrm{miss}}$-trigger, featuring a zero lepton (0L) selection, while *control regions* (CRs) abundant with background events of different types use the 1L-trigger with one (1L) or two (2L) leptons. These control regions are then used to calculate *normalisation factors* (μ_{bkg}) that scale the MC background expectations to match the data. This scaling is then tested in 0L *validation regions* (VRs) that are low on signal events but feature kinematics similar to the SRs. All regions are designed to be orthogonal to one another and therefore can be statistically combined to achieve greater sensitivity to the signal.

4.2 Statistical Interpretation

The HistFitter statistical framework [148] is used to make a global fit of all SRs and CRs. A log-likelihood fit is performed of the observed data and expected MC yields in the SRs and CRs, including the systematic uncertainties on the MC yields. For each normalised background i, the ratio between the expected yield in a SR ($\mathrm{MC}_{i,\mathrm{SR}}$) and the CR ($\mathrm{MC}_{i,\mathrm{CR}}$) is used to define a *transfer factor* (TF) than can then be used to estimate the expected number of background events of type i in the SR ($N_{i,\mathrm{SR}}^{\mathrm{exp}}$), given the number of observed events in the corresponding CR ($N_{i,\mathrm{CR}}$) by

$$N_{i,\mathrm{SR}}^{\mathrm{exp}} = \underbrace{\left(\frac{\mathrm{MC}_{i,\mathrm{SR}}}{\mathrm{MC}_{i,\mathrm{CR}}}\right)}_{\text{Transfer Factor } i} \cdot N_{i,\mathrm{CR}} = \mu_i \cdot \mathrm{MC}_{i,\mathrm{SR}}\,, \tag{4.1}$$

where the equation is rewritten using the normalisation factors for background i ($\mu_i = N_{i,\mathrm{CR}}/\mathrm{MC}_{i,\mathrm{CR}}$) instead. This background estimation using TFs allows for partial cancel-

lation of the systematic uncertainties.

The fit is then performed by building a likelihood function. It is the product of Poisson distributions of the expected and observed event counts in the SRs ($\mathcal{P}_{\text{SR}}$) and in the CRs ($\mathcal{P}_{\text{CR}}$), and also additional Gaussian distributions to include the systematic uncertainty constraints $\mathcal{C}_{\text{syst}}$. Following Reference [148], the likelihood function L can be written as

$$\begin{aligned} L(\mathbf{n}, \boldsymbol{\theta}^0 | \mu_{\text{sig}}, \boldsymbol{\mu}_p, \boldsymbol{\theta}) =& \mathcal{P}_{\text{SR}} \times \mathcal{P}_{\text{CR}} \times \mathcal{C}_{\text{syst}} \\ =& \prod_{i \in \text{SR}} P\left(n_i | \lambda_i\left(\mu_{\text{sig}}, \boldsymbol{\mu}_p, \boldsymbol{\theta}\right)\right) \times \prod_{i \in \text{CR}} P\left(n_i | \lambda_i\left(\mu_{\text{sig}}, \boldsymbol{\mu}_p, \boldsymbol{\theta}\right)\right) \\ & \times C_{\text{syst}}(\boldsymbol{\theta}^0, \boldsymbol{\theta}) \,. \end{aligned} \tag{4.2}$$

The $P(n_i)$ terms indicate Poisson distributions of n_i, the number of observed events in the bin i. The expectations of the Poisson distributions λ_i are functions that depend on the signal and background sources (p), the nuisance parameters that parametrise the systematic uncertainties ($\boldsymbol{\theta}$), the normalisation parameters ($\boldsymbol{\mu}_p$) and also the signal strength (μ_{sig}). The probability density function $C_{\text{syst}}(\boldsymbol{\theta}^0, \boldsymbol{\theta})$ is including the systematic uncertainties, where $\boldsymbol{\theta}^0$ are the central values of the systematic variations around which the nominal values $\boldsymbol{\theta}$ are allowed to vary in the fitting procedure. The systematic term is the product of the probability distributions of the individual systematic uncertainties:

$$C_{\text{syst}}(\boldsymbol{\theta}^0, \boldsymbol{\theta}) = \prod_{j \in systs} G(\theta_j^0 - \theta_j) \,, \tag{4.3}$$

where G are Gaussians of unit width. In the following, the three fit configurations that are used with this likelihood are discussed.

Background-only fit

The background-only fit estimates the total background in the SRs and VRs, without assuming a specific signal model by setting $\mu_{\text{sig}} = 0$. Only the information from the CRs enters the likelihood in Equation (4.2) and the corresponding normalisation factors μ_i are derived. They can then be used to calculate the expected number of events in the SRs and VRs.

Model-dependent fit

In contrast to the background-only fit, the model-dependent fit assumes a specific signal as input. If there was a significant excess in the background-only fit, then the model-dependent fit can be used to measure the signal strength μ_{sig} of the model under consideration. If there is no excess, this fit can be used to set exclusion limits on the model in question. The model-dependent fit is performed simultaneously on the CRs and SRs, adding the signal sample to the CRs to take into account possible signal contamination of the CRs.

By conducting this fit using multiple signal models with different properties, an exclusion contour can be interpolated in this signal parameter space. In this work the signal parameters are the masses of the $\tilde{t}_1$ and of the $\tilde{\chi}_1^0$, so that an exclusion contour can be derived in the ($m(\tilde{t}_1)$, $m(\tilde{\chi}_1^0)$) plane. To decide whether a signal model in question is

excluded, a hypothesis test is performed with μ_{sig} as the parameter of interest. If this test yields a p-value of less than 0.05 (probability to reject the background-only hypothesis), then the signal model is excluded at the 95% Confidence Level (CL) [149].

Model-independent fit

This last fit configuration enables to look for arbitrary BSM models that could enter the SR selections. These limits can be used to easily check whether a model can be excluded by current measurements. The model-independent fit is very similar to the model-dependent fit, with the difference that no signal contamination is allowed. Instead of adding a signal model in the fit, a 'dummy signal' is used with the number of signal events that enter a SR added as a parameter to the fit. This allows to investigate μ_{sig} of the dummy signal. SR bins are treated separately to not require assumptions on how the signal is distributed among the SR bins. The value of μ_{sig} where the CLs drop below 5% then is used to receive an upper limit on the visible cross-section (σ_{vis}) of an arbitrary BSM production process, which is defined as

$$\sigma_{\text{vis}} = \sigma_{\text{BSM}} \cdot \epsilon_{\text{sel}} \cdot \epsilon_{\text{acc}} \,, \tag{4.4}$$

where ϵ_{sel} and ϵ_{acc} are the selection efficiency and the detector acceptance.

4.3 Datasets and Simulated Samples

As shown previously in Figure 2.2, the pile-up conditions in the individual Run 2 data taking years were very different, increasing from $\langle\mu\rangle = 13.4$ in 2015 to $\langle\mu\rangle = 37.8$ and 36.1 in 2017 and 2018 respectively. Since much more luminosity was accumulated in the last two years of data taking, the average pile-up over the complete Run 2 dataset however is $\langle\mu\rangle = 33.7$.

A total of $156\,\text{fb}^{-1}$ of pp collisions were delivered by the LHC during Run 2, which is reduced to $139\,\text{fb}^{-1} \pm 1.7\%$ of *good quality data* [150], as only collisions recorded in stable beam conditions and with all detector systems operational are used for physics analyses.

MC simulation techniques [151] are used in ATLAS to model both SM and BSM physics processes. This enables the estimation of the expected number of SM background events and also of the BSM model in question. In this way, a statistical analysis of these expectations and the measured number of events in data can be done to confirm or reject the SM, find or exclude a specific BSM model or give model-independent cross-section limits.

The modelling of pp collision events is complicated due to the proton substructure, initial and final state radiation and the fact that QCD can not be treated perturbatively at low energies. Due to these complications, the simulation of pp collisions is divided into multiple steps as illustrated in Figure 4.3, of which the most important are:

- The **hard scatter** production cross-section is computed by selecting two partons from Parton Distribution Functions (PDFs) and setting the factorisation and renormalisation scales [152–154]. The matrix element is then computed in perturbation theory.

- All partons are allowed to radiate or split into additional partons in a process called **parton showering**. This leads to initial and final state radiation and also the formation of showers.
- As the individual parton energies decrease in the process of parton showering, confinement occurs and colour-neutral hadrons are formed in the **hadronisation** stage.
- Pile-up is simulated by separately generating **soft QCD** events that are overlaid to the hard scatter event.
- The **detector response** to the generated final state particles is then simulated using a simulation of the ATLAS detector in GEANT4 [155].

The simulated events then undergo the same reconstruction as the collision data (see Chapter 3) and can be used to design the analysis selections.

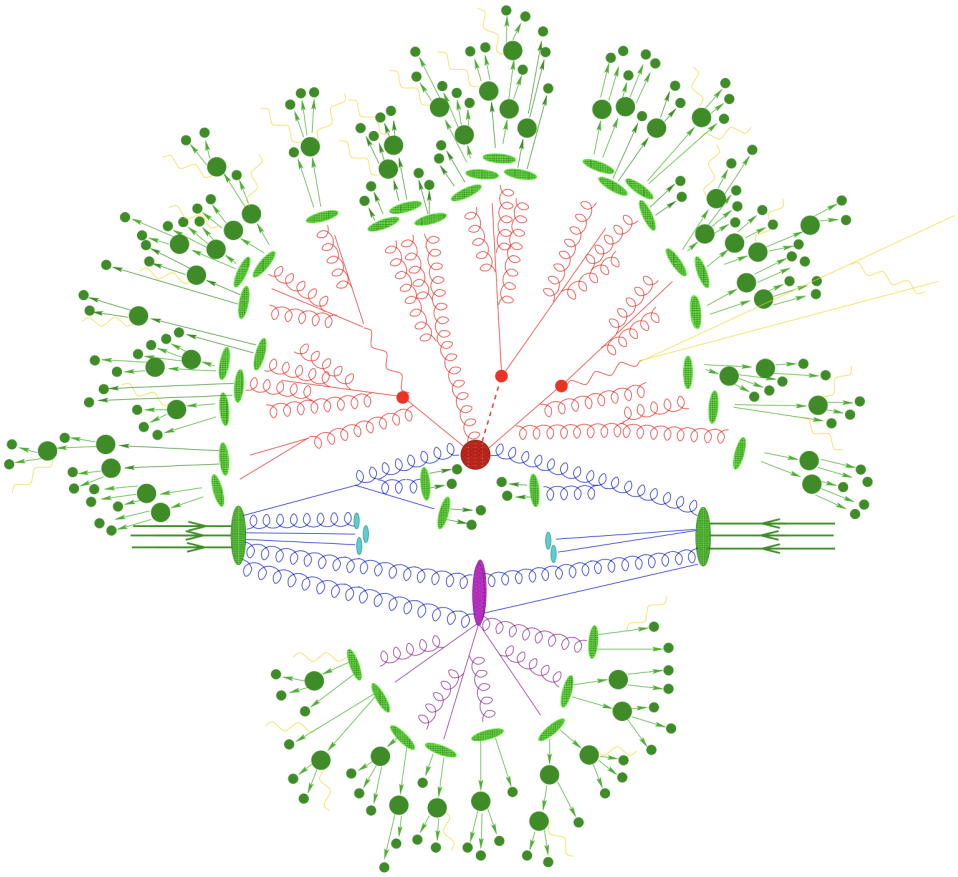

Figure 4.3: Schematic representation of the MC simulation of a $t\bar{t}H$ event. The blue lines indicate the partons of the protons, some of which then form the hard scatter process (large red dot) and secondary interactions (purple). The t, $\bar{t}$ and H then decay (red dots) and the decay products of the hard and secondary interaction shower (red and purple lines) which leads to the formation of hadrons (light green blobs) that then decay (dark green blobs). The emission of photons (yellow curly lines) can take place at any point. such as for example from leptons (yellow straight lines). Taken from Reference [156].

The MC generators used to model the SM background are listed in Table 4.1. The

$tc+E_{\mathrm{T}}^{\mathrm{miss}}$ SUSY signal was modelled using the MadGraph [157] v.2.8.1 generator at next-to-leading-order (NLO) with the NNPDF3.0NLO [158] PDF set. This was interfaced to Pythia [159] 8.244, which is parametrized according to the ATLAS 14 tune [160] with NNPDF2.3LO for the modelling of the $\tilde{t}$ decay, parton showering, hadronisation and underlying event (UE). The heavy-flavour hadron decays were modelled by passing them through EvtGEN [161] v.1.7. The calculation of the matrix element is done at tree level, allowing the emission of up to two additional partons. NNPDF3.0 [158] was used for the PDFs and the matching of the matrix element to the parton shower is done using the CKKW-L [162] prescription, with a matching scale set to $m(\tilde{t}_1)/4$. The signal cross-sections are calculated to next-to-next-to-leading-order (NNLO) accuracy in α_s, adding the resummation of soft gluon emission at next-to-next-to-leading-logarithmic accuracy (NNLO+NNLL) [163–165].

Process	**Matrix element event generator**	**Matrix element PDF**	**PS and hadronisation**	**UE tune**	**Cross-section calculation**
W/Z+jets	Sherpa 2.2.1 [156]	NNPDF3.0NNLO	Sherpa	Default	NNLO [166]
$t\bar{t}+W/Z$	MadGraph5 2.3.3	NNPDF3.0	Pythia 8	A14	NLO [157]
tZ	MadGraph5 2.3.3	NNPDF2.3LO	Pythia 8	A14	LO
tW/Z	MadGraph5 2.3.3	NNPDF2.3LO	Pythia 8	A14	NLO [157]
$t\bar{t}$	Powheg-Box [167]	NNPDF2.3LO	Pythia 8	A14	NNLO+NNLL [168, 169]
Single top	Powheg-Box	NNPDF2.3LO	Pythia 8	A14	NNLO+NNLL [170–172]
Diboson	Sherpa 2.2.1-2.2.2	NNPDF3.0NNLO	Sherpa	Default	NLO
$tc+E_{\mathrm{T}}^{\mathrm{miss}}$	MadGraph5 v2.8.1	NNPDF2.3LO	Pythia 8	A14	NNLO+NNLL

Table 4.1: List of the MC generators used to generate the nominal background samples and the $tc+E_{\mathrm{T}}^{\mathrm{miss}}$ SUSY signal.

The signal samples were generated with a requirement of $E_{\mathrm{T}}^{\mathrm{miss}} > 100\,\mathrm{GeV}$ at truth-level to ensure the availability of enough signal events. The detector response is then obtained by using the ATLAS full simulation in GEANT4 [155]. The signal samples were produced in three MC campaigns, dedicated to the 2015+2016 (MC16a), the 2017 (MC16d) and the 2018 (MC16e) datasets. These MC campaigns are scaled with a pile-up profile and re-weighted, so that the MC pile-up distribution matches with the data from each year. A total of 94 different $tc+E_{\mathrm{T}}^{\mathrm{miss}}$ scenarios were considered, with $m(\tilde{t}_1)$ between 400 and 1300 GeV and $\tilde{\chi}_1^0$ masses of up to 650 GeV. The $\tilde{t}_1$ BRs were set to $\mathrm{BR}(\tilde{t}_1 \to t\tilde{\chi}_1^0) = \mathrm{BR}(\tilde{t}_1 \to c\tilde{\chi}_1^0) = 0.5$, resulting in around 50% of events with a $tc+E_{\mathrm{T}}^{\mathrm{miss}}$ final state, while 25% feature the $tt+E_{\mathrm{T}}^{\mathrm{miss}}$ and another 25% have a $cc+E_{\mathrm{T}}^{\mathrm{miss}}$ final state. Figure 4.4 shows the number of simulated events required to pass the $E_{\mathrm{T}}^{\mathrm{miss}}$ filter in every signal scenario for the MC16e campaign. The $(m(\tilde{t}_1), m(\tilde{\chi}_1^0))$ points at (900 GeV, 1 GeV), (700 GeV, 400 GeV) and (550 GeV, 375 GeV) feature larger statistics to optimise the SR selections for these signal scenarios.

4.4 Object Selections

This section describes the selection criteria for the electrons, muons and jets used for the analysis, based on the reconstruction discussed in Chapter 3. Basic selections are first applied to build *baseline* objects that are used to remove overlapping objects and to

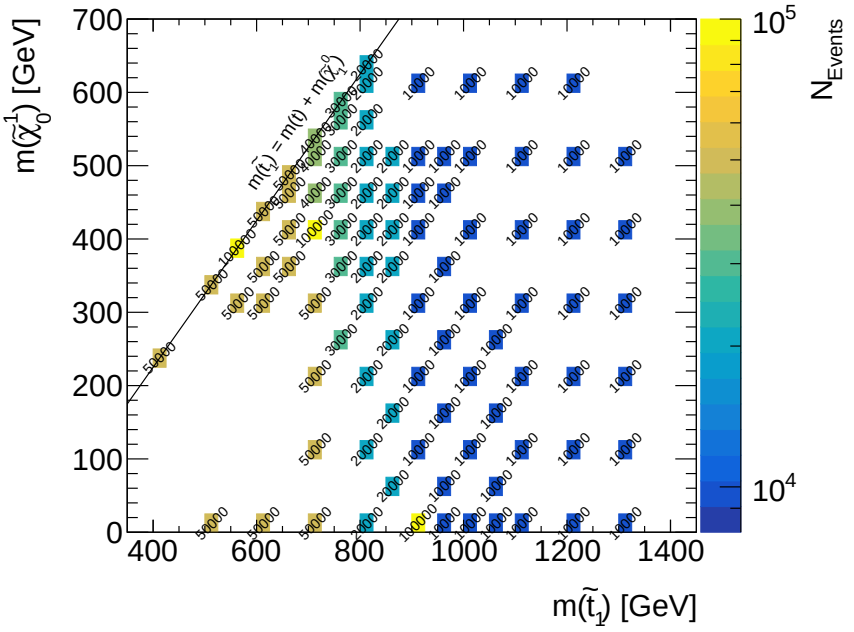

Figure 4.4: Number of MC simulated signal events for different masses of the $\tilde{t}_1$ and the $\tilde{\chi}_1^0$ in the MC16e campaign.

calculate the $E_{\mathrm{T}}^{\mathrm{miss}}$. Tighter selection criteria are then used to build *signal* objects that are used in the analysis selections.

Table 4.2 lists the baseline and signal requirements for electrons and muons. Baseline electrons need to fulfil loose [140] identification requirements (ID) and need to contain a hit in the IBL (LooseAndBLayer). Signal electrons are required to satisfy the tight ID WP, while both types of muons use the medium WP [144]. The signal electron objects furthermore need to fulfil the tight isolation WP [144], while the signal muons must pass the FCLoose requirements (FCHighPtCaloOnly for $p_{\mathrm{T}} > 200\,\mathrm{GeV}$) [173].

Parameter	**Baseline *e***	**Signal *e***	**Baseline *μ***	**Signal *μ***
p_{T} [GeV]	> 4.5	> 10	> 4.0	> 10
$\lvert\eta\rvert$	< 2.47		< 2.7	
ID	LooseAndBLayer	Tight	Medium	
$z_0 \sin(\theta)$ [mm]	< 0.5		< 0.5	
$\lvert d_0/\sigma_{d_0}\rvert$	–	< 5	–	< 3
Isolation				
$p_{\mathrm{T}} \leq 200\,\mathrm{GeV}$	–	Tight	–	FCLoose
$p_{\mathrm{T}} > 200\,\mathrm{GeV}$	–	Tight	–	FCHighPtCaloOnly

Table 4.2: Object criteria for baseline and signal leptons.

Both small-R jets, with a cone size of $R = 0.4$, and large-R jets with $R = 1.0$ are used. Table 4.3 lists the selections of the baseline and signal small-R jets (referred to as *jets*) and the large-R jets. The JVT score selection is applied to enhance the suppression of

pile-up jets.

Parameter	Baseline jet Signal jet	Large-R jet
p_{T} [GeV]	> 20	–
$\sum_{i \in \mathrm{jet}} \lvert p_{\mathrm{T,i}} \rvert$ [GeV]	–	> 150
$\lvert\eta\rvert$	< 2.8	< 2.2
JVT score	–	> 0.5 for $p_{\mathrm{T}} < 60\,\mathrm{GeV}$, $\lvert\eta\rvert < 2.4$

Table 4.3: Object criteria for baseline and signal jets and the large-R jets.

The b- and c-tagging is performed using the DL1r algorithm introduced in Section 3.3. All jets that are not identified as a b-jet are then evaluated by the c-tagger (*c-tagging with b-veto*). Figure 4.5.a shows a scan of the b-jet and light-jet rejections for various values of f_b and thresholds of DL1r$_c$. The selected c-tag WP is featuring a c-jet efficiency of 20% (20% c-tag WP) with b- and light-jet rejections of $\epsilon_b^{-1} = 30$ and $\epsilon_{\mathrm{light}}^{-1} = 60$, which corresponds to $f_b = 0.28$ and a threshold of DL1r$_c > 1.315$. The c-tagging efficiencies on simulated events need to be scaled to data. Figure 4.5.b shows that these scaling factors are compatible with unity within the uncertainties for the various bins in p_{T}.

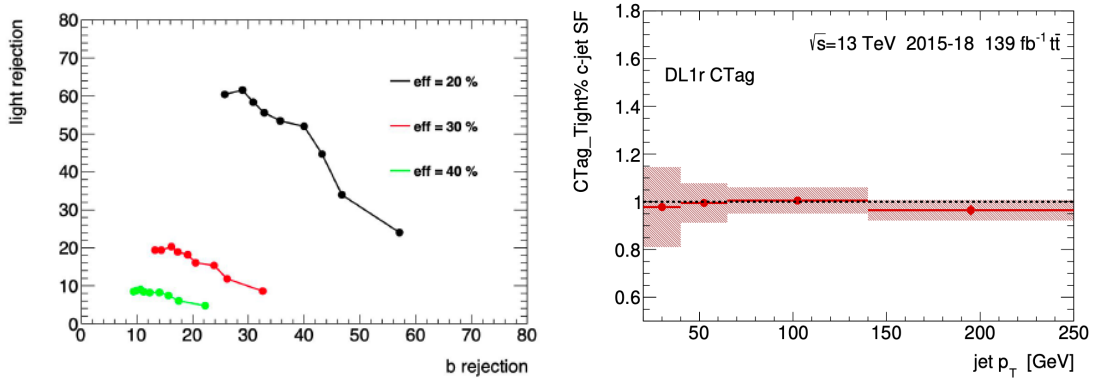

(a) (b)

Figure 4.5: b-jet and light-jet rejection ratios for various c-jet efficiencies (a) and the derived scaling factors and their uncertainties for multiple bins in p_{T} for the 20% c-jet WP. The vertical error bars indicate the statistical uncertainty in the data while the coloured show the total uncertainty also taking into account systematic uncertainties.

The analysis also uses top-tagging on large-R jets [147], which is rather different than the tagging of light-, b- and c-jets. In kinematic regions with a boosted signal topology, the decay products from the top can be close enough to be reconstructed into a single $R = 1.0$ jet. The jet mass and substructure information are then used by a Deep Neural Network (DNN) to define a top-tagger. This analysis uses the *inclusive* top-tagger at an 80% efficiency WP, tagging jets with $p_{\mathrm{T}} \in [350, 2500]$ GeV and jet masses of $m_j \in [40, 600]$ GeV. Figure 4.6 shows the scaling factor for the various top-tagging bins up to p_{T} of 1000 GeV.

With the individual objects defined, an Overlap Removal (OR) procedure is applied onto the baseline objects to prevent double counting of energy deposits among different objects

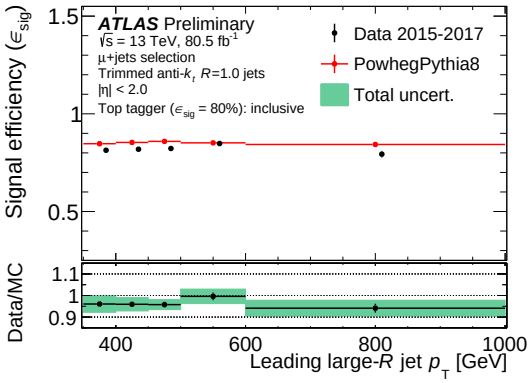

Figure 4.6: Efficiencies and their uncertainties for multiple bins in p_{T} for the 80% WP of the inclusive top-tagger. The vertical error bars indicate the statistical uncertainty in the data while the coloured show the total uncertainty also taking into account systematic uncertainties. Taken from Reference [147].

and to resolve ambiguities. The OR is done as follows:

- A calorimeter-tagged muon is rejected, if it shares an ID track with an electron. If the muon however is not a calorimeter-tagged muon, then the electron is rejected.
- If an electron and a jet, that is not a b-jet, are within $\Delta R < 0.2$, then the jet is rejected and the electron is kept, unless the jet has a p_{T} of $> 100\,\mathrm{GeV}$.
- Reject an electron if it is within $\Delta R < 0.4$ of a jet.
- If a muon and a jet, that is not a b-jet and has less than three tracks associated to it, are ghost associated [174–176] or closer than $\Delta R < 0.2$, then the jet is rejected.
- If a jet and a muon are closer than $\Delta R < 0.4$ then the muon is rejected and the jet is kept.

4.5 Preselections and Variables

A first set of selections, referred to as *preselections*, is used to check the agreement between MC and data and to design the SRs, CRs and VRs on top of them. Table 4.4 shows the first set of preselections that is used both for Region A and B, while Table 4.5 shows the definition of the preselections that are only used in Region C. In the following, some of the used variables are explained:

- $E_{\mathrm{T}}^{\mathrm{miss}}$: Since the SUSY signal features large $E_{\mathrm{T}}^{\mathrm{miss}}$, the $E_{\mathrm{T}}^{\mathrm{miss}}$-trigger is used in the 0L preselections to target the signal. A selection of $E_{\mathrm{T}}^{\mathrm{miss}} > 250\,\mathrm{GeV}$ ensures the full efficiency of the trigger.
- $E_{\mathrm{T},\ell\ell}^{\mathrm{miss}}$: Same as $E_{\mathrm{T}}^{\mathrm{miss}}$, but the lepton p_{T}'s are subtracted to mimic the $E_{\mathrm{T}}^{\mathrm{miss}}$ in the $Z \to \nu\nu$ background process. This variable is only used in the 2L regions.
- N_{jets}, $N_{b-\mathrm{jets}}$ and $N_{c-\mathrm{jets}}$: The number of signal jets, b- and c-tagged jets respectively. The signal features a b-jet, a c-jet and jets from the hadronic W decay,

which is why $N_{\text{jets}} \geq 3$, $N_{b-\text{jets}} \geq 1$ and $N_{c-\text{jets}} \geq 1$ are applied. Especially the requirement of at least one c-jet reduces the contribution of many SM background processes.

- $\min(\Delta\phi(j^{1-4}, E_{\text{T}}^{\text{miss}}))$ and $\min(\Delta\phi(j^{1-3}, E_{\text{T}}^{\text{miss}}))$: The minimum distance in ϕ between the four or three leading jets and the $E_{\text{T}}^{\text{miss}}$. This variable is used to reject the multi-jet background in events that feature a large $E_{\text{T}}^{\text{miss}}$ due to the mismeasurement of jets. In the 2L regions, $E_{\text{T},\ell\ell}^{\text{miss}}$ is used instead of $E_{\text{T}}^{\text{miss}}$.
- $m_{\ell\ell}$: The mass of the di-lepton system used to select $Z+\text{jets}$ background events in the 2L regions.
- m_T: The *transverse mass* reconstructs the mass of a particle that decays to one visible particle with momentum p_{T} and one invisible particle. It is defined as $\sqrt{2p_{\text{T}}E_{\text{T}}^{\text{miss}}(1-\cos(\Delta\phi))}$ [177], where the lepton p_{T} and ϕ are used in the 1L regions.
- $m_T(c, E_{\text{T}}^{\text{miss}})_{\text{min}}$: Same as m_T, but the c-jet is used instead of the lepton. If there are multiple c-jets, the minimum of the transverse masses between the individual c-jets and the $E_{\text{T}}^{\text{miss}}$ is taken.
- Object-based $E_{\text{T}}^{\text{miss}}$ significance [178]: $\mathcal{S}$ is defined as $\mathcal{S} = \sqrt{\left|E_{\text{T}}^{\text{miss}}\right|^2/\sigma_{\text{L}}^2(1-\rho_{\text{LT}}^2)}$. It uses the total momentum resolution (σ_{L}) and the correlation factor between the longitudinal and transverse momentum resolution of each jet (ρ_{LT}) to reject events where large $E_{\text{T}}^{\text{miss}}$ arises from poorly measured jets.
- m_{eff}: The effective mass is defined as $\text{m}_{\text{eff}} = \sum_{i\in\text{jets}} p_{\text{T}}^{\text{jet}_i} + E_{\text{T}}^{\text{miss}}$ and is used to select events that feature a combination of high $E_{\text{T}}^{\text{miss}}$ and large jet p_{T}'s.

Variable	**0L preselection**	**1L preselection**	**2L preselection**
Baseline leptons	0	–	
Signal leptons	–	1	2
Dilepton system flavour	–		Same flavour
Dilepton system sign	–		Opposite sign
Trigger	$E_{\text{T}}^{\text{miss}}$ Trigger		1L Trigger
$E_{\text{T}}^{\text{miss}}$	$\geq$ 250 GeV		$\leq$ 150 GeV
$E_{\text{T},\ell\ell}^{\text{miss}}$	–		$\geq$ 250 GeV
N_{jets}	≥ 3	≥ 2	≥ 2
$N_{b-\text{jets}}$	≥ 1		
$N_{\text{c}-\text{jets}}$	≥ 1		
$\Delta\phi(j^{1-4}, E_{\text{T}}^{\text{miss}})$	≥ 0.4		–
$\Delta\phi(j^{1-4}, E_{\text{T},\ell\ell}^{\text{miss}})$	–		≥ 0.4
$m_{\ell\ell}$	–		[76,106]
$m_{\text{T,min}}^{\text{c}}$	$\geq$ 150 GeV		–

Table 4.4: Preselections for the Regions A and B.

Variable	**0L preselection**	**1L preselection**	**2L preselection**
Baseline leptons	0	–	
Signal leptons	–	1	2
Dilepton system flavour	–		Same flavour
Dilepton system sign	–		Opposite sign
Trigger	$E_{\mathrm{T}}^{\mathrm{miss}}$ Trigger		1L Trigger
$E_{\mathrm{T}}^{\mathrm{miss}}$	≥ 250 GeV		< 100
$E_{\mathrm{T},\ell\ell}^{\mathrm{miss}}$	–		≥ 250 GeV
N_{jets}	≥ 3		
$N_{b-\mathrm{jets}}$	≥ 1		
$N_{\mathrm{c-jets}}$	≥ 1		
$\Delta\phi(j^{1-3}, E_{\mathrm{T}}^{\mathrm{miss}})$	≥ 0.3		–
$\Delta\phi(j^{1-3}, E_{\mathrm{T},\ell\ell}^{\mathrm{miss}})$	–		≥ 0.3
Leading jet flavour	Light jet (not b- or c-tagged)		
$\mathcal{S}$	> 6		
$m_{\mathrm{T,min}}^{\mathrm{c}}$	> 100 GeV		
$p_{\mathrm{T}}^{\mathrm{jet}_1}$	> 100 GeV		
$p_{\mathrm{T}}^{\mathrm{jet}_4}$	≥ 30		
$\mathrm{m_T}$	–	> 30 GeV	–
$m_{\ell\ell}$	–		[86,105]

Table 4.5: Preselections for Region C.

The $E_{\mathrm{T}}^{\mathrm{miss}}$ and $p_{\mathrm{T}}^{\mathrm{jet}_1}$ distributions for the Region A and B preselections are shown in Figure 4.7 and in Figure 4.8 for the Region C preselections. The agreement between data and MC is good in the 0L and 2L preselections, while the 1L ones show data/MC ratios of below one. This is due to mismodelling of the $t\bar{t}$ background which is taken care of by control regions later.

The various kinematic regions are using different approaches to enhance the sensitivity for the SUSY signal. The signal regions A and B (SRA and SRB) use selections on the variables discussed in the previous section to reject as many SM events as possible, while keeping decent expected signal yields. Furthermore, they also use top-tagging on large-R jets to look for boosted top quarks. In contrast to this, the design of the signal region C (SRC) follows the *machine learning* (ML) approach: A ML model is trained on MC events to discriminate between signal and background events, based on low-level information such as the jet kinematics. The resulting model is applied onto the data to create a score indicating how likely an event is to be a signal or background event. A selection on this score then is applied to define the SR in the same way as in SRA and SRB.

The following two sections describe the input data and architecture (Section 4.6) and the optimisation and performance (Section 4.7) of the Neural Network classifier developed for Region C.

4.6 Neural Network Classifier

Neural Networks (NNs) have become broadly used tools in many different areas of particle physics such as flavour-tagging with the DL1r algorithm discussed previously. NNs are a class of machine learning models that consist of artificial *neurons* organised in multiple layers as illustrated in Figure 4.9. Each neuron of the NN gives an output according to

$$\sigma(f(\vec{x})) = \sigma(\vec{x} \cdot \vec{w} + w_0)\,, \tag{4.5}$$

where $\vec{x}$ are the input data to the neuron and $\vec{w}$ are the weights associated with these inputs. The *activation function* (σ) then computes the output of a neuron. Typical activation functions are the sigmoid ($\sigma(x) = 1/(1+e^{-x})$) or Rectified Linear Unit (ReLU, $\sigma(x) = \max(0, x)$). The last layer of neurons calculate the output scores of the NN.

The classifier presented in this work is designed to predict the class membership of an event. A total of three classes are defined: the $tc + E_{\mathrm{T}}^{\mathrm{miss}}$ signal class, the $t\bar{t}$ background class and the W or Z + jets (V + jets) background class. A *supervised learning* approach is pursued in which the NN is given *training* data including *labels* indicating the true class membership of the events and an iterative learning procedure is executed. The learning starts with *forward propagation*, which means that the class predictions for the training data are calculated using Equation (4.5) with the kinematic properties of the events as inputs $\vec{x}$ and weights $\vec{w}$, where the latter are randomly initialised in the first iteration. The predicted and true class memberships are compared to calculate the *loss*. The NN weights are then adjusted to minimise the loss (*backpropagation*) using methods such as Stochastic Gradient Descent (SGD) or the Adam algorithm [180] and the procedure is repeated until the loss is not decreasing any more or other stop criteria are fulfilled.

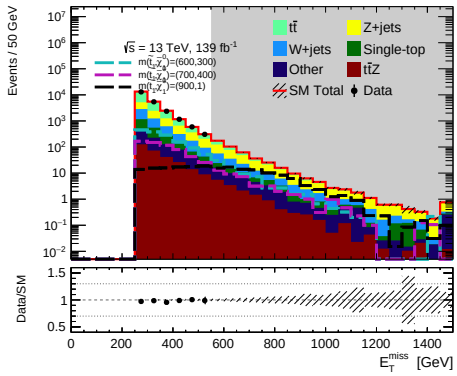

(a) 0L preselection

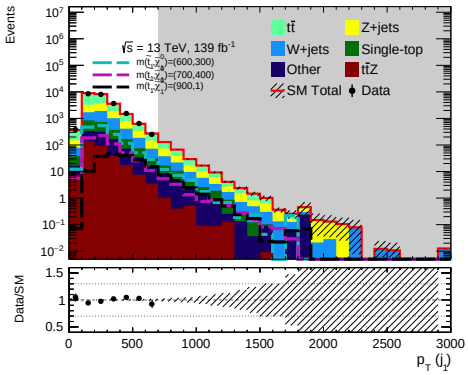

(b) 0L preselection

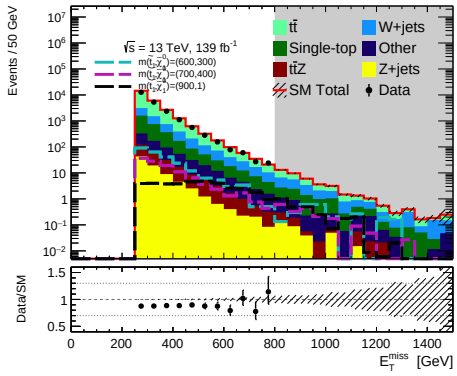

(c) 1L preselection

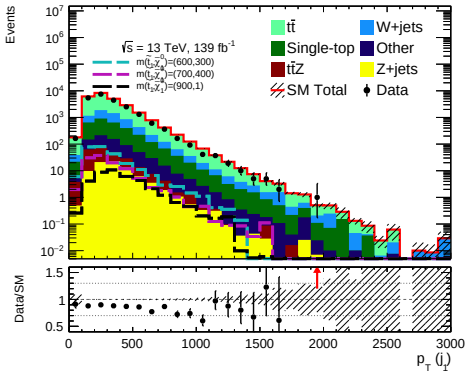

(d) 1L preselection

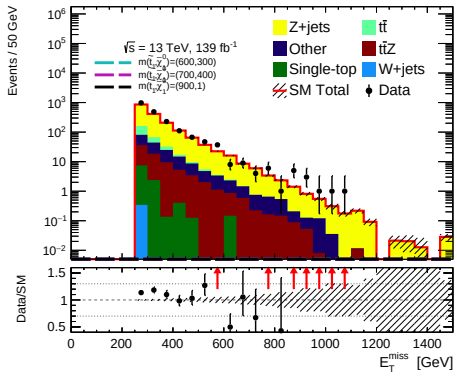

(e) 2L preselection

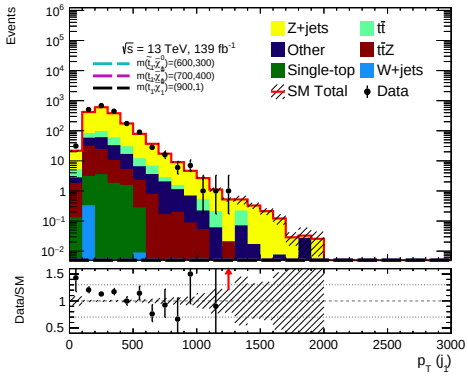

(f) 2L preselection

Figure 4.7: $E_{\mathrm{T}}^{\mathrm{miss}}$ (left) and leading jet p_{T} (right) distributions for the 0L (top), 1L (middle) and 2L (bottom) preselections of Region A and B. The stacked contributions from the SM background are shown with the expected signal yields of representative models overlaid with dashed lines. The bottom panel shows for each bin the ratio between the data and the SM background expectation from MC. The shaded bands indicate the statistical uncertainty and areas with a significant fraction of signal events expected are blinded (grey areas). Overflow events are added to the rightmost bin.

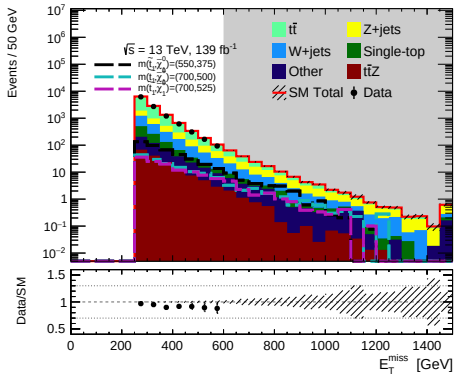

(a) 0L preselection

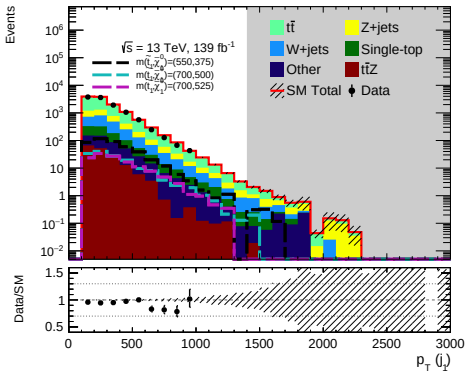

(b) 0L preselection

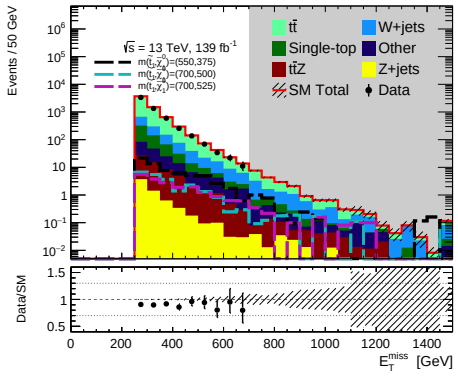

(c) 1L preselection

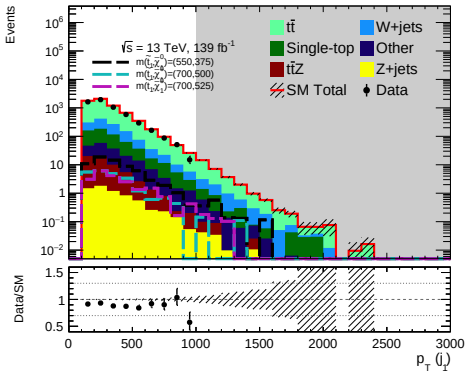

(d) 1L preselection

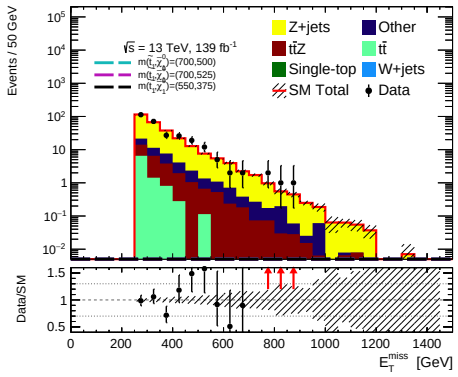

(e) 2L preselection

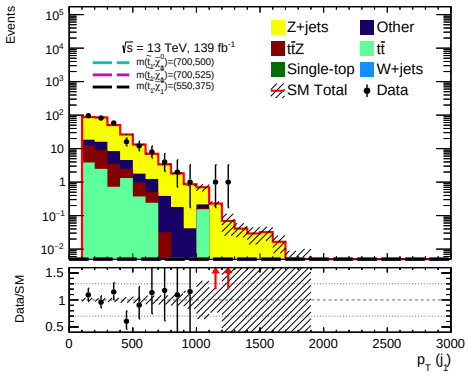

(f) 2L preselection

Figure 4.8: $E_{\mathrm{T}}^{\mathrm{miss}}$ (left) and leading jet p_{T} (right) distributions for the 0L (top), 1L (middle) and 2L (bottom) preselections of Region C. The stacked contributions from the SM background are shown with the expected signal yields of representative models overlaid with dashed lines. The bottom panel shows for each bin the ratio between the data and the SM background expectation from MC. The shaded bands indicate the statistical uncertainty and areas with a significant fraction of signal events expected are blinded (grey areas). Overflow events are added to the rightmost bin.

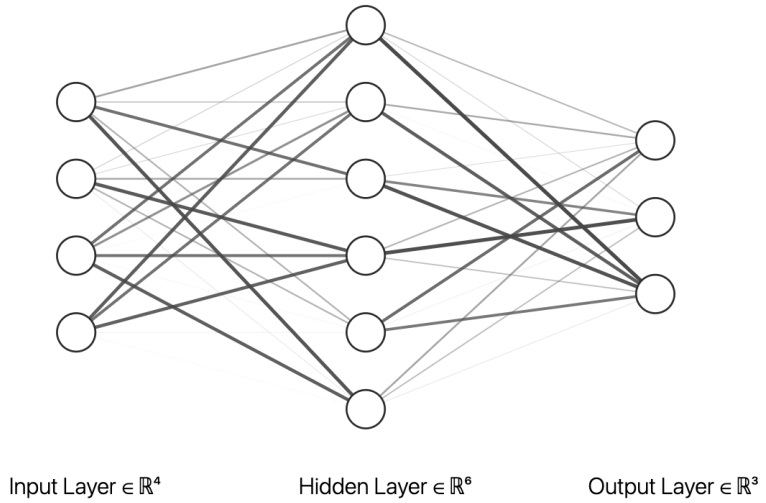

Figure 4.9: Representation of a NN with one input layer of four inputs, one hidden layer with six neurons and one output layer with three output neurons. The line strengths represent the different values of the NN weights. Image generated using Reference [179].

Finally, the classification performance of the NN is evaluated on an independent dataset called the *validation set*. Since the NN was not trained on this set, possible *overtraining* on the training set can be recognised if the loss on the validation set is higher than on the training set. This can be the case if the NN is not learning general patterns in the data, but remembers the characteristics of the training data 'by heart'. A third independent dataset called the *testing set* is introduced to give an unbiased estimation of the performance of a NN model.

The NN developed for the discrimination between SUSY and SM events in the compressed region uses the PyTorch framework [181]. In the following, the input data and architecture of the NN are discussed in more detail.

Input data

The NN is trained with MC signal and background samples that pass the SRC 0L preselection as defined in Table 4.5. For the SUSY signal, only samples with $\Delta m(\tilde{t}_1, \tilde{\chi}_1^0) = 175$ and 200 GeV were used. These events were furthermore required to feature mixed decays of the $\tilde{t}_1$ pairs (one decaying to $t + \tilde{\chi}_1^0$, the other decaying to $c + \tilde{\chi}_1^0$) so that the NN would focus on distinguishing $tc + E_{\mathrm{T}}^{\mathrm{miss}}$events from the SM background. For the background input data, only the samples containing the three main backgrounds of the 0L preselection were used, which are $t\bar{t}$, $Z+$jets and $W+$jets as can be seen in Figure 4.8. All available signal and $W+$jets events are used, while a random subset of 100k and 50k events are used from the $t\bar{t}$ and $Z+$jets samples. The $W+$jets and $Z+$jets samples are combined into the $V+$jets class as these two backgrounds featured similar output score shapes. Finally, the input events are randomly split into the training (64%), validation set (16%) and testing set (20%). Table 4.6 summarises the number of events used by the NN for the different classes.

Class	**Event type**	$\boldsymbol{N}_{\textbf{total}}$	$\boldsymbol{N}_{\textbf{training}}$	$\boldsymbol{N}_{\textbf{validation}}$	$\boldsymbol{N}_{\textbf{testing}}$
Signal	$tc + E_{\mathrm{T}}^{\mathrm{miss}}$	13'263	8'488	2'122	2'653
$t\bar{t}$	$t\bar{t}$	100'000	64'000	16'000	20'000
$V+\mathrm{jets}$	$W+\mathrm{jets}$	26'735	17'110	4'277	5'348
	$Z+\mathrm{jets}$	50'000	32'000	8'000	10'000

Table 4.6: Number of MC signal and background events used for the training, validation and testing of the NN classifier, as well as the total number of available events.

The events are then weighted according to their class i by

$$w_i = \frac{max(N_i)}{N_i} \tag{4.6}$$

with w_i being the weight of the events and N_i the number of events in class i. In this way there is no incentive for the NN to optimise the weights to solely achieve good performance on the class that features the most events in the training set.

The NN is receiving two types of low-level input variables to train its weight: continuous input variables such as the p_{T} or η, that can be ordered (for example from low to high), and categorical input variables that do not have a defined order, such as the flavour of a jet. These two kinds of input variables need to be treated differently by the NN.

Continuous input variables are normalised to have a mean of 0 and standard deviation of 1. This is performed on the set of all events passing preselection and mixed decay selection. In contrast to this, categorical input variables are not normalised but converted into multiple floats that contain the same information in a process called *embedding*. The number of floats (N_{floats}), an input variable is embedded into, is defined by

$$N_{\mathrm{floats}} = (N_{\mathrm{categories}} + 1) \cdot m_{\mathrm{e}}\,, \tag{4.7}$$

with $N_{\mathrm{categories}}$ being the number of possible values the input variable can take, and m_{e} a *hyperparameter* called *embedding multiplicity*. Hyperparameters describe the properties of the NN architecture and are optimised to achieve the best possible model performance.

Some input variables can have unphysical default values if the corresponding object does not exist in the MC sample. In an event with only five jets for example, all variables corresponding to the sixth jet have values of -99 or -999. This is dealt with by replacing such values with the mean of the variable among the whole dataset and adding an additional input variable indicating that such a replacement has taken place. This results in new categorical input variables such as *ptJet6_is_missing*. This completes the list of input variables used by the NN:

- Jet p_{T}, η, $\Delta\phi(j, E_{\mathrm{T}}^{\mathrm{miss}})$ for leading six jets (type: continuous).
- Jet p_{T}, η, $\Delta\phi(j, E_{\mathrm{T}}^{\mathrm{miss}})$ for leading two b- and c-jets (type: continuous).
- $E_{\mathrm{T}}^{\mathrm{miss}}$ (type: continuous).
- N_{jets}, $N_{\mathrm{c-jets}}$, $N_{b-\mathrm{jets}}$ (type: continuous).

- Flavour (untagged, b-tagged or c-tagged) of second to sixth jet (type: categorical).

- Variables indicating missing objects: missing of fourth, fifth or sixth jet, missing of subleading b- or c-jet

These are in total 34 continuous and 10 categorical input variables. N_{jets}, $N_{c-\text{jets}}$ and $N_{b-\text{jets}}$ could also have been treated as categorical variables as they have discrete possible values. Tests however showed that defining these variables as continuous parameters increases the classification performance of the NN.

Architecture

The NN consists of one or more fully connected hidden layers. This means that every neuron of one layer is connected to every neuron of the previous and next layer. The number of input neurons is equal to the number of continuous parameters plus the embedded categorical parameters as defined in Equation (4.7). The number and size of the hidden layers is defined by the hyperparameter *hidden layer sizes*. After the input and each hidden layer there is an activation function and additionally there can be *dropout* [182] and *batch normalisation* layers [183]. The hyperparameter *activation function* defines how the neurons are activated. This can either be a sigmoid, ReLU or a Leaky ReLU function (ReLU but with a slope in the negative part). The property of the dropout layer is defined by the hyperparameter *dropout probability*, which is the probability that a neuron is randomly ignored in the training stage. This can be specified independently for the first and the following dropout layers. This technique can be used to prevent overtraining and help generalisation since the NN can not learn very specific features of a certain event of training set as the corresponding input neurons are deactivated in every few training cycles. The hyperparameter *use batch normalisation* then defines whether to use the batch normalisation layer. Finally, the order of the activation function, dropout and batch normalisation layer is defined by the hyperparameter *layer order*.

The loss is calculated using the cross entropy loss [184] and the weight update is done with the Adam algorithm [180]. The corresponding hyperparameters are the *learning rate*, that defines the step size of the weight update, and *weight decay* that adds a L2 penalty to the loss function to discourages large weights, again forcing the NN to generalise. SGD was also tested for usage but yielded inferior results compared to Adam. The learning is performed in batches of sizes defined by the hyperparameter *batch size*. The NN is allowed to run up to 1000 times over the complete dataset (1000 epochs), but early stopping is done if the loss on the validation set does not improve for 50 epochs. The goal of early stopping is to prevent overfitting on the training set which would lead to a higher loss on the validation set.

Finally, the output of the NN consists of three output neurons that are showing the probability of an event to have a certain class (NN signal score, NN $t\bar{t}$ score and NN V+jets score). The following section discusses how the NN hyperparameters summarised in Table 4.7 are optimised and presents the performance of the best NN model.

Hyperparameter name	**Short explanation**
Hidden layer sizes	Number of hidden layers and neurons per layer (e.g 200 neurons in first and 100 neurons in second hidden layer
Dropout probability	Probability for each neuron to be ignored in training, specified separately for first and following dropout layers
Embedding multiplicity	Defines how many float input variables are used to embed a categorical input (see Equation (4.7))
Batch size	Number of events that are used for one update of the NN weights
Learning rate	Step size for each learning step over a batch
Weight decay	L2 penalty to regularise the NN by discouraging high weights
Layer order	Order of batch normalisation, dropout layer and activation function after input and hidden layers (e.g BAD: Batch normalisation – Activation function – Dropout layer)
Activation function	Activation function used (Sigmoid, ReLU, Leaky ReLU)
Use batch normalisation	Whether to use batch normalisation layers

Table 4.7: Summary of the hyperparameters of the NN classifier with short explanation.

4.7 Neural Network Optimisation and Performance

The various hyperparameters of the NN were optimised in multiple steps of grid-searching the hyperparameter space for the optimal combination. The models were rated by their loss on the testing set. To exclude models which were showing large overfitting on the training set, the χ^2 per number of degrees of freedom (χ^2/ndof) between the binned validation and training set was evaluated for all the output scores and classes. A χ^2/ndof of smaller than unity indicates underfitting, while a value of more than unity shows overfitting. Models with a χ^2/ndof of more than 1.5 for any output score were removed from the testing loss ranking.

The optimisation was conducted in multiple steps of grid-searching the hyperparameter space. First steps were concerned with roughly optimising the *hidden layer sizes*, *dropout probabilities* and strength of *weight decay*. Later iterations then optimised the other hyperparameters. Table 4.8 shows the possible values that the hyperparameters could take in these steps and the final values of the most performant model that was received in a last finer optimisation of the hidden layer sizes.

The best model features two hidden layers with 96 neurons each and learning rates and weight decays of 10^{-3} and $3 \cdot 10^{-3}$ respectively. The large weight decay, the small batch size of 128 and the large dropouts of 0.2 and 0.5 are necessary to force the NN model to generalise and prevent overfitting. Models with less strong regularisation feature smaller testing losses, but have larger χ^2/ndof.

Hyperparameter name	**Possible values**	**Best value**
Hidden layer sizes	1–4 hidden layers with 64, 128, 256, 512, 1024 or 2048 neurons evenly distributed to hidden layers	two hidden layers with 96 neurons each
Dropout probability	0.2, 0.3, 0.4 or 0.5 for first and other dropout layers separately	0.2 for first and 0.5 for other hidden layers
Embedding multiplicity	0.1, 0.5 or 0.75	0.1
Batch size	64, 128, 256, 512	128
Learning rate	3e-3, 1e-3 or 3e-4	1e-3
Weight decay	1e-2, 3e-3 or 1e-3	3e-3
Layer order	ADB, DAB, ABD, DBA, BAD	ABD (activation function, batch normalisation, dropout)
Activation function	Sigmoid, ReLU or Leaky ReLU with slopes of 0.01, 0.02, 0.04 or 0.08	Leaky ReLU with slope 0.01
Use batch normalisation	True, False	True

Table 4.8: List of the possible values for the various hyperparameters considered in the optimisation process and the values of the best performing model.

Figure 4.10 shows the loss and accuracy evolution for the best model. Both the training and the validation loss are decreasing steadily until epoch 131 (validation loss of 0.802), when no further improvement in the next 50 epochs is recorded on the validation set and the training is stopped. The accuracies of the classes are defined by the ratio of correctly classified events for a given class divided by the total number of events in this class. In the accuracy calculation an event is considered to belong to the most probable class (max[signal score, $t\bar{t}$ score, V+jet score]). This metric shows a very similar performance of the NN on the training and validation set.

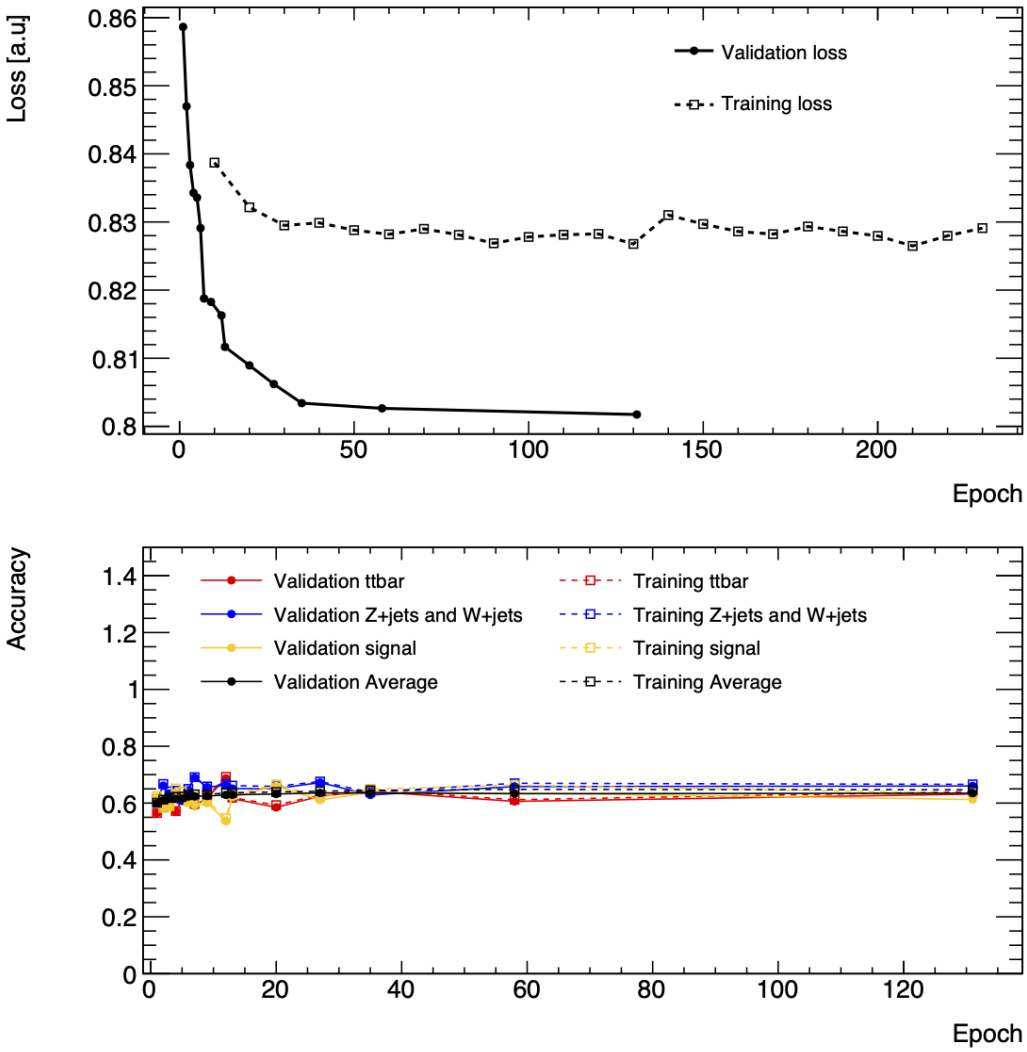

Figure 4.10: Top: Evolution of training loss (dashed line) and validation loss if improved (solid line) for the best NN model. Bottom: Evolution of training (dashed lines) and validation (solid lines) accuracies per class for epochs where the validation loss reached a new minimum.

Figure 4.11 shows the signal, $t\bar{t}$ and V + jets output score distributions of the final model together with ratio plots of the validation and training distributions per class. All χ^2/ndof values are close to unity which shows that no strong overfitting is taking place. A clear separation between the signal and the various backgrounds can be achieved, while also some discrimination can be gained between the backgrounds.

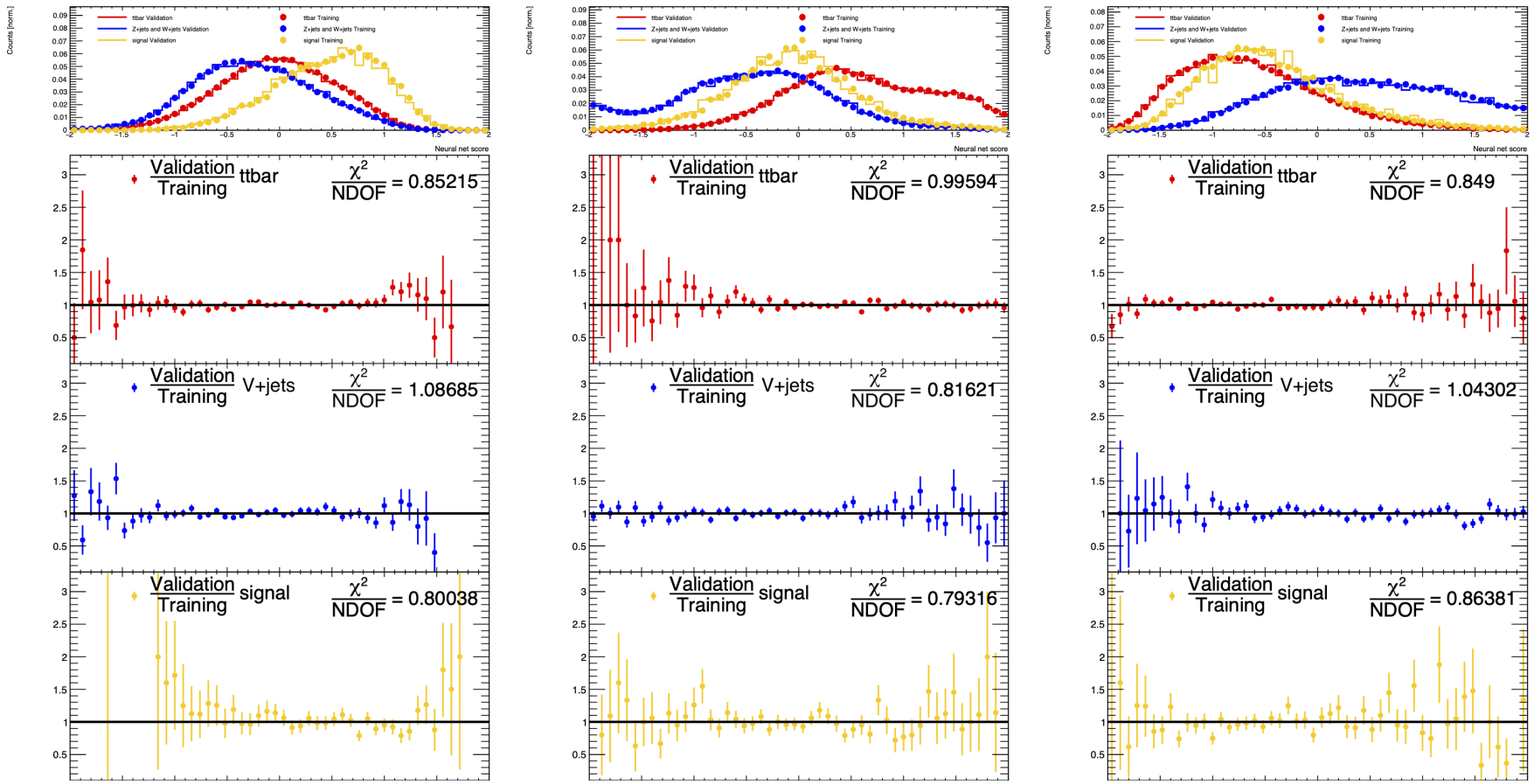

(a) (b)

Figure 4.11: NN signal (a), $t\bar{t}$ (b) and $V+\text{jets}$ score (c) distributions. The top plots show the NN score values on the training (dots) and validation set (line), while the lower plots show the ratio of the validation to the training distributions for each class. For each ratio plot the χ^2/ndof is shown.

To check that the chosen NN model is also performing well and does not feature large overfitting when trained with different events, k-fold cross validation [185] is performed. The 80% of data making up the training and validation set are split in $k = 5$ folds (16% of the total number of events each), where five different NN models are trained using one of the five splits as validation and the others as training data. The performance of these five models is compared to gauge the impact of using different events for training. The average loss within these five folds is 0.805 ± 0.003 and the χ^2/ndof values are listed in Table 4.9. With very similar losses between the various folds and χ^2/ndof values that are close to unity and have small errors, the chosen NN proves to give similar performance when trained on different events.

Score	**Sample**	**Mean χ^2/ndof**	**Std.**
$t\bar{t}$ score	$t\bar{t}$ sample	0.951	0.155
$t\bar{t}$ score	$V+$jets sample	0.977	0.157
$t\bar{t}$ score	Signal sample	1.107	0.183
$V+$jets score	$t\bar{t}$ sample	0.806	0.085
$V+$jets score	$V+$jets sample	1.032	0.192
$V+$jets score	Signal sample	1.102	0.25
Signal score	$t\bar{t}$ sample	0.881	0.14
Signal score	$V+$jets sample	0.861	0.232
Signal score	Signal sample	1.1	0.261

Table 4.9: χ^2/ndof values of the different scores and samples between the training and validation sets in the five folds of k-fold cross validation.

With the best NN model found and verified, the next section discusses the definition of the SRs, where the NN signal score is used for the definition of SRC.

4.8 Signal Region Definition

The signal regions were defined using the statistical significance (Z) as a tool to optimise the sensitivity of the SRs to the $tc + E_{\mathrm{T}}^{\mathrm{miss}}$ signal. The significance used is based on a profile-likelihood ratio test introduced by Reference [186] and is given by

$$Z = \left(2(s+b) \ln \left[\frac{(s+b)(b+\sigma_b^2)}{b^2 + (s+b)\sigma_b^2} \right] - \frac{b^2}{\sigma_b^2} \ln \left[1 + \frac{\sigma_b^2 s}{b(b+\sigma_b^2)} \right] \right)^{1/2} , \tag{4.8}$$

where s and b are the number of expected signal and background events and σ_b is the uncertainty on b.

Signal Region A

SRA targets signals with $\Delta m(\tilde{t}_1, \tilde{\chi}_1^0)$ higher than $\sim 400\,\mathrm{GeV}$. The most important selection is the requirement of at least one top-tagged large-R jet using the DNN discussed in Section 4.4. This strongly suppresses the $V+$jets background, while keeping around half of the signal events. The further SRA selections and binning to increase the significance are listed in Table 4.10.

Variable	**SRA**
Preselection	0L
$N_{\mathrm{tops}}^{\mathrm{DNN}}(R = 1.0)$	≥ 1
$m_{\mathrm{T,min}}^{\mathrm{c}}$ [GeV]	≥ 200
$m_{\mathrm{T,min}}^{\mathrm{b}}$ [GeV]	≥ 200
$m_{\mathrm{T,close}}^{\mathrm{j}}$ [GeV]	≥ 100
$\mathcal{S}$ $[\sqrt{GeV}]$	≥ 18
Leading jet flavour	b or c
$m_{\mathrm{T2}}(J_{R=1.0}^{b}, c)$ [GeV]	[450,575], [575,∞]

Table 4.10: Definition of SRA on top of the Region A and B 0L preselection described in Table 4.4. SRA is split into two $m_{\mathrm{T2}}(J_{R=1.0}^{b}, c)$ bins for the model-dependent fit.

Requiring a $m_{\mathrm{T,min}}^{\mathrm{c}}$ and $m_{\mathrm{T,min}}^{\mathrm{b}}$ of more than 200 GeV then reduces the $t\bar{t}$ background. $Z+$jets is further reduced by selecting high values for the transverse mass of the jet closest in ϕ to the $E_{\mathrm{T}}^{\mathrm{miss}}$ ($m_{\mathrm{T,close}}^{\mathrm{j}}$) and of the *stransverse mass* [187, 188] of the b-tagged large-R jet and the c-jet ($m_{\mathrm{T2}}(J_{R=1.0}^{b}, c) \geq 450\,\mathrm{GeV}$). The stransverse mass tries to reconstruct the mass of a pair of particles that both decay semi-invisibly and is defined as

$$m_{\mathrm{T2}}(\mathbf{p}_{\mathrm{T}}^{\alpha}, \mathbf{p}_{\mathrm{T}}^{\beta}) = \min_{\mathbf{q}_{\mathrm{T}}^1 + \mathbf{q}_{\mathrm{T}}^2 = \mathbf{p}_{\mathrm{T}}^{\mathrm{miss}}} \left\{ \max \left(m_{\mathrm{T}}^2(\mathbf{p}_{\mathrm{T}}^{\alpha}, \mathbf{q}_{\mathrm{T}}^1), m_{\mathrm{T}}^2(\mathbf{p}_{\mathrm{T}}^{\beta}, \mathbf{q}_{\mathrm{T}}^2), \right) \right\} , \tag{4.9}$$

where $\mathbf{p}_{\mathrm{T}}^{\alpha}$ and $\mathbf{p}_{\mathrm{T}}^{\beta}$ are the momenta of the two measured visible decay products. The minimum of the expression in the curly brackets is taken over all possible choices of $\mathbf{q}_{\mathrm{T}}^1$ and $\mathbf{q}_{\mathrm{T}}^2$ that satisfy $\mathbf{q}_{\mathrm{T}}^1 + \mathbf{q}_{\mathrm{T}}^2 = \mathbf{p}_{\mathrm{T}}^{\mathrm{miss}}$. SM backgrounds feature an end-point of $m_{\mathrm{T2}}(J_{R=1.0}^{b}, c)$ at low values (e.g 175 GeV for $t\bar{t}$), while the $tc + E_{\mathrm{T}}^{\mathrm{miss}}$ signal has a high end-point for large $\tilde{t}_1$ masses. Orthogonality to SRC, that features a light leading jet,

is achieved through the leading b- or c-jet requirement and finally, $\mathcal{S} > 18\sqrt{\text{GeV}}$ is required to further reduce backgrounds with small $E_{\text{T}}^{\text{miss}}$ and to enable orthogonality to the validation region discussed later. Figure 4.12 shows the distributions of the most important SRA selection variables before the selection is applied (*n-1 plot*). SRA is split into two $m_{\text{T2}}(J^b_{R=1.0}, c)$ bins to target the different $\tilde{t}_1$ masses efficiently. The dominant backgrounds in SRA are $Z+\text{jets}$ and single-top.

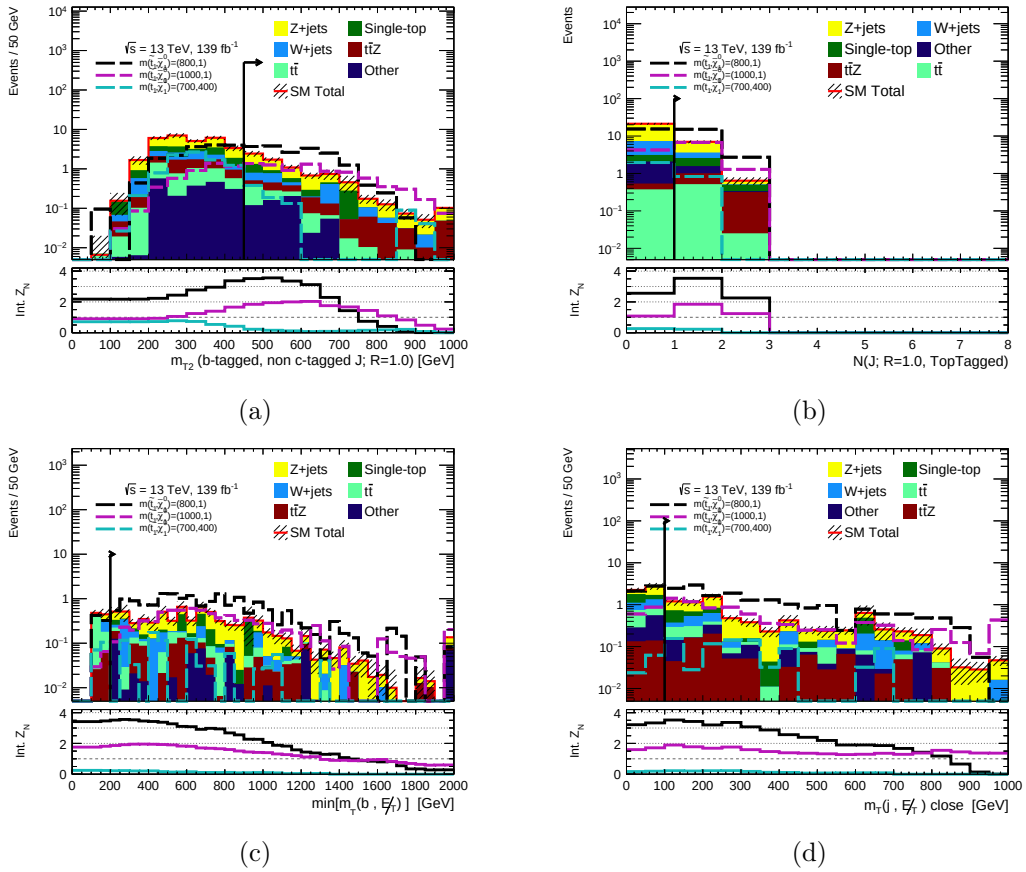

Figure 4.12: N-1 plots of the $m_{\text{T2}}(J^b_{R=1.0}, c)$ (a), $N^{\text{DNN}}_{\text{tops}}(R = 1.0)$ (b), $m^{\text{b}}_{\text{T,min}}$ (c) and $m^{\text{j}}_{\text{T,close}}$ (d) variables used in the definition of SRA. The stacked contributions from the SM background are shown with the expected signal yields of representative models overlaid with dashed lines. The shaded band indicates the statistical uncertainty on the background expectation and the lower panel shows the integrated significance for the considered signal models. Overflow events are added to the rightmost bin.

Signal Region B

SRB targets signals featuring $\Delta m(\tilde{t}_1, \tilde{\chi}^0_1) \sim 300\,\text{GeV}$, where SRA is lacking sensitivity. As the top is not as boosted as in SRA, requiring at least one top-tagged large-R jet would remove many signal events. SRB is therefore split to be able to separately design selections that target both kinematics with zero top-tagged jets (SRB0) and one or more top-tagged jets (SRB1). Table 4.11 lists all the selections, where $m^{\text{c}}_{\text{T,max}}$ and $m^{\text{b}}_{\text{T,max}}$ are the maxima of the transverse mass between the corresponding jets and the $E_{\text{T}}^{\text{miss}}$. The orthogonality between SRA and SRB1, that both target at least one top-tagged jet, is

ensured through the $m_{\mathrm{T2}}(J^b_{R=1.0}, c) \in [200, 450]$ GeV selection on SRB1, that does not reject many signal events in SRB1 due to the smaller $\Delta m(\tilde{t}_1, \tilde{\chi}^0_1)$.

Variable	**SRB0**	**SRB1**
Preselection	0L	
$N^{\mathrm{DNN}}_{\mathrm{tops}}(R = 1.0)$	0	≥ 1
$E^{\mathrm{miss}}_{\mathrm{T}}$ [GeV]	≥ 300	–
N_{jets}	≥ 5	≥ 3
$p^{b_1}_{\mathrm{T}}$ [GeV]	–	≥ 100
$p^{c_1}_{\mathrm{T}}$ [GeV]	≥ 100	
$p^{j_2}_{\mathrm{T}}$ [GeV]	≥ 100	–
$p^{j_4}_{\mathrm{T}}$ [GeV]	≥ 50	–
$m^{\mathrm{c}}_{\mathrm{T,min}}$ [GeV]	≥ 150	≥ 300
$m^{\mathrm{c}}_{\mathrm{T,max}}$ [GeV]	≥ 400	–
$m^{\mathrm{b}}_{\mathrm{T,min}}$ [GeV]	≥ 200	
$m^{\mathrm{b}}_{\mathrm{T,max}}$ [GeV]	[200,700]	–
$\mathcal{S}$ $[\sqrt{GeV}]$	≥ 10	≥ 17
$m_{\mathrm{T2}}(J^b_{R=1.0}, c)$ [GeV]	≥ 150	[200,450]
Leading jet flavour	b or c	
$m^{\mathrm{j}}_{\mathrm{T,close}}$ [GeV]	[100,150],[150,400],[400,∞]	[100,150],[150,300],[300,500],[500,∞]

Table 4.11: Definition of SRB0 and SRB1 on top of the Region A and B 0L preselection depicted in Table 4.4. SRB0 and SRB1 are both binned in $m^{\mathrm{j}}_{\mathrm{T,close}}$ for the model-dependent fit.

Figure 4.13 shows some n-1 plots of SRB0 and SRB1. Since SRB0 requires no top-tagged jets, the contamination with the V + jets background is high. This is counteracted by various selections on the jet p_{T}'s and $m^{\mathrm{j}}_{\mathrm{T,close}}$. The selections that add the most significance to SRB1 are $\mathcal{S} > 17\sqrt{\mathrm{GeV}}$ and $m^{\mathrm{b}}_{\mathrm{T,min}} > 200\,\mathrm{GeV}$. In the same way as in SRA, the dominant backgrounds for SRB1 are Z + jets and single-top. SRB0 has W+ jets as the sub-leading background instead of single-top. Both SRB0 and SRB1 are binned in $m^{\mathrm{j}}_{\mathrm{T,close}}$ to further optimise the significance in the model-dependent fit.

Signal Region C

SRC is defined only by a selection on three variables, as shown in Table 4.12. The NN signal score selection of ≥ 0.75 is used to suppress all backgrounds, while keeping most signal events. A selection of $\Delta\mathrm{R}(j_1, j_2) > 1.0$ then reduces the $t\bar{t}$ background. The effective mass is used to further enhance the significance by requiring $\mathrm{m_{eff}} > 750\,\mathrm{GeV}$. Figure 4.14 shows the n-1 plots of these three selections.

The Region C strategy of using a NN score selection to define SRC has the benefit that a high signal selection efficiency is achieved and therefore many signal events enter SRC. This enables the use of a 2D model-dependent fit where SRC is first binned in $\mathrm{m_{eff}}$ slices of 250 GeV to target different $\tilde{t}_1$ masses as signal scenarios with higher $m(\tilde{t}_1)$ can yield higher effective masses. The $\mathrm{m_{eff}}$ bins are then further split in $m^{\mathrm{j}}_{\mathrm{T,close}}$ as shown in

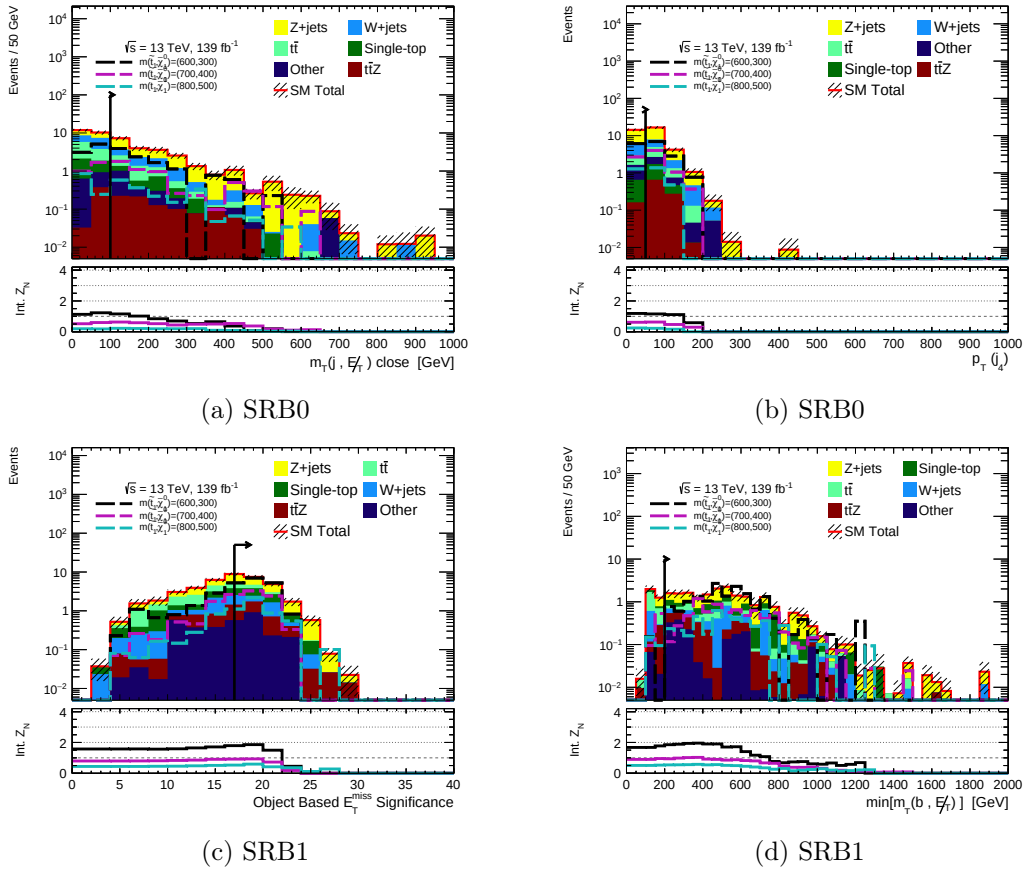

(a) SRB0

(b) SRB0

(c) SRB1

(d) SRB1

Figure 4.13: N-1 plots of the $m^{\mathrm{j}}_{\mathrm{T,close}}$ (a) and $p_{\mathrm{T}}^{\mathrm{jet}_4}$ (b) selections of SRB0 and of $\mathcal{S}$ (c) and $m^{\mathrm{b}}_{\mathrm{T,min}}$ (d) for SRB1. The stacked contributions from the SM background are shown with the expected signal yields of representative models overlaid with dashed lines. The shaded band indicates the statistical uncertainty on the background expectation and the lower panel shows the integrated significance for the considered signal models. Overflow events are added to the rightmost bin.

Variable	**SRC**
Preselection	0L
NN signal score	> 0.75
$\Delta\mathrm{R}(j_1, j_2)$	> 1.0
$\mathrm{m_{eff}}$ [GeV]	> 750

Table 4.12: Definition of SRC on top of the Region C 0L preselection depicted in Table 4.5.

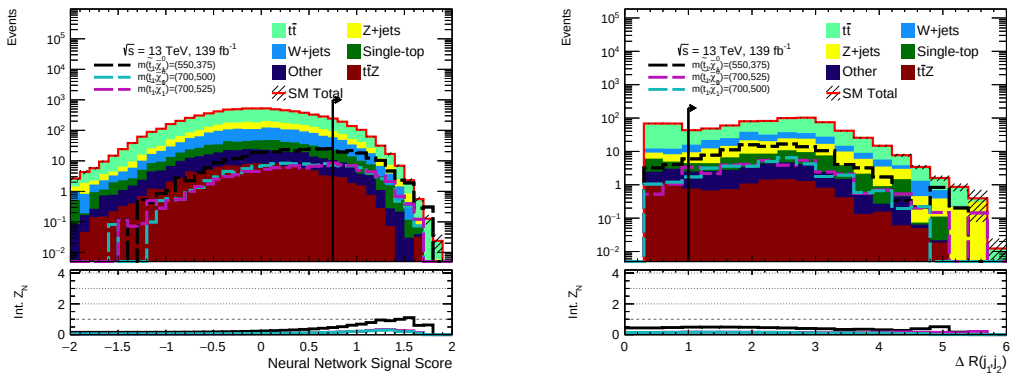

(a) (b)

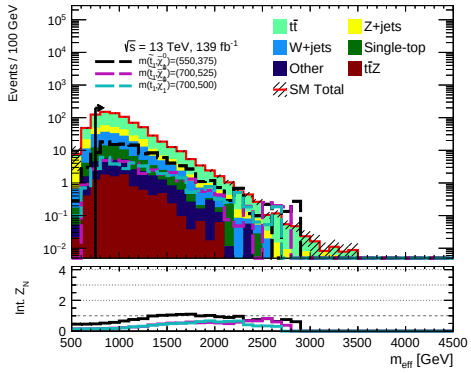

(c)

Figure 4.14: N-1 plots of the NN signal score (a), $\Delta R(j_1, j_2)$ (b) and m_{eff} (c) selections of SRC. The stacked contributions from the SM background are shown with the expected signal yields of representative models overlaid with dashed lines. The shaded band indicates the statistical uncertainty on the background expectation and the lower panel shows the integrated significance for the considered signal models. Overflow events are added to the rightmost bin.

Table 4.13. Low-m_{eff} regions are split into four $m^{\text{j}}_{\text{T,close}}$ bins of 100 GeV and the two highest m_{eff} are inclusive in $m^{\text{j}}_{\text{T,close}}$ due to the small number of events. Figure 4.15 shows the corresponding $m^{\text{j}}_{\text{T,close}}$ distributions for all m_{eff} bins and it can be seen that the dominant backgrounds are either $t\bar{t}$ or $Z+$jets (at high $m^{\text{j}}_{\text{T,close}}$), with $W+$jets being subdominant for certain m_{eff} and $m^{\text{j}}_{\text{T,close}}$ combinations (e.g for $m_{\text{eff}} \in [1250, 1500]$ for low $m^{\text{j}}_{\text{T,close}}$).

Region	$\mathbf{m_{eff}}$ **[GeV]**	$\boldsymbol{m^{\text{j}}_{\text{T,close}}}$ **[GeV]**	**model-indep. fit [GeV]**
SRC750	[750,1000]	[0,100], [100,200], [200,300], [300,∞]	$m^{\text{j}}_{\text{T,close}} > 200$
SRC1000	[1000,1250]	[0,100], [100,200], [200,∞]	$m^{\text{j}}_{\text{T,close}} > 200$
SRC1250	[1250,1500]	[0,100], [100,∞]	$m^{\text{j}}_{\text{T,close}} > 200$
SRC1500	[1500,1750]	[0,100], [100,∞]	
SRC1750	[1750,2000]	–	
SRC2000	≥ 2000	–	

Table 4.13: Selections for the 2D model-dependent fit in m_{eff} and $m^{\text{j}}_{\text{T,close}}$ as well as the model-independent fit used in SRC.

4.9 Background Estimation

The 1L and 2L preselection defined in Table 4.4 and Table 4.5 are used to design CRs to normalise the dominant backgrounds in the signal regions. VRs are then defined to check the extrapolation from the CRs to the SRs.

Region A and B Control Regions

Control regions targeting the $Z+$jets and the single-top background are designed to normalise these backgrounds in SRA and SRB. The selections are listed in Table 4.14.

The Region A and B 2L preselection is used to design CRs for the $Z+$jets background that is dominant in both SRA and SRB. CRZB0 is requiring no top-tagged large-R jets, while CRZAB1 targets one or more tops. Since no large differences in the $Z+$jets background are expected between CRZB0 and CRZABA, they are together used to define a common $\mu_{Z,\text{AB}}$ scaling factor for all SRA and SRB regions. The p_{T} of the sub-leading lepton is required to be at least 30 GeV to ensure a constant offline lepton trigger efficiency. The CRZB0 definition contains the same selections of transverse masses, N_{jets} and $\mathcal{S}$ as SRB0 to be kinematically similar to it. In CRZAB1 however, only the selection of $\mathcal{S} > 17\sqrt{\text{GeV}}$ is maintained as not many events pass the requirement of at least one top-tagged large-R jet.

Only one single-top control region is designed as this background is substantial solely in SRA and SRB1. Using the 1L preselection and requiring $N^{\text{DNN}}_{\text{tops}}(R = 1.0) \geq 1$, CRstAB1 is designed to normalise the single-top background in SRA and SRB1. High selections on the transverse masses suppress $t\bar{t}$ contributions that are dominant at low values. Table 4.15 presents the expected and observed yields of CRZB0, CRZAB1 and

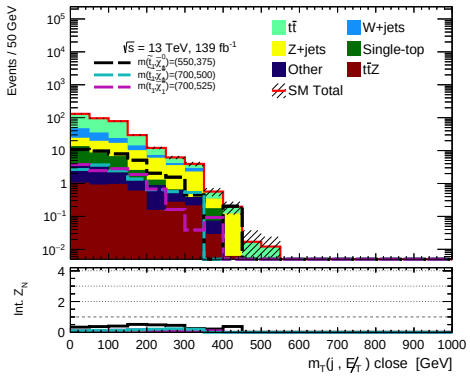

(a) $m_{eff} \in [750, 1000]$

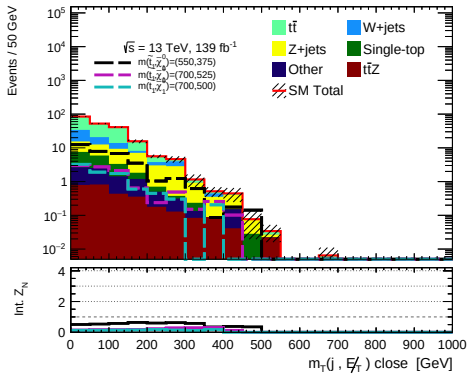

(b) $m_{eff} \in [1000, 1250]$

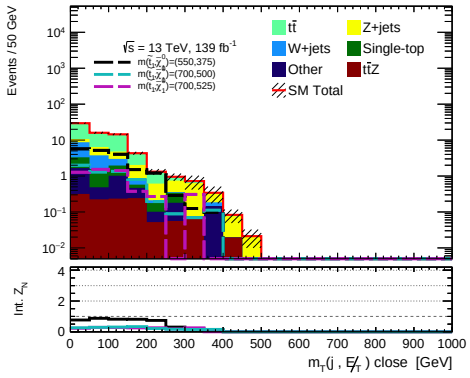

(c) $m_{eff} \in [1250, 1500]$

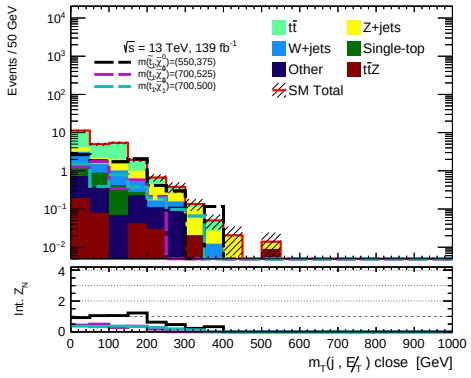

(d) $m_{eff} \in [1500, 1750]$

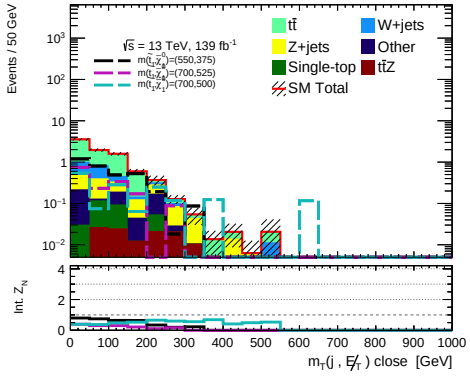

(e) $m_{eff} \in [1750, 2000]$

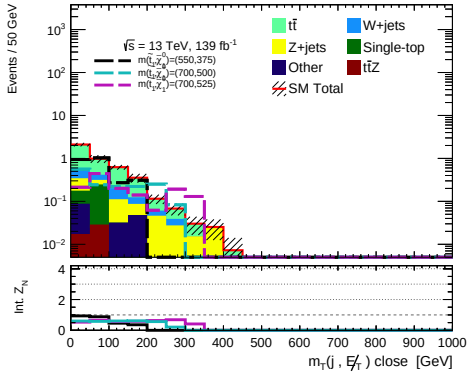

(f) $m_{eff} \in [2000, \infty]$

Figure 4.15: $m^{j}_{T,close}$ distributions for the SRC m_{eff} bins defined in Table 4.13. The stacked contributions from the SM background are shown with the expected signal yields of representative models overlaid with dashed lines. The shaded band indicates the statistical uncertainty on the background expectation and the lower panel shows the integrated significance for the considered signal models. Overflow events are added to the rightmost bin.

Variable	**CRZB0**	**CRZAB1**	**CRstAB1**
Preselection	2L		1L
$p_{\mathrm{T}}^{\ell_2}$ [GeV]	≥ 30		–
$N_{\mathrm{tops}}^{\mathrm{DNN}}(R=1.0)$	0	≥ 1	
N_{jets}	≥ 5	≥ 3	
$m_{\mathrm{T,min}}^{\mathrm{c}}$ [GeV]	≥ 150	–	≥ 300
$m_{\mathrm{T,max}}^{\mathrm{c}}$ [GeV]	≥ 400	–	
$m_{\mathrm{T,min}}^{\mathrm{b}}$ [GeV]	≥ 200	–	≥ 300
$m_{\mathrm{T,max}}^{\mathrm{b}}$ [GeV]	≥ 200	–	
$m_{\mathrm{T,close}}^{\mathrm{j}}$ [GeV]	≥ 100	–	≥ 100
$\mathcal{S}$ [$\sqrt{\mathrm{GeV}}$]	≥ 10	≥ 17	[12,22]
Leading jet flavour	b or c		

Table 4.14: Definitions of CRZB0, CRZAB1 and CRstAB1 on top of the Region A and B 1L and 2L preselections depicted in Table 4.4.

CRstAB1 before the fit, where no large difference between the MC expectation and data is observed.

CRs	CRZB0	CRZAB1	CRstAB1
Observed events	35	41	43
MC exp. SM events	32.75 ± 2.86	44.64 ± 3.34	48.50 ± 9.93
MC exp. W events	0.00 ± 0.00	0.00 ± 0.00	11.26 ± 5.19
MC exp. Z events	29.83 ± 2.17	38.33 ± 2.17	0.11 ± 0.04
MC exp. others events	1.35 ± 0.52	2.28 ± 0.96	1.19 ± 0.84
MC exp. st events	$0.00^{+0.19}_{-0.00}$	$0.00^{+0.00}_{-0.00}$	22.60 ± 0.00
MC exp. ttZ events	1.30 ± 0.50	4.02 ± 1.55	0.72 ± 0.28
MC exp. ttbar events	$0.27^{+0.80}_{-0.27}$	$0.00^{+0.06}_{-0.00}$	12.63 ± 4.74

Table 4.15: Expected pre-fit yields of the Region A and B CRs as well as the observed number of events.

Region A and B Validation Region

To check the modelling of the $Z+$jets background after applying the $\mu_{Z,\mathrm{AB}}$ scaling factor, a VR for the $Z+$jets background of SRA and SRB is defined referred to as VRZ. Most selections of VRZ are similar to the SRs, but some selections are inverted to reject signal events and enrich the $Z+$jets background. In this way, the selections of $m_{\mathrm{T,max}}^{\mathrm{c}} \leq 400\,\mathrm{GeV}$ and $\mathcal{S} \in [15, 17]\ \sqrt{\mathrm{GeV}}$ are applied to make VRZ orthogonal to SRB0 and SRA/SRB1 respectively.

Variable	**VRZ**
Preselection	SRA/B 0L
N_{jets}	[3-8]
$p_{\text{T}}^{b_1}$ [GeV]	≥ 200
$p_{\text{T}}^{c_1}$ [GeV]	≤ 200
$N_{\text{tops}}^{\text{DNN}}(R = 1.0)$	–
$m_{\text{T,min}}^{\text{c}}$ [GeV]	≥ 200
$m_{\text{T,max}}^{\text{c}}$ [GeV]	≤ 400
$m_{\text{T,min}}^{\text{b}}$ [GeV]	≥ 200
$m_{\text{T,close}}^{\text{j}}$ [GeV]	≥ 150
$\mathcal{S}$ [$\sqrt{\text{GeV}}$]	[15,17]
Leading jet flavour	b or c

Table 4.16: Definition of VRZ on top of the region A and B 0L preselection depicted in Table 4.4.

Region C Control Regions

Control regions are defined for SRC to normalise the $t\bar{t}$, $Z+$jets and $W+$jets backgrounds with the selections given in Table 4.17. All CRs feature a selection on the NN signal score of more than 0 to be kinematically close to SRC, but have the higher statistics necessary (SRC: NN signal score > 0.75). The selection on $\Delta\text{R}(j_1, j_2)$ then is identical to SRC. The CRs are orthogonal to SRC by the usage of the 1L or 2L preselections instead of the 0L one in the same way as done in the regions A and B.

Selection	**CRCtt750**	**CRCtt1000**	**CRC1250**	**CRCW**	**CRCZ**
NN signal score	≥ 0.0				
$\Delta\text{R}(j_1, j_2)$	≥ 1.0				
Preselection	1L				2L
$N_{b-\text{jets}}$	≥ 2			==1	≥ 1
$m_{\text{T,min}}^{\text{c}}$ [GeV]	≥ 100			≥ 150	≥ 100
m_{T} [GeV]	> 30			[30,120]	–
m_{eff} [GeV]	[750,1000]	[1000,1250]	> 1250	–	–
NN $V+$jets score	–			> 0	–
$\Delta\text{R}(b_1, l_1)$	–			≥ 1.8	–
$p_{\text{T}}^{\ell_2}$ [GeV]	–				≥ 30

Table 4.17: Definition of the CRs of region C based on the 1L and 2L Region C preselections defined in Table 4.5.

The $t\bar{t}$ background is normalised by CRCtt that requires at least 2 b-tagged jets on top of the 1L region C preselection. This selection is already sufficient to achieve a high purity and statistics for this CR, as $t\bar{t}$ is the dominant background. Figure 4.16 shows the m_{eff} distribution of this selection, where a decreasing data/MC ratio can be observed going to higher m_{eff}. CRCtt is therefore binned in m_{eff} using the same intervals as

in the binning of SRC and separate scaling factors ($\mu_{tt,750}, \mu_{tt,1000}, \mu_{tt,1250}$) are derived. The bins at effective masses of more than 1250 GeV are however combined to ensure a sufficient number of events.

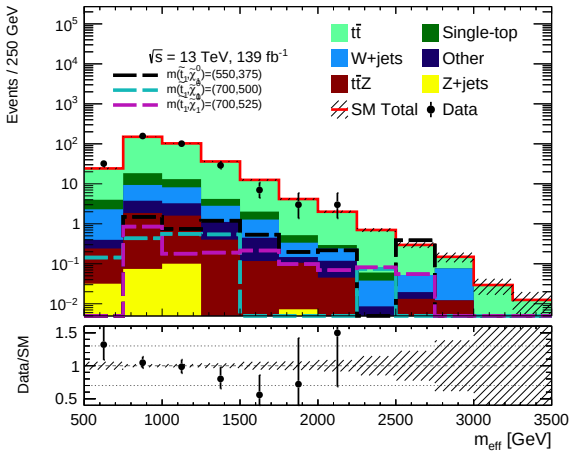

Figure 4.16: m_{eff} distribution in CRCtt before binning. The stacked contributions from the SM background are shown with the expected signal yields of representative models overlaid with dashed lines. The bottom panel shows for each bin the ratio between the data and the SM background expectation from MC. The shaded bands indicate the statistical uncertainty. Overflow events are added to the rightmost bin. The data/MC ratio is observed to be decreasing going to higher m_{eff}.

In contrast to CRCtt, the $W+$jets CR (CRCW) is more challenging to design due to the high contamination of $t\bar{t}$ events even when requiring only one b-jet. Selections on $m^{c}_{T,min}$, m_T and $\Delta R(b_1, l_1)$ help reducing the $t\bar{t}$ contamination, but no satisfactory $W+$jets purity can be achieved. This is where the multiclass feature of the NN classifier comes into play: the $V+$jets score can distinguish between $W+$jets and $t\bar{t}$ events, which is used to further suppress the latter by employing a selection of > -0.5. Figure 4.17 shows the n-1 distributions of the number of b-jets and the NN $V+$jets score for the CRCW selection. Overall a $W+$jets purity of 48% is achieved.

The last CR of region C is CRCZ used to normalise the $Z+$jets background. Except for the NN signal score and $\Delta R(j_1, j_2)$ selections common to all region C CRs, only one additional selection on the sub-leading lepton p_T is applied on top of the region C 2L preselection. In the same way as for CRZB0 and CRZAB1, this selection is to ensure a flat efficiency of the lepton trigger. Due to the 2L requirement, not a single MC generated signal event passes the CRCZ selection and the purity in $Z+$jets is 87%.

Table 4.18 and Table 4.19 show the expected yields before the fit and also the observed data for the CRs of Region C. Already before the background-only fit, the CRs show a decent data/MC agreement except for the $t\bar{t}$ CRs where the decreasing trend in m_{eff} was discussed previously.

Region C Validation Regions

To check the extrapolation from the CRs to the SRC in region C, validation regions are defined based on the Region C 0L preselection as shown in Table 4.20. The NN signal

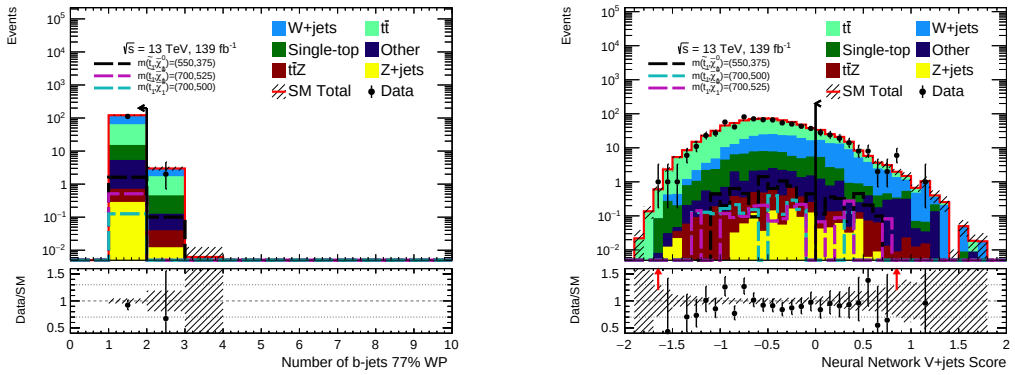

(a) (b)

Figure 4.17: N-1 plots of the number of b-tagged jets (a) and the NN $V+$jets score (b) selections of CRCW. The stacked contributions from the SM background are shown with the expected signal yields of representative models overlaid with dashed lines. The bottom panel shows for each bin the ratio between the data and the SM background expectation from MC. The shaded bands indicate the statistical uncertainty. Overflow events are added to the rightmost bin.

CRs	CRCtt750	CRCtt1000	CRCtt1250	Total
Observed events	157	101	42	300
MC exp. SM events	149.51 ± 7.19	102.32 ± 4.20	55.71 ± 2.44	307.54 ± 13.32
MC exp. W events	5.59 ± 1.47	4.92 ± 1.15	2.98 ± 0.66	13.49 ± 2.13
MC exp. Z events	0.07 ± 0.04	0.10 ± 0.08	$0.01^{+0.01}_{-0.01}$	0.19 ± 0.08
MC exp. others events	1.30 ± 0.43	1.32 ± 0.48	0.77 ± 0.33	3.39 ± 1.06
MC exp. st events	9.08 ± 7.43	4.92 ± 4.17	2.37 ± 1.81	16.37 ± 13.04
MC exp. ttZ events	1.79 ± 0.58	1.50 ± 0.48	0.68 ± 0.25	3.96 ± 1.27
MC exp. ttbar events	131.68 ± 0.34	89.55 ± 0.20	48.91 ± 0.11	270.14 ± 0.38

Table 4.18: Expected pre-fit yields of CRCtt as well as the observed number of events.

CRs	CRCW	CRCZ
Observed events	112	108
MC exp. SM events	115.39 ± 13.87	101.58 ± 3.60
MC exp. W events	56.28 ± 0.14	0.00 ± 0.00
MC exp. Z events	0.29 ± 0.10	87.91 ± 0.01
MC exp. others events	3.16 ± 1.87	3.82 ± 1.24
MC exp. st events	9.93 ± 9.02	$0.00^{+0.13}_{-0.00}$
MC exp. ttZ events	0.43 ± 0.16	7.41 ± 2.30
MC exp. ttbar events	45.30 ± 10.45	2.43 ± 0.90

Table 4.19: Expected pre-fit yields of CRCW and CRCZ as well as the observed number of events.

score is used to target similar kinematics as in SRC, but with less signal events. The lower bound of the signal score of zero is identical to the CRs, while the upper bound is set at a value of 0.5, leaving a gap to SRC to limit the signal contamination. To properly check the modelling of the $t\bar{t}$ background, which is normalised by a binned $t\bar{t}$ CR, VRC is also binned in m_{eff} with the same binning as SRC, except for the high-m_{eff} region due to low statistics. Since different backgrounds are dominant in the various m_{eff} bins, the extrapolation between the CRs and the SRs can be checked simultaneously for all backgrounds. To ensure that the signal contamination is less than 15%, VRC1750 features an additional selection of $E_T^{miss} < 600\,GeV$.

Variable	**VRC750**	**VRC1000**	**VRC1250**	**VRC1500**	**VRC1750**
Preselection	SRC 0L				
NN signal score	[0, 0.5]				
$\Delta R(j_1, j_2)$	> 1.0				
E_T^{miss} [GeV]	–				< 600
m_{eff} [GeV]	[750,1000]	[1000,1250]	[1250,1500]	[1500,1750]	[1750,∞]

Table 4.20: Definition of VRC on top of the 0L preselection depicted in Table 4.5.

4.10 Systematic Uncertainties

Systematic uncertainties from various sources are considered. Experimental systematic uncertainties originate from the detector and the reconstruction of the analysis objects, while theoretical systematic uncertainties come from the modelling of the SM and SUSY by the means of MC simulation. The evaluation of systematic uncertainties in all CRs and SRs is carried out by varying the quantity in question and computing all yields using these varied quantities. For the experimental uncertainties this means that for example scale factors are varied within their uncertainty, while for theoretical uncertainties different algorithms than the nominal are used for the various steps of MC generation. As discussed in Section 4.2, these variations are added to the background-only fit as independent nuisance parameters in the form of Gaussians. In the fit, the CRs are used to reduce the systematic uncertainties of the dominant backgrounds while adding statistical uncertainties due to the limited number of events in the CRs.

The first type of experimental systematic uncertainties are originating from flavour-tagging, which plays a crucial role in the $tc + E_T^{miss}$ analysis as a selection on the number of b- and c-tagged jets is part of every SR and CR. The b-tagging uncertainties [139] are implemented as a reduced nuisance parameter set consisting of the uncertainties on the b-tag efficiency (shown in Figure 3.5), the c- and light-jet mis-tag rate and also the b- and light jet p_T extrapolation. Uncertainties on the c-tagging are treated in the same manner with the uncertainty on the c-tagging efficiency, and the mistag rate of b- and light-jets added as nuisance parameters. For Regions A and B, also uncertainties on the top-tagging efficiency and the inefficiency scaling factors are taken into account [147].

The jet energy scale and resolution (JES and JER) systematic uncertainties [189,190] are evaluated using a reduced set of nuisance parameters – seven for JES and eight for JER. For large-R jets, the JES and JER uncertainties are evaluated similarly, but additionally

the jet mass scale and resolution (JMS and JMR) systematic uncertainties are taken into account as well to calibrate the jet mass [191]. Another systematic uncertainty to consider for jets is concerning the JVT efficiency.

The energy scale and resolution systematic uncertainties of the leptons are estimated in a similar manner as for the JES and JER systematic uncertainties. For leptons, the uncertainties on the scaling factors from the identification, isolation, reconstruction and trigger are considered as well. Since the leptons are only used in the CRs, their contribution to the total systematic uncertainty is very small.

The uncertainties on the energy scale and resolution of all objects are propagated to the $E_{\mathrm{T}}^{\mathrm{miss}}$ calculation. Furthermore, three nuisance parameters are included that are related to the soft term of the $E_{\mathrm{T}}^{\mathrm{miss}}$: the soft term resolution parallel and perpendicular to the $E_{\mathrm{T}}^{\mathrm{miss}}$ and the soft term resolution scale [192].

The last components of the experimental uncertainties are concerning the pile-up and luminosity. The latter is treated by adding a nuisance parameter for the 1.7% uncertainty of the luminosity measurement, as discussed in the beginning of this chapter. Finally, a nuisance parameter is added to cover the systematic uncertainty related to the pile-up re-weighting of the MC events to match the distributions of data.

The theoretical systematic uncertainties are estimated by changing the various MC generator components listed in Table 4.1 or by varying the renormalisation and factorisation scales, the CKKW matching and the resummation scales. Furthermore, the systematic uncertainty arising from the initial and final state radiation is estimated [193] for the $t\bar{t}$ and single-top backgrounds. The latter also features a systematic uncertainty coming from the difference between the diagram removal and diagram subtraction [194] scheme.

Table 4.21 lists the most relevant systematics for SRC. The total systematic uncertainties are between 9 and 27%, with the dominant sources being the uncertainties on the $t\bar{t}$ and $W+$jets scaling factors and $t\bar{t}$ parton showering uncertainty (SRC1250–SRC2000). Uncertainties related to the JET JER and b-tagging are also relevant. In SRA and SRB, the uncertainties related to the single-top background, top- and c-tagging are of greater importance with total uncertainties of 21 to 36%.

Uncertainty of channel	SRC750	SRC1000	SRC1250	SRC1500	SRC1750	SRC2000
Total background expectation	370.89	203.12	55.99	20.46	6.61	3.43
Total statistical ($\sqrt{N_{\text{exp}}}$)	±19.26	±14.25	±7.48	±4.52	±2.57	±1.85
Total background systematic	±34.05 [9.18%]	±21.66 [10.66%]	±8.19 [14.63%]	±3.37 [16.49%]	±1.14 [17.25%]	±0.93 [27.10%]
μ_ttbar_750	**±24.28 [6.5%]**	±0.00 [0.00%]	±0.00 [0.00%]	±0.00 [0.00%]	±0.00 [0.00%]	±0.00 [0.00%]
μ_W	**±16.14 [4.4%]**	**±10.15 [5.0%]**	**±2.80 [5.0%]**	±1.01 [4.9%]	±0.35 [5.3%]	±0.15 [4.4%]
α_FT_EFF_B_systematics	**±12.85 [3.5%]**	**±6.50 [3.2%]**	±1.66 [3.0%]	±0.56 [2.7%]	±0.20 [3.0%]	±0.11 [3.1%]
α_ttbar_theory_GEN	±11.59 [3.1%]	±4.72 [2.3%]	±1.66 [3.0%]	±0.70 [3.4%]	±0.00 [0.01%]	±0.05 [1.5%]
α_st_theory_PS	±9.99 [2.7%]	±2.92 [1.4%]	±1.04 [1.9%]	±0.79 [3.9%]	±0.24 [3.7%]	±0.24 [6.9%]
α_CTAGWEIGHT	±8.88 [2.4%]	±4.91 [2.4%]	±1.90 [3.4%]	±0.72 [3.5%]	±0.13 [2.0%]	±0.12 [3.6%]
α_JET_JER_EffectiveNP_1	±7.14 [1.9%]	±3.17 [1.6%]	±2.27 [4.1%]	±1.07 [5.2%]	±0.15 [2.3%]	±0.13 [3.8%]
α_JET_JER_EffectiveNP_2	±6.72 [1.8%]	±1.60 [0.79%]	±2.68 [4.8%]	±0.96 [4.7%]	**±0.53 [8.0%]**	±0.08 [2.2%]
μ_Z_C	±6.32 [1.7%]	±3.96 [1.9%]	±1.14 [2.0%]	±0.46 [2.3%]	±0.13 [1.9%]	±0.06 [1.7%]
α_JET_JER_EffectiveNP_4	±5.23 [1.4%]	±3.85 [1.9%]	±1.68 [3.0%]	**±1.04 [5.1%]**	±0.15 [2.3%]	±0.01 [0.42%]
α_JET_JER_EffectiveNP_7	±4.97 [1.3%]	±4.29 [2.1%]	±2.00 [3.6%]	±0.92 [4.5%]	±0.17 [2.6%]	±0.06 [1.7%]
α_st_theory_DS	±4.36 [1.2%]	±2.47 [1.2%]	±0.43 [0.76%]	±0.24 [1.2%]	±0.00 [0.06%]	±0.20 [5.8%]
α_JET_JER_EffectiveNP_5	±3.90 [1.1%]	±3.98 [2.0%]	±1.55 [2.8%]	±0.57 [2.8%]	±0.11 [1.7%]	±0.11 [3.1%]
α_JET_JER_EffectiveNP_3	±3.08 [0.83%]	±3.36 [1.7%]	±2.06 [3.7%]	±0.94 [4.6%]	±0.36 [5.4%]	±0.06 [1.7%]
α_JET_JER_DataVsMC_MC16	±3.00 [0.81%]	±2.39 [1.2%]	±0.55 [0.99%]	±0.14 [0.69%]	±0.03 [0.43%]	±0.07 [2.1%]
α_st_theory_GEN	±2.92 [0.79%]	±5.20 [2.6%]	±0.62 [1.1%]	±0.43 [2.1%]	±0.23 [3.5%]	±0.16 [4.7%]
α_ttbar_theory_PS	±2.91 [0.78%]	±2.15 [1.1%]	**±4.97 [8.9%]**	**±1.24 [6.1%]**	**±0.59 [9.0%]**	**±0.67 [19.5%]**
α_JET_Flavor_Response	±2.35 [0.63%]	±2.68 [1.3%]	±0.69 [1.2%]	±0.59 [2.9%]	±0.01 [0.18%]	±0.14 [4.2%]
α_JET_GroupedNP_1	±1.42 [0.38%]	±2.90 [1.4%]	±0.42 [0.75%]	±0.47 [2.3%]	±0.02 [0.29%]	±0.18 [5.4%]
α_JET_GroupedNP_3	±0.48 [0.13%]	±0.14 [0.07%]	±0.17 [0.30%]	±0.19 [0.91%]	±0.15 [2.2%]	±0.07 [2.0%]
α_JET_GroupedNP_2	±0.12 [0.03%]	±2.64 [1.3%]	±0.40 [0.72%]	±0.33 [1.6%]	±0.02 [0.25%]	±0.08 [2.3%]
α_FT_EFF_extrapolation	±0.07 [0.02%]	±0.06 [0.03%]	±0.07 [0.13%]	±0.08 [0.41%]	±0.04 [0.60%]	±0.07 [2.0%]
μ_ttbar_1250	±0.00 [0.00%]	±0.00 [0.00%]	**±6.03 [10.8%]**	**±2.12 [10.3%]**	**±0.77 [11.7%]**	**±0.41 [12.0%]**
μ_ttbar_1000	±0.00 [0.00%]	**±14.61 [7.2%]**	±0.00 [0.00%]	±0.00 [0.00%]	±0.00 [0.00%]	±0.00 [0.00%]
γ_stat_SRC2000_cuts_bin_0	±0.00 [0.00%]	±0.00 [0.00%]	±0.00 [0.00%]	±0.00 [0.00%]	±0.00 [0.00%]	**±0.24 [7.1%]**
γ_stat_SRC1500_cuts_bin_1	±0.00 [0.00%]	±0.00 [0.00%]	±0.00 [0.00%]	±0.44 [2.2%]	±0.00 [0.00%]	±0.00 [0.00%]

Table 4.21: Expected yields and list of uncertainties larger than 2% in the various m_{eff} bins of SRC. The uncertainties can be correlated and therefore can add up in quadrature to larger values than the total background uncertainty. The three dominant uncertainties in each region are written in bold.

4.11 Background-only Fit Results

This section presents the results of the global background-only fit including all regions. The expected and observed event yields in the CRs after the background-only fit are shown in Table 4.22. The corresponding normalisation factors are listed in Table 4.23. They are close to unity except for the $t\bar{t}$ CR for $m_{\text{eff}} > 1250\,\text{GeV}$ and for CRstAB1.

CRs	CRZB0	CRZAB1	CRstAB1
Observed events	35	41	43
Fitted bkg events	33.11 ± 4.49	43.00 ± 5.35	43.00 ± 6.52
Fitted W events	0.00 ± 0.00	0.00 ± 0.00	11.01 ± 5.13
Fitted Z events	30.05 ± 4.57	36.89 ± 5.59	0.11 ± 0.04
Fitted others events	1.35 ± 0.51	2.20 ± 0.95	1.18 ± 0.85
Fitted st events	$0.01^{+0.19}_{-0.01}$	$0.00^{+0.00}_{-0.00}$	17.60 ± 11.78
Fitted ttZ events	1.31 ± 0.50	3.90 ± 1.53	0.73 ± 0.28
Fitted ttbar events	$0.39^{+0.79}_{-0.39}$	$0.00^{+0.06}_{-0.00}$	12.37 ± 4.69

CRs	CRCtt750	CRCtt1000	CRCtt1250	Total
Observed events	157	101	42	300
Fitted bkg events	157.00 ± 12.55	101.00 ± 10.06	42.00 ± 6.47	300.0 ± 17.4
Fitted W events	5.44 ± 2.15	4.96 ± 1.91	3.06 ± 1.14	13.5 ± 4.6
Fitted Z events	0.07 ± 0.04	0.10 ± 0.08	0.01 ± 0.01	0.2 ± 0.1
Fitted others events	1.25 ± 0.42	1.22 ± 0.48	0.75 ± 0.34	3.2 ± 1.1
Fitted st events	10.15 ± 7.35	5.41 ± 4.13	2.45 ± 1.79	18.0 ± 12.9
Fitted ttZ events	1.79 ± 0.58	1.52 ± 0.48	0.69 ± 0.25	4.0 ± 1.3
Fitted ttbar events	138.29 ± 14.45	87.79 ± 10.98	35.04 ± 7.04	261.1 ± 22.1

CRs	CRCW	CRCZ
Observed events	112	108
Fitted bkg events	112.00 ± 10.58	108.00 ± 10.39
Fitted W events	57.41 ± 17.10	0.00 ± 0.00
Fitted Z events	0.31 ± 0.11	94.34 ± 10.97
Fitted others events	2.98 ± 1.84	3.87 ± 1.23
Fitted st events	10.21 ± 8.97	$0.00^{+0.13}_{-0.00}$
Fitted ttZ events	0.42 ± 0.16	7.41 ± 2.29
Fitted ttbar events	40.66 ± 10.61	2.39 ± 0.90

Table 4.22: Background-only fit results for all CRs, with an integrated luminosity of $139\,\text{fb}^{-1}$. Both statistical and systematic uncertainties are considered.

Normalisation factor	**Value**
$\mu_{\mathrm{Z,AB}}$	0.98 ± 0.14
$\mu_{\mathrm{st,AB1}}$	0.78 ± 0.52
$\mu_{\mathrm{W,C}}$	1.02 ± 0.30
$\mu_{\mathrm{Z,C}}$	1.07 ± 0.13
$\mu_{t\bar{t},750\text{–}1000}$	1.05 ± 0.11
$\mu_{t\bar{t},1000\text{–}1250}$	0.98 ± 0.12
$\mu_{t\bar{t},1250}$	0.72 ± 0.14

Table 4.23: Normalisation factors obtained in the combined background-only fit.

With the normalisation factors calculated, the fitted and observed yields of the validation regions VRZ and VRC can be examined in Table 4.24. Good agreement between the fitted expected background events and the observed events can be seen in all validation regions with the largest discrepancy being in the VRC1500 region, where only 80.33 ± 11.12 events are expected, but 101 are observed. The significances of the VRs are summarised in Figure 4.18.

VRs	VRZ
Observed events	70
Fitted bkg events	71.87 ± 14.23
Fitted W events	10.62 ± 6.49
Fitted Z events	45.73 ± 8.62
Fitted others events	1.52 ± 1.48
Fitted st events	$5.82^{+5.86}_{-5.82}$
Fitted ttZ events	1.22 ± 0.51
Fitted ttbar events	6.96 ± 4.14

VRs	VRC750	VRC1000	VRC1250	VRC1500	VRC1750
Observed events	1126	637	246	101	23
Fitted bkg events	1200.19 ± 99.22	683.13 ± 63.27	228.72 ± 29.97	80.33 ± 11.12	28.01 ± 4.74
Fitted W events	177.88 ± 58.16	101.97 ± 33.76	40.87 ± 13.26	15.58 ± 5.21	4.35 ± 1.55
Fitted Z events	178.39 ± 26.45	106.87 ± 14.18	44.27 ± 5.81	16.04 ± 2.76	6.01 ± 1.02
Fitted others events	15.71 ± 5.04	10.53 ± 4.10	3.85 ± 1.52	2.17 ± 0.69	$0.71^{+0.81}_{-0.71}$
Fitted st events	65.47 ± 43.55	33.61 ± 24.72	13.00 ± 9.99	5.12 ± 5.11	1.74 ± 1.50
Fitted ttZ events	16.51 ± 5.05	11.83 ± 3.64	4.68 ± 1.48	1.72 ± 0.72	0.55 ± 0.25
Fitted ttbar events	746.23 ± 93.70	418.33 ± 71.74	122.06 ± 34.76	39.69 ± 11.98	14.65 ± 4.47

Table 4.24: Background-only fit results for VRZ and VRC with an integrated luminosity of $139\,\mathrm{fb}^{-1}$. Both statistical and systematic uncertainties are considered.

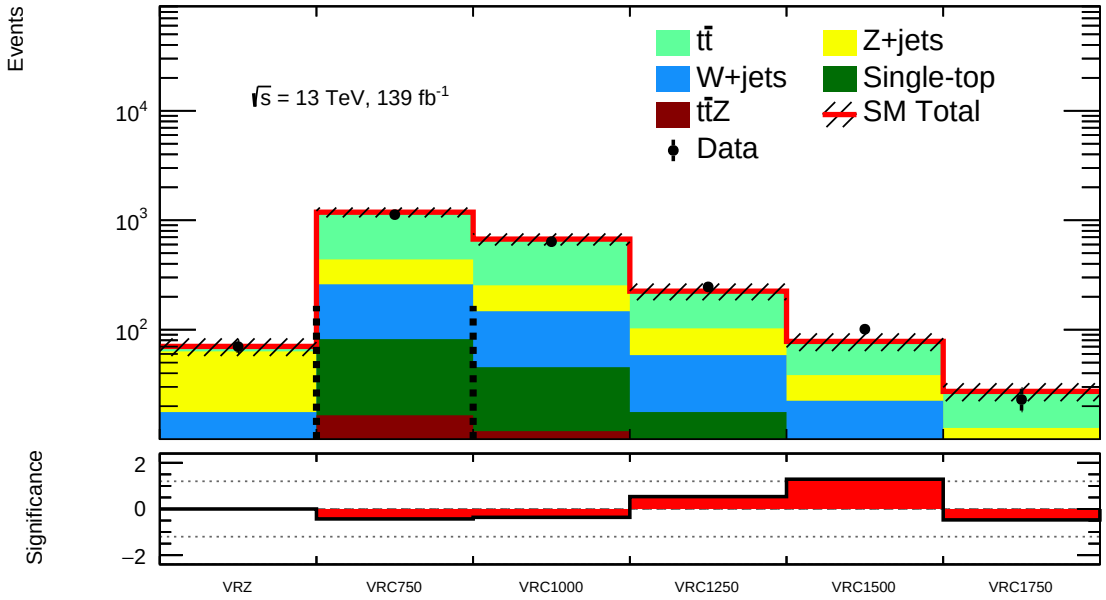

Figure 4.18: Post-fit expected and observed yields in the VRs (top panel) and the derived significance in the combined background-only fit (bottom panel). Both statistical and systematic uncertainties are taken into account.

The expected yields of the SM background and some $tc+E_{\mathrm{T}}^{\mathrm{miss}}$ signals in all the SRs are presented in Tables 4.25–4.31 with -1 for the observed event yields as the SRs have not been unblinded yet.

SRs	SRA_450	SRA_575
Observed events	-1	-1
Fitted bkg events	4.29 ± 0.98	2.74 ± 0.78
Fitted W events	0.67 ± 0.31	0.38 ± 0.19
Fitted Z events	2.16 ± 0.59	1.29 ± 0.29
Fitted others events	0.14 ± 0.07	$0.19^{+0.33}_{-0.19}$
Fitted st events	$0.59^{+0.82}_{-0.59}$	$0.31^{+0.61}_{-0.31}$
Fitted ttZ events	0.32 ± 0.16	0.45 ± 0.18
Fitted ttbar events	0.42 ± 0.20	$0.11^{+0.13}_{-0.11}$
$m(\tilde{t}_1, \tilde{\chi}_1^0) = (900, 1)$	5.75 ± 0.48	7.46 ± 0.55

Table 4.25: Background-only fit results for SRA binned in $m_{\mathrm{T2}}(J^b_{R=1.0}, c)$ with an integrated luminosity of $139\,\mathrm{fb}^{-1}$. Both statistical and systematic uncertainties are considered.

SRs	SRB0_100	SRB0_150	SRB0_400
Observed events	−1	−1	−1
Fitted bkg events	6.51 ± 1.62	11.92 ± 2.90	2.45 ± 0.69
Fitted W events	1.11 ± 0.65	2.81 ± 1.41	$0.35^{+0.50}_{-0.35}$
Fitted Z events	3.44 ± 1.21	5.82 ± 1.05	1.82 ± 0.65
Fitted others events	0.23 ± 0.09	0.09 ± 0.08	0.10 ± 0.04
Fitted st events	$0.32^{+0.41}_{-0.32}$	$0.97^{+1.11}_{-0.97}$	$0.04^{+0.23}_{-0.04}$
Fitted ttZ events	0.22 ± 0.10	0.61 ± 0.26	$0.08^{+0.08}_{-0.08}$
Fitted ttbar events	1.20 ± 0.61	1.61 ± 1.00	$0.06^{+0.09}_{-0.06}$
$m(\tilde{t}_1, \tilde{\chi}^0_1) = (600, 300)$	3.90 ± 0.95	5.93 ± 1.12	1.00 ± 0.29
$m(\tilde{t}_1, \tilde{\chi}^0_1) = (700, 400)$	1.80 ± 0.36	2.64 ± 0.41	0.68 ± 0.60

Table 4.26: Background-only fit results for SRB0 binned in $m^{\mathrm{j}}_{\mathrm{T,close}}$ with an integrated luminosity of $139\,\mathrm{fb}^{-1}$. Both statistical and systematic uncertainties are considered.

SRs	SRB1_100	SRB1_150	SRB1_300	SRB1_500
Observed events	−1	−1	−1	−1
Fitted bkg events	3.64 ± 1.32	4.85 ± 1.05	6.83 ± 2.05	2.36 ± 0.74
Fitted W events	$0.65^{+0.78}_{-0.65}$	0.69 ± 0.60	0.55 ± 0.51	0.40 ± 0.20
Fitted Z events	0.82 ± 0.44	2.09 ± 0.57	3.40 ± 1.01	1.56 ± 0.45
Fitted others events	0.54 ± 0.23	0.20 ± 0.11	0.28 ± 0.11	0.01 ± 0.01
Fitted st events	$0.68^{+0.93}_{-0.68}$	0.68 ± 0.57	$1.23^{+1.69}_{-1.23}$	$0.19^{+0.47}_{-0.19}$
Fitted ttZ events	0.36 ± 0.22	0.82 ± 0.41	0.74 ± 0.31	0.04 ± 0.04
Fitted ttbar events	0.59 ± 0.32	0.37 ± 0.27	0.63 ± 0.43	$0.15^{+0.19}_{-0.15}$
$m(\tilde{t}_1, \tilde{\chi}^0_1) = (600, 300)$	3.87 ± 0.88	2.60 ± 0.71	8.81 ± 1.32	1.07 ± 0.44
$m(\tilde{t}_1, \tilde{\chi}^0_1) = (700, 400)$	0.86 ± 0.24	2.23 ± 0.38	3.73 ± 0.48	0.77 ± 0.21

Table 4.27: Background-only fit results for SRB1 binned in $m^{\mathrm{j}}_{\mathrm{T,close}}$ with an integrated luminosity of $139\,\mathrm{fb}^{-1}$. Both statistical and systematic uncertainties are considered.

SRs	SRC750_0	SRC750_100	SRC750_200	SRC750_300
Observed events	−1	−1	−1	−1
Fitted bkg events	235.6 ± 25.8	111.6 ± 11.8	18.8 ± 4.1	5.0 ± 2.2
Fitted W events	40.6 ± 15.0	10.9 ± 3.8	1.9 ± 1.1	$0.8^{+1.1}_{-0.8}$
Fitted Z events	24.8 ± 5.2	18.8 ± 3.7	8.5 ± 1.9	2.3 ± 1.2
Fitted others events	3.1 ± 1.3	0.8 ± 0.8	0.5 ± 0.2	0.1 ± 0.1
Fitted st events	15.7 ± 11.8	6.7 ± 6.0	0.5 ± 0.5	$0.1^{+0.2}_{-0.1}$
Fitted ttZ events	2.0 ± 0.7	1.5 ± 0.5	0.5 ± 0.4	0.2 ± 0.1
Fitted ttbar events	149.4 ± 23.3	72.8 ± 11.3	7.0 ± 3.0	$1.4^{+2.1}_{-1.4}$
$m(\tilde{t}_1, \tilde{\chi}_1^0) = (550, 375)$	20.58 ± 1.65	13.02 ± 1.37	3.61 ± 0.71	0.65 ± 0.30
$m(\tilde{t}_1, \tilde{\chi}_1^0) = (700, 525)$	6.21 ± 0.77	4.67 ± 0.68	0.83 ± 0.28	0.13 ± 0.10

Table 4.28: Background-only fit results for SRC750 binned in $m^{\mathrm{j}}_{\mathrm{T,close}}$ with an integrated luminosity of $139\,\mathrm{fb}^{-1}$. Both statistical and systematic uncertainties are considered.

SRs	SRC1000_0	SRC1000_100	SRC1000_200
Observed events	−1	−1	−1
Fitted bkg events	134.8 ± 16.1	55.9 ± 6.0	12.4 ± 2.0
Fitted W events	26.2 ± 9.3	5.9 ± 2.3	2.0 ± 0.8
Fitted Z events	15.5 ± 2.4	12.1 ± 2.1	6.4 ± 1.3
Fitted others events	1.5 ± 0.6	0.7 ± 0.3	0.2 ± 0.2
Fitted st events	$9.9^{+12.8}_{-9.9}$	2.9 ± 2.3	$0.5^{+0.5}_{-0.5}$
Fitted ttZ events	1.6 ± 0.6	0.8 ± 0.5	0.5 ± 0.2
Fitted ttbar events	80.1 ± 13.4	33.6 ± 5.8	2.7 ± 0.7
$m(\tilde{t}_1, \tilde{\chi}_1^0) = (550, 375)$	20.33 ± 1.70	10.33 ± 1.22	3.29 ± 0.71
$m(\tilde{t}_1, \tilde{\chi}_1^0) = (700, 525)$	5.71 ± 0.75	2.78 ± 0.53	1.24 ± 0.33

Table 4.29: Background-only fit results for SRC1000 binned in $m^{\mathrm{j}}_{\mathrm{T,close}}$ with an integrated luminosity of $139\,\mathrm{fb}^{-1}$. Both statistical and systematic uncertainties are considered.

SRs	SRC1250_0	SRC1250_100	SRC1500_0	SRC1500_100
Observed events	−1	−1	−1	−1
Fitted bkg events	37.9 ± 6.4	18.1 ± 2.8	13.3 ± 2.9	7.1 ± 1.2
Fitted W events	8.0 ± 2.8	1.4 ± 0.8	2.6 ± 1.0	0.8 ± 0.6
Fitted Z events	4.9 ± 0.9	4.9 ± 1.4	1.7 ± 0.7	2.3 ± 0.5
Fitted others events	0.8 ± 0.3	0.4 ± 0.1	0.4 ± 0.1	0.2 ± 0.1
Fitted st events	3.1 ± 3.1	1.3 ± 1.3	$1.2^{+1.4}_{-1.2}$	$0.4^{+1.0}_{-0.4}$
Fitted ttZ events	0.5 ± 0.2	0.7 ± 0.2	0.3 ± 0.1	0.1 ± 0.1
Fitted ttbar events	20.6 ± 6.4	9.4 ± 2.6	7.2 ± 1.9	3.3 ± 0.8
$m(\tilde{t}_1, \tilde{\chi}^0_1) = (550, 375)$	10.89 ± 1.26	7.27 ± 0.97	4.47 ± 0.78	4.61 ± 0.84
$m(\tilde{t}_1, \tilde{\chi}^0_1) = (700, 525)$	2.81 ± 0.52	2.37 ± 0.47	3.02 ± 0.52	1.13 ± 0.31

Table 4.30: Background-only fit results for SRC1250 and SRC1500 binned in $m^{\mathrm{j}}_{\mathrm{T,close}}$ with an integrated luminosity of $139\,\mathrm{fb}^{-1}$. Both statistical and systematic uncertainties are considered.

SRs	SRC1750	SRC2000
Observed events	−1	−1
Fitted bkg events	6.61 ± 1.14	3.43 ± 0.93
Fitted W events	1.17 ± 0.46	0.51 ± 0.21
Fitted Z events	1.08 ± 0.22	0.51 ± 0.10
Fitted others events	0.10 ± 0.04	$0.08^{+0.12}_{-0.08}$
Fitted st events	$0.31^{+0.54}_{-0.31}$	$0.25^{+0.53}_{-0.25}$
Fitted ttZ events	0.10 ± 0.06	$0.02^{+0.05}_{-0.02}$
Fitted ttbar events	3.85 ± 1.01	2.05 ± 0.84
$m(\tilde{t}_1, \tilde{\chi}^0_1) = (550, 375)$	3.31 ± 0.65	2.55 ± 0.61
$m(\tilde{t}_1, \tilde{\chi}^0_1) = (700, 525)$	1.58 ± 0.37	1.38 ± 0.37

Table 4.31: Background-only fit results for the unbinned SRC1750 and SRC2000 regions with an integrated luminosity of $139\,\mathrm{fb}^{-1}$. Both statistical and systematic uncertainties are considered.

4.12 Interpretation

If there are no significant deviations from the SM seen once unblinded, limits on both model-independent and the simplified model described in Section 1.7 will be extracted.

Model-independent limits are calculated as described in Section 4.2. In SRA, SRB0 and SRB1, the binning in $m_{\mathrm{T2}}(J^b_{R=1.0}, c)$ and $m^{\mathrm{j}}_{\mathrm{T,close}}$ is removed to receive inclusive SRs, while for SRC the selections described in Table 4.13 are used to have three model-independent regions for SRC. Table 4.32 shows the expected (S^{95}_{exp}) and observed (S^{95}_{obs}) upper limits at 95% CL on the number of BSM events in the various model-independent SRs. The CL of the background-only hypothesis is denoted by $\mathrm{CL_B}$ and p_0 is the discovery p-value with the associated significance Z.

Signal channel	$\langle\epsilon\sigma\rangle^{95}_{\mathrm{obs}}$[fb]	S^{95}_{obs}	S^{95}_{exp}	CL_B	$p(s=0)$ (Z)
SRA	0.12	16.3	$14.3^{+5.7}_{-3.9}$	0.67	0.32 (0.48)
SRB0	0.28	39.4	$30.9^{+12.5}_{-5.4}$	0.71	0.29 (0.56)
SRB1	0.20	27.6	$25.4^{+9.6}_{-6.0}$	0.71	0.28 (0.58)
SRC750_disc	0.35	49.1	$35.1^{+15.1}_{-6.1}$	0.82	0.18 (0.93)
SRC1000_disc	0.24	32.8	$26.3^{+11.7}_{-4.2}$	0.68	0.32 (0.48)
SRC1250_disc	0.15	20.9	$20.0^{+8.3}_{-4.3}$	0.61	0.38 (0.29)

Table 4.32: Blinded discovery fit results of all discovery signal regions. Left to right: 95% CL upper limits on the visible cross-section ($\langle\epsilon\sigma\rangle^{95}_{\mathrm{obs}}$) and on the number of signal events (S^{95}_{obs}). The third column (S^{95}_{exp}) shows the 95% CL upper limit on the number of signal events, given the expected number (and $\pm1\sigma$ excursions on the expectation) of background events. The last two columns indicate the $\mathrm{CL_B}$ value, i.e. the confidence level observed for the background-only hypothesis, and the discovery p-value ($p(s=0)$).

The model-dependent limits are drawn using the $tc + E^{\mathrm{miss}}_{\mathrm{T}}$ simplified model presented in Section 1.7 with the $\tilde{t}_1$ and $\tilde{\chi}^0_1$ mass combinations shown in Figure 4.4. Figure 4.19 presents the expected 95% CL exclusion limits in the $(m(\tilde{t}_1), m(\tilde{\chi}^0_1))$ plane. SRA is most sensitive at large $\tilde{t}_1$ and low $\tilde{\chi}^0_1$ masses, while SRB can exclude higher $\tilde{\chi}^0_1$ masses. SRC is sensitive to $\Delta m(\tilde{t}_1, \tilde{\chi}^0_1) \sim 175\,\mathrm{GeV}$, where SRB is not effective. These different exclusion limits follow from the analysis strategy formulated in Section 4.1.

Since all SRs are mutually exclusive, the SRs can all be combined in a common fit so that the p-value can be reduced in each signal scenario. Figure 4.20 shows this combined exclusion limit. It is expected to exclude the $tc + E^{\mathrm{miss}}_{\mathrm{T}}$ signal hypothesis up to masses of almost 1050 GeV in the mass of the $\tilde{t}_1$ in the boosted region. The largest exclusion in $m(\tilde{\chi}^0_1)$ is achieved in the compressed region for the $(m(\tilde{t}_1), m(\tilde{\chi}^0_1)) = (600, 425)$ signal scenario. Heavy neutralinos with masses of 400 GeV are expected to be excluded up to $\tilde{t}_1$ masses of 900 GeV.

The model-dependent exclusion fit can also be interpreted in the $(m(\tilde{t}_1), \mathrm{BR}(\tilde{t}_1 \to t + \tilde{\chi}^0_1))$ plane. This is done by reweighting the MC simulated signal events depending on their

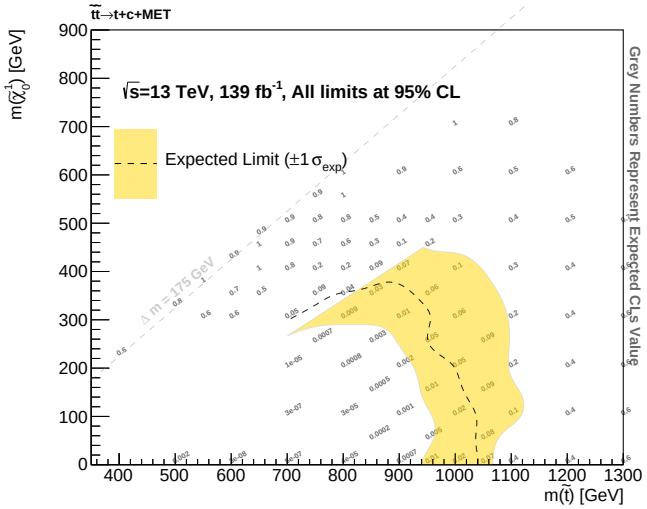

(a)

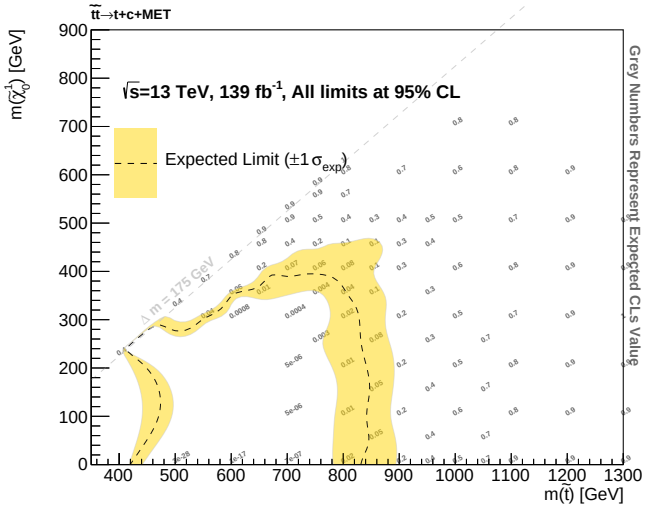

(b)

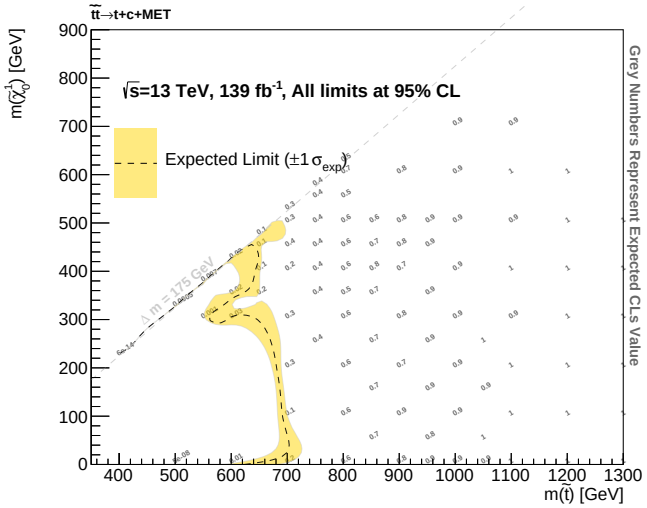

(c)

Figure 4.19: Expected exclusion contours with only statistical uncertainties at the 95% CL in the $(m(\tilde{t}_1), m(\tilde{\chi}_1^0))$ plane for the SRA (a), SRB (b) and SRC (c) region. The dashed line indicates the 95% CL expected limit, while the yellow band shows the 1σ uncertainty on this limit.

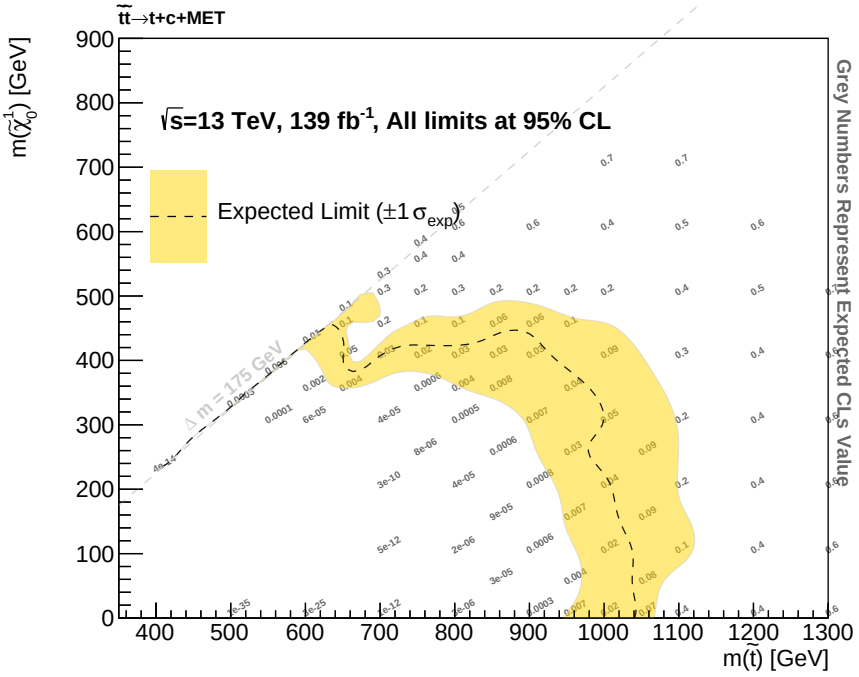

Figure 4.20: Expected exclusion contours with only statistical uncertainties at the 95% CL in the $(m(\tilde{t}_1), m(\tilde{\chi}_1^0))$ plane for the combined fit. The dashed line indicates the 95% CL expected limit, while the yellow band shows the 1σ uncertainty on this limit.

decay type ($tt + E_{\mathrm{T}}^{\mathrm{miss}}$, $tc + E_{\mathrm{T}}^{\mathrm{miss}}$ or $cc + E_{\mathrm{T}}^{\mathrm{miss}}$) at truth level. The resulting exclusion limits for $\tilde{\chi}_1^0$ masses of 300 GeV and 1 GeV are shown in Figure 4.21. BRs larger than 0.5 are expected to be excluded up to $\tilde{t}_1$ masses of 1000 GeV both for $m(\tilde{\chi}_1^0) = 300$ and 1 GeV. The expected exclusion limit for $\mathrm{BR}(\tilde{t}_1 \rightarrow t + \tilde{\chi}_1^0) < 0.5$ is weakened the smaller the BR becomes. For a BR of zero, only $m(\tilde{t}_1)$ of up to ~ 700 GeV are expected to be excluded, showing that the $tc + E_{\mathrm{T}}^{\mathrm{miss}}$ analysis is more sensitive to $tt + E_{\mathrm{T}}^{\mathrm{miss}}$ final states ($\mathrm{BR}(\tilde{t}_1 \rightarrow t + \tilde{\chi}_1^0) \sim 1$) than to $cc + E_{\mathrm{T}}^{\mathrm{miss}}$ ($\mathrm{BR}(\tilde{t}_1 \rightarrow t + \tilde{\chi}_1^0) \sim 0$). This is due to the requirement of at least one top-tagged large-R jet in SRA and SRB1, that is very difficult to fulfil for a $cc + E_{\mathrm{T}}^{\mathrm{miss}}$. They furthermore only rarely will have a b-jet in the final state which is required by all SRs.

The analysis presented in this thesis is the first one to specifically target models featuring non-MFV SUSY. The expected limits for the $tc + E_{\mathrm{T}}^{\mathrm{miss}}$ simplified model are strongly improving on the limits derived by the reinterpretation of the 36.1 fb^{-1} ATLAS $tt + E_{\mathrm{T}}^{\mathrm{miss}}$ and $cc + E_{\mathrm{T}}^{\mathrm{miss}}$ analyses performed in Reference [31]. Comparing their exclusion limit in the $(m(\tilde{t}_1), \mathrm{BR}(\tilde{t}_1 \rightarrow t + \tilde{\chi}_1^0))$ plane from Figure 1.6 to Figure 4.21b it can be seen that this work has finally charted this new region of SUSY phase space. The expected exclusion limits are even on-par with the 300 fb^{-1} prospect of Reference [31] for BRs of ~ 0.5, while being superior in also targeting pure tt or $cc + E_{\mathrm{T}}^{\mathrm{miss}}$ final states. For compressed signal scenarios with $\Delta(m(\tilde{t}_1), m(\tilde{\chi}_1^0)) \sim m(t)$, the expected exclusion limit reaches the $(m(\tilde{t}_1), m(\tilde{\chi}_1^0)) = (600, 425)$ mass point, which is even superior to the 3000 fb^{-1} prospect of Reference [31]. This is achieved mostly thanks to the NN developed for SRC which enabled to efficiently discriminate the SUSY signal from the SM background in the compressed region.

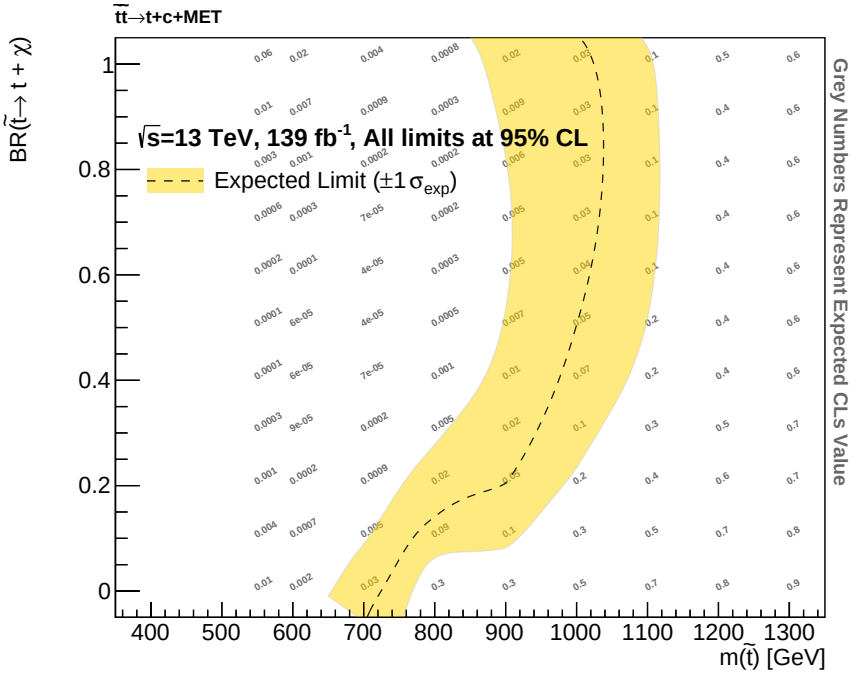

(a)

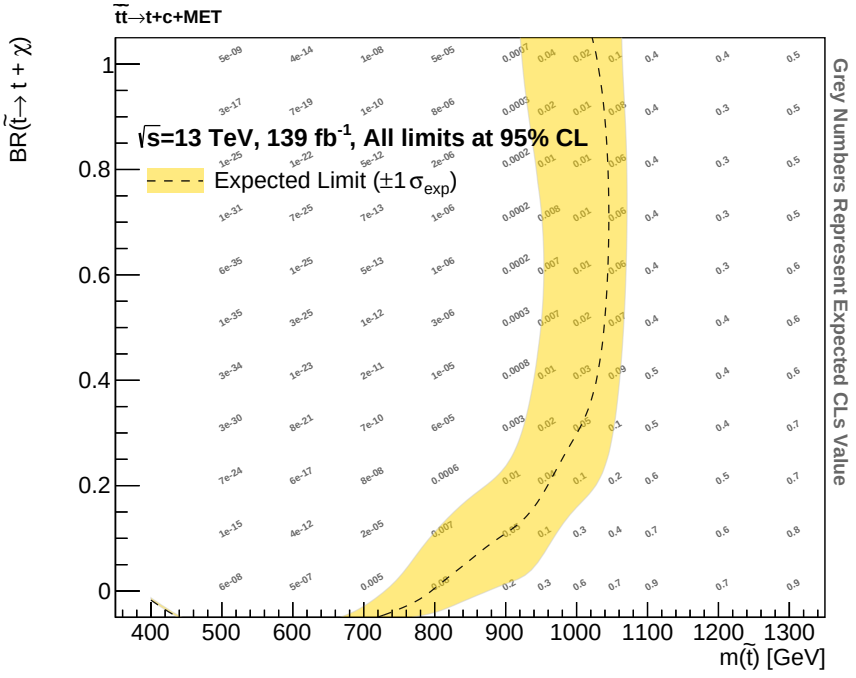

(b)

Figure 4.21: Expected exclusion contours with only statistical uncertainties at the 95% CL in the $(m(\tilde{t}_1), \mathrm{BR}(\tilde{t}_1 \to t + \tilde{\chi}_1^0))$ plane for the combined fit and a $\tilde{\chi}_1^0$ mass of 300 GeV (a) and 1 GeV (b). The dashed line indicates the 95% CL expected limit, while the yellow band shows the 1σ uncertainty on this limit.

Chapter 5

Upgrading the ATLAS Experiment for High Luminosity

Although recent findings by LHCb [195] and new measurements of the anomalous magnetic moment of the muon ($g-2$, [196]) point into the direction that lepton flavour universality may not hold, no BSM physics has been discovered until the release of this work except for neutrino oscillations – the SM proves to describe nature very well, as already discussed in Section 1.1. Nevertheless, many well motivated SUSY or other BSM theories featuring particles with $O(\text{TeV})$ masses can be neither discovered nor excluded yet given the integrated luminosity collected at the LHC experiments. Run 3 of the LHC will add an additional $L = 350\,\text{fb}^{-1}$ at $\sqrt{s} = 13\text{–}14\,\text{TeV}$, more than doubling the currently available dataset. In order to drastically expand the reach of BSM searches and to enable precise measurements of SM properties such as the Higgs self-coupling however, a much larger integrated luminosity is needed. This is the motivation to further upgrade the LHC accelerator complex to deliver a higher instantaneous luminosity in the context of the HL-LHC program. This upgrade of the LHC is scheduled to take place in 2025–2027 in the Long Shutdown 3 (LS3) as presented in Figure 5.1. Some preparatory work and injection chain upgrades are already being done in the LS2 taking place at the time of writing.

This chapter firstly describes the HL-LHC project in Section 5.1 and lists the consequent requirements for the ATLAS detector. Section 5.2 introduces the new ATLAS Inner Tracker (ITk) that replaces the ID to cope with the HL-LHC requirements. The new TDAQ system and the completely replaced readout system of the ITk then are discussed in Section 5.3 and Section 5.4, respectively. The following sections present the author's work on the development and testing of the new *Optosystem*, responsible for the optical-electrical conversion and aggregation of all ITk Pixel data links. Section 5.5 first describes the key components of the Optosystem, which are used in the conceptual design (Section 5.6) and the technical implementation (Section 5.7) of the Optosystem. Finally, the last two sections describe the development of multiple test setups and summarise the derived test results of Optosystem components and prototypes.

Figure 5.1: Current timeline of the LHC and HL-LHC programs. The installation of the HL-LHC mainly takes place in the LS3 in 2025-2027. At the same time, ATLAS and CMS will undergo their HL upgrades. Taken from Reference [197].

5.1 The High-Luminosity Large Hadron Collider

The HL-LHC project [32] significantly increases the physics capabilities of the LHC. It will feature an $\mathcal{L}$ of up to $7.5 \times 10^{34}\,\mathrm{cm}^{-2}\mathrm{s}^{-1}$, which is more than three times higher than the instantaneous luminosity in Run 2 (see Figure 2.2). This enables the HL-LHC to collide in one year as many protons as the current LHC has since 2011, resulting in a total integrated luminosity of 3000–4000 fb^{-1}.

To enable the high-luminosity phase of the LHC, the injection chain needs to be upgraded as well [198]. This is done during LS2, with the replacement of Linac 2 by Linac 4 [199] as the most significant component. Linac 4 accelerates H^- instead of protons to an increased energy of 160 MeV. The electrons are stripped away from H^- by a thin carbon foil after Linac 4, obtaining protons. This is expected to increase the beam brightness (intensity/emittance) after the following PSB by a factor of 2. The latter is upgraded to allow for an extraction energy of 2 instead of 1.4 GeV. Finally, the PS and SPS also will be upgraded to handle the increased injection energy and beam current.

The first major upgrade to the LHC are new triplet quadrupole magnets located around the ATLAS and CMS interaction points. The new $\mathrm{Nb_3Sn}$ focusing magnets feature a 11–12 T magnetic field (8.33 T currently), which is used to reduce the β^* at the interaction points. This increases the peak instantaneous luminosity described in Equation (2.3), but also enlarges the beam size at the triplets, leading to a larger crossing angle needed to keep the two beams far enough separated when sharing a common beam pipe. To counteract the accompanying reduction of $\mathcal{L}$, the HL-LHC introduces RF *crab cavities*. They generate a transverse electric field that rotates the bunches by half the crossing angle each so that they collide head-on.

Figure 5.2 shows the instantaneous luminosity achieved by the HL-LHC in comparison to the LHC during one and multiple proton fills. To limit both the energy deposition in the interaction region magnets and the pile-up in the interaction points, the HL-LHC employs

a luminosity levelling scheme that limits $\mathcal{L}$ to $5 \times 10^{34}\,\mathrm{cm}^{-2}\mathrm{s}^{-1}$ ($7.5 \times 10^{34}\,\mathrm{cm}^{-2}\mathrm{s}^{-1}$ in the ultimate HL-LHC scenario), but also prolongs the individual proton fills. Instantaneous luminosities of 5 to $7.5 \times 10^{34}\,\mathrm{cm}^{-2}\mathrm{s}^{-1}$ however still lead to pile-up conditions of up to $\langle\mu\rangle \approx 200$ and radiation doses much higher than at the LHC. The large integrated luminosity leads to more radiation damage, which would degrade the performance of the current detectors very swiftly. Furthermore, the tracking of particles coming from an average of 200 simultaneous pp interactions cannot be handled by the current tracking detectors in LHC experiments. In the course of the HL-LHC upgrade, the LHC experiments therefore must be upgraded as well. The following section discusses the largest component of the HL upgrade of the ATLAS detector, which is the replacement of the current ID with the ITk during LS3.

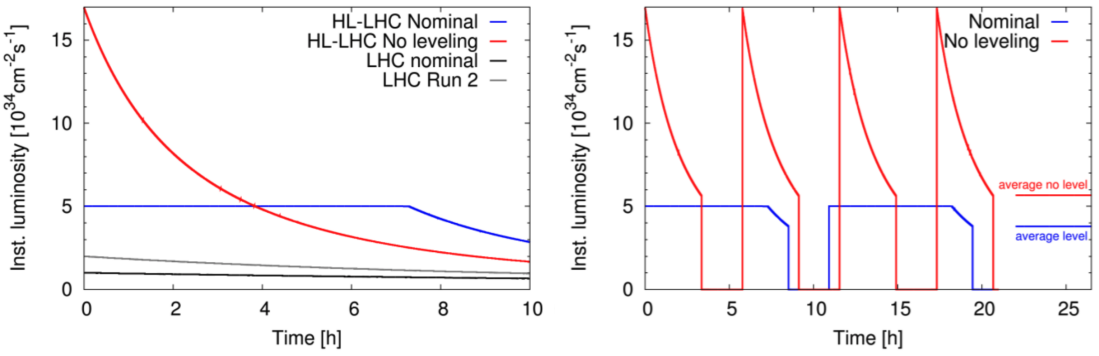

(a) (b)

Figure 5.2: Evolution of the instantaneous luminosity in the HL-LHC during one fill compared with the LHC (a) and for multiple fills indicating the average instantaneous luminosity with and without luminosity levelling (b). Taken from Reference [32].

5.2 The ATLAS Inner Tracker

The ITk [34, 35] is the vertexing and tracking detector of the HL ATLAS detector that is designed to deal with the challenges posed by the HL-LHC. In more detail these requirements are [34]:

- Full detector coverage for tracks with $p_\mathrm{T} > 1\,\mathrm{GeV}$ originating from a luminous region of $|z| < 15\,\mathrm{cm}$ and $r < 2\,\mathrm{mm}$.
- Reconstruction of tracks from the primary vertex up to $|\eta| < 4$.
- Equal or better tracking performance than in the ID in pile-up conditions of $\langle\mu\rangle \approx 200$.
- Radiation resistant for the 10 years of operation at $\mathcal{L}$ of up to $7.5 \times 10^{34}\,\mathrm{cm}^{-2}\mathrm{s}^{-1}$ (replacement of innermost components after 5 years).

These requirements are met by an all-silicon tracker design that consists of two subdetectors: an inner Pixel and an outer Strip subdetector. In contrast to the ID, there is no TRT-like subdetector. The layout of the ITk is presented in Figure 5.3 and features barrel and end-cap sections similar to the ID.

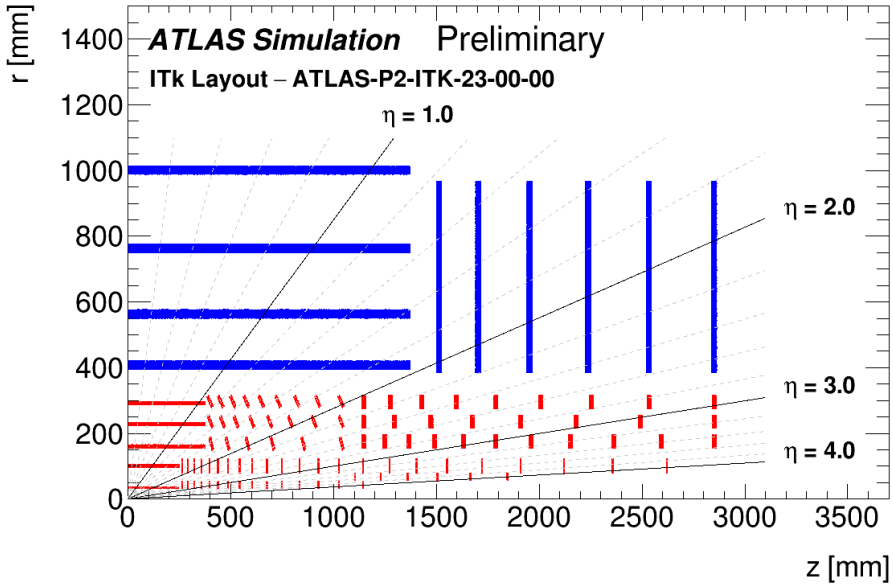

Figure 5.3: Current layout of one quarter the ITk. Only the sensing elements are shown, with the red areas indicating the Pixel and the blue areas showing the Strip sensors. Taken from Reference [200].

The Strip detector [34] instruments the region of $|\eta| < 2.7$ with four barrel layers and six end-cap rings on each side of the barrel. They are located at $385\,\text{mm} < r < 1000\,\text{mm}$ and up to $|z| < 2850\,\text{mm}$, featuring double modules with a pitch of 69–85 μm in $r \times \phi$. The modules are arranged with a stereo angle to allow for the measurement of z (r) in the Strip barrel (end-caps). While the pitch of these sensors is comparable to the SCT, the ITk Strip detector has a tenfold increased number of channels due to the larger instrumented volume.

The ITk Pixel detector is made up of five layers of hybrid pixel sensor modules, where silicon sensors are bump-bonded to RD53 FE chips [201,202] featuring a pitch of $50 \times 50\,\mu\text{m}^2$. In the low-$z$ region, the sensors are sitting on local support structures called *staves* that are parallel to the beam pipe. The collection of all staves makes up the barrel. Sensors at higher z are located on *rings* that are positioned orthogonal to the beam pipe – they make up the end-caps. The local supports are responsible for the mechanical stability, cooling and the routing of the electrical services from the modules to the end of the local supports (and vice versa). The properties of all local supports are listed in Table 5.1 for the staves and in Table 5.2 for the rings. The innermost barrel layer and the R0 and R0.5 rings are instrumented with single chip modules (one FE per module) of 3D sensors due to their superior radiation tolerance and low power dissipation, while the rest of the ITk Pixel uses quad modules (four FEs per module) of planar sensors [35, 203].

The pixel modules are further grouped into three subsystems: the Inner System (IS), the Outer Barrel (EB) and the Outer End-cap (EC). The IS consists of the two innermost barrel layers up to $|z| < 250\,\text{mm}$ and inner end-cap rings that form two end-caps adjacent to the barrel section. The latter are of crucial importance to extend the coverage of the ITk to $|\eta| < 4$. Due to the proximity to the interaction point and the large η coverage, the IS receives the largest amount of radiation damage of the ITk as displayed in Figure 5.5. It is therefore designed to be replaceable since the radiation dose accumulated after

Layer	Radius [mm]	Rows of sensors	Sensors per row		Type	Hits
			flat	inclined		
0	34	12	12	–	singlet	1
1	99	20	6	–	quads	1
2	160	32	9	6	quads	1
3	228	44	9	8	quads	1
4	291	56	9	9	quads	1

Table 5.1: Parameters of one half-barrel of the ITk pixel system in the latest ITk design (ATLAS-P2-ITK-23-00-00, [200]). Particles originating from $z = +15\,\text{cm}$ are expected to leave one hit in each of the five barrel layers.

Layer	Radius [mm]	Rings	Sensors per ring	Type	Hits
R0	33.2	15	18	singlet	2–4
R0.5	58.70	6	30	singlet	3–4
R1	80.00	23	20	quads	2–4
R2	154.50	11	32	quads	1–2
R3	214.55	8	44	quads	1
R4	274.60	9	52	quads	1

Table 5.2: Parameters of one end-cap of the ITk pixel system in the latest ITk design (ATLAS-P2-ITK-23-00-00, [200]). The radius indicates the distance of the closest sensor of a ring to the beam pipe. Particles originating from $z = +15\,\text{cm}$ are expected to leave between one and four hits in each of the five end-cap layers, as each layer consists of multiple rings.

2000 fb^{-1} will exceed the radiation tolerance of many IS components.

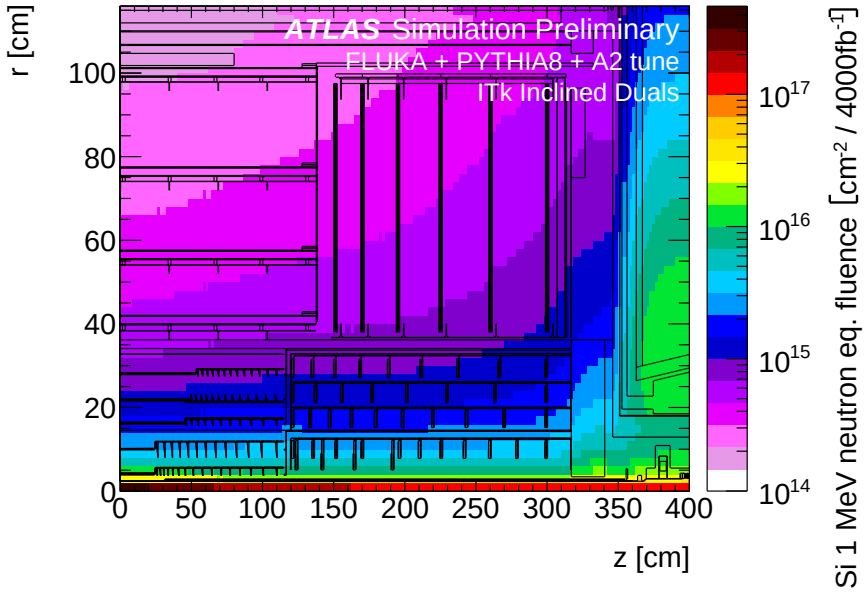

Figure 5.4

Figure 5.5: Distribution of the non-ionising energy loss in units of 1 MeV neutron equivalent fluence after an integrated luminosity of 4000 fb^{-1} in the ITk. The simulation is done using FLUKA [204] on the ITk layout presented in Reference [35]. Taken from Reference [205].

The OB is made up of 2-m long staves with sensor modules parallel to the beam pipe for $|z| < 400$ mm and an *inclined section*, where the modules are inclined with reference to the beam pipe. This arrangement ensures the hermeticity of the ITk while simultaneously minimising the number of sensors needed. Moreover, it reduces the material budget of the OB, improving the tracking performance.

Finally, the OE consists of the layer 2–4 rings whose location is also optimised to ensure hermeticity. Both the OB and the OE are designed to sustain 4000 fb^{-1} of radiation damage and do not require replacement.

To further reduce the material budget of the Pixel services, multiple Pixel sensor modules are powered in series, only requiring one set of powering cables. Only modules located on the same local support can be part of the same Serial Powering (SP) chain.

The combined ITk Pixel and Strip detectors ensure that charged particles with p_{T} of more than 1 GeV leave at least 9 hits in a silicon layer up to $|\eta| < 4$ as shown in Figure 5.6, fulfilling the first above-mentioned requirement. This is a significant improvement compared to the ID that features a maximum of 8 silicon hits.

The expected tracking performance of the ITk is shown in Figure 5.7. The track reconstruction efficiency is comparable to Run 2 while being subject to fivefold higher pile-up and providing coverage up to $|\eta| < 4$. Furthermore, the fake rate is reduced by one order of magnitude thanks to the 9 silicon hits in the ITk (7 in loose Run 2 selection) [35].

The expected impact parameter resolutions are shown in Figure 5.8 and are comparable

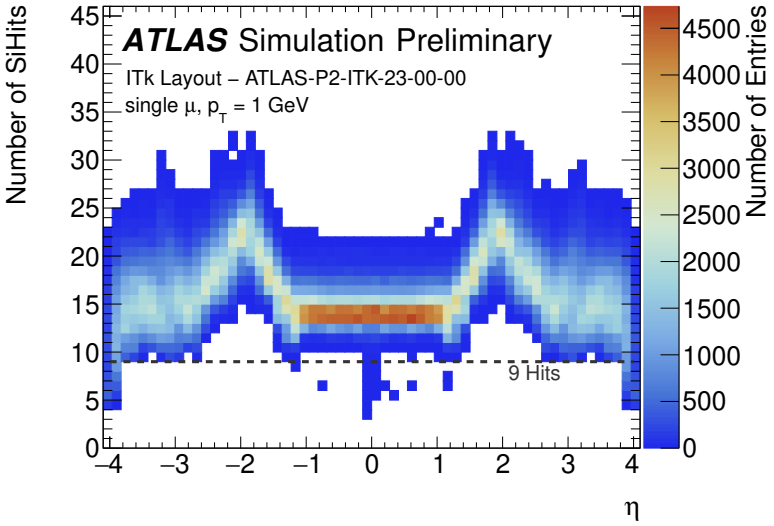

Figure 5.6: Number of silicon hits in the ITk as a function of η for muons with $p_{\mathrm{T}} = 1\,\mathrm{GeV}$ coming from the luminous region. Taken from Reference [200].

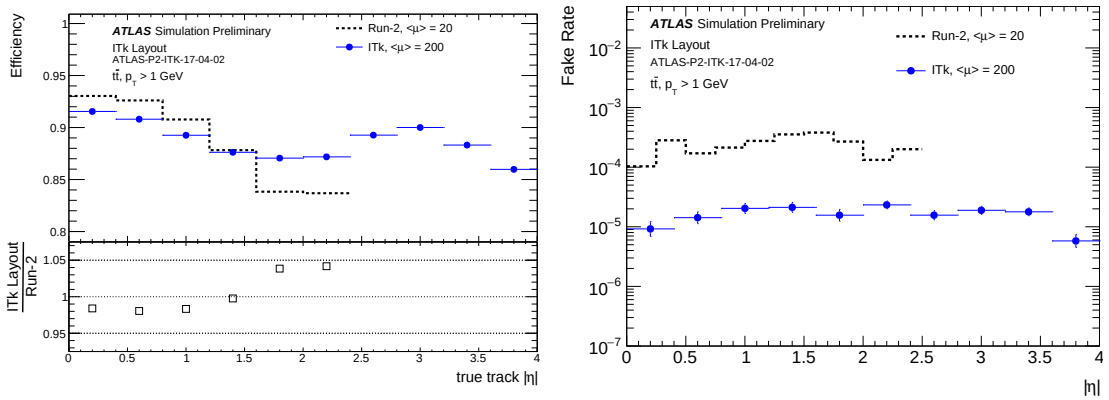

(a) (b)

Figure 5.7: Comparison of the track reconstruction efficiency (a) and fake rate (b) as a function of $|\eta|$ for hard-scatter tracks with a p_{T} of 1 GeV in simulated $t\bar{t}$ events. The Run 2 reconstruction performance with $\langle\mu\rangle = 20$ is used as comparison. Taken from Reference [206].

to Run 2, discussed in Section 3.1. This means that all the requirements on the ITk in terms of performance are fulfilled.

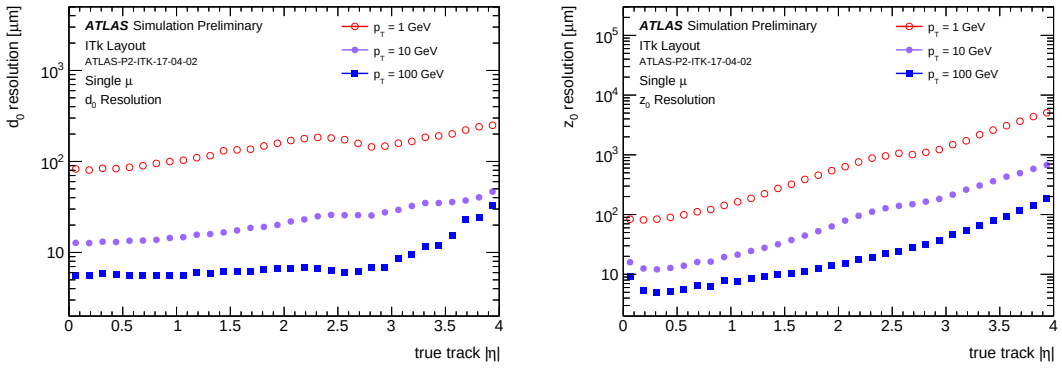

(a) (b)

Figure 5.8: Transverse (a) and longitudinal (b) impact parameter resolutions as a function of $|\eta|$ for single muons of 1, 10 and 100 GeV of p_{T}. Taken from Reference [206].

Overall the ITk has a pixel sensor surface of 12.83 m^2 [200], making it the largest Pixel detector at the HL-LHC. Due to the higher instantaneous luminosity and pile-up, also the TDAQ and readout systems need to be upgraded as discussed in the next sections.

5.3 High-Luminosity Trigger and Data Acquisition System

An upgrade of the ATLAS TDAQ system is required to increase the L0 trigger rate. Without such an increase, trigger thresholds would be increased, leading to a loss of acceptance in many SM and BSM data analyses. This is illustrated in Figure 5.9 for the $E_{\mathrm{T}}^{\mathrm{miss}}$-trigger used in Chapter 4.

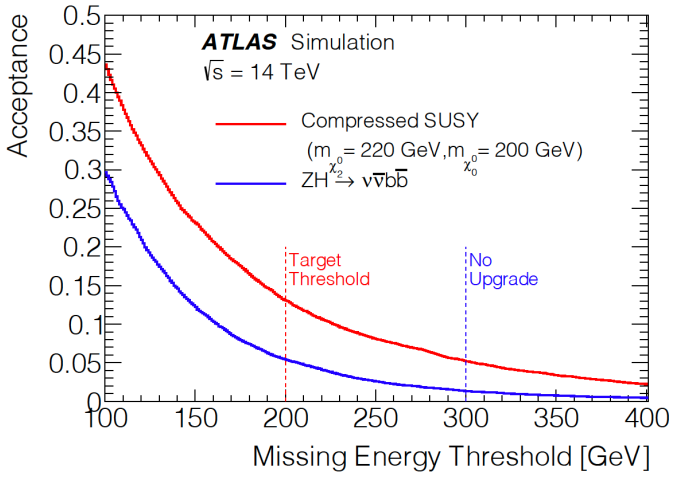

Figure 5.9: Integrated acceptance as a function of the $E_{\mathrm{T}}^{\mathrm{miss}}$ threshold for a compressed SUSY and a SM scenario. Not upgrading the TDAQ system would lead to an increased threshold of 300 GeV compared to 200 GeV in Run 2 [207]. Taken from Reference [207].

The HL ATLAS TDAQ system [207], schematically depicted in Figure 5.10, features an increased L0 trigger rate of 1 MHz (up from 100 kHz). Similarly to Run 2, part of the MS and calorimeter data is used to take the first trigger decision. The Central Trigger Processor (CTP) transmits the L0 trigger to the ITk, the calorimeters and the MS by the Front-End Link Exchange (FELIX, [208]) system. FELIX then receives the event data from the detectors and forwards the data for further processing. A total of 10 kHz ($\sim$ 1 kHz currently) of events are selected by the Event Filter and are saved to disk.

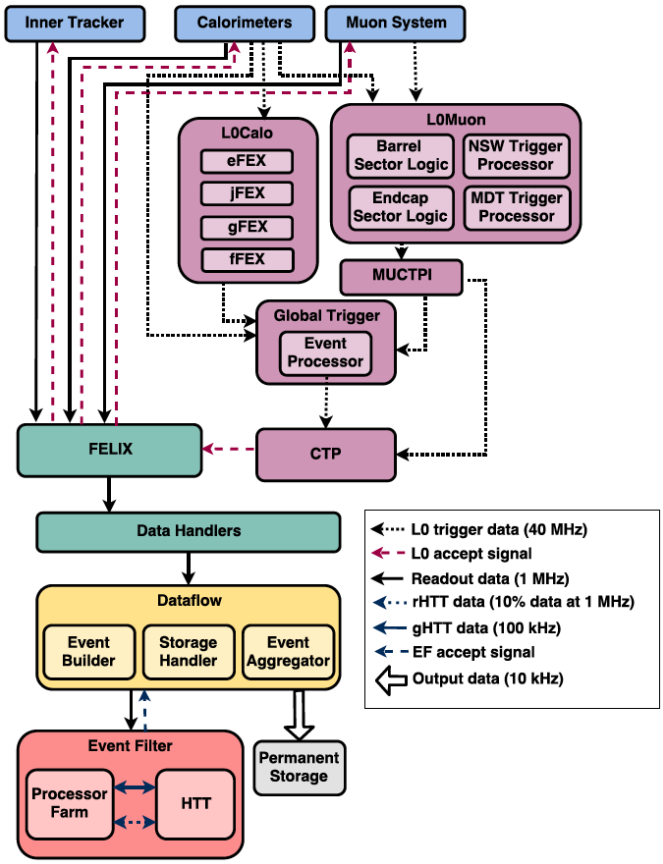

Figure 5.10: Schematic representation of the baseline HL ATLAS TDAQ system. Taken from Reference [207].

The increased L0 trigger rate, together with a larger number of readout channels and higher channel occupancies, leads to a larger amount of bandwidth needed to read out the Pixel detector. It is increased by a factor of more than one hundred in the ITk Pixel compared to the Run 2 pixel detector. The readout system therefore needs to be completely replaced as well in LS2.

5.4 The Inner Tracker Pixel Data Transmission System

Table 5.3 lists the number of pixel modules in the three subsystems, their types and the required number of *uplinks* and *downlinks* for a module and in total. The uplinks are carrying the FE data out of the detector to the FELIX back-end, while the downlinks transmit the TTC information from FELIX to the FEs. The number of links per pixel

module depends on the location: low-r and high-η regions such as the IS and the forward OE rings feature up to four uplinks per module. The ITk Pixel detector features a total of 17'812 uplinks and 8'372 downlinks.

Subsystem	**Module type**	**Modules**	**Links/module** Up	Down	**Uplinks**	**Downlinks**
IS barrel	singlet	288	4	$\frac{1}{3}$	1152	96
	quads	240	2	1	480	240
IS end-caps	singlet	900	2–3	$\frac{1}{3}$	2340	300
	quads	920	4	1	3680	920
OB	quads	4472	1–2	1	5432	4472
OE	quads	2344	1–4	1	4728	2344
Total	–	**9164**	–	–	**17812**	**8372**

Table 5.3: The number of modules and the resulting uplinks and downlinks for the various ITk Pixel subsystems. The number of uplinks per module can differ depending on the layer in which the module resides. Three single modules receive a common downlink which is why they have 1/3 downlink per module.

The readout system has to fulfil the following set of requirements to not limit the full potential of the ITk:

- Reliable transmission of the uplinks and downlinks between the FEs and FELIX at the required bandwidths.
- Small contribution to material budget to limit multiple scattering deteriorating the performance of the ATLAS detector.
- Power consumption of less than 10 kW to comply with the ITk cooling budget.
- Radiation tolerant readout components for 4000 fb^{-1} (2000 fb^{-1} for IS).
- Follow ITk Grounding and Shielding (G&S) policy as described in Reference [35].

The RD53 FEs are configured and triggered via 160 Mb/s electrical downlink signals, while they send out their hit data over 1.28 Gb/s lines. These electrical signals are transmitted using low-voltage differential signalling (LVDS, [209]). The two resulting outputs feature currents flowing in opposite directions, leading to a cancellation of the EM fields and therefore a smaller susceptibility to environmental noise. The uplink data is furthermore encoded using the 64b/66b Aurora protocol [35, 210]. The up- and downlinks and also other electrical lines such as power and monitoring lines go along the flexible module Printed Circuit Board (PCB) and reach the Patch Panel 0 (PP0) PCB that is mounted on the local support. The PP0 is the single point of contact for the electrical lines from the modules connected to the PP0 to outside of ATLAS.

The FELIX system is located outside of the ATLAS detector in the USA15 service cavern. The links between the FELIX back-end and the detector have lengths of ~ 100 m, which is too long for data transmission over copper cables due to the attenuation of the electrical signals along them. This is why the electrical signals coming from the FEs

are converted to optical ones and are transmitted over optical fibres to FELIX (and vice versa). Fibres feature a much smaller attenuation of the signals and have higher bandwidth capabilities. The smaller cable cross-section and material budget compared to copper cables are additional advantages. The conversion between electrical and optical signals takes place inside of ATLAS. For the ITk Pixel detector, this task is performed by the Optosystem.

The Optosystem design evolved drastically since the ITk Pixel Technical Design Report (see Reference [35]), as the overall layout of the Pixel data transmission system changed. The original concept pursued the *active cable* idea [35], in which electrical signals at up to 5.12 Gb/s would be transmitted over AWG30 (American Wire Gauge) twinaxial cables (twinax) over distances of ~ 6 m to then be converted to optical signals by the Optosystem just outside of the ITk. The Aggregator ASIC was envisaged to be located on the PP0 and would merge (or *aggregate*) up to four 1.28 Gb/s electrical uplinks into one 5.12 Gb/s high-speed link, which would then be transmitted over the twinax cable. The aggregation of electrical signals reduces the number of cables and therefore the material budget contribution of the data transmission system. At the other end, the Gigabit Cable Receiver 1 (GBCR1, [211, 212]) was planned to receive and recover the high-speed uplink signals. The latter would then be converted to optical signals by the Optosystem that also was planned to provide the GBCR1 and Aggregator chips with power.

The active cable concept was dropped at the end of 2018 since the Aggregator development was delayed and no longer fitted the schedule of the ITk. Instead of the Aggregator, the low-power Gigabit Transceiver (lpGBT, [213, 214]) is used to aggregate multiple low-speed links into high-speed links and fan-out one high-speed downlink into multiple low-speed downlinks. The Versatile Link$^+$ Transceiver (VTRx+, [215]) then performs the opto-electrical (and vice versa) conversion.

5.5 Key Components of the Optosystem

This section describes in detail the VTRx+ and lpGBT components of the Optosystem, which are crucial for the following discussion of the conceptual design and technical implementation of the Optosystem and the tests of the latter.

Versatile Link$^+$ Transceiver

The Versatile Link$^+$ (VL+, [216]) is a bi-directional optical data link system designed to deliver high-throughput and high radiation resistance for operation in HL-LHC experiments. As shown in Figure 5.11, it consists of three parts: an on-detector transceiver (VTRx+), passive optical components and commercial off-the-shelf back-end transmitters and receivers.

The VL+ operates uplinks at up to 10.24 Gb/s and downlinks at 2.56 Gb/s as shown in Table 5.4, which also lists environmental specifications. The extended grade on-detector components are used due to their superior tolerance to non-ionising energy loss (NIEL). The VL+ furthermore is specified to resist a total ionising dose (TID) of 1 MGy (1 Gy = J/kg).

The VTRx+ module [217] has a size of $20 \times 10\,\text{mm}^2$ and consists of four parts, re-

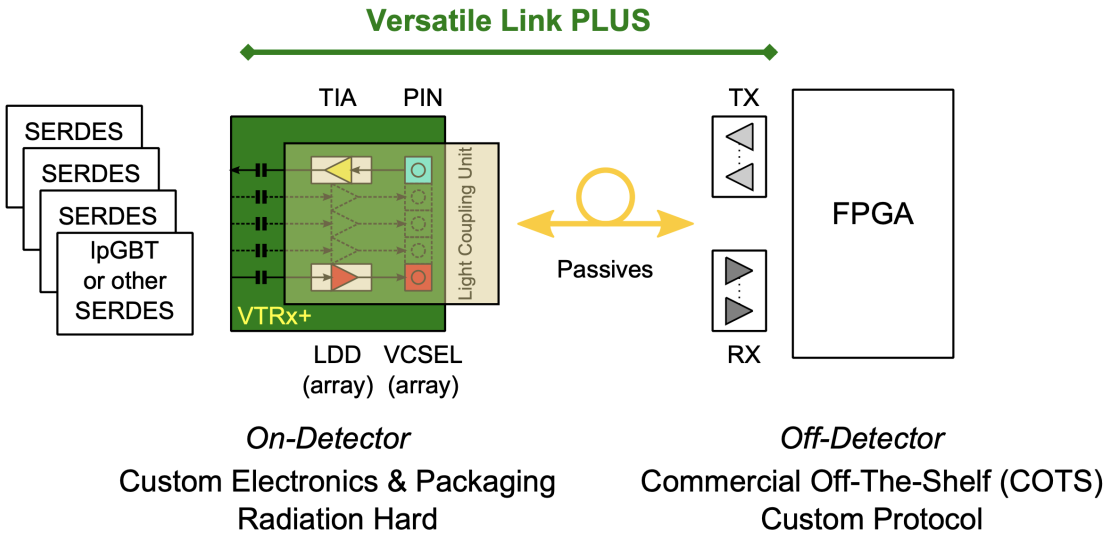

Figure 5.11: Simplified diagram of the VL+ architecture. Taken from Reference [215].

Parameter	Min.	Typ.	Max.	Unit
Uplink bit rate			10.24	Gb/s
Downlink bit rate			2.56	Gb/s
BER			10^{-12}	
Link length		50	150	m
TID tolerance			1	MGy
NIEL tolerance			10^{15}	neutrons/cm^2
Hadron tolerance			10^{15}	hadrons/cm^2
VTRx+ temperature	-35		60	°C
Passives in-detector temperature	-35		60	°C

Table 5.4: Specifications of the extended grade VL+ system [216].

sponsible either for the transmission (Tx) or reception (Rx) of optical signals that are interconnected on a PCB:

- The p-i-n doped diode (PIN diode) generates an electrical pulse from the incoming Rx optical signal.
- The GBTIA [218] amplifies the electrical Rx signal from the PIN diode.
- The LDQ10 laser diode driver [219] generates the currents needed for the vertical-cavity surface-emitting lasers (VCSELs) in the optical signal Tx. The bias and modulation currents as well as pre-emphasis can be configured over an I2C [220] interface.
- An array of four VCSELs transform the LDQ10 currents into an optical signal.

The VL+ operates at wavelengths of 850 nm. Table 5.5 presents the optical signal power budget of the complete VL+ chain. In the uplink direction, the VTRx+ Tx (VTx+) is specified to have an optical modulation amplitude (OMA) of at least −5.2 dBm. As the back-end Rx is sensitive to optical signals of at least −12.5 dBm (Rx sensitivity), an overall power budget of at least 7.3 dB is available in the uplink direction. Adding the effects of attenuation in 100 m of fibres, radiation damage to fibres, optical signal insertion loss and other effects, the remaining margin of the optical data transmission amounts to at least 0.9 dB. Similar considerations result in a margin of > 1.975 dB in the downlink direction. The power budget of the VL+ chain and also some VTRx+ specifications are verified later in Section 5.8.

Property	**Uplink** **VTx+ → Rx (10 Gb/s)**	**Downlink** **Tx → VRx+ (2.5 Gb/s)**
Tx OMA [dBm]	> -5.2	> -1.6
Rx sensitivity [dBm]	< -12.5	< 13.1
Power budget [dB]	> 7.3	> 11.5
Margin [dB]	> 0.9	> 1.975

Table 5.5: Power budget of the complete VL+ extended grade chain between the on-detector transmitter and receiver (VTx+ and VRx+) and the corresponding back-end components (Rx and Tx). Adapted from Reference [216].

Low-power Gigabit Transceiver

The lpGBT [213,214] is a multi-purpose ASIC developed for aggregation and monitoring in high-radiation environments such as the HL-LHC detectors. The lpGBT needs to be operated together with a back-end firmware running on a Field-Programmable Gate Array (FPGA). This is the lpGBT-FPGA core [221, 222] that encodes (decodes) the downlink (uplink) information to (from) the lpGBT. The package of the lpGBT ASIC has a size of $9 \times 9\,\mathrm{mm}^2$ with a power consumption of ~ 400 mW. It can either be operated with an external reference clock or by the usage of its clock data recovery (CDR) circuit, which uses the incoming downlink to synchronise its internal oscillator to the clock embedded in the data.

The lpGBT expects a 2.56 Gb/s incoming downlink, which is then fanned out to individual links of either 80, 160 or 320 Mb/s. Figure 5.12 shows the structure of one downlink frame, which is transmitted at a frequency of 40 MHz and encoded by the lpGBT-FPGA core. Only half of the bandwidth can be used to accommodate the low-speed link data (D field), while the other half transmits the internal control (IC) data to configure the lpGBT, the external control (EC) data, that can be used to configure other lpGBTs, and the Forward Error Correction bits (FEC field). The FEC implementation in the lpGBT is based on Reed-Solomon Codes [214, 223] and allows for detection and correction of up to 12 consecutive bit errors in the transmitted data. Before the transmission, the downlink frame is furthermore interleaved (mingling of bits in a frame in a defined order) and scrambled (replacement of bits depending on their content) to make it DC-balanced (similar amount of '1's and '0's).

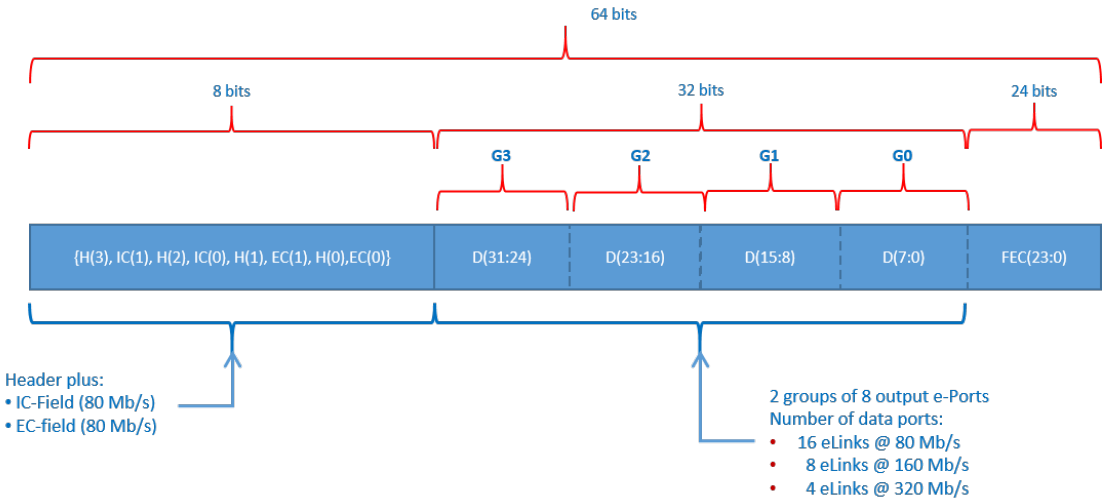

Figure 5.12: Structure of the downlink frame of the lpGBT. Taken from Reference [214].

In the uplink direction, the lpGBT can either be operated at 5.12 or 10.24 Gb/s, aggregating input e-links with speeds between 0.16 and 1.28 Gb/s. The frame structure is similar to the one of the downlink, but has a total of 128 (5.12 Gb/s) or 256 bits (10.24 Gb/s) due to larger D and FEC fields. There are two possible FEC encoding schemes: FEC5 and FEC12, where 5 and 12 (10 and 24) consecutive bit errors can be corrected in the 5.12 (10.24) Gb/s mode. The uplink again features the IC and EC fields, which contain the lpGBT responses to the corresponding downlink IC and EC commands. The uplink is as well scrambled and interleaved by the lpGBT.

Additional to the aggregation functionality, the lpGBT as well features General Purpose Input Output (GPIO) pins, I2C masters, analogue-to-digital converters (ADC) and clock outputs that can be used to configure or monitor other components.

5.6 Conceptual Design of the Optosystem

The Optosystem could either be part of the PP0s, with low-speed electrical link (e-link) lengths of only ~ 1 m, or in the same location as in the active cable concept just outside of the ITk, with e-links of ~ 6 m until there. The first option is similar to the strat-

egy that the CMS experiment is pursuing for its HL tracker (see Reference [224]). This data transmission layout is favourable since the material budget of the data links can be reduced and the assembly is simpler. Furthermore, it is easier to ensure sufficient data transmission quality since the e-links are short and suitable radiation-tolerant optical fibres are available [225]. The radiation tolerance of the VTRx+ is however not sufficiently high to guarantee reliable operation over the whole HL-LHC lifetime. The VTRx+ is specified for a NIEL of up to 3×10^{15} 1 MeV n_{eq}/cm^2, which is not enough to cover the expected NIEL at the PP0 locations of up to 2.5×10^{15} 1 MeV n_{eq}/cm^2 [226] with appropriate safety factors added to account for the uncertainty of the radiation simulation. Due to the structure of the ITk, individual components on the PP0s can not be accessed and replaced after the ITk commissioning. The Optosystem components therefore are put outside of the ITk, onto the ITk end-plates at $|z| = 3500$ mm and $r = 1450$–2450 mm, as depicted on Figure 5.13. The electrical signals from the RD53 FEs are transmitted over ~ 6 m long AWG34 twinax cables (smaller diameter than AWG30) from the PP0 to the Optosystem (and vice versa). The e-links have speeds of 1.28 and 0.16 Gb/s in the uplink and downlink direction, respectively.

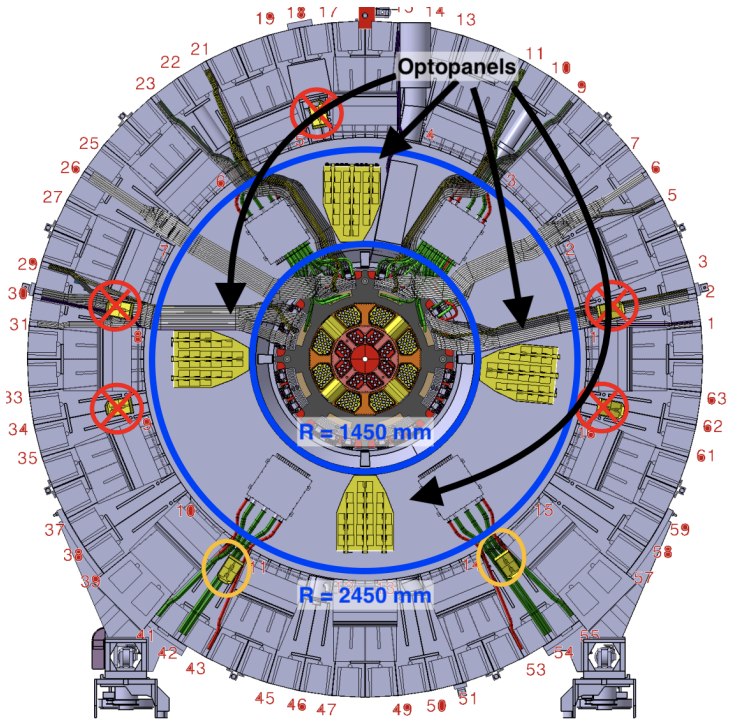

Figure 5.13: The Optosystem is located on the ITk end-plates ($|z| = 3500$ mm) on both sides of ATLAS. It is distributed into four *Optopanels*. Taken and adapted from Reference [227].

The Optosystem has to fulfil the following requirements to ensure the proper functionality of the complete data transmission chain:

- Aggregation and opto-electrical conversion of all up- and downlinks.
- Bit error rate (ratio of wrongly transmitted and total transmitted bits) of BER $< 10^{-12}$ over the complete data transmission chain, including the Optosystem.

- Tolerance to the expected radiation levels at the ITk end-plates of 50 kGy and 7×10^{14} 1 MeV n_{eq}/cm^2 [228], with no safety factor applied yet.
- Cooling and efficient powering of the Optosystem components and also monitoring of the latter to ensure reliable operation
- Ease of access to allow replacement of components.
- Compact design to fit in available volume on the ITk end-plate.

The developed concept of the Optosystem is schematically depicted in Figure 5.14. The AWG34 twinax cables are directly connecting the PP0 with the Cable Termination Board PCBs, each of which is connected to a single *Optoboard*. A total of up to 24 1.28 Gb/s uplinks and eight 160 Mb/s downlinks can be handled by each Optoboard. Because of the large attenuation and added jitter of the electrical signals when transmitted over ~ 6 m long twinax cables, a modified version of the previously discussed GBCR1 is added to the Optosystem: the GBCR2 ASIC [212] (from now referred to as *GBCR*) equalises the uplink signals and retimes them with a 1.28 GHz clock supplied by the lpGBT. The GBCR, furthermore, adds pre-emphasis to the downlink signals. In this way the jitter and attenuation requirements of the electrical transmission can be fulfilled. A total of four GBCR and lpGBT ASICs are on each Optoboard, where the lpGBTs are responsible for the aggregation of the electrical uplinks and the fan-out of the high-speed downlink. The lpGBT is furthermore used to monitor and to control and configure all components of the Optosystem, including the VTRx+ module that is responsible for the opto-electrical conversion of the aggregated signals and is mounted on the Optoboard. Optical fibres connect the Optosystem to FELIX, completing the data transmission chain.

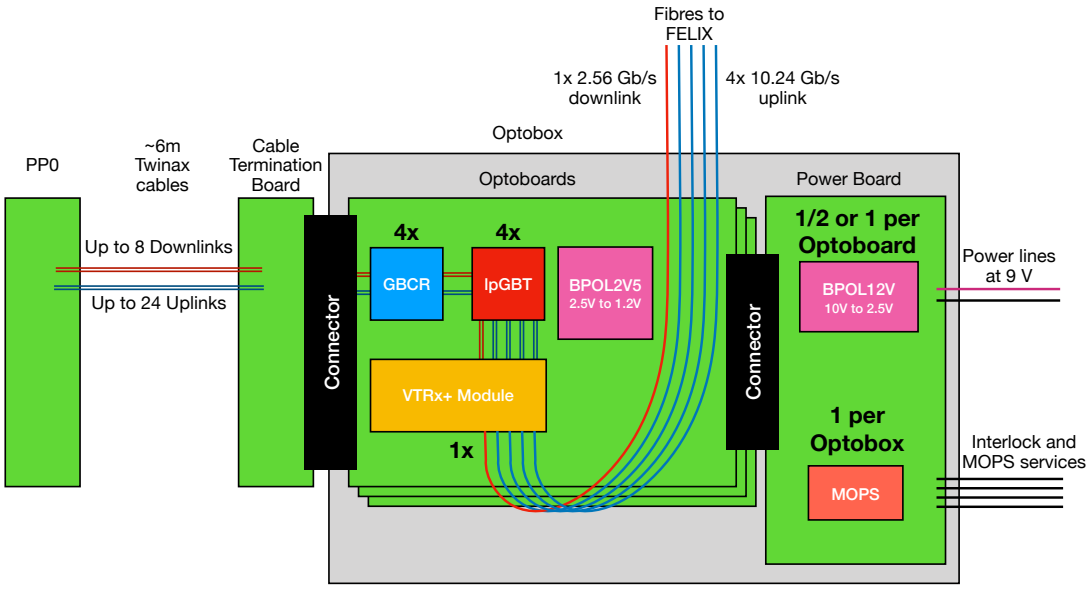

Figure 5.14: Conceptual layout of the Optosystem as part of the ITk Pixel data transmission system. Blue lines indicate uplinks, while red lines show downlinks. All electrical lines are LVDS (two lines), while the curved lines indicate fibres.

Opto Power Supplies located in the ATLAS service caverns power the Optosystem with

voltages of $\sim 9\,\mathrm{V}$ that are locally converted in two stages to 2.5 and 1.2 V using the bPOL12V [229] and bPOL2V5 [230] DCDC converters. Each Optoboard features a bPOL2V5, while the bPOL12V are located on a separate *Power Board* PCB servicing multiple Optoboards. The powering scheme of the Optosystem ensures that modules on a different SP chain are not serviced by Optoboards powered by the same bPOL12V DCDC converter.

The Optosystem features a dedicated cooling system to keep the active components at ambient temperature. Component and ambient temperatures as well as DCDC output voltages are monitored by the lpGBT and Monitoring of Pixel System (MOPS, [231]) ASICs and the Optosystem is integrated into the ATLAS interlock system [232] for rapid shutdown in case of powering or cooling failures.

Optoboards and the Power Board are located inside of *Optoboxes* that can be easily replaced. The Optoboxes are attached to *Optopanels* that are mounted on the ITk end-plate.

5.7 Technical Design of the Optosystem

The technical implementation of the Optosystem concept is depicted in Figure 5.15, following the conceptual design presented in Section 5.6. The following text discusses the various components of this technical design in detail.

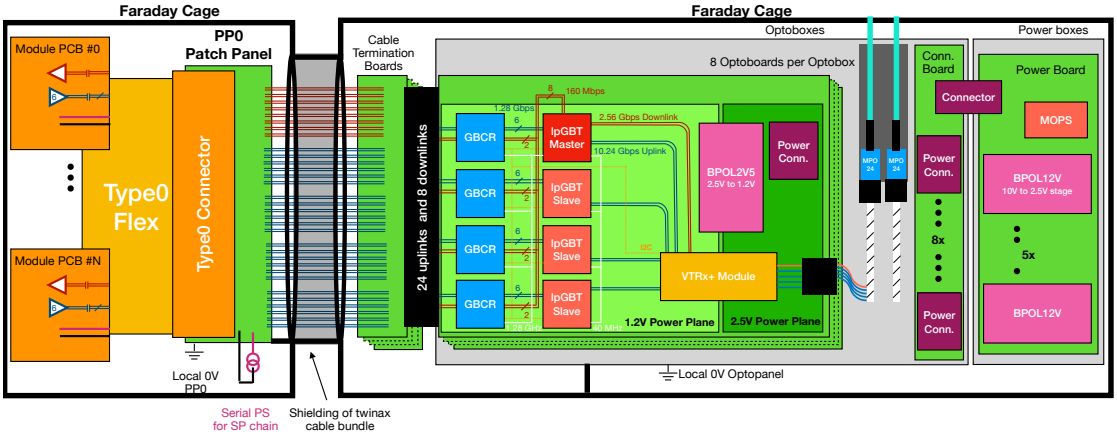

Figure 5.15: Schematic layout of the ITk Pixel readout system focusing on the Optosystem. Red lines indicate downlinks, blue lines show uplinks and white and yellow lines depict internal clock and I2C lines.

Cable Termination Board

The twinax cables bundles of up to 24 uplinks and eight downlinks are soldered onto the Cable Termination Board, which is linked to a single Optoboard by a connector. The twinax bundles are wrapped by a shield to extend the Faraday cage of the ITk to the

Optosystem.

Optoboard

The Optoboard is the key unit of the Optosystem and takes care of the electrical signal recovery, aggregation and optical-electrical (and vice versa) conversion of the 32 e-links from the cable termination board. Either one or two Optoboards are needed to service the modules of each SP chain. Figure 5.16 shows a CAD view and picture of the Optoboard V1 prototype with all its components.

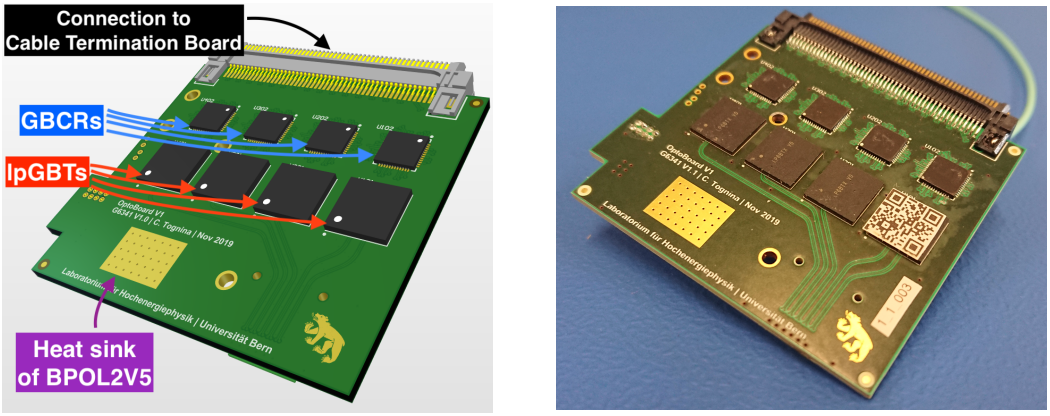

(a) (b)

Figure 5.16: CAD view (a) and picture (b) of the back side of the Optoboard V1 prototype, indicating the relevant visible parts.

Each of the four GBCRs handles six uplinks and two downlinks. The GBCRs are operated in retiming mode, in which they use 1.28 GHz reference clocks. Each GBCR has an associated lpGBT that aggregates the six 1.28 Gb/s uplinks into a single high-speed signal. The lpGBTs are operated in the 10.24 Gb/s mode with FEC12, able to correct 24 consecutive bits. Three lpGBTs are operated as transmitters, while the lpGBT *master* is a transceiver that additionally takes care of the fan-out of the 2.56 Gb/s downlink signal into the 160 Mb/s e-links. The lpGBT master uses the high-speed downlink to recover a clock from the incoming data (CDR), which it synchronises with its internal oscillator. This synchronisation ensures the correct interpretation of the received downlink frames. The internal clock is then also used to generate 1.28 GHz clocks for the retiming of the GBCRs and to give a 40 MHz reference clock to the other three lpGBTs. The high-speed downlink, furthermore, contains commands to configure the lpGBT master (IC field). By using one of the I2C masters of the lpGBT master, the configuration of the other lpGBTs, GBCRs and the VTRx+ is possible. The lpGBT master also embeds the response of the communication into its high-speed uplink.

Figure 5.17 shows how the high-speed and low-speed electrical lines are routed on the Optoboard V1 prototype. The high-speed downlink and uplinks are transmitted between the lpGBT and VTRx+ module over electrical connections (*traces*) with lengths of 24.5–47.0 mm. The Optoboard design aims at minimising these trace lengths to limit the potential of these signals to pick up noise and being attenuated. The trace lengths of the two lines making up an high-speed LVDS signal furthermore are matched in length to 0.04 mm and only take turns with large radii to limit the signal disturbance to the

minimum.

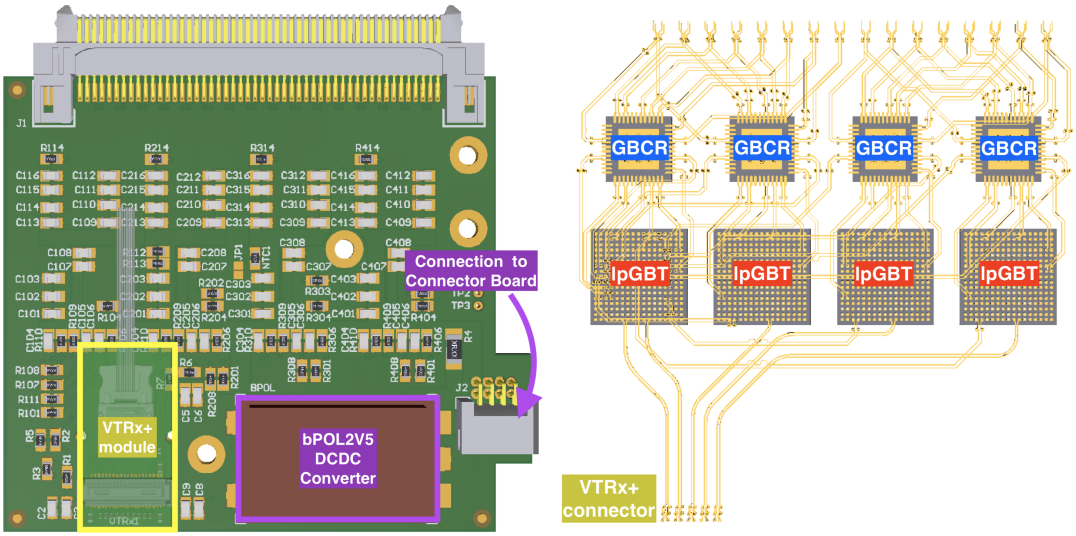

(a) (b)

Figure 5.17: CAD view of the front side of the Optoboard V1 indicating the relevant visible parts (a) and only the uplink and downlink electrical lines (b). The lines between the VTRx+ connector and the lpGBTs are high-speed (10.24 and 2.56 Gb/s), while the ones between the lpGBTs, GBCRs and to the top of the Optoboard are low-speed e-links (1.28 and 0.16 Gb/s).

The VTRx+ module takes care of the opto-electrical (and vice versa) conversion of these high-speed signals. The VCSELs emit their light into four of the 12 fibres of the VTRx+ pigtail. The 2.5 V supply voltage of the VCSELs are directly received from the Power Board [233, 234], while the lpGBT, GBCR and VTRx+ 1.2 V supply voltages are generated by the bPOL2V5 that is located on a small separate PCB mounted on the Optoboard. The power consumption of a fully populated Optoboard is 3.5 W, assuming an efficiency of the bPOL2V5 of 70%. This is equivalent to a current of 1.4 A.

Optobox

The Optoboards are tightly screwed to an 'L'-shaped aluminium profile that makes thermal contact with the Optobox and connects the Optoboards to the common ground. A total of up to eight Optoboards are contained in an Optobox and share a common Power Board and a *Connector Board* PCB. Figure 5.18 depicts the Optobox V1 prototype with the connectors to the Cable Termination Boards and the fibre connectors.

Power Board

The Power Board features up to five bPOL12V DCDC converters that receive a voltage of $\sim$ 10 V from the power supplies and transform it to 2.5 V. Since the bPOL12V features a maximum output current of 4 A [229], each bPOL12V can supply a maximum of two Optoboards with power. The Power Board, furthermore, features the MOPS for the monitoring of the bPOL12V output voltages and negative temperature coefficient (NTC) thermistors located on the Optoboards. Two NTCs on the Power Board and the

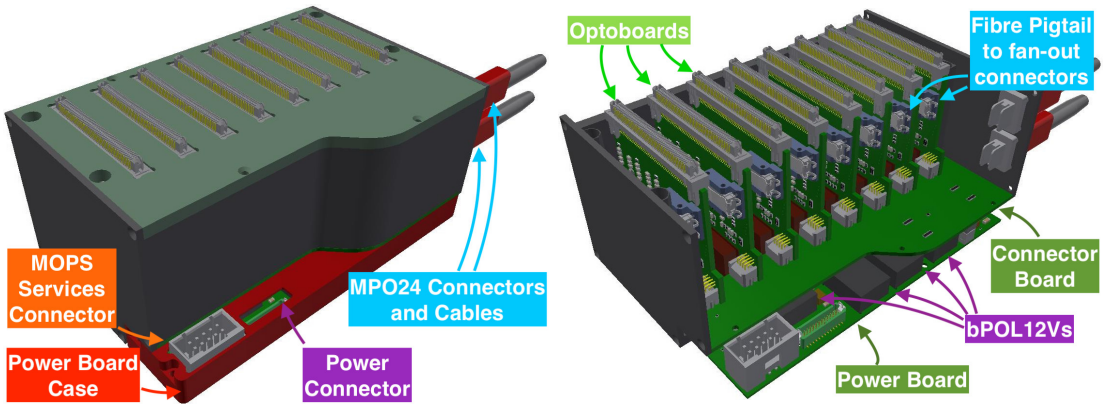

(a) (b)

Figure 5.18: CAD model of the Optobox V1 prototype when closed (a) and open (b). No fibres and service cables are shown.

Connector Board are directly linked to the interlock system, which can disable the Opto Power Supplies in case of high temperatures inside an Optobox. Figure 5.19 shows the schematic path of the power, monitoring and interlock lines inside an Optobox. The Power Board is within an aluminium case to separate it from the connecting cables. During installation, the Power Board and its case are screwed onto the Optopanel and then the Optobox is attached on top of it.

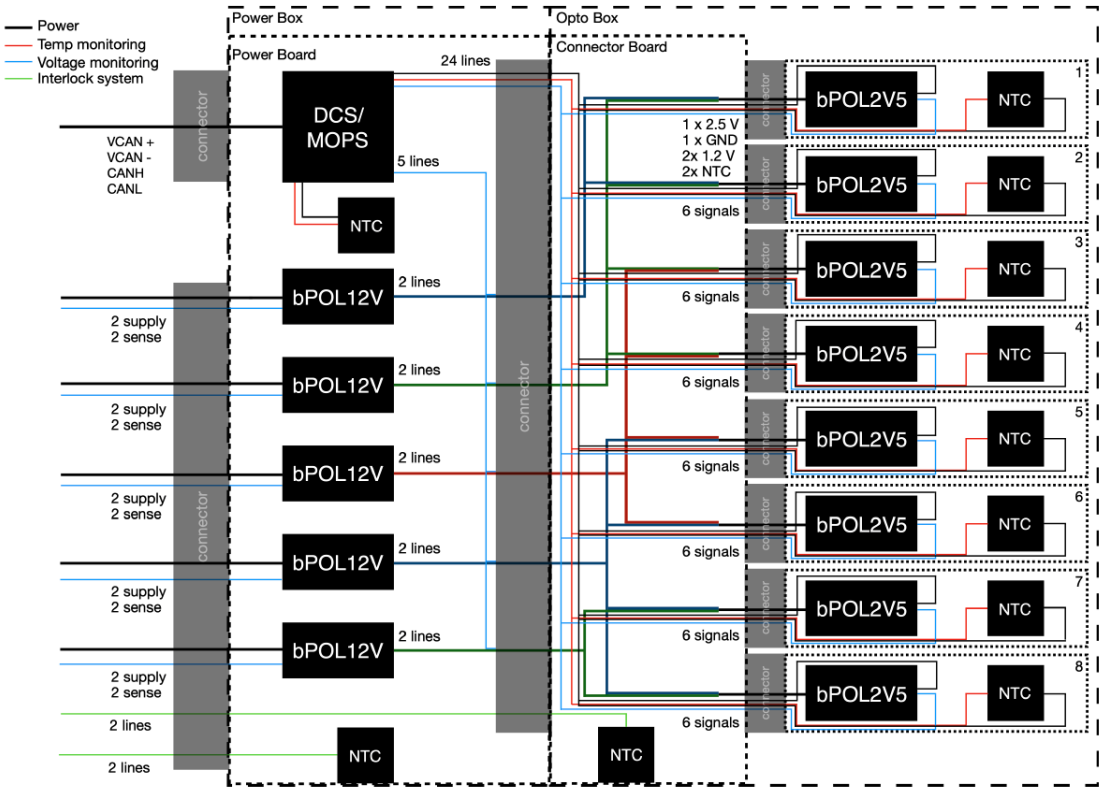

Figure 5.19: Path of the power, monitoring and interlock lines inside the Optosystem.

Connector Board

The Connector Board [235] mates the Optoboards with the Power Board. Since either one or two Optoboards are needed to service an SP chain and Optoboards of different SP chains are not allowed to be powered together, one or two Optoboards are powered by a bPOL12V. The Connector Board takes care of the correct mapping of the five bPOL12V to the eight Optoboards to account for this, depending on the Pixel SP chain modularities.

Fibre Cables

The components of the optical part of the data transmission are shown in Figure 5.20. Depending on the Pixel subsystem modularity, the used fibres of either four, six or eight VTRx+ pigtails are collected by one optical fan-out into Multi-fibre Push On (MPO) fibre cables with a total of 24 fibres (MPO24). One Optobox includes up to two such fibre fan-outs that are connected to MPO24 connectors at a side wall of the Optobox (see Figure 5.18). On the outside, trunk cables with 144 fibres are used to group the optical signals from six MPO24 connectors and guide the optical signals out of ATLAS. Before being connected to the FELIX system, the optical links are sorted into uplinks and downlinks by shuffle boxes.

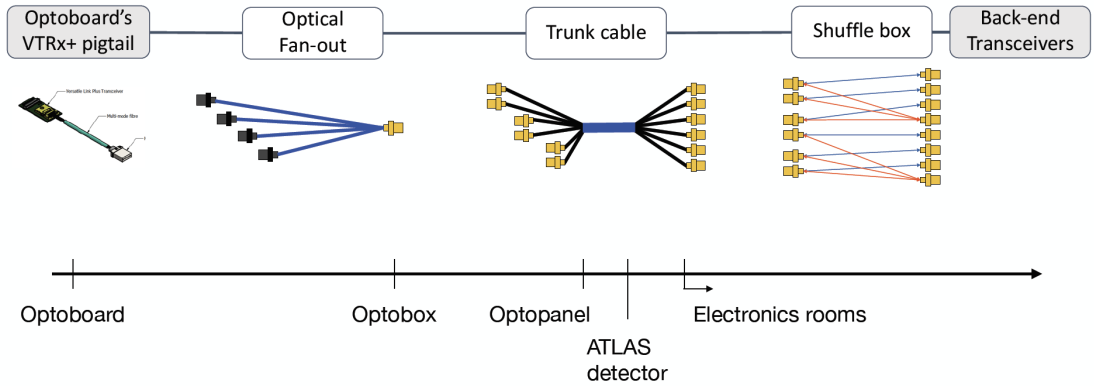

Figure 5.20: The elements of the optical data transmission path. Taken from Reference [236].

Optopanel

The Optosystem is spread around eight locations on the ITk end-plates as previously shown in Figure 5.13. Each location features the same *Optopanel*, an aluminium Faraday cage to which all Power Boards and Optoboxes are attached. In order to fit all the required 224 Optoboxes, they are arranged in an trapezoidal-like manner shown in Figure 5.21. The Optoboxes are grouped in rows in a staggered configuration to profit of the fact that the total cross-section of the twinax cables reduces with r, while the one of the power, monitoring and fibre cables increases. At the large-r end, the Optopanels feature a patch panel. The powering, MOPS and interlock cables are connected to this patch panel, while the optical trunk cables pass through the patch panel openings. The Optopanel base plate includes pipes that are used to cool the Optosystem components. There is only a single ground connection to the ITk reference ground to prevent ground

loops, minimising electronic noise and interference. The Optopanel is part of the ITk Faraday cage by the usage of conductive shielding material around the twinax cable bundles and an isolator around the Optopanels and between the ITk end-plate and the Optosystem.

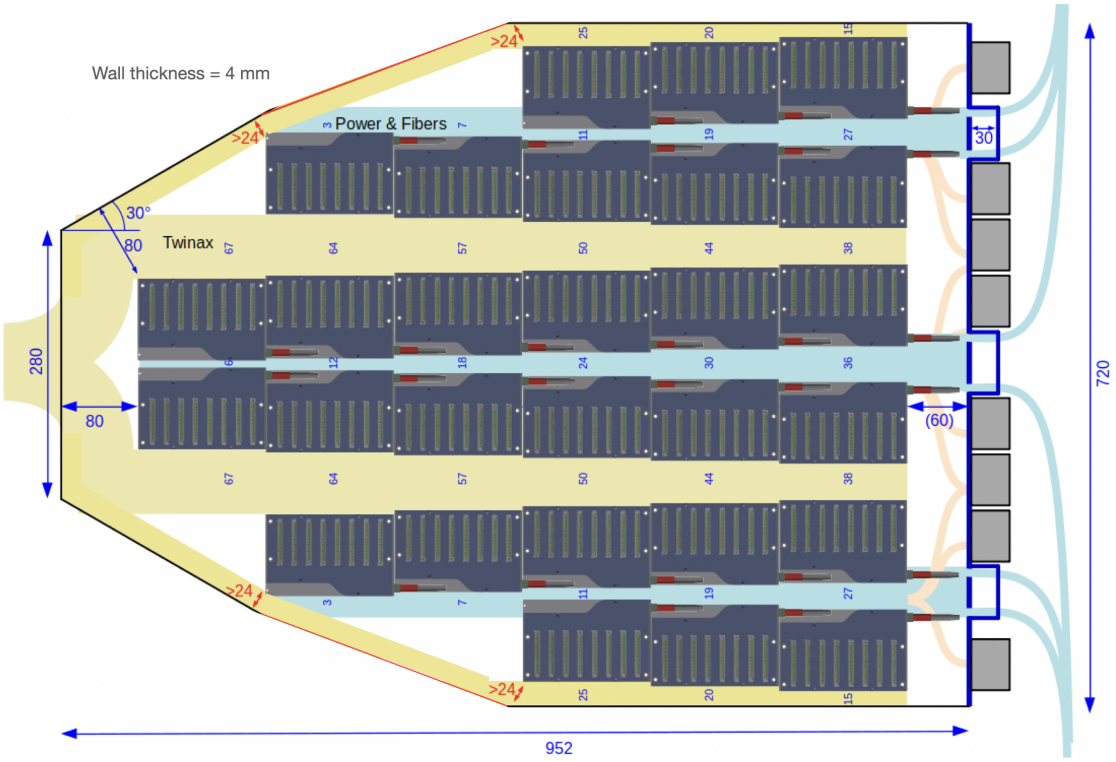

Figure 5.21: Top view of one Optopanel with the yellow areas indicating the routing of twinax cables and the blue areas showing space used for the optical, MOPS, powering and interlock cables.

This concludes the discussion of the technical design of the Optosystem. The compact Optoboard as the base unit and the collection of monitoring and powering responsibilities into the Power Board lead to a space-efficient system. The configurable connection scheme between the Optoboards and the Power Board deals with the different PP0 modularities of the IS, OB and OE, minimising the number of DCDC converters and powering cables needed. The usage of the GBCR ensures reliable electrical transmission. Thanks to the modularity of the Optosystem, single Optoboxes can be replaced in case of component failures. All requirements on the Optosystem listed in Section 5.6 are therefore fulfilled in this technical design.

5.8 Versatile Link$^+$ Transceiver Test Setup Development and Results

The functionality of VTRx+ module prototypes was validated through measurements of the BER in an optical link test setup. As depicted in Figure 5.22, this system consisted of the VTRx+ mounted on a custom-made carrier board, a commercial enhanced Small

Form-factor Pluggable (SFP+) transceiver simulating the VL+ back-end transceiver, a variable optical attenuator and the KC705 FPGA board [237]. The VTRx+ carrier board is plugged to the FPGA board using the FPGA Mezzanine Card High Pin Count (FMC-HPC) interface. The VTRx+ is powered by the FPGA board using regulators on the carrier board.

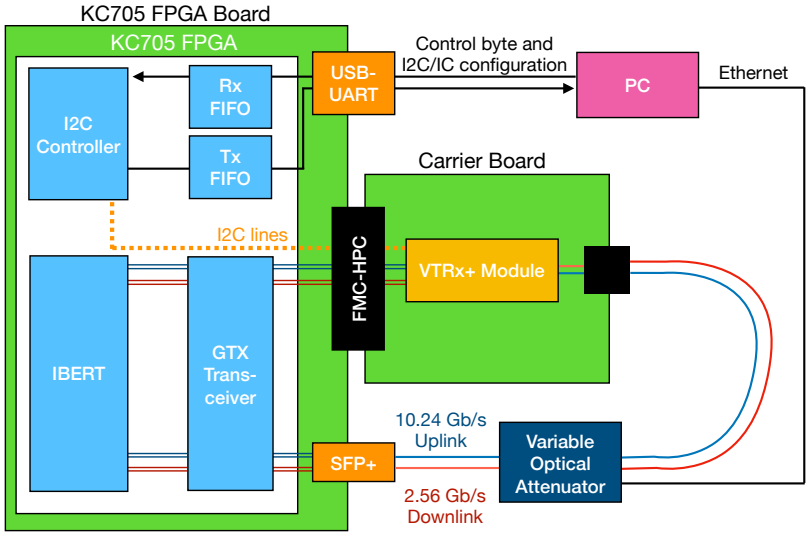

(a)

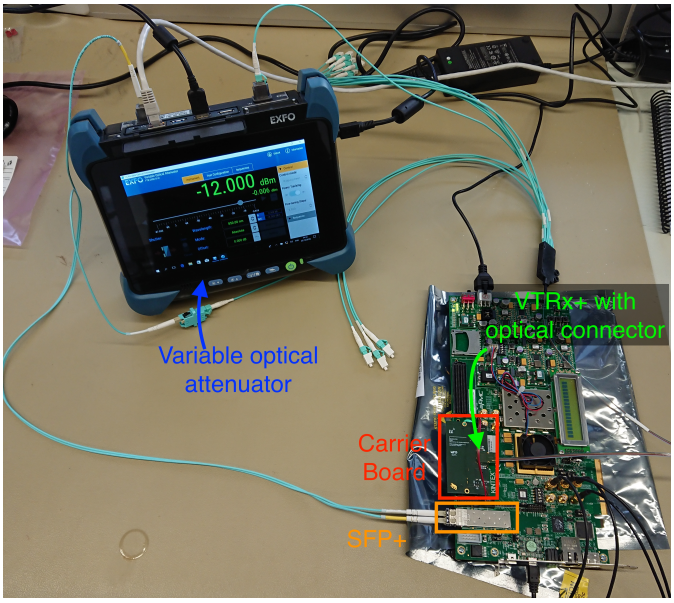

(b)

Figure 5.22: Schematic layout (a) and picture (b) of the VTRx+ test setup. The various components of the firmware running in the FPGA are depicted in light blue, while orange indicates physical components on the FPGA board.

The VTRx+ is configured via the I2C protocol using an FPGA firmware written in the VHSIC Hardware Description Language (VHDL, [238]). The USB-UART serial interface is used to send commands from a PC to the FPGA, containing a control byte to indicate the type of transaction, the VTRx+ address as well as the register address and data to be read or written. In the FPGA, a first-in first-out (FIFO) is filled with the sent

information. The *I2C Controller* part of the firmware then instantiates an I2C read or write+read action over the I2C bus of the KC705 board, to which the VTRx+ is connected over the FMC-HPC connection.

The Xilinx Integrated Bit Error Rate Test (IBERT) Intellectual Property (IP) block [239] is used to generate and send Pseudo-Random Bit Sequences (PRBS) of various lengths. To test the Tx functionality of the VTRx+, these PRBS are sent out of the FPGA using a GTX transceivers [240] connected to the FMC-HPC socket. The VTRx+ then converts this 10.24 Gb/s electrical signal to an optical signal, that is sent out through the pigtail to an optical fibre. The optical signal then is received back by an SFP+ transceiver that converts the received light back to an electrical signal. The IBERT IP block compares the sent and received data and calculates the BER. To test the Rx of the VTRx+, the PRBS sequence is sent in the opposite direction.

An FTB-3500-CI-EI variable optical attenuator [241] is used to damp the optical signal to a certain power. In this way, artificial optical fibre cable lengths can be simulated and the specification of the VL+ system on the power budget (see Table 5.5) can be tested. The configuration of the VTRx+ by the KC705, the IBERT IP block and the attenuator are all controlled by a computer using a Python script.

The setup was used to measure the BER for different optical power levels (decibel milliwatt, dBm) using PRBS sequences of length 31 (PRBS31). The results for the default configuration of the VTRx+ V5 prototype are shown in Figure 5.23. In the downlink direction at 2.5 Gb/s, the VTRx+ Rx is able to achieve a BER $< 10^{-12}$ at a Tx optical modulation amplitude (OMA) of around -15 dBm, which is better than the specification of -13.1 dBm (see Table 5.5). Even bandwidths of 5 Gb/s would be possible within specifications.

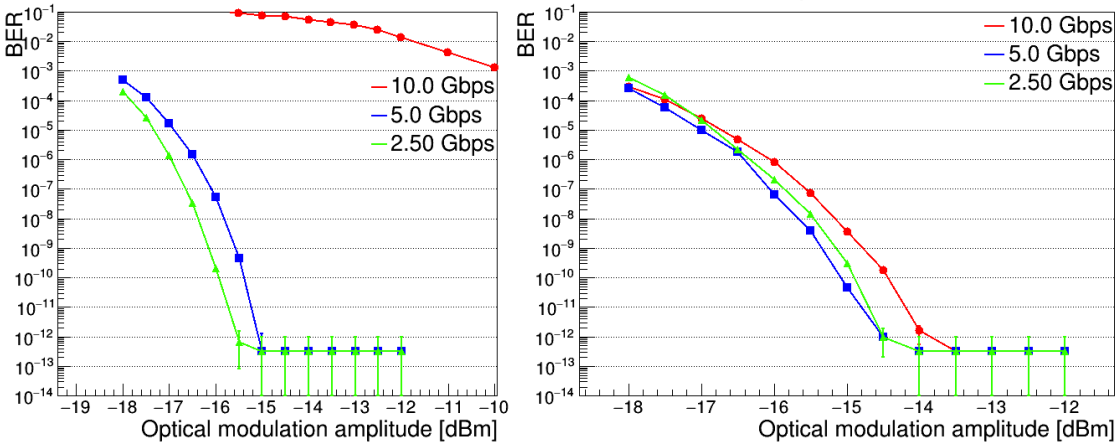

(a) (b)

Figure 5.23: Measured BER for different optical signal power at 2.5, 5 and 10 Gb/s in the downlink (a) and uplink (b) direction using a VTRx+ V5 prototype and an SFP+ reference transceiver.

In the uplink direction, the chain of VTRx+ and VL+ back-end receiver is specified to achieve BER $< 10^{-12}$ for Rx sensitivities of -12.5 dBm. The results show that this is already the case at amplitudes of ≈ -13.5 dBm at the required bandwidth of 10 Gb/s. Tests done with modulation and bias currents different than the default further showed

that different configurations of the LDQ10 can all fulfil the specifications on the uplink BER.

To test the low-level characteristics of the VTRx+ alone, the test setup was used to make eye diagrams of the VTRx+ Tx output. An Agilent 8163B optical-electrical converter [242] was used to convert the optical uplink from the VTRx+ to an electrical signal that was then fed into an DSA91204A 12 GHz oscilloscope [243] to record the eye diagrams.

The eye diagram of the VTRx+ Tx at 10 Gb/s is shown in Figure 5.24 using the default configuration of the LDQ10, all Tx channels enabled and a PRBS of length 7 (PRBS7).

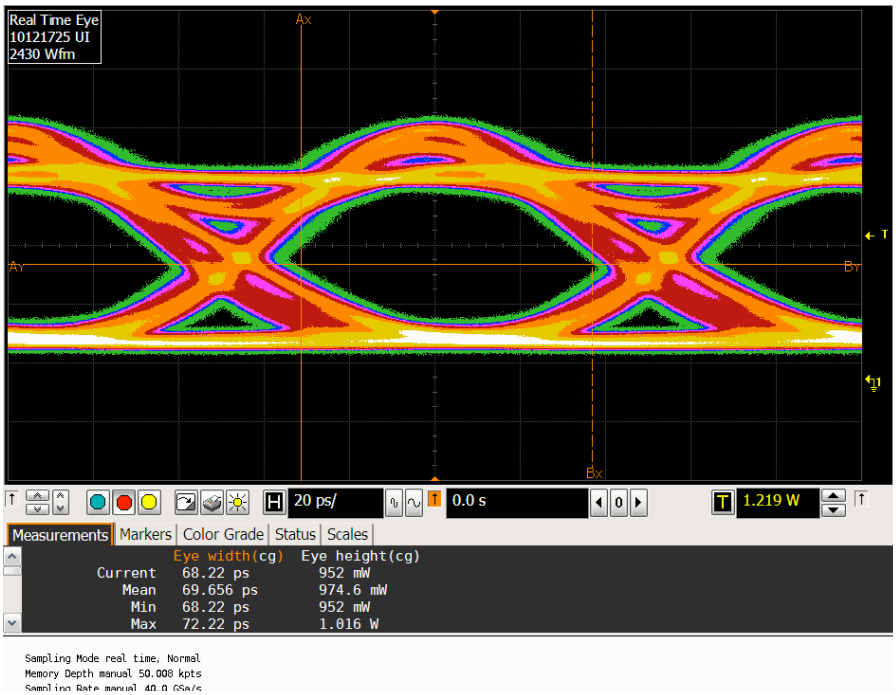

Figure 5.24: Optical eye diagram of one Tx channel of the VTRx+ V5 prototype.

The eye is observed to have a large opening with the individual measured eye diagram parameters and their specified values in Table 5.6. The limited bandwidth of the optical-electrical converter and the oscilloscope were not considered, which means that the measured eye diagram jitter and rise/fall time values should be taken as an upper limit. The high jitter values can also be explained by an unstable clock and power-supply of the KC705 that was used to drive the electrical high-speed uplink signal to the VTRx+ via the carrier board.

5.9 Optoboard Test Setup Development and Results

When the first samples of the lpGBT ASIC were available, the VTRx+ test setup was extended to test the first Optoboard prototype, the Optoboard V0 depicted in Figure 5.25. This prototype contained only the VTRx+, one lpGBT and no GBCR yet, which is sufficient however to verify the fundamental working principles of the Optosystem: the optical-electrical conversion of high-speed signals, the configuration of the Optosystem through the optical link and the aggregation of the e-links.

Eye diagram parameter	Measured value	Specification [217]
Tx OMA [dBm]	1.23	> -5.2
Tx extinction ratio [dB]	≈ 8	> 3
Eye opening [%]	79	> 60
Rise time [ps]	32.3	< 44
Fall time [ps]	46.7*	< 44
Total jitter (BER $< 10^{-12}$) [ps]	51.1	< 25
Deterministic jitter [ps]	40.81	< 12

Table 5.6: Eye diagram parameters for the eye diagram in Figure 5.24 and from the VTRx+ specifications [217]. *: No correction for overshoot of signal was applied.

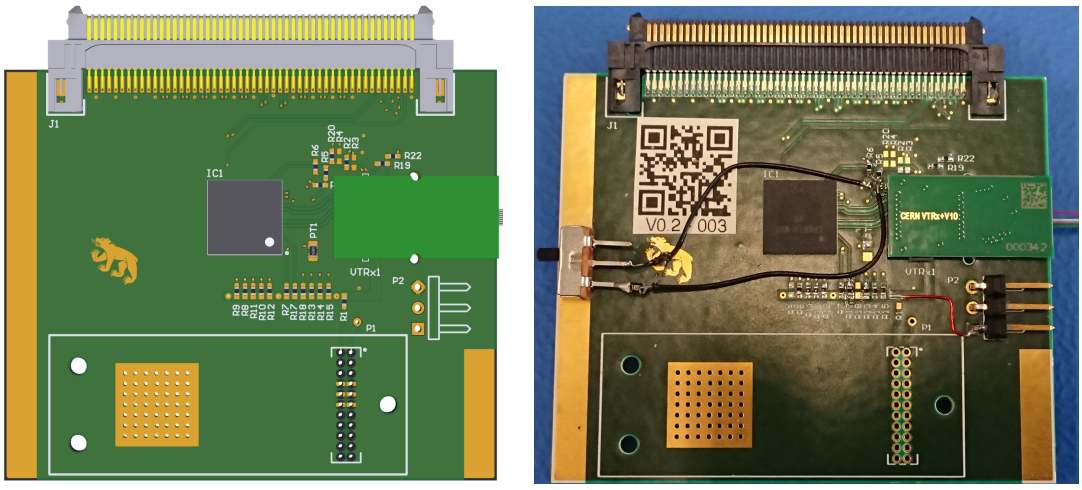

(a) (b)

Figure 5.25: CAD view (a) and photo (b) of the Optoboard V0 prototype.

Figure 5.26 shows the schematic layout and a picture of the Optoboard test setup. A custom-made FMC adapter PCB connects the FPGA board to the Optoboard via the ERF+ERM connector pair [244] that normally connects the Cable Termination Board to the Optoboard. In this way, the e-links signals of the lpGBT can be analysed by an Integrated Logic Analyser (ILA, [245]) and an I2C connection is established.

The lpGBT and VTRx+ can be configured in the same way as described before over I2C, but now also the communication with the Optoboard over the optical links is possible by using the IC field in the down- and uplink. The Rx FIFO is filled with the IC field data. Among others, this data contains the lpGBT address, the register address and data to be written/read similarly to the I2C transaction discussed in Section 5.8. The IC data is then sent to the lpGBT-FPGA core in chunks of two bits per 40 MHz clock cycle and is embedded into the downlink frame (see Figure 5.12).

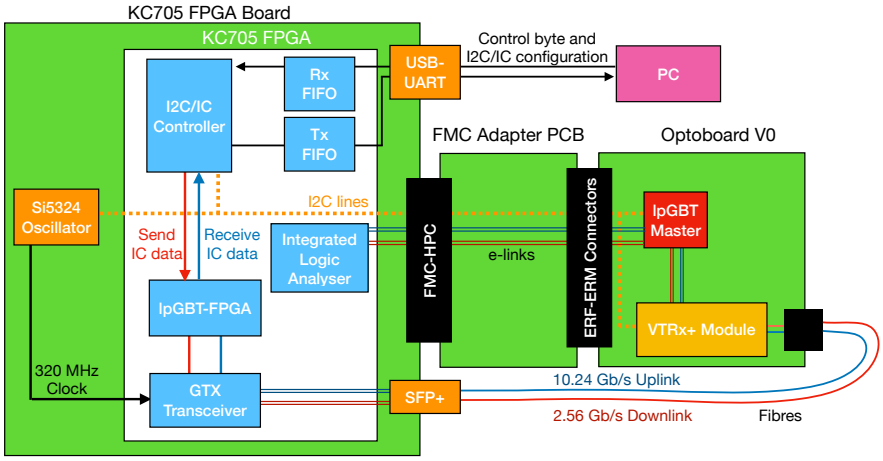

(a)

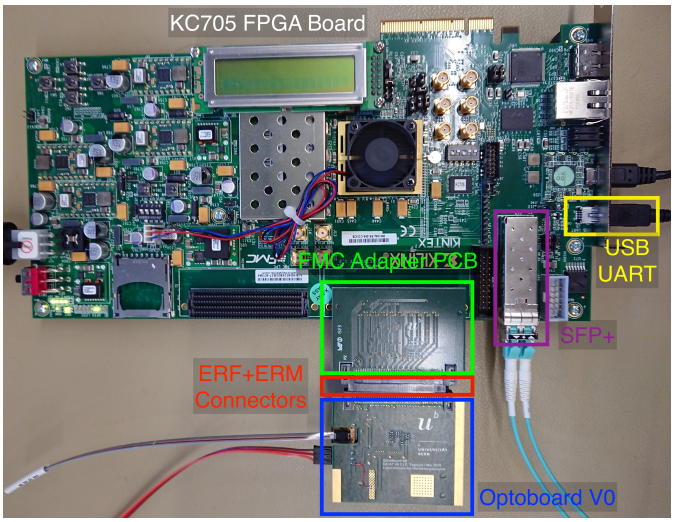

(b)

Figure 5.26: Schematic layout (a) and picture (b) of the Optoboard test setup. The various components of the firmware running in the FPGA are depicted in light blue, while orange indicates physical components on the FPGA board.

The GTX transceiver then sends out the 2.56 Gb/s downlink over the SFP+ transceiver,

using the Si5324 oscillator [246] of the KC705 FPGA board at a frequency of 320 MHz as reference clock.

The Optoboard test setup was used to verify the interplay between the lpGBT, the optical data transmission and the firmware running on the KC705, including the lpGBT-FPGA core. The lpGBT ASIC was successfully configured both over I2C and over the IC field of the high-speed optical link. Using the I2C master of the lpGBT, also the VTRx+ could be configured over I2C, validating the working principle of the Optoboard component configuration that will be used in the detector. The lpGBT was also successfully configured to generate 40 MHz output clocks to be used for the three transmitter-only lpGBTs used on the final Optoboard.

Finally, an increasing counter was injected into one of the downlink data fields of the lpGBT-FPGA. Looking at the resulting e-link signal after the complete downlink chain (SFP+ – fibre – VTRx+ – lpGBT), the counter could be seen in the corresponding e-link, qualitatively showing the working principle of the Optosystem.

With the optical data transmission and the inner working of the Optoboard verified, the next tests out of the scope of this work consist of BER tests also over the electrical part of the ITk Pixel data transmission chain. Since the Optoboard V1 prototype features all four lpGBTs and GBCRs, it includes all the functionalities of the final Optoboard. This enables tests of the complete data transmission chain of the ITk Pixel down to the RD53 FE.

Conclusions

This thesis describes the work of the author inside the ATLAS collaboration between 2018 and 2021, during which he has signed over a hundred ATLAS publications and contributed equally to the search for flavour-mixing SUSY and to the high-luminosity upgrade of the ATLAS detector.

The SUSY search presented in this thesis is to be published soon and for the first time searches for the $tc + E_{\mathrm{T}}^{\mathrm{miss}}$ final state in a dedicated analysis. It uses simultaneous b- and c-tagging and also the recently developed large-R jet top-tagging technique to target this unique final state. The compressed region of phase-space was investigated using a newly developed NN event classifier that I developed and which proved to be useful not only for the definition of the signal region, but also to increase the purity of the $W+$jets control region thanks to the multiclass capability of the developed NN classifier.

If no statistically significant deviation from the SM will be found when the analysis will be unblinded, limits on the visible cross-section of generic BSM models and also on simplified $tc + E_{\mathrm{T}}^{\mathrm{miss}}$ signal scenarios will be set. Exclusion limits of up to $\sim 1050\,\mathrm{GeV}$ in $m(\tilde{t}_1)$ and $425\,\mathrm{GeV}$ in $m(\tilde{\chi}_1^0)$ are expected to be set at the 95% CL as shown here:

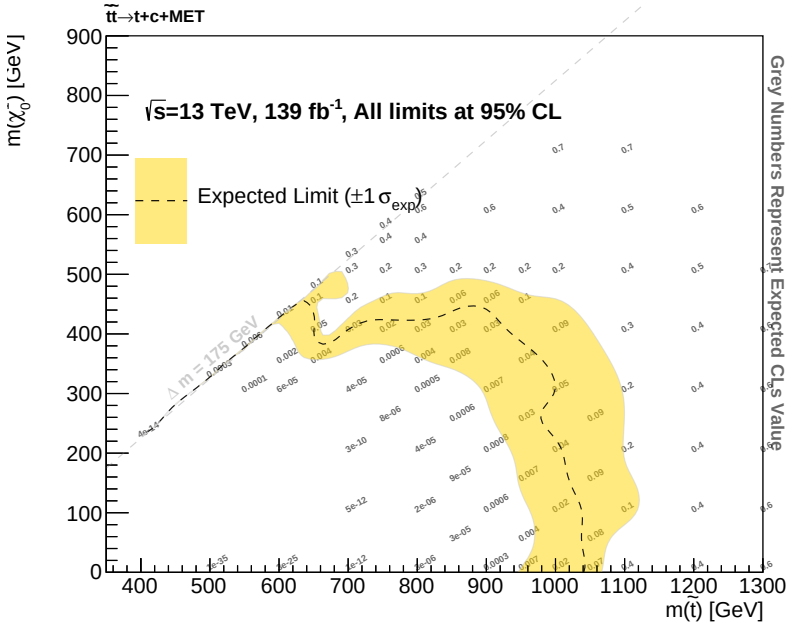

This signifies a large improvement over the exclusion derived by reinterpretation of the $36.1\,\mathrm{fb}^{-1}$ $tt + E_{\mathrm{T}}^{\mathrm{miss}}$ and $cc + E_{\mathrm{T}}^{\mathrm{miss}}$ analyses done by Reference [31]. The expected limit

is also superior to the LHC Run 3 projection ($300\,\text{fb}^{-1}$ and $\sqrt{s} = 14\,\text{TeV}$) of a dedicated $tc + E_{\text{T}}^{\text{miss}}$ analysis performed by the same reference, which proposed this search. The improvement is largest in the compressed region, thanks to the NN classifier that I developed, trained and deployed: the expected exclusion limit is extended to the two-body kinematic limit at $\Delta m(\tilde{t}_1, \tilde{\chi}_1^0) \sim 175\,\text{GeV}$ for neutralino masses of up to 425 GeV.

The $tc + E_{\text{T}}^{\text{miss}}$ search is an example for the fact that there are many well motivated BSM models out there with more complex signatures that wait for dedicated analyses to tackle them. Novel analysis techniques exploit ML tools such as NNs and boosted decision trees to more efficiently suppress the SM background, enabling to target these complex BSM signatures. Besides the definition of analysis objects, ML techniques are also especially relevant to target compressed regions of phase space. There, they can exploit the correlation between event objects and expand the discovery potential for BSM models as done in the compressed signal region of this search. Future SUSY searches should therefore focus on compressed regions of phase space and more complex SUSY signatures, where the usage of ML is crucial. SUSY is still far from being excluded and will remain an important research topic in ATLAS due to its theoretically appealing properties. Specifically, searches for third generation squarks are important, since their masses should not be much heavier than the EW scale for SUSY to solve the Hierarchy Problem.

Run 3 of the LHC between 2022 and 2024 is expected to deliver additional $\sim 350\,\text{fb}^{-1}$ of pp collisions at $\sqrt{s} = 13$ to 14 TeV. This will more than double the available dataset, but is not sufficient, for example, for measurements of the Higgs self-coupling and for drastic improvements of the $\tilde{t}$ pair production exclusion limits. The LHC will therefore be upgraded to deliver even more pp collisions to the experiments in the context of the HL-LHC project. The ATLAS detector will as well undergo an upgrade to be able to withstand the even harsher radiation environment and to perform tracking at pile-up levels of up to $\langle\mu\rangle \sim 200$.

The biggest upgrade of ATLAS consists of the replacement of its innermost detector with the Inner Tracker (ITk). A higher trigger rate and more tracks due to the larger instantaneous luminosity will also require the development of a completely new readout system, in which I was heavily involved. As such, I demonstrated the feasibility of using the low-power Gigabit Transceiver (lpGBT) instead of the delayed Aggregator ASIC in the Pixel Optosystem. With this input, the ATLAS ITk Data Transmission Task Force then gave recommendations on a revamped Pixel readout scheme, featuring a direct transmission of all Pixel links between the front-ends and the Optosystem via 6-m-long electrical links. The Optosystem then performs the recovery, aggregation and electrical-optical conversion of all links, using the lpGBT, and connects to the back-end system via optical fibres. These recommendations were followed by the collaboration and I then was one of the driving forces in the conceptual and technical design of the Optosystem.

I developed the concept and technical implementation of the Optoboard and Optobox from first sketches to prototypes. Furthermore, I developed the strategy of the mapping between the Optosystem and the front-ends, optimising the complexity and required space of the Optosystem, and defined the components of the optical data transmission chain. A picture of the second prototype of the developed Optoboard can be seen here:

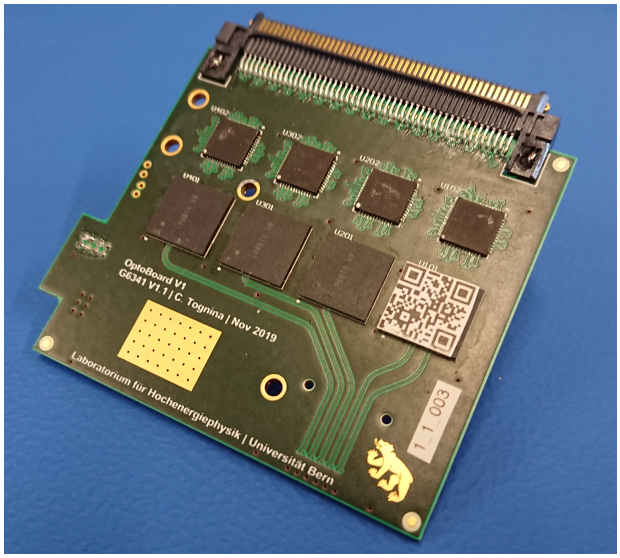

To test the working principle of the Optosystem, I designed and built test setups that enable the communication with Optoboards through the optical links in the same manner as in operation. To achieve this, I wrote an FPGA firmware in VHDL, adapting the lpGBT-FPGA back-end firmware [222] to our setup, implementing communication with a computer and adding the possibility to perform bit error rate tests over the optical links. I used these setups to test the VTRx+ opto-electrical converter performance and successfully verified the Optosystem configuration concept. The setups are to date used in most of the performed Optosystem tests. The Optosystem passed both the internal service specification and preliminary design reviews and is scheduled for production in 2022. It will be installed in ATLAS during 2026 and will handle every bit of information sent to and received by the over 32'000 pixel front-ends.

The large pile-up and radiation damage at the HL-LHC and also the requirement to fit into the existing ATLAS detector posed many challenges to the design of the Pixel detector and readout. Due to the unavailability of the Aggregator ASIC, the readout concept described in the ITk Pixel Technical Design Report [35] had to be modified using the lpGBT instead. Since the transmission of data is performed at lower bandwidths, more twinax cables are needed – heavily increasing the material budget of the Pixel services. This lead to the decision to lower the L0 trigger rate from 4 down to 1 MHz, limiting the physics capabilities of ATLAS. My work on the ITk Pixel readout system showed me that not only the sensor and front-end characteristics are important, but that a holistic approach towards detector design is crucial for the successful construction and operation of a tracker. Aspects such as readout, powering, grounding and monitoring should therefore be taken into account already at an early design phase. Detectors at future colliders such as the Future Circular Collider (FCC, [247]) offer the possibility to start the detector design from an almost blank page. While detectors at the FCC-ee [248] must be designed to feature very low material budget, the FCC-hh [249] poses unrivalled requirements on radiation hardness. It is therefore crucial to benefit from the insight gained in the design and operation of detectors at the HL-LHC especially in these two areas.

Bibliography

[1] S. L. Glashow, *The renormalizability of vector meson interactions*, Nuclear Physics **10** (1959) 107–117. Cited on pages 1, 6, and 9.

[2] S. Weinberg, *A Model of Leptons*, Physical Review Letters **19** (1967) 1264–1266. Cited on pages 1, 6, and 9.

[3] A. Salam and J. Ward, *Electromagnetic and weak interactions*, Physics Letters **13** (1964) 168–171. Cited on pages 1, 6, and 9.

[4] G. 't Hooft and M. Veltman, *Regularization and renormalization of gauge fields*, Nuclear Physics B **44** (1972) 189–213. Cited on pages 1 and 6.

[5] L. Evans and P. Bryant, *LHC Machine*, Journal of Instrumentation **3** (2008) S08001–S08001. Cited on pages 1, 21, and 23.

[6] ATLAS Collaboration, *Observation of a new particle in the search for the Standard Model Higgs boson with the ATLAS detector at the LHC*, Physics Letters B **716** (2012) 1–29. Cited on pages 1 and 6.

[7] CMS Collaboration, *Observation of a new boson at a mass of 125 GeV with the CMS experiment at the LHC*, Physics Letters B **716** (2012) 30–61. Cited on pages 1 and 6.

[8] S. Weinberg, *Implications of dynamical symmetry breaking*, Physical Review D **13** (1976) 974–996. Cited on pages 1 and 11.

[9] L. Susskind, *Dynamics of spontaneous symmetry breaking in the Weinberg-Salam theory*, Physical Review D **20** (1979) 2619–2625. Cited on pages 1 and 11.

[10] Particle Data Group, *Review of Particle Physics*, Progress of Theoretical and Experimental Physics **2020** (2020). Cited on pages 1, 8, 11, and 39.

[11] R. Barbieri and G. Giudice, *Upper bounds on supersymmetric particle masses*, Nuclear Physics B **306** (1988) 63–76. Cited on pages 1 and 11.

[12] B. de Carlos and J. Casas, *One-loop analysis of the electroweak breaking in supersymmetric models and the fine-tuning problem*, Physics Letters B **309** (1993) 320–328. Cited on pages 1 and 11.

[13] J. L. Feng, *Naturalness and the Status of Supersymmetry*, Annual Review of Nuclear and Particle Science **63** (2013) 351–382. Cited on pages 1 and 11.

[14] P. Ramond, *Dual Theory for Free Fermions*, Physical Review D **3** (1971) 2415–2418. Cited on pages 1 and 11.

[15] A. Neveu and J. Schwarz, *Factorizable dual model of pions*, Nuclear Physics B **31** (1971) 86–112. Cited on pages 1 and 11.

[16] J.-L. Gervais and B. Sakita, *Field theory interpretation of supergauges in dual models*, Nuclear Physics B **34** (1971) 632–639. Cited on pages 1 and 11.

[17] Y. A. Gelfand and E. P. Likhtman, *Extension of the algebra of Poincare group generators and violation of P invariance*, JETP Lett. **13** (1971) 323–325, https://cds.cern.ch/record/433516. Cited on pages 1 and 11.

[18] J. Wess and B. Zumino, *Supergauge invariant extension of quantum electrodynamics*, Nuclear Physics B **78** (1974) 1–13. Cited on pages 1 and 11.

[19] D. Volkov and V. Akulov, *Is the neutrino a goldstone particle?*, Physics Letters B **46** (1973) 109–110. Cited on pages 1 and 11.

[20] S. P. Martin, *A Supersymmetry Primer*, pp. , 1–153. World Scientific, Apr., 2010. Cited on pages 1, 11, 12, 13, 14, 15, and 16.

[21] ATLAS Collaboration, *SUSY Summary Plots June 2021*, tech. rep., CERN, Geneva, Jun, 2021. http://cds.cern.ch/record/2771785. Cited on page 1.

[22] CMS Collaboration, *CMS Supersymmetry Physics Results*, 2021. https://twiki.cern.ch/twiki/bin/view/CMSPublic/PhysicsResultsSUS. last accessed 07.07.2021. Cited on page 1.

[23] ATLAS Collaboration, *The ATLAS Experiment at the CERN Large Hadron Collider*, Journal of Instrumentation **3** (2008) S08003–S08003. Cited on pages 1, 24, 26, 29, 30, 31, 32, and 33.

[24] ATLAS Collaboration, *Search for a scalar partner of the top quark in the all-hadronic $t\bar{t}$ plus missing transverse momentum final state at $\sqrt{s} = 13$ TeV with the ATLAS detector*, The European Physical Journal C **80** (2020) 1–44. Cited on page 1.

[25] ATLAS Collaboration, *Search for supersymmetry in final states with charm jets and missing transverse momentum in 13 TeV pp collisions with the ATLAS detector*, Journal of High Energy Physics **2018** (2018). Cited on pages 1 and 16.

[26] G. D'Ambrosio, G. Giudice, G. Isidori, and A. Strumia, *Minimal flavour violation: an effective field theory approach*, Nuclear Physics B **645** (2002) 155–187. Cited on pages 1 and 16.

[27] K. De Causmaecker, et al., *General squark flavour mixing: constraints, phenomenology and benchmarks*, Journal of High Energy Physics **2015** (2015) 1–30. Cited on pages 1 and 16.

[28] M. Blanke, et al., *Flavoured naturalness*, Journal of High Energy Physics **2013** (2013) 22. Cited on pages 1 and 16.

[29] J. Bendavid, et al., *Les Houches 2017: physics at TeV colliders standard model working group report*, 2018. arXiv:1803.07977. Cited on pages 1 and 16.

[30] A. Bartl, et al., *Impact of squark generation mixing on the search for squarks decaying into fermions at LHC*, Physics Letters B **698** (2011) 380–388. Cited on pages 1 and 16.

[31] A. Chakraborty, et al., *Flavour-violating decays of mixed top-charm squarks at the LHC*, The European Physical Journal C **78** (2018). Cited on pages 1, 16, 17, 18, 90, and 121.

[32] CERN Yellow Reports: Monographs, *CERN Yellow Reports: Monographs, Vol. 10 (2020): High-Luminosity Large Hadron Collider (HL-LHC): Technical design report*, 2020. https://e-publishing.cern.ch/index.php/CYRM/issue/view/127. Cited on pages 2, 94, and 95.

[33] A. Dainese, et al., *Report on the Physics at the HL-LHC, and Perspectives for the HE-LHC*, tech. rep., Geneva, Switzerland, 2019. Cited on page 2.

[34] ATLAS Collaboration, *Technical Design Report for the ATLAS Inner Tracker Strip Detector*, Tech. Rep. CERN-LHCC-2017-005. ATLAS-TDR-025, CERN, Geneva, 4, 2017. http://cds.cern.ch/record/2257755. Cited on pages 2, 95, and 96.

[35] ATLAS Collaboration, *Technical Design Report for the ATLAS Inner Tracker Pixel Detector*, Tech. Rep. CERN-LHCC-2017-021. ATLAS-TDR-030, CERN, Geneva, 9, 2017. http://cds.cern.ch/record/2285585. Cited on pages 2, 95, 96, 98, 102, 103, and 123.

[36] M. K. E. L. Planck, *Über eine Verbesserung der Wienschen Spektralgleichung*, pp. , 175–178. Vieweg+Teubner Verlag, 1978. Cited on page 5.

[37] M. K. E. L. Planck, *Zur Theorie des Gesetzes der Energieverteilung im Normalspectrum*, Verhandl. Dtsc. Phys. Ges. **2** (1900) 237, https://cds.cern.ch/record/262745. Cited on page 5.

[38] *The quantum theory of the emission and absorption of radiation*, Proceedings of the Royal Society of London. Series A, Containing Papers of a Mathematical and Physical Character **114** (1927) 243–265. Cited on page 5.

[39] A. Romer, *Proton or prouton?: Rutherford and the depths of the atom*, American Journal of Physics **65** (1997) 707–716. Cited on page 5.

[40] J. Chadwick, *The existence of a neutron*, Proceedings of the Royal Society of London. Series A, Containing Papers of a Mathematical and Physical Character **136** (1932) 692–708. Cited on page 5.

[41] J. Chadwick and M. Goldhaber, *The nuclear photoelectric effect*, Proceedings of the Royal Society A: Mathematical, Physical and Engineering Sciences **151** (1935) 479–493. Cited on page 5.

[42] M. Gell-Mann, *A schematic model of baryons and mesons*, Physics Letters **8** (1964) 214–215. Cited on page 5.

[43] G. Zweig, *An SU_3 model for strong interaction symmetry and its breaking; Version 2*, https://cds.cern.ch/record/570209, Version 1 is CERN preprint 8182/TH.401, Jan. 17, 1964. Cited on page 5.

[44] H. W. Kendall, *Deep inelastic scattering: Experiments on the proton and the observation of scaling*, Reviews of Modern Physics **63** (1991) 597–614. Cited on page 5.

[45] L. D. Lella and C. Rubbia, *The Discovery of the W and Z Particles*, pp. , 137–163. World Scientific, July, 2015. Cited on page 6.

[46] P. W. Higgs, *Broken Symmetries and the Masses of Gauge Bosons*, Physical Review Letters **13** (1964) 508–509. Cited on pages 6 and 9.

[47] P. W. Higgs, *Broken symmetries, massless particles and gauge fields*, Physics Letters **12** (1964) 132–133. Cited on pages 6 and 9.

[48] F. Englert and R. Brout, *Broken Symmetry and the Mass of Gauge Vector Mesons*, Physical Review Letters **13** (1964) 321–323. Cited on pages 6 and 9.

[49] G. S. Guralnik, C. R. Hagen, and T. W. B. Kibble, *Global Conservation Laws and Massless Particles*, Physical Review Letters **13** (1964) 585–587. Cited on pages 6 and 9.

[50] T. Becher, *Lecture notes on Standard Model*, May, 2017. University of Bern. Cited on page 6.

[51] ATLAS Collaboration, *Standard Model Summary Plots March 2021*, Tech. Rep. ATL-PHYS-PUB-2021-005, CERN, Geneva, Mar, 2021. http://cds.cern.ch/record/2758261. Cited on page 6.

[52] E. Fermi, *Zur Quantelung des idealen einatomigen Gases*, Zeitschrift für Physik **36** (1926) 902–912. Cited on page 7.

[53] P. A. M. Dirac, *On the theory of quantum mechanics*, Proceedings of the Royal Society of London. Series A, Containing Papers of a Mathematical and Physical Character **112** (1926) 661–677. Cited on page 7.

[54] S. N. Bose, *Plancks Gesetz und Lichtquantenhypothese*, Zeitschrift für Physik **26** (1924) 178–181. Cited on page 7.

[55] A. Einstein, *Quantum theory of the monatomic ideal gas*, Sitzungsberichte der Preussischen Akademie der Wissenschaften, Physikalisch-mathematische Klasse (1924) 261–267, http://www.fisica.uns.edu.ar/albert/archivos/46/156/495246252_apuntes.pdf. Cited on page 7.

[56] D. Galbraith and C. Burgard, *Diagram of the Standard Model of particle physics, created at the CERN Webfest 2012*, 2012. https://davidgalbraith.org/portfolio/ux-standard-model-of-the-standard-model. last accessed 11.03.2021. Cited on page 7.

[57] H. Fritzsch, M. Gell-Mann, and H. Leutwyler, *Advantages of the color octet gluon picture*, Physics Letters B **47** (1973) 365–368. Cited on page 7.

[58] O. W. Greenberg, *Spin and Unitary-Spin Independence in a Paraquark Model of Baryons and Mesons*, Physical Review Letters **13** (1964) 598–602. Cited on page 7.

[59] M. Y. Han and Y. Nambu, *Three-Triplet Model with Double SU(3) Symmetry*, Physical Review **139** (1965) B1006–B1010. Cited on page 7.

[60] C. N. Yang and R. L. Mills, *Conservation of Isotopic Spin and Isotopic Gauge Invariance*, Physical Review **96** (1954) 191–195. Cited on page 7.

[61] D. J. Gross and F. Wilczek, *Ultraviolet Behavior of Non-Abelian Gauge Theories*, Physical Review Letters **30** (1973) 1343–1346. Cited on page 7.

[62] H. D. Politzer, *Reliable Perturbative Results for Strong Interactions?*, Physical Review Letters **30** (1973) 1346–1349. Cited on page 7.

[63] S. Dawson, *Introduction to Electroweak Symmetry Breaking*, in *High Energy Physics and Cosmology, 1998 Summer School*. Jan., 1999. arXiv:hep-ph/9901280 [hep-ph]. Cited on page 9.

[64] A. Pich, *The Standard Model of Electroweak Interactions*, arXiv:0705.4264 [hep-ph]. Cited on page 9.

[65] N. Cabibbo, *Unitary Symmetry and Leptonic Decays*, Physical Review Letters **10** (1963) 531–533. Cited on page 10.

[66] M. Kobayashi and T. Maskawa, *CP-Violation in the Renormalizable Theory of Weak Interaction*, Progress of Theoretical Physics **49** (1973) 652–657. Cited on page 10.

[67] A. D. Sakharov, *Violation of CP-invariance, C-asymmetry, and baryon asymmetry of the Universe*, pp. , 84–87. World Scientific, Nov., 1998. Cited on page 10.

[68] G. R. Farrar and M. E. Shaposhnikov, *Baryon asymmetry of the Universe in the standard model*, Physical Review D **50** (1994) 774–818. Cited on page 10.

[69] M. Gavela, M. Lozano, J. Orloff, and O. Pène, *Standard model CP-violation and baryon asymmetry (I). Zero temperature*, Nuclear Physics B **430** (1994) 345–381. Cited on page 10.

[70] P. Huet and E. Sather, *Electroweak baryogenesis and standard model CP violation*, Physical Review D **51** (1995) 379–394. Cited on page 10.

[71] K. Garrett and G. Duda, *Dark Matter: A Primer*, Advances in Astronomy **2011** (2011) 1–22. Cited on page 11.

[72] H. Georgi and S. L. Glashow, *Unity of All Elementary-Particle Forces*, Physical Review Letters **32** (1974) 438–441. Cited on page 11.

[73] S. Coleman and J. Mandula, *All Possible Symmetries of theSMatrix*, Physical Review **159** (1967) 1251–1256. Cited on page 11.

[74] R. Haag, J. T. Łopuszański, and M. Sohnius, *All possible generators of supersymmetries of the S-matrix*, Nuclear Physics B **88** (1975) 257–274. Cited on page 11.

[75] P. Fayet, *Supersymmetry and weak, electromagnetic and strong interactions*, Physics Letters B **64** (1976) 159–162. Cited on page 14.

[76] P. Fayet, *Spontaneously broken supersymmetric theories of weak, electromagnetic and strong interactions*, Physics Letters B **69** (1977) 489–494. Cited on page 14.

[77] P. Langacker, *Precision tests of the standard model*, in *1st International Symposium on Particles, Strings and Cosmology*. 8, 1990. Cited on page 14.

[78] J. Ellis, S. Kelley, and D. Nanopoulos, *Probing the desert using gauge coupling unification*, Physics Letters B **260** (1991) 131–137. Cited on page 14.

[79] U. Amaldi, W. de Boer, and H. Fürstenau, *Comparison of grand unified theories with electroweak and strong coupling constants measured at LEP*, Physics Letters B **260** (1991) 447–455. Cited on page 14.

[80] P. Langacker and M. Luo, *Implications of precision electroweak experiments for* m_t, ρ_0, $\sin^2\theta_W$, *and grand unification*, Physical Review D **44** (1991) 817–822. Cited on page 14.

[81] C. Giunti, C. W. Kim, and U. W. Lee, *Running coupling constants and grand unification models*, Modern Physics Letters A **06** (1991) 1745–1755. Cited on page 14.

[82] S. Dimopoulos and D. Sutter, *The supersymmetric flavor problem*, Nuclear Physics B **452** (1995) 496–512. Cited on page 15.

[83] A. Djouadi, et al., *The Minimal supersymmetric standard model: Group summary report*, arXiv preprint hep-ph/9901246 (1999), https://arxiv.org/abs/hep-ph/9901246. Cited on page 15.

[84] A. Djouadi, J.-L. Kneur, and G. Moultaka, *SuSpect: A Fortran code for the Supersymmetric and Higgs particle spectrum in the MSSM*, Computer Physics Communications **176** (2007) 426–455. Cited on page 15.

[85] Super-Kamiokande Collaboration, C. Regis, et al., *Search for proton decay via* $p \to \mu^+ K^0$ *in Super-Kamiokande I, II, and III*, Phys. Rev. D **86** (2012) 012006, https://link.aps.org/doi/10.1103/PhysRevD.86.012006. Cited on page 16.

[86] Super-Kamiokande Collaboration, K. Abe, et al., *Search for proton decay via* $p \to \nu K^+$ *using* 260 kiloton $\cdot$ year *data of Super-Kamiokande*, Phys. Rev. D **90** (2014) 072005, https://link.aps.org/doi/10.1103/PhysRevD.90.072005. Cited on page 16.

[87] Super-Kamiokande Collaboration, K. Abe, et al., *Search for proton decay via* $p \to e^+\pi^0$ *and* $p \to \mu^+\pi^0$ *in* 0.31 *megaton* $\cdot$ *years exposure of the Super-Kamiokande water Cherenkov detector*, Phys. Rev. D **95** (2017) 012004, https://link.aps.org/doi/10.1103/PhysRevD.95.012004. Cited on page 16.

[88] M. Ciuchini, et al., *Soft SUSY breaking grand unification: Leptons vs quarks on the flavor playground*, Nuclear Physics B **783** (2007) 112–142. Cited on page 16.

[89] ATLAS Collaboration, *Search for top-squark pair production in final states with one lepton, jets, and missing transverse momentum using 36 fb^{-1} of $\sqrt{s} = 13$ TeV pp collision data with the ATLAS detector*, Journal of High Energy Physics **2018** (2018). Cited on page 16.

[90] C. Merlassino, *Novel searches for top squarks at the LHC*, 2019. https://cds.cern.ch/record/2698582. Presented 24 Oct 2019. Cited on page 19.

[91] R. Steerenberg, et al., *Operation and Performance of the Cern Large Hadron Collider During Proton Run 2*, Proceedings of the 10th Int. Particle Accelerator Conf. **IPAC2019** (2019) Australia. Cited on page 22.

[92] E. A. Mobs, *The CERN accelerator complex. Complexe des accélérateurs du CERN*, 10, 2016. https://cds.cern.ch/record/2225847. last accessed 01.06.2021. Cited on page 22.

[93] M. Solfaroli, *Review of 2017 operation*, 1, 2018. https://indico.cern.ch/event/676124/contributions/2767793/. LHC performance workshop, Chamonix 2018. Cited on page 23.

[94] C. Borschensky, et al., *Squark and gluino production cross sections in pp collisions at $\sqrt{s} = 13$, 14, 33 and 100 TeV*, The European Physical Journal C **74** (2014). Cited on page 23.

[95] ATLAS Collaboration, *Public Luminosity measurements of the ATLAS detector*, https://twiki.cern.ch/twiki/bin/view/AtlasPublic/LuminosityPublicResultsRun2. last accessed 28.03.2021. Cited on page 23.

[96] J. Pequenao, *Computer generated image of the whole ATLAS detector*, 3, 2008. https://cds.cern.ch/record/1095924. last accessed 01.06.2021. Cited on page 24.

[97] H. Bethe, *Zur Theorie des Durchgangs schneller Korpuskularstrahlen durch Materie*, Annalen der Physik **397** (1930) 325–400. Cited on page 25.

[98] F. Bloch, *Zur Bremsung rasch bewegter Teilchen beim Durchgang durch Materie*, Annalen der Physik **408** (1933) 285–320. Cited on page 25.

[99] ATLAS Collaboration, *Inner Detector Technical Design Report*, tech. rep., 1997. https://cds.cern.ch/record/331063. Cited on page 26.

[100] ATLAS Collaboration, M. Capeans, et al., *ATLAS Insertable B-Layer Technical Design Report*, tech. rep., Sep, 2010. https://cds.cern.ch/record/1291633. Cited on pages 26 and 27.

[101] ATLAS Collaboration, *Track Reconstruction Performance of the ATLAS Inner Detector at $\sqrt{s} = 13$ TeV*, Tech. Rep. ATL-PHYS-PUB-2015-018, CERN, Geneva, Jul, 2015. https://cds.cern.ch/record/2037683. Cited on pages 27 and 37.

[102] ATLAS Collaboration, *Study of the material of the ATLAS inner detector for Run 2 of the LHC*, Journal of Instrumentation **12** (2017) P12009–P12009. Cited on page 28.

[103] D. Bertsche, *Opto-box: Optical modules and mini-crate for ATLAS pixel and IBL detectors*, EPJ Web of Conferences **126** (2016) 05002. Cited on page 27.

[104] ATLAS IBL collaboration, *Production and integration of the ATLAS Insertable B-Layer*, Journal of Instrumentation **13** (2018) T05008–T05008. Cited on page 28.

[105] D. Robinson, *Operational experience of the ATLAS SemiConductor Tracker and Pixel Detector, 25th international workshop on Vertex Detectors*, 2011. https://indico.cern.ch/event/452781/contributions/2297473/attachments/1342645/2022618/Vertex2016_DR.pdf. last accessed 25.03.2021. Cited on page 28.

[106] ATLAS TRT collaboration, *The ATLAS TRT electronics*, Journal of Instrumentation **3** (2008) P06007–P06007. Cited on page 28.

[107] G. Ripellino, *The alignment of the ATLAS Inner Detector in Run-2*, in *Proceedings of Fourth Annual Large Hadron Collider Physics — PoS(LHCP2016)*. Sissa Medialab, Sept., 2016. Cited on page 28.

[108] ATLAS TRT collaboration, *The ATLAS Transition Radiation Tracker (TRT) proportional drift tube: design and performance*, Journal of Instrumentation **3** (2008) P02013–P02013. Cited on page 29.

[109] ATLAS Collaboration, *Operation and performance of the ATLAS Tile Calorimeter in Run 1*, The European Physical Journal C **78** (2018). Cited on page 30.

[110] ATLAS Collaboration, *Technical Design Report for the Phase-I Upgrade of the ATLAS TDAQ System*, Tech. Rep. CERN-LHCC-2013-018. ATLAS-TDR-023, Sep, 2013. https://cds.cern.ch/record/1602235. Final version presented to December 2013 LHCC. Cited on page 32.

[111] ATLAS Collaboration, *Overview of the TDAQ system in Run 2*, https://twiki.cern.ch/twiki/bin/view/AtlasPublic/ApprovedPlotsDAQ. last accessed 28.03.2021. Cited on page 33.

[112] M. zur Nedden, *The LHC Run 2 ATLAS trigger system: design, performance and plans*, Journal of Instrumentation **12** (2017) C03024–C03024. Cited on page 33.

[113] ATLAS Collaboration, *Performance of the ATLAS track reconstruction algorithms in dense environments in LHC Run 2*, The European Physical Journal C **77** (2017). Cited on pages 35 and 36.

[114] A. Salzburger, *Optimisation of the ATLAS Track Reconstruction Software for Run-2*, Journal of Physics: Conference Series **664** (2015) 072042. Cited on page 35.

[115] T. Cornelissen, et al., *The new ATLAS track reconstruction (NEWT)*, Journal of Physics: Conference Series **119** (2008) 032014. Cited on pages 35 and 36.

[116] R. Frühwirth, *Application of Kalman filtering to track and vertex fitting*, Nuclear Instruments and Methods in Physics Research Section A: Accelerators, Spectrometers, Detectors and Associated Equipment **262** (1987) 444–450. Cited on page 35.

[117] F. Meloni, *Primary vertex reconstruction with the ATLAS detector*, Journal of Instrumentation **11** (2016) C12060–C12060. Cited on page 36.

[118] ATLAS Collaboration, *Vertex Reconstruction Performance of the ATLAS Detector at* $\sqrt{s} = 13TeV$, Tech. Rep. ATL-PHYS-PUB-2015-026, CERN, Geneva, Jul, 2015. https://cds.cern.ch/record/2037717. Cited on page 37.

[119] W. Lampl, et al., *Calorimeter Clustering Algorithms: Description and Performance*, Tech. Rep. ATL-LARG-PUB-2008-002. ATL-COM-LARG-2008-003, CERN, Geneva, Apr, 2008. https://cds.cern.ch/record/1099735. Cited on pages 37 and 42.

[120] ATLAS Collaboration, *Topological cell clustering in the ATLAS calorimeters and its performance in LHC Run 1*, The European Physical Journal C **77** (2017). Cited on page 37.

[121] A. Hrynevich, *ATLAS jet and missing energy reconstruction, calibration and performance in LHC Run-2*, Journal of Instrumentation **12** (2017) C06038–C06038. Cited on pages 37 and 38.

[122] ATLAS Collaboration, *Jet reconstruction and performance using particle flow with the ATLAS Detector*, The European Physical Journal C **77** (2017). Cited on pages 37 and 38.

[123] M. Cacciari, G. P. Salam, and G. Soyez, *The anti-k_t jet clustering algorithm*, Journal of High Energy Physics **2008** (2008) 063–063. Cited on page 38.

[124] B. Isildak, *Measurement of the differential dijet production cross section in proton-proton collisions at* $\sqrt{s} = 7$ *TeV*, 2013. Cited on page 38.

[125] ATLAS Collaboration, *Determination of jet calibration and energy resolution in proton-proton collisions at* $\sqrt{s} = 8$ *TeV using the ATLAS detector*, The European Physical Journal C **80** (2020). Cited on page 38.

[126] ATLAS Collaboration, *Tagging and suppression of pileup jets with the ATLAS detector*, Tech. Rep. ATLAS-CONF-2014-018, CERN, Geneva, May, 2014. https://cds.cern.ch/record/1700870. Cited on page 38.

[127] ATLAS Collaboration, *Selection of jets produced in 13 TeV proton-proton collisions with the ATLAS detector*, Tech. Rep. ATLAS-CONF-2015-029, CERN, Geneva, Jul, 2015. https://cds.cern.ch/record/2037702. Cited on page 38.

[128] Heavy Flavor Averaging Group Collaboration, Y. Amhis, et al., *Averages of b-hadron, c-hadron, and τ-lepton properties as of 2018*, arXiv:1909.12524 [hep-ex]. Cited on page 39.

[129] ATLAS Collaboration, *Calibration of light-flavour b-jet mistagging rates using ATLAS proton-proton collision data at* $\sqrt{s} = 13$ *TeV*, Tech. Rep. ATLAS-CONF-2018-006, CERN, Geneva, Apr, 2018. https://cds.cern.ch/record/2314418. Cited on page 39.

[130] ATLAS Collaboration, *Performance of the ATLAS Secondary Vertex b-tagging Algorithm in 900 GeV Collision Data*, Tech. Rep. ATLAS-CONF-2010-004, CERN, Geneva, Jun, 2010. https://cds.cern.ch/record/1273194. Cited on page 39.

[131] ATLAS Collaboration, *ATLAS b-jet identification performance and efficiency measurement with $t\bar{t}$ events in pp collisions at $\sqrt{s} = 13$ TeV*, The European Physical Journal C **79** (2019). Cited on pages 39 and 40.

[132] ATLAS Collaboration, C. Varni, *Tracking and flavour-tagging performance at ATLAS*, Tech. Rep. ATL-PHYS-PROC-2020-085, CERN, Geneva, Oct, 2020. https://cds.cern.ch/record/2742644. Cited on pages 39 and 40.

[133] ATLAS Collaboration, *Secondary vertex finding for jet flavour identification with the ATLAS detector*, Tech. Rep. ATL-PHYS-PUB-2017-011, CERN, Geneva, Jun, 2017. https://cds.cern.ch/record/2270366. Cited on page 39.

[134] ATLAS Collaboration, *Topological b-hadron decay reconstruction and identification of b-jets with the JetFitter package in the ATLAS experiment at the LHC*, Tech. Rep. ATL-PHYS-PUB-2018-025, CERN, Geneva, Oct, 2018. https://cds.cern.ch/record/2645405. Cited on page 40.

[135] ATLAS Collaboration, *Optimisation and performance studies of the ATLAS b-tagging algorithms for the 2017-18 LHC run*, Tech. Rep. ATL-PHYS-PUB-2017-013, CERN, Geneva, Jul, 2017. https://cds.cern.ch/record/2273281. Cited on pages 40 and 41.

[136] ATLAS Collaboration, *Identification of Jets Containing b-Hadrons with Recurrent Neural Networks at the ATLAS Experiment*, Tech. Rep. ATL-PHYS-PUB-2017-003, CERN, Geneva, Mar, 2017. https://cds.cern.ch/record/2255226. Cited on page 40.

[137] ATLAS Collaboration, P. J. Windischhofer, *Heavy-flavour jet tagging in ATLAS*, https://cds.cern.ch/record/2706702. Cited on page 40.

[138] ATLAS Collaboration, *Expected performance of the 2019 ATLAS b-taggers*, http://atlas.web.cern.ch/Atlas/GROUPS/PHYSICS/PLOTS/FTAG-2019-005. FTAG-2019-005. Cited on page 41.

[139] ATLAS Collaboration, *Simulation-based extrapolation of b-tagging calibrations towards high transverse momenta in the ATLAS experiment*, tech. rep., CERN, Geneva, Mar, 2021. https://cds.cern.ch/record/2753444. Cited on pages 41 and 79.

[140] ATLAS Collaboration, *Electron reconstruction and identification in the ATLAS experiment using the 2015 and 2016 LHC proton–proton collision data at $\sqrt{s} = 13$ TeV*, The European Physical Journal C **79** (2019). Cited on pages 41, 42, and 52.

[141] ATLAS Collaboration, *Improved electron reconstruction in ATLAS using the Gaussian Sum Filter-based model for bremsstrahlung*, Tech. Rep. ATLAS-CONF-2012-047, CERN, Geneva, May, 2012. https://cds.cern.ch/record/1449796. Cited on page 42.

[142] ATLAS Collaboration, *Electron efficiency measurements with the ATLAS detector using 2012 LHC proton–proton collision data*, The European Physical Journal C **77** (2017). Cited on page 42.

[143] ATLAS Collaboration, *Measurement of the photon identification efficiencies with the ATLAS detector using LHC Run 2 data collected in 2015 and 2016*, The European Physical Journal C **79** (2019). Cited on page 42.

[144] ATLAS Collaboration, *Muon reconstruction performance of the ATLAS detector in proton–proton collision data at* $\sqrt{s} = 13$ *TeV*, The European Physical Journal C **76** (2016). Cited on pages 42 and 52.

[145] ATLAS Collaboration, *Performance of missing transverse momentum reconstruction with the ATLAS detector using proton–proton collisions at* $\sqrt{s} = 13$ *TeV*, The European Physical Journal C **78** (2018). Cited on pages 43 and 44.

[146] ATLAS Collaboration, *TST systematics using 2015-2018 data*, Jetm-2020-02. https://atlas.web.cern.ch/Atlas/GROUPS/PHYSICS/PLOTS/JETM-2020-02/. Cited on page 44.

[147] ATLAS Collaboration, *Boosted hadronic vector boson and top quark tagging with ATLAS using Run 2 data*, tech. rep., CERN, Geneva, Jul, 2020. http://cds.cern.ch/record/2724149. Cited on pages 45, 53, 54, and 79.

[148] M. Baak, et al., *HistFitter software framework for statistical data analysis*, The European Physical Journal C **75** (2015). Cited on pages 47 and 48.

[149] A. L. Read, *Presentation of search results: the* CL_s *technique*, Journal of Physics G: Nuclear and Particle Physics **28** (2002) 2693–2704. Cited on page 49.

[150] ATLAS Collaboration, *Luminosity determination in pp collisions at* $\sqrt{s} = 13$ *TeV using the ATLAS detector at the LHC*, tech. rep., CERN, Geneva, Jun, 2019. http://cds.cern.ch/record/2677054. Cited on page 49.

[151] A. Buckley, et al., *General-purpose event generators for LHC physics*, Physics Reports **504** (2011) 145–233. Cited on page 49.

[152] G. T. Bodwin, *Factorization of the Drell-Yan cross section in perturbation theory*, Physical Review D **31** (1985) 2616–2642. Cited on page 49.

[153] J. C. Collins, D. E. Soper, and G. Sterman, *Factorization for short distance hadron-hadron scattering*, Nuclear Physics B **261** (1985) 104–142. Cited on page 49.

[154] J. C. Collins, D. E. Soper, and G. Sterman, *Soft gluons and factorization*, Nuclear Physics B **308** (1988) 833–856. Cited on page 49.

[155] S. Agostinelli, et al., *Geant4—a simulation toolkit*, Nuclear Instruments and Methods in Physics Research Section A: Accelerators, Spectrometers, Detectors and Associated Equipment **506** (2003) 250–303. Cited on pages 50 and 51.

[156] T. Gleisberg, et al., *Event generation with SHERPA 1.1*, Journal of High Energy Physics **2009** (2009) 007–007. Cited on pages 50 and 51.

[157] J. Alwall, et al., *The automated computation of tree-level and next-to-leading order differential cross sections, and their matching to parton shower simulations*, Journal of High Energy Physics **2014** (2014). Cited on page 51.

[158] R. D. Ball, et al., *Parton distributions for the LHC run II*, Journal of High Energy Physics **2015** (2015). Cited on page 51.

[159] T. Sjöstrand, et al., *An introduction to PYTHIA 8.2*, Computer Physics Communications **191** (2015) 159–177. Cited on page 51.

[160] ATLAS Collaboration, *ATLAS Pythia 8 tunes to 7 TeV data*, tech. rep., CERN, Geneva, Nov, 2014. https://cds.cern.ch/record/1966419. Cited on page 51.

[161] D. J. Lange, *The EvtGen particle decay simulation package*, Nuclear Instruments and Methods in Physics Research Section A: Accelerators, Spectrometers, Detectors and Associated Equipment **462** (2001) 152–155. Cited on page 51.

[162] L. Lönnblad and S. Prestel, *Matching tree-level matrix elements with interleaved showers*, Journal of High Energy Physics **2012** (2012). Cited on page 51.

[163] W. Beenakker, et al., *Stop production at hadron colliders*, Nuclear Physics B **515** (1998) 3–14. Cited on page 51.

[164] W. Beenakker, et al., *Supersymmetric top and bottom squark production at hadron colliders*, Journal of High Energy Physics **2010** (2010). Cited on page 51.

[165] W. Beenakker et al., *Squark and gluino hadroproduction*, Int. J. Mod. Phys. A **26** (2011) 2637, arXiv:1105.1110 [hep-ph]. Cited on page 51.

[166] S. Catani, et al., *Vector Boson Production at Hadron Colliders: A Fully Exclusive QCD Calculation at Next-to-Next-to-Leading Order*, Physical Review Letters **103** (2009). Cited on page 51.

[167] S. Alioli, P. Nason, C. Oleari, and E. Re, *A general framework for implementing NLO calculations in shower Monte Carlo programs: the POWHEG BOX*, Journal of High Energy Physics **2010** (2010). Cited on page 51.

[168] M. Cacciari, et al., *Top-pair production at hadron colliders with next-to-next-to-leading logarithmic soft-gluon resummation*, Physics Letters B **710** (2012) 612–622. Cited on page 51.

[169] M. Czakon and A. Mitov, *Top++: A program for the calculation of the top-pair cross-section at hadron colliders*, Computer Physics Communications **185** (2014) 2930–2938. Cited on page 51.

[170] N. Kidonakis, *Next-to-next-to-leading-order collinear and soft gluon corrections fort-channel single top quark production*, Physical Review D **83** (2011). Cited on page 51.

[171] N. Kidonakis, *Two-loop soft anomalous dimensions for single top quark associated production with aW-orH-*, Physical Review D **82** (2010). Cited on page 51.

[172] N. Kidonakis, *Next-to-next-to-leading logarithm resummation fors-channel single top quark production*, Physical Review D **81** (2010). Cited on page 51.

[173] ATLAS Collaboration, *Electron and photon performance measurements with the ATLAS detector using the 2015–2017 LHC proton-proton collision data*, Journal of Instrumentation **14** (2019) P12006–P12006. Cited on page 52.

[174] ATLAS Collaboration, *Performance of jet substructure techniques for large-R jets in proton-proton collisions at* $\sqrt{s} = 7$ *TeV using the ATLAS detector*, Journal of High Energy Physics **2013** (2013). Cited on page 54.

[175] M. Cacciari, G. P. Salam, and G. Soyez, *The catchment area of jets*, Journal of High Energy Physics **2008** (2008) 005–005. Cited on page 54.

[176] M. Cacciari and G. P. Salam, *Pileup subtraction using jet areas*, Physics Letters B **659** (2008) 119–126. Cited on page 54.

[177] V. Barger, A. D. Martin, and R. J. N. Phillips, *Perpendicularev mass fromW decay*, Zeitschrift für Physik C Particles and Fields **21** (1983) 99–101. Cited on page 55.

[178] ATLAS Collaboration, *Object-based missing transverse momentum significance in the ATLAS detector*, tech. rep., CERN, Geneva, Jul, 2018. https://cds.cern.ch/record/2630948. Cited on page 55.

[179] A. LeNail, *Webtool to generate neural network image representations*, http://alexlenail.me/NN-SVG/index.html. last accessed 12.05.2021. Cited on page 60.

[180] D. P. Kingma and J. Ba, *Adam: A Method for Stochastic Optimization*, 2017. arXiv:1412.6980. Cited on pages 57 and 62.

[181] A. Paszke, et al., *PyTorch: An Imperative Style, High-Performance Deep Learning Library*, pp. , 8024–8035. Curran Associates, Inc., 2019. arXiv:1912.01703. Cited on page 60.

[182] N. Srivastava, et al., *Dropout: a simple way to prevent neural networks from overfitting*, The journal of machine learning research **15** (2014) 1929–1958, https://jmlr.org/papers/v15/srivastava14a.html. Cited on page 62.

[183] S. Ioffe and C. Szegedy, *Batch normalization: Accelerating deep network training by reducing internal covariate shift*, pp. , 448–456, PMLR. 2015. arXiv:1502.03167. Cited on page 62.

[184] I. J. Good, *Rational Decisions*, Journal of the Royal Statistical Society. Series B (Methodological) **14** (1952) 107–114, http://www.jstor.org/stable/2984087. Cited on page 62.

[185] F. Mosteller and J. W. Tukey, *Data analysis, including statistics*, Handbook of social psychology **2** (1968) 80–203. Cited on page 67.

[186] G. Cowan, K. Cranmer, E. Gross, and O. Vitells, *Asymptotic formulae for likelihood-based tests of new physics*, The European Physical Journal C **71** (2011) 1–19. Cited on page 68.

[187] C. Lester and D. Summers, *Measuring masses of semi-invisibly decaying particle pairs produced at hadron colliders*, Physics Letters B **463** (1999) 99–103. Cited on page 68.

[188] A. Barr, C. Lester, and P. Stephens, *A variable for measuring masses at hadron colliders when missing energy is expected; m_{T2}: the truth behind the glamour*, Journal of Physics G: Nuclear and Particle Physics **29** (2003) 2343–2363. Cited on page 68.

[189] ATLAS Collaboration, *Jet energy scale measurements and their systematic uncertainties in proton-proton collisions at $\sqrt{s} = 13$ TeV with the ATLAS detector*, Physical Review D **96** (2017). Cited on page 79.

[190] ATLAS Collaboration, *Jet energy resolution in proton-proton collisions at $\sqrt{s} = 7$ TeV recorded in 2010 with the ATLAS detector*, The European Physical Journal C **73** (2013). Cited on page 79.

[191] ATLAS Collaboration, *In situ calibration of large-radius jet energy and mass in 13 TeV proton–proton collisions with the ATLAS detector*, The European Physical Journal C **79** (2019). Cited on page 80.

[192] ATLAS Collaboration, *E_T^{miss} performance in the ATLAS detector using 2015-2016 LHC p-p collisions*, tech. rep., CERN, Geneva, Jun, 2018. https://cds.cern.ch/record/2625233. Cited on page 80.

[193] ATLAS Collaboration, *Studies on top-quark Monte Carlo modelling for Top2016*, tech. rep., CERN, Geneva, Sep, 2016. https://cds.cern.ch/record/2216168. Cited on page 80.

[194] S. Frixione, et al., *Single-top hadroproduction in association with aWboson*, Journal of High Energy Physics **2008** (2008) 029–029. Cited on page 80.

[195] LHCb Collaboration, *Test of lepton universality in beauty-quark decays*, 2021. Cited on page 93.

[196] Muon $g-2$ Collaboration, *Measurement of the Positive Muon Anomalous Magnetic Moment to 0.46 ppm*, Physical Review Letters **126** (2021), https://doi.org/10.1103/physrevlett.126.141801. Cited on page 93.

[197] HL-LHC project group, *LHC/HL-LHC Plan (last update January 2021)*, 2021. https://hilumilhc.web.cern.ch/sites/hilumilhc.web.cern.ch/files/images/HL-LHC-plan-2021-1.pdf. last accessed 23.04.2021. Cited on page 94.

[198] H. Damerau, et al., *LHC Injectors Upgrade, Technical Design Report*. Dec, 2014. https://cds.cern.ch/record/1976692. Cited on page 94.

[199] L. Arnaudon, et al., *Linac4 Technical Design Report*, tech. rep., CERN, Geneva, Dec, 2006. https://cds.cern.ch/record/1004186. Cited on page 94.

[200] ATLAS Collaboration, *ITk Pixel Layout Updates*, Itk-2020-002, 04, 2020, https://atlas.web.cern.ch/Atlas/GROUPS/PHYSICS/PLOTS/ITK-2020-002/. Cited on pages 96, 97, 99, and 100.

[201] J. Chistiansen and M. Garcia-Sciveres, *RD Collaboration Proposal: Development of pixel readout integrated circuits for extreme rate and radiation*, tech. rep., CERN, Geneva, Jun, 2013. https://cds.cern.ch/record/1553467. Cited on page 96.

[202] RD53 Collaboration, M. Garcia-Sciveres, *RD53B Design Requirements*, tech. rep., CERN, Geneva, Feb, 2019. https://cds.cern.ch/record/2663161. Cited on page 96.

[203] T. Flick, *The phase II ATLAS Pixel upgrade: the Inner Tracker (ITk)*, Journal of Instrumentation **12** (2017) C01098–C01098. Cited on page 96.

[204] T. Böhlen, et al., *The FLUKA Code: Developments and Challenges for High Energy and Medical Applications*, Nuclear Data Sheets **120** (2014) 211–214. Cited on page 98.

[205] ATLAS Collaboration, *Public radiation simulation results, Phase II ITk Inclined Duals (April 2018)*, 2018. https://twiki.cern.ch/twiki/bin/view/AtlasPublic/RadiationSimulationPublicResults. last accessed 28.04.2021. Cited on page 98.

[206] ATLAS Collaboration, *Latest Performance Studies of the ATLAS Inner Tracker (ITk) in the HL-LHC*, 2020. https://atlas.web.cern.ch/Atlas/GROUPS/PHYSICS/PLOTS/IDTR-2019-009/. IDTR-2019-009. Cited on pages 99 and 100.

[207] ATLAS Collaboration, *Technical Design Report for the Phase-II Upgrade of the ATLAS TDAQ System*, tech. rep., CERN, Geneva, Sep, 2017. https://cds.cern.ch/record/2285584. Cited on pages 100 and 101.

[208] J. Anderson, et al., *FELIX: a High-Throughput Network Approach for Interfacing to Front End Electronics for ATLAS Upgrades*, Journal of Physics: Conference Series **664** (2015) 082050. Cited on page 101.

[209] Telecommunications Industry Association et al., *Electrical Characteristics of Low Voltage Differential Signalling (LVDS) Interface Circuits*. Telecommunications Industry Association, 1996. Cited on page 102.

[210] XILINX, *Aurora 64B/66B Protocol Specification*, 10, 2014. https://www.xilinx.com/support/documentation/ip_documentation/aurora_64b66b_protocol_spec_sp011.pdf. last accessed 05.05.2021. Cited on page 102.

[211] C. Chen, et al., *A gigabit transceiver for the ATLAS inner tracker pixel detector readout upgrade*, Journal of Instrumentation **14** (2019) C07005–C07005. Cited on page 103.

[212] C. Chen, et al., *1.28 and 5.12 Gbps multi-channel twinax cable receiver ASICs for the ATLAS Inner Tracker Pixel Detector upgrade*, Nuclear Instruments and Methods in Physics Research Section A: Accelerators, Spectrometers, Detectors and Associated Equipment **981** (2020) 164439. Cited on pages 103 and 108.

[213] P. Moreira, *The LpGBT project status and overview*, 2016. https://indico.cern.ch/event/468486/contributions/1144369/attachments/1239839/1822836/aces.2016.03.08.pdf. ACES 2016 - Fifth Common ATLAS CMS Electronics Workshop for LHC Upgrades. Cited on pages 103 and 105.

[214] lpGBT Team, *Manual of the lpGBT*, 4, 2021. https://lpgbt.web.cern.ch/lpgbt/v0/lpGBT.pdf. last accessed 04.05.2021, internal to CERN users. Cited on pages 103, 105, and 106.

[215] C. Soós, et al., *Versatile Link PLUS transceiver development*, Journal of Instrumentation **12** (2017) C03068–C03068. Cited on pages 103 and 104.

[216] L. O. J. Troska, C. Soos, *The Versatile Link$^+$ Application Note*, 2020. https://edms.cern.ch/ui/file/2149674/1/VTRxPlusApplicationNote.pdf. last accessed 03.05.2021. Cited on pages 103, 104, and 105.

[217] J. Troska, *Versatile Link$^+$ Transceiver (VTRx$^+$), revision v2.6*, 2021. https://edms.cern.ch/ui/file/1719329/1/VTRxPlus_spec.pdf. last accessed 03.05.2021. Cited on pages 103 and 118.

[218] P. Moreira, P. Gui, and M. Menouni, *The GBTIA, a 5 Gbit/s Radiation-Hard Optical Receiver for the SLHC Upgrades*, 2009. http://cds.cern.ch/record/1235833. Cited on page 105.

[219] Z. Zeng, et al., *LDQ10: a compact ultra low-power radiation-hard 4 × 10 Gb/s driver array*, Journal of Instrumentation **12** (2017) P02020–P02020. Cited on page 105.

[220] NXP Semiconductors, *I^2C-bus specification and user manual, Rev. 6*, 4, 2014. https://www.nxp.com/docs/en/user-guide/UM10204.pdf. last accessed 03.05.2021. Cited on page 105.

[221] J. M. Mendez, S. Baron, S. Kulis, and J. Fonseca, *New LpGBT-FPGA IP: Simulation model and first implementation*, in *Proceedings of Topical Workshop on Electronics for Particle Physics — PoS(TWEPP2018)*. Sissa Medialab, May, 2019. Cited on page 105.

[222] lpGBT Team, *lpGBT-FPGA Core repository*, https://gitlab.cern.ch/gbt-fpga/lpgbt-fpga. last accessed 01.06.2021. Cited on pages 105 and 123.

[223] I. S. Reed and G. Solomon, *Polynomial Codes Over Certain Finite Fields*, Journal of the Society for Industrial and Applied Mathematics **8** (1960) 300–304. Cited on page 106.

[224] CMS Collaboration, *The Phase-2 Upgrade of the CMS Tracker*, tech. rep., CERN, Geneva, Jun, 2017. https://cds.cern.ch/record/2272264. Cited on page 107.

[225] T. Wijnands, et al., *Optical absorption in commercial single mode optical fibers in a high energy physics radiation field*, IEEE transactions on nuclear science **55** (2008) 2216–2222. Cited on page 107.

[226] J. Pater, et al., *High-speed Data Transmission Task Force Report*, 03, 2019. ATLAS internal document. Cited on page 107.

[227] M. Janda, *ITk service update*, 09, 2020. https://indico.cern.ch/event/950039/contributions/3997443/attachments/2108242/3546073/ITk_service_update.pdf. ITk Week workshop September 2020. Cited on page 107.

[228] J. K. Anders, et al., *ITk Pixel - Supporting documentation for PDR: The Optosystem*, 03, 2020. ATLAS internal document. Cited on page 108.

[229] F. Faccio, et al., *The bPOL12V DCDC converter for HL-LHC trackers: towards production readiness*, in *Proceedings of Topical Workshop on Electronics for Particle Physics — PoS(TWEPP2019)*. Sissa Medialab, Mar., 2020. Cited on pages 109 and 111.

[230] G. Ripamonti, et al., *2.5V step-down DCDCs: a radiation-hard solution for power conversion*, in *Proceedings of Topical Workshop on Electronics for Particle Physics — PoS(TWEPP2019)*. Sissa Medialab, Mar., 2020. Cited on page 109.

[231] A. Walsemann, et al., *A CANopen based prototype chip for the Detector Control System of the ATLAS ITk Pixel Detector*, in *Proceedings of Topical Workshop on Electronics for Particle Physics — PoS(TWEPP2019)*. Sissa Medialab, Mar., 2020. Cited on page 109.

[232] T. Henss, et al., *The hardware of the ATLAS Pixel Detector Control System*, Journal of Instrumentation **2** (2007) P05006–P05006. Cited on page 109.

[233] R. Müller, *Characterisation of the optical-electrical data conversion system for the ATLAS ITk upgrade*, Master's thesis, Albert Einstein Center for Fundamental Physics, University of Bern, 2020. Cited on page 111.

[234] J. A. Kunzmann, *Power distribution for the Optosystem of the ATLAS ITk Pixel Detector*, Bachelor Thesis, Albert Einstein Center for Fundamental Physics, University of Bern, 8, 2020. Cited on page 111.

[235] K. Vyithiyalingam, *Design and Performance Studies of the Optosystem for the ATLAS Inner Tracker Detector towards HL-LHC*, Master's thesis, Albert Einstein Center for Fundamental Physics, University of Bern, 8, 2020. Cited on page 113.

[236] L. Franconi, *ITk Pixel data transmission: Summary of the status and future tests*, 02, 2021. https://indico.cern.ch/event/920306/contributions/4213787/attachments/2184265/3690331/20210204_Franconi_ITkWeek_DataTransmission_v1.pdf. ITk Week workshop February 2021. Cited on page 113.

[237] XILINX, *KC705 Evaluation Board for the Kintex-7 FPGA, v1.9*, 2019. https://www.xilinx.com/support/documentation/boards_and_kits/kc705/ug810_KC705_Eval_Bd.pdf. last accessed 03.05.2021. Cited on page 115.

[238] *IEEE Standard for VHDL Language Reference Manual*, IEEE Std 1076-2019 (2019) 1–673. Cited on page 115.

[239] XILINX, *Integrated Bit Error Ratio Tester 7 Series GTX Transceivers v3.0*, 6, 2016. https://www.xilinx.com/support/documentation/ip_documentation/ibert_7series_gtx/v3_0/pg132-ibert-7series-gtx.pdf. last accessed 03.05.2021. Cited on page 116.

[240] XILINX, *7 Series FPGAs GTX/GTH Transceivers User Guide*, 8, 2018. https://www.xilinx.com/support/documentation/user_guides/ug476_7Series_Transceivers.pdf. last accessed 03.05.2021. Cited on page 116.

[241] EXFO, *LTK-1 benchmark optical kits specification sheet*, 08, 2020. https://www.exfo.com/umbraco/surface/file/download/?ni=10965&cn=en-US&pi=5625. last accessed 06.05.2021. Cited on page 116.

[242] Keysight Technologies, *Agilent 8163B data sheet*, 3, 2018. https://www.keysight.com/us/en/assets/7018-01037/data-sheets/5988-3924.pdf. last accessed 04.05.2021. Cited on page 117.

[243] Keysight Technologies, *DSA91204A data sheet*, 9, 2017. https://www.keysight.com/ch/de/assets/7018-01734/data-sheets/5989-7819.pdf. last accessed 04.05.2021. Cited on page 117.

[244] Samtec, *Specifications of the ERF8/ERM8 connectors*, 10, 2015. https://suddendocs.samtec.com/productspecs/erm8-erf8.pdf. last accessed 03.05.2021. Cited on page 119.

[245] XILINX, *Integrated Logic Analyzer v6.2: LogiCORE IP Product Guide*, 10, 2016. https://www.xilinx.com/support/documentation/ip_documentation/ila/v6_2/pg172-ila.pdf. last accessed 29.05.2021. Cited on page 119.

[246] Silicon Labs, *Any-frequency precision clock multiplier/jitter attenuator*, 2014. https://www.silabs.com/documents/public/data-sheets/Si5324.pdf. last accessed 29.05.2021. Cited on page 120.

[247] FCC Collaboration, *FCC Physics Opportunities*, The European Physical Journal C **79** (2019), https://doi.org/10.1140/epjc/s10052-019-6904-3. Cited on page 123.

[248] FCC Collaboration, *FCC-ee: The Lepton Collider*, The European Physical Journal Special Topics **228** (2019) 261–623. Cited on page 123.

[249] FCC Collaboration, *FCC-hh: The Hadron Collider*, The European Physical Journal Special Topics **228** (2019) 755–1107. Cited on page 123.

Declaration of consent

on the basis of Article 18 of the PromR Phil.-nat. 19

Name/First Name: Ilg, Armin

Registration Number: 12-119-087

Study program: PhD in Physics

Bachelor ☐ Master ☐ Dissertation ☑

Title of the thesis: Novel Analysis Techniques and High-Speed Readout to Search for New Physics

Supervisor: Prof. Michele Weber

I declare herewith that this thesis is my own work and that I have not used any sources other than those stated. I have indicated the adoption of quotations as well as thoughts taken from other authors as such in the thesis. I am aware that the Senate pursuant to Article 36 paragraph 1 litera r of the University Act of September 5th, 1996 and Article 69 of the University Statute of June 7th, 2011 is authorized to revoke the doctoral degree awarded on the basis of this thesis.
For the purposes of evaluation and verification of compliance with the declaration of originality and the regulations governing plagiarism, I hereby grant the University of Bern the right to process my personal data and to perform the acts of use this requires, in particular, to reproduce the written thesis and to store it permanently in a database, and to use said database, or to make said database available, to enable comparison with theses submitted by others.

Bern, 05.07.2021

Place/Date

Signature